

**The application of Laser Induced
Breakdown Spectroscopy (LIBS) to
the analysis of geological samples in
simulated extra-terrestrial
atmospheric environments**

N. S. LUCAS

Ph.D. Thesis

2007

Contents

Contents	
List of Tables.....	iv
List of Figures	v
Acknowledgements	xii
7 Acknowledgements	xii
Declaration	xiii
Abbreviations	xiv
Abstract	xv
1. Introduction	1
1.1 Background	1
1.2 Planet and Moon Environments	3
1.3 Rock Composition.....	6
2. History and Uses.....	8
2.1 Scientific History of LIBS	8
2.3 Uses, Types and Divisions	10
3. Theory	12
3.1 Laser.....	12
3.2 Induced (Laser Ablation)	14
3.3 Breakdown (Plasmas).....	21
3.3.1 <i>Conditions Local to Emitting Particle</i>	24
3.3.2 <i>Conditions Along Entire Emission Path</i>	26
3.4 Spectroscopy	30
3.5 Pressure Related Processes	35
3.6 Power Related Processes.....	39
3.7 Gas Related Processes.....	39
3.9 Optical Fibres	41
3.10 Spectral Resolution/Diffraction	42
3.11 Detectors	44
3.12 Timing	44
3.13 Limit of Detection	45
4. Development of LIBS.....	51
4.1 Experimental Apparatus.....	51
4.2 Laser Optimisation	52
4.3 Light Coupling Optics.....	55
4.4 System Malfunction Evaluation.....	56
4.4.1 <i>EPROM:</i>	56
4.4.2 <i>Stepper Motor:</i>	56
4.4.3 <i>Mirror:</i>	58
4.4.4 <i>PTG Cable:</i>	58
4.4.5 <i>Software:</i>	58
4.4.6 <i>PTG Card/Timing:</i>	59
4.5 Grating Efficiencies	65
4.6 Dummy's Guides	66
5. Development of Pressure Apparatus.....	69
5.1 Experimental Apparatus.....	69
5.2 Dome Window	69
5.3 Sample Stage.....	71

5.5 Optical Fibre.....	72
5.4 Vacuum Apparatus.....	74
5.5 General High Pressure/Vacuum Apparatus	75
5.6 Leak Detection and Calibration	76
5.7 Optical Bench Layout Incorporating Vacuum Chamber	77
6. Experimental Results	78
6.1 Development of Experimentation Techniques.....	78
6.1.1 General Experimental Parameters	78
6.1.2 Characterisation/Calibration.....	79
6.1.3 Optimum Fluence	81
6.1.4 Imaging	84
6.1.5 Matrix Identification	85
6.2 Depth Profiling.....	88
6.3 Samples	94
6.3.1 Silicon.....	94
6.3.2 Sandstone	95
6.3.3 Slate.....	96
6.3.4 Marble.....	97
6.4 Energy-dispersive X-ray spectroscopy (EDX).....	99
6.5 Temporal Delay.....	102
6.6 Gate Width Variations.....	109
6.7 Power Variations.....	111
6.8 Surface Weathering.....	116
6.9 Pressure and Gaseous Content Variations.....	125
6.9.1 Pressure Variations.....	125
6.9.2 Ambient Gas Interference	136
6.9.3 Wavelength Variations	139
7. Errors, Conclusions and Further Work	145
7.1 Errors.....	145
7.2 Conclusions	147
7.3. Further Work.....	152
References	153
Appendices	161
Appendix A:	161
<i>Comparative study of laser induced breakdown spectroscopy and secondary ion mass spectrometry applied to dc magnetron sputtered as-grown copper indium diselenide (CIS)</i>	161
Appendix B:	168
<i>LIBS and Remote Raman Spectroscopy References By Los Alamos National Laboratory (LANL) and Collaborators</i>	168
Appendix C:	169
<i>Theoretical Models of the Laser-Solid Interaction</i> ⁴⁹	169
Appendix D:	170
<i>Acton Research Corporation, SpectraPro 500i Specifications:</i>	170
Appendix E:	172
<i>Grating Efficiency Curves</i>	172
Appendix F:.....	173
<i>Lens Database, compiled by N. Lucas:</i>	173
<i>Lens Data:</i>	176
<i>Paraxial Constants:</i>	176

Appendix G:	177
<i>Controller/Software Sweeps, Author N. Lucas</i>	177
Appendix H:	185
<i>Dummys Guide to:</i>	185
<i>Acton Spectrometer with WinSpec and Grams software.</i>	185
<i>Author N. Lucas</i>	185
Appendix I:	196
<i>Dummys Guide to:</i>	196
<i>Spectrophotometer plotting operation</i>	196
<i>Author N. Lucas</i>	196
Appendix J:	197
<i>Dummys Guide to:</i>	197
<i>Conversion from WinSpec to Grams & Multifile Building</i>	197
<i>Author N. Lucas</i>	197
Appendix K:	200
<i>Notes pertaining to catalogue data of elemental line spectra</i>	200
Appendix L:	203
<i>Pascal program for spectral line search, Author N. Lucas</i>	203
Appendix M:	207
<i>Access queries to interrogate spectral data, Author N. Lucas</i>	207
Appendix N:	209
<i>VBA program for spectral line search, Author N. Lucas</i>	209
Appendix O:	212
<i>VBA programmes for data analysis, correlation and formatting. Author N. Lucas</i>	212
Appendix P:.....	217
<i>Pascal program to analyse the intensity of selected emission peaks, Author N. Lucas</i>	217
Appendix Q:	219
<i>Pascal program to calculate the relative standard deviation of a dataset, Author N. Lucas</i>	219
Appendix R:	220
<i>Dummys Guide to:</i>	220
<i>Acquire a Depth Profile</i>	220
<i>Author N. Lucas</i>	220

List of Tables

- Table 1.1: Pressure and Gaseous environments within the chosen experimental range¹⁻³.
- Table 3.1: Doppler and Stark widths from literature³⁴, with electron densities of 10^{17}.cm^{-3} .
- Table 3.2: Energy ordering of subshells
- Table 3.3: Spectroscopic notation with respect to azimuthal quantum number.
- Table 3.4: Pressure values and corresponding mean free paths. (calculated from equation 3.20)
- Table 4.1: Table showing wavelength reproducibility errors, Grating 2400g/mm
- Table 4.2: Table showing wavelength reproducibility errors, Grating 600g/mm
- Table 4.3: Table showing wavelength reproducibility errors, Grating 150g/mm.
- Table 6.1: Elemental ratios of constituents in sandstone
- Table 6.2: Elemental ratios of constituents in weathered sandstone
- Table 6.3: Elemental ratios of constituents in pale slate
- Table 6.3: Elemental ratios of constituents in dark slate

List of Figures

- Figure 1.1: Illustrative study of LIBS timeline. (Composite drawn from many sources)
- Figure 1.2: Image of the atmospheric regions of Titan in comparison to Earth⁵.
- Figure 1.3: Possible present-day structure of Titan's interior¹².
- Figure 1.4: Image of Titan's surface taken by the Huygens lander on January 14th, 2005¹⁴.
- Figure 2.1: LIBS publications by year groupings³⁰
- Figure 3.1: Illustration of the pumping arrangement of a Nd:YAG laser.
- Figure 3.2: Surelite laser optical layout
- Figure 3.3: Illustration of possible transitions of electrons. (Composite drawn from many sources)
- Figure 3.4: Schematic diagram of plasma propagation³⁴
- Figure 3.5: Graph showing matrix effect evident in samples containing both sand and lead⁸⁰.
- Figure 3.6: Saha factors applied to nitrogen⁹⁹ (pressure=0.1Pa)
- Figure 3.7: Energy level diagram for one electron atom. (composite drawn from many sources)
- Figure 3.8: Influences on atomic energy levels¹⁰³.
- Figure 3.9: Absorption bands of methane from 750-940nm¹¹⁴
- Figure 3.10: Image of total internal reflection inside a optical fibre.
- Figure 3.11: Illustration of diffraction parameters for a grating.
- Figure 3.12: Illustration of diffraction parameters for a blazed grating.
- Figure 3.13: An image intensifier tube
- Figure 3.14: Illustration of timing requirements for LIBS experiments.
- Figure 4.1: Setup and image of beam profile capture using CCD camera
- Figure 4.2: Setup and circuit diagram of beam profile capture using photodiode
- Figure 4.3: Charts showing beam profile from photodiode capture, the different colours represent the beam intensity
- Figure 4.4: Light coupling optics lens setup diagram
- Figure 4.5: Transmission response of orange perspex.
- Figure 4.6: Schematic of the system timing using pulse generator
- Figure 4.7: Circuit diagram of impedance matching circuit
- Figure 4.8: Circuit diagram of delay circuit
- Figure 4.9: Schematic of the system timing using delay and impedance circuit.
- Figure 4.10: Schematic of the system timing, showing redundant parts of system to be removed for calibration.
- Figure 4.11: Schematic of the system timing, showing setup with external timing box.
- Figure 4.12: Schematic of the final arrangement for the timing setup of the LIBS system
- Figure 4.13: Schematic of the final arrangement for the timing setup of the LIBS system, with inherent delays shown.
- Figure 4.14: Intensity versus wavelength chart for mercury lamp emissions obtained from spectrometer captures and NIST values.

- Figure 4.15: Grating efficiencies versus wavelength
- Figure 4.16: Intensity versus wavelength for gratings corrected for their efficiency wavelength response
- Figure 5.1: Working drawings of HPVA chamber
- Figure 5.2: Chart showing transmission curve for the HPVA dome.
- Figure 5.3: Image to show micrometer feedthroughs of sample stage on the HPVA
- Figure 5.4: Image to show sample stage and coupling bracket
- Figure 5.5: Image of configuration of fibre bundle at the spectrometer end
- Figure 5.6: Drawing of optical fibre feedthrough, courtesy of John Cowpe and Richard Pilkington
- Figure 5.7: Image showing alignment of fibre end
- Figure 5.8: Image showing optical fibre feedthrough
- Figure 5.9: Schematic of vacuum apparatus setup
- Figure 5.10: Schematic of high pressure/vacuum apparatus setup
- Figure 5.11: Calibration of 100sccm MFC
- Figure 5.12: Calibration of 20sccm MFC
- Figure 5.13: Rate of fill of HPVA
- Figure 5.14: Leak rate of vacuum apparatus
- Figure 5.15: Image of Praxair Bourdon gauge
- Figure 5.16: Average of three sets of measurements for calibration of the Bourdon gauge when used at pressures below atmospheric
- Figure 5.17: Schematic of optical bench setup
- Figure 6.1: Graph showing fluctuations in cadmium lamp intensity over time
- Figure 6.2: Calibration using mercury lamp, 150grooves/mm grating
- Figure 6.3: Calibration using mercury lamp, 600grooves/mm
- Figure 6.4: Calibration using mercury lamp, 2400grooves/mm
- Figure 6.5: Copper emission spectrum
- Figure 6.6: Chart showing fluence at varying distances from the focal point of the final lens
- Figure 6.7: Emission intensity versus distance from focal point for CIS and its constituents
- Figure 6.8: Spectrometer image of cadmium emission lines
- Figure 6.9: Imaged size of spectrometer entrance slit versus actual vernier reading
- Figure 6.10: Spectral responses of solder matrix and its constituent parts
- Figure 6.11: Solder emission spectrum
- Figure 6.12: Addition of constituent species emission spectra. (Sn, Pb, Cu, rosin flux)
- Figure 6.13: Solder emission spectrum minus lead emission spectrum
- Figure 6.14: Solder emission spectra minus lead and tin emission spectra
- Figure 6.15: Solder emission spectrum minus lead, tin and copper emission spectra
- Figure 6.16: Solder emission spectrum minus lead, tin and copper emission spectra
- Figure 6.17: Shot versus intensity plot to illustrate removal of CIS on silicon substrate, $1.33 \times 10^8 \text{Wcm}^{-2}$
- Figure 6.18: Shot versus intensity plot to illustrate removal of CIS on glass substrate, $1.33 \times 10^8 \text{Wcm}^{-2}$

- Figure 6.19: SIMS comparison of copper, indium and selenium depth distributions
- Figure 6.20: RBS plot showing experimental results cross referenced with simulated results
- Figure 6.21: Images of ablation crater's on thin film CIS sample deposited on silicon.
- Figure 6.22: SEM image showing an ablation crater
- Figure 6.23: Image of silicon sample after laser ablation, the circles are ablation craters.
- Figure 6.24: Silicon sample in atmospheric conditions, 150g/mm grating
- Figure 6.25: Silicon Sample in atmospheric conditions, 2400g/mm grating
- Figure 6.26: Images of sandstone samples, with ablation craters clearly visible. Both were taken from a larger block shown on the left, where organic residues can be seen building up on the surface, the clean stone visible underneath.
- Figure 6.27: Sandstone sample emission spectrum in atmospheric conditions, 2400g/mm
- Figure 6.28: Slate sample showing ablation craters and re-deposition of material around the crater.
- Figure 6.29: Pale slate sample in atmospheric conditions, 2400g/mm grating
- Figure 6.30: Dark slate sample in atmospheric conditions, 2400g/mm grating
- Figure 6.31: Pale slate sample in 1 bar nitrogen fill, 2400g/mm grating
- Figure 6.32: Dark slate sample in 1 bar nitrogen fill, 2400g/mm grating
- Figure 6.33: Images of marble samples, the one on the left showing the crystalline structure, the one on the right showing the ablation craters and in some cases the re-deposition from a partial or full methane content atmosphere.
- Figure 6.34: Marble sample in atmospheric conditions, 2400g/mm grating
- Figure 6.35: Marble sample emission spectrum, 1 bar nitrogen fill, 2400g/mm grating
- Figure 6.36: Marble sample emission spectrum, in vacuum as emission lines exhibit self-reversal at other pressures, 2400g/mm grating
- Figure 6.37: Sandstone EDX image
- Figure 6.38: Sandstone EDX image, 4* original magnification to resolve iron and copper peaks.
- Figure 6.39: Weathered sandstone EDX image
- Figure 6.40: EDX Image of marble sample
- Figure 6.41: Pale slate EDX image
- Figure 6.42: Dark slate EDX image
- Figure 6.43: Delay variation, silicon sample, atmospheric pressure
- Figure 6.44: Delay variation, silicon sample, 1.5 bar pressure of gas mixture 94%N₂ 6%CH₄
- Figure 6.45: Delay versus emission intensity of the silicon emission line at 251.61 nm in different samples. Averaged over 15 shots, 1.5 bar pressure with gas mixture 94%N₂ 6%CH₄
- Figure 6.46: Delay variation, silicon sample, 1.5 bar pressure of gas mixture 93%N₂ 7%CH₄.
- Figure 6.47: Delay variation, silicon sample, under vacuum pressure of 3×10^{-4} mb.

- Figure 6.48: Delay variation, sandstone sample, under vacuum pressure of 5×10^{-2} mb.
- Figure 6.49: Silicon pressure variations, delay 600 ns
- Figure 6.50: Silicon delay variations, pressure 3×10^{-4} mb
- Figure 6.51: Silicon delay variations, pressure 4×10^{-6} mb
- Figure 6.52: Width variation in microseconds at 1.5 bar with 6% CH₄ 94% N₂ gaseous mixture, silicon sample
- Figure 6.53: Width variation in microseconds at 1.5 bar with 6% CH₄ 94% N₂ gaseous mixture, silicon sample
- Figure 6.54: Width variation in microseconds at 1.5 bar with 5% CH₄ 95% N₂ gaseous mixture, silicon sample
- Figure 6.55: Width variation in microseconds at 1.5 bar with 7% CH₄ 93% N₂ gaseous mixture, silicon sample
- Figure 6.56: Width variation in microseconds at 1.5 bar with 6% CH₄ 94% N₂ gaseous mixture, sandstone sample
- Figure 6.57: Schematic diagram of optical bench setup for power variations
- Figure 6.58: Power output with relation to iris size
- Figure 6.59: Power variation (mJ/pulse) on silicon sample, gas composition: 5% CH₄ 95% N₂
- Figure 6.60: Power variation (mJ/pulse) on sandstone sample, gas composition: 5% CH₄ 95% N₂
- Figure 6.61: Power variation (mJ/pulse) on silicon sample, gas composition: 7% CH₄ 93% N₂
- Figure 6.62: Power Variation on Sandstone Sample, gas composition: 6% CH₄ 94% N₂
- Figure 6.63: Averaged over 15 shots, Power Variation on Sandstone Sample, gas composition: 6% CH₄ 94% N₂
- Figure 6.64: Logarithmic plot of power variation, sandstone sample, gas composition: 6% CH₄ 94% N₂
- Figure 6.65: Power variation on silicon sample, gas composition: 6% CH₄ 94% N₂
- Figure 6.66: Power variation on weathered sandstone sample, gas composition: 6% CH₄ 94% N₂
- Figure 6.67: Weathered sample 3D emission spectra, 15 shots
- Figure 6.68: Weathered sample spectrum, first shot
- Figure 6.69: Weathered sample spectrum, fifteenth shot
- Figure 6.70: Image of weathered sandstone sample, showing green algae build-up.
- Figure 6.71: Weathered surface emission intensity reduction with shot number in atmospheric conditions
- Figure 6.72: Comparison of silicon line emission intensity increase with shot number in atmospheric conditions
- Figure 6.73: Weathered sample spectrum, first shot at 5×10^{-2} mb
- Figure 6.74: Weathered sample spectrum, fifteenth shot at 5×10^{-2} mb
- Figure 6.75: Weathered surface lines emission intensity reduction with shot number at 5×10^{-2} mb
- Figure 6.76: Comparison of silicon line emission intensity increase with shot number at 5×10^{-2} mb
- Figure 6.77: Weathered sample emission spectrum, first shot at 1.5 bar nitrogen fill

- Figure 6.78: Weathered sample emission spectrum, fifteenth shot at 1.5 bar nitrogen fill
- Figure 6.79: Weathered surface lines emission intensity reduction with 1.5 bar nitrogen fill
- Figure 6.80: Comparison of silicon line emission intensity increase with shot number at 1.5 bar nitrogen fill
- Figure 6.81: Weathered sample emission spectrum, first shot at 1.5 bar methane fill
- Figure 6.82: Weathered sample emission spectrum, fifteenth shot at 1.5 bar methane fill
- Figure 6.83: Weathered surface lines emission intensity reduction with a 1.5 bar methane fill
- Figure 6.84: Comparison of silicon line emission intensity increase with shot number with a 1.5 bar methane fill
- Figure 6.85: Silicon and iron emission line intensity increase with shot number
- Figure 6.86: Weathered sample emission spectrum, first shot at 1.5 bar, 6% CH₄ 94% N₂ fill
- Figure 6.87: Weathered sample emission spectrum, fifteenth shot at 1.5 bar, 6% CH₄ 94% N₂ fill
- Figure 6.88: Weathered surface lines emission intensity reduction with shot number, 1.5 bar 6% CH₄ 94% N₂ fill
- Figure 6.89: Comparison of silicon line emission intensity increase with shot number, 1.5 bar 6% CH₄ 94% N₂ fill
- Figure 6.90: Single shot emission spectrum of silicon sample showing intensity change with pressure, with N₂ as filling gas
- Figure 6.91: 15 shot average, silicon sample, intensity change with pressure, with N₂ as filling gas
- Figure 6.92: Silicon sample emission intensity change with pressure, with 5%/95% mixture as filling gas, variation in millibar
- Figure 6.93: Silicon sample emission intensity change with pressure, with 6% 94% mix as filling gas, variation in millibar
- Figure 6.94: Simplified silicon sample emission intensity change with pressure, with 6% 94% mix as filling gas, variation in millibar
- Figure 6.95: Silicon sample emission intensity change with pressure, with 7%/93% mixture as filling gas, variation in millibar
- Figure 6.96: Silicon sample emission intensity change with pressure, with CH₄ as filling gas, variation in millibar
- Figure 6.97: Sandstone sample emission intensity change with pressure, with N₂ as filling gas, variation in millibar
- Figure 6.98: Sandstone sample emission intensity change with pressure, with CH₄ as filling gas, variation in millibar
- Figure 6.99: Sandstone sample emission intensity change with pressure, with 6%/94% mix as filling gas, variation in millibar
- Figure 6.100: Simplified sandstone samples emission intensity change with pressure, with 6% 94% mix as filling gas, variation in millibar
- Figure 6.101: Chart showing emission intensity change with pressure, with N₂ as filling gas, silicon sample.
- Figure 6.102: Change in emission intensity with pressure variations, 5/95 mix as filling gas, silicon sample

- Figure 6.103: Change in emission intensity with pressure variations , 6/94 mix as filling gas, silicon sample
- Figure 6.104: Change emission intensity with pressure variations, 7/93 mix as filling gas, silicon sample
- Figure 6.105: Change emission intensity with pressure variations, CH₄ as filling gas, silicon sample.
- Figure 6.106: Plot of specific emission line intensity variations from each sample with respect to pressure.
- Figure 6.107: Silicon sample, emission signal with different gaseous content at 1.5 bar
- Figure 6.108: Silicon sample, carbon line emission signal with different gaseous content at 1.5 bar
- Figure 6.109: Silicon sample, carbon emission intensity for various gas fills
- Figure 6.110: Silicon sample, carbon and silicon emission intensities for various gas fills
- Figure 6.111: Plot of silicon and carbon emission intensities from silicon sample, normalised to silicon.
- Figure 6.112: Sandstone sample, carbon and silicon emission intensities for various gas fills
- Figure 6.113: Plot of silicon and carbon emission intensities from sandstone sample, normalised to silicon
- Figure 6.114: Marble sample, carbon, silicon and oxygen emission intensities for various gas fills
- Figure 6.114: Plot of silicon, carbon and oxygen emission intensities from marble sample, normalised to silicon
- Figure 6.115: Emission intensities of various marble emission lines showing variations due to pressure and gaseous content
- Figure 6.116: Pressure variation of Ca(II) 393.37nm and Ca (II) 396.85nm in marble, with N₂ fill. Showing self reversal due to pressure.
- Figure 6.117: Simplified Pressure variation of Ca(II) 393.37nm and Ca (II) 396.85nm in marble, with N₂ fill. Showing self reversal due to pressure.
- Figure 6.118: Pressure versus intensity variation of calcium emission lines from marble sample, with nitrogen filling gas.
- Figure 6.119: Image of dark slate sample showing ferrous reduction spheres.
- Figure 6.120: Image of slate sample showing 'sooting' of the surface from re-deposition at the ablation craters.
- Figure 6.121: Pale slate, emission intensity change with pressure variations, nitrogen filling gas, wavelength centre at 252nm.
- Figure 6.122: Pale slate, emission intensity change with pressure variations, nitrogen filling gas, wavelength centre at 276nm.
- Figure 6.123: Dark slate, emission intensity change with pressure variations, nitrogen filling gas, wavelength centre at 252nm.
- Figure 6.124: Dark slate, emission intensity change with pressure variations, nitrogen filling gas, wavelength centre at 276nm.
- Figure 6.125: Pale slate, pressure versus intensity variations with nitrogen filling gas
- Figure 6.126: Dark slate, pressure versus intensity variations with nitrogen filling gas

- Figure 7.1: One standard deviation of delay versus emission intensity of the silicon emission line at 251.61 nm in different samples. Averaged over 15 shots, 1.5 bar pressure with gas mixture 94%N₂ 6%CH₄
- Figure 7.2: One standard deviation of power versus intensity variations on sandstone sample, gas composition: 6%CH₄ 94%N₂
- Figure 7.3: One standard deviation of change in intensity with pressure, with N₂ as filling gas, silicon sample.
- Figure 7.4: One standard deviations of change in intensity with pressure, with 6/94 mix as filling gas, silicon sample
- Figure 7.5: One standard deviation of change in intensity with pressure, with CH₄ as filling gas, silicon sample.

Acknowledgements

I would initially like to thank all those I worked closely with in the Laser Group at Salford University. To Richard Pilkington for his help and his enthusiasm with P.L.O.P. and Christmas escapes to the country. Robin Hill, without his help to pull it out of the bag I would never have submitted my thesis. Stuart Astin for his kindness of heart and quiet unassuming knowledge and patience with lessons. Helen Brown for mutual expulsion of stress and ‘ciggie break’ escapes. To John Cowpe for his knowledge on vacuum apparatus and systems and to Garry Rowsell for his ‘think tank’ help.

Thanks must go to other staff at Salford University. Jay Smith, for his ingenuity. Steve Hurst and Mike Hulme for their workshop ‘wizardary’. To Bruce (and the voices) and Paul Murphy for their PC know how. Graham Keeler and Brian James for their computer programming and interfacing help. Allan Boardman for his valuable support. Dave armour for his guidance on plasma processes and Keren Maloney for her help and patience with administration support.

External to the university I would like to thank Nigel Murphy and John Wilkinson at Universal Imaging Corporation for their continued support throughout the project.

I give thanks to EPSRC for my funding. I also would like to thank the institutions who made it possible for me to attend conferences with their generous financial support, namely; The Rank Prize Funds; The European Space Agency, The International Astronautics Federation and to Dave Wright of the British Rocketry Oral History Programme.

Thank you to my friends, who I am very lucky to say are too numerous to name, for their help in all things, especially the low times. I give special thanks to Liz Forshaw for unwavering support in all things non-physicsy. To Chris Rollins and Adam Theis for their invaluable CAD help. To my Physiotherapist Byron Clithero, without his help I would still be in agony, unable to work.

Not least I give thanks to my family, without their help, support and love I would have never achieved such dizzy heights!

Declaration

The computer programs and dummy's guides written in this work have been developed by the thesis author.

Abbreviations

ADC	Astronomical Data Centre
CCD	charged-coupled device
CF-LIBS	calibration free laser induced breakdown spectroscopy
CIS	copper indium diselenide
EDX	X-Ray dispersive analysis
EPROM	electronic prompt
ESA	European Space Agency
FO	optical fibre
HPVA	high pressure/vacuum apparatus
IBM	International Business Machines Corporation
ICCD	intensified charged-coupled device
KTP	potassium titanyl phosphate
LANL	Los Alamos national laboratory
LASER	light amplification by stimulated emission of radiation
LED	light emitting diode
LIBS	laser induced breakdown spectroscopy
LOD	limit of detection
LSAW	laser-supported absorption wave
LSCW	laser-supported combustion wave
LSDW	laser-supported detonation wave
LSRW	laser-supported radiation wave
LTE	local thermodynamic equilibrium
LTSD	lens to surface/sample distance
MCP	micro-channel plate
MFC	mass flow controller
MFP	mean free path
MUT	material under test
NASA	National Aeronautics Space Administration
Nd:YAG	neodymium: yttrium-aluminum-garnet
NIST	National Institute of Standards and Technology
PCB	printed circuit board
PTG	programmable timing generator
RBS	Rutherford Backscattering
SEM	scanning electron microscope
SIMS	secondary ion mass spectrometry
TEM ₀₀	fundamental transverse mode
UV-VIS	ultraviolet-visible
VBA	visual basic for applications

Abstract

Laser induced breakdown spectroscopy (LIBS) is a technique that can determine the elemental composition and quantities of a sample by the spectral analysis of a laser induced plume.

This study was undertaken to develop, characterise and assess the use of the LIBS technique on geological samples in different pressure and gaseous environments. The experimental range chosen was dictated by the planetary conditions on Titan and other extra-terrestrial bodies with the samples analysed chosen to complement a range of rock types.

A LIBS system was developed, together with associated experimental apparatus able to acquire results in varying pressure and gaseous environments. The capability of LIBS to analyse weathered rock samples was investigated under various ambient conditions; pressures of 160×10^3 Pa to 0.4×10^{-3} Pa and ambient gaseous mixtures of air, nitrogen and methane.

Particular attention was paid to temporal and power considerations under such regimes. As was expected, the chosen delay time to optimise the emission signals needed to be increased with increasing ambient pressure. At power values as low as 28.5 mJ/pulse (using a 6 ns pulse from a doubled Nd:YAG laser at 532 nm) a valid emission signal could be obtained. Increasing the laser power resulted in a reduction in the overall signal to noise ratio.

It was observed that ambient methane quenches the optical emission signal due to non-radiative transitions. In spite of this, valid qualitative data are obtainable, even when emissions due to carbon transitions from both the sample and the gaseous environment, are present.

Results are presented which support the premise that the LIBS technique can be used to investigate both the surface and depth compositions of geological samples under extra-terrestrial conditions.

1. Introduction

1.1 Background

The main thrust of this research study was to fully commission a laser induced breakdown spectroscopy (LIBS) system for use at Salford University. This equipment was developed to incorporate apparatus able to analyse LIBS in varying pressure environments.

Once commissioned a study was undertaken to examine the effects of pressure and different gaseous environments on the LIBS technique, paying particular attention to temporal affects and power considerations. The environments chosen varied from pressures of 160×10^3 Pa to 0.4×10^{-3} Pa with different gaseous mixtures of air, nitrogen and methane.

This work was personally carried out from conception to completion, with a view to ascertaining the ability of the LIBS technique to acquire good analytical data in the atmosphere of the moon Titan, a previously unexplored experimental environment.

LIBS is a technique that can determine the elemental composition and quantities of a sample by analysis of emission from a laser induced plume. A high power laser is focused onto the material of interest creating a plume; this plume expands over time and spectral emissions result from the relaxation of the constituent excited species. The atomic spectral lines are then used to analyse the material.

The timeline involved in LIBS analysis can be broken down and summarised, illustrated in figure 1.1, each section being explained in greater detail in the following theory chapter.

- 1) Incidence of the laser pulse upon the sample.
- 2) Absorption and heating of the sample via the incident laser energy
- 3) Priming electrons initiate the laser ablation process
- 4) The surface of the sample is broken down and ablated.

- 5) The plume itself acts to shield the sample surface from the remaining incident laser light.
- 6) After the laser pulse finishes the plume expands away from the surface
- 7) Once the plume has dissipated some constituents may be re-deposited on the sample surface.

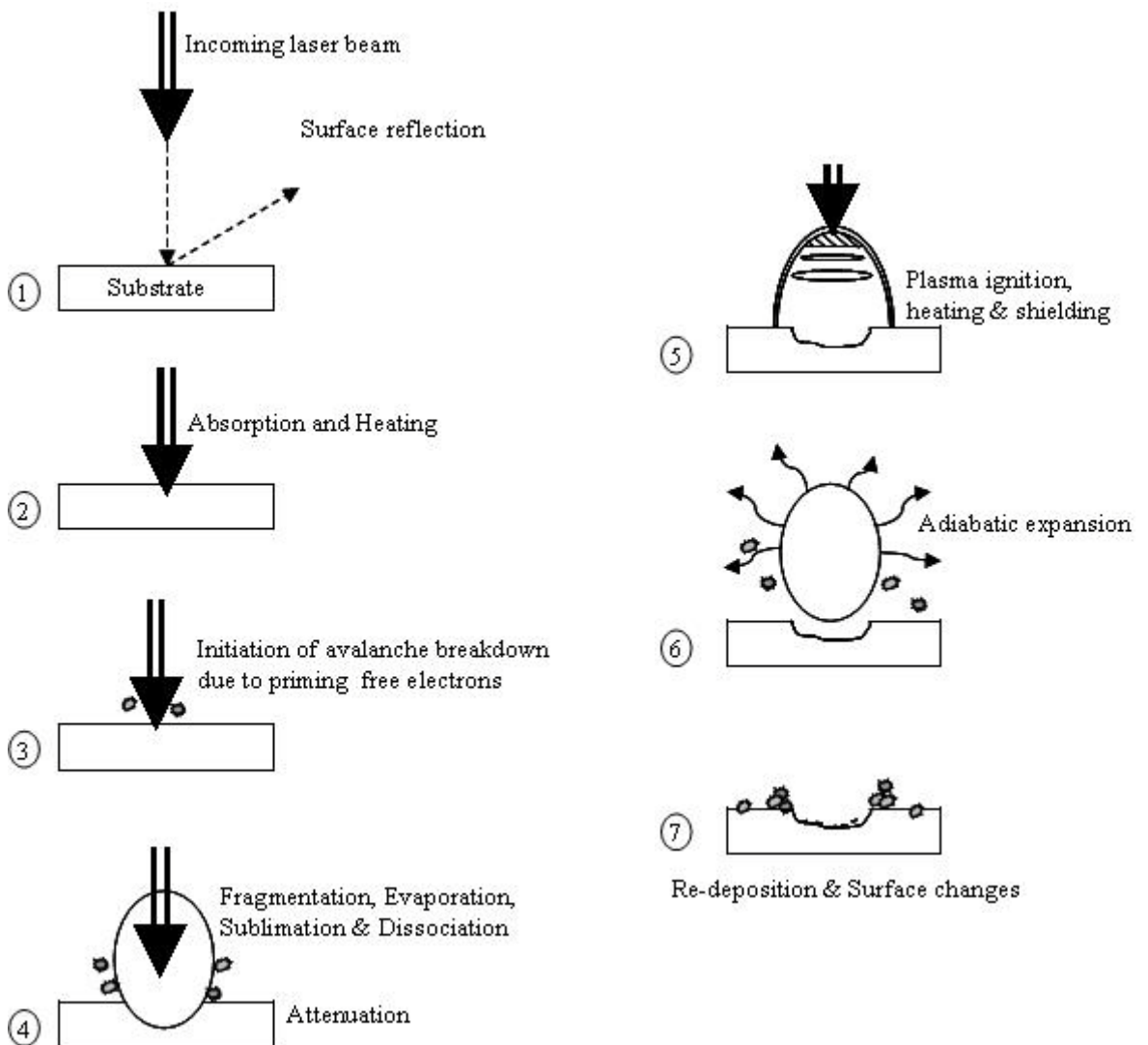


Figure 1.1: Illustrative study of LIBS timeline.
(Composite drawn from many sources)

1.2 Planet and Moon Environments

The experimental range chosen accounted for the atmospheric conditions on varying moons and planets in our solar system, paying particular attention to that of Titan, one of the moons of Saturn.

LIBS is of particular interest for space applications due to its capability for use at stand-off distances, thus eliminating the possibility of cross contamination of samples. Titan is one of the moons of Saturn and of particular importance as it is the only known moon with a fully developed thick atmosphere that is rich in organic compounds. As such Titan may be a clue as to how life began on Earth.

Planets and moons that lie within the experimental parameters used in this study are shown in table 1.1. As can be seen, many atmospheric pressures fall within the experimental range, as do some gaseous atmospheric contents. As such the results obtained in this study could prove valuable for many extra-terrestrial applications.

Planet	Moon	Atmospheric pressure (millibar)	Gaseous atmospheric content
	Titan	1500	98.4% nitrogen and 1.6% methane
	Triton	0.01	99.9% nitrogen, 0.1% methane
Mars		7.6	carbon dioxide 95.32%, nitrogen 2.7%, argon 1.6%, oxygen 0.13%
Uranus		1200	hydrogen 83%, helium 15%, methane 1.99%, ammonia 0.01% plus traces of other gases
Neptune		1000-3000	hydrogen 84%, helium 12%, methane 2%, ammonia 0.01%, plus traces of other gases
Jupiter		700	trace amounts of methane, water vapour and ammonia
Saturn		1400	molecular hydrogen
<i>Pluto</i>		<i>0.0015-0.003</i>	<i>nitrogen & methane</i>
	<i>Europa</i>	<i>1.00E-08</i>	<i>methane 10.5 ppb</i>

Table 1.1: Pressure and gaseous environments within the chosen experimental range¹⁻³.

Previous studies have been undertaken to ascertain the capability of the LIBS technique in Martian, Venetian and the low pressure environments of moons and asteroids. These are described in sections 2.3 and 3.7.

These reports have been so successful that missions have been planned¹¹ incorporating a LIBS instrument for analysis of rocks and soils on the Martian surface. The first mission is being planned for launch in 2009, on board the NASA's Mars Science Laboratory and the second, a LIBS-Raman combined instrument, is being planned to launch in 2011 by the European Space Agency on the ExoMars rover mission.

To complement these studies this research was aimed at Titan, to establish if this technique can also be used in this distinct and currently un-explored environment.

Since this study was undertaken, new data has been acquired from a mission to Saturn and Titan. The spacecraft in this mission is called Cassini-Huygens, and it reached Saturn on July 1, 2004, the first Huygens data being reported by ESA on January 21st 2005.

Previously Titan had been examined by the space missions Voyager 1 and Voyager 2. Voyager 1's mission had been diverted specifically to make a closer pass of Titan, but unfortunately this mission's instrumentation range did not include an instrument that could penetrate Titan's haze.

Since the Cassini-Huygens probe much more information is known or has been validated about the atmosphere, surface and composition of Titan. At Titan's surface the temperature mean is 94K, (-179°C). This low temperature is significant as at these temperatures water ice does not sublime, and as such the atmosphere is nearly free of any water vapour⁴. Titan's atmospheric pressures were thought to be 1.5 bar (150 kPa), and have since been confirmed to be 1.467 bar, (146.7 kPa).

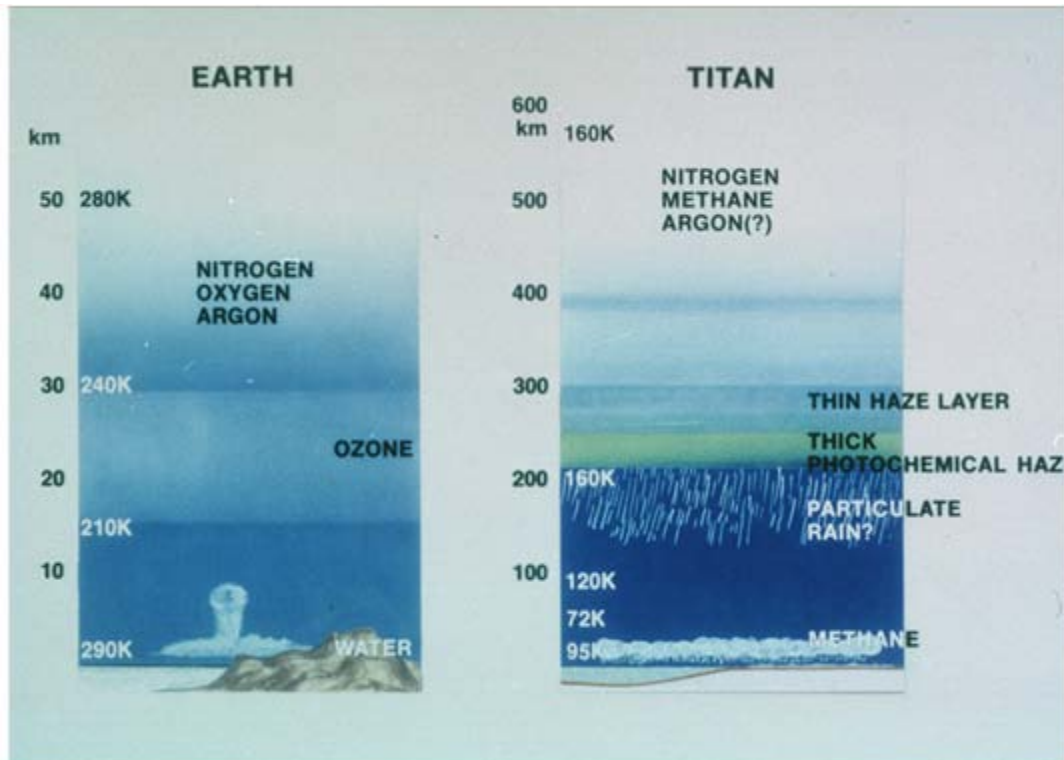


Figure 1.2: Image of the atmospheric regions of Titan in comparison to Earth⁵.

Titan's atmosphere is now known to contain 98.4% nitrogen and 1.6% methane, but this methane content is known to increase to 5% near the surface and there has been indication that the surface landing site of the Huygens probe was soaked in methane⁶.

The amount of methane abundant in Titan's atmosphere is somewhat a mystery as the solar winds in the early solar system should have cleared the atmosphere of methane content. Leading theories believe that in early formation, methane was frozen as water-ice or 'clathrates' which have since melted releasing methane into the atmosphere.

At the time of implementation of experimentation, (before the Cassini-Huygens mission data was obtained on atmospheric composition), the compositional content of Titan was thought to be 94% nitrogen and 6% methane. A percent variance of these compositions was covered in the experimental parameters.

1.3 Rock Composition

At the time of experimentation, the types of rock found on Titan were virtually unknown. It was thought that there were seas of liquid hydrocarbons⁷ and that Titan's bulk composition was water ice with approximately 65% rock-metal material⁸. It was proposed that Titan was dense due to its gravitational compression⁹ and its structure was differentiated into several layers composed of different crystal forms of ice¹⁰ and that its interior may once have contained a hot liquid layer consisting of water and ammonia between the ice crust and the rocky core¹¹.

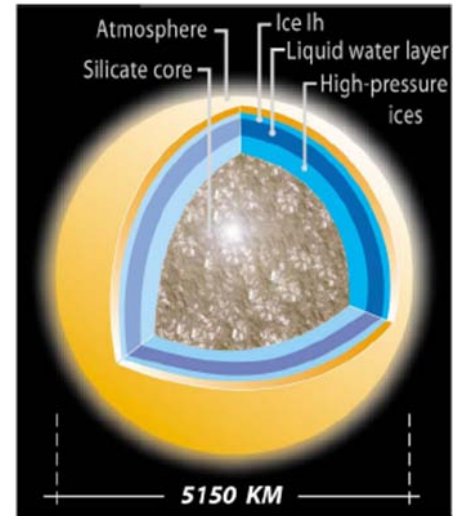


Figure 1.3: Possible present-day structure of Titan's interior¹².



Figure 1.4: Image of Titan's surface taken by the Huygens lander on January 14th, 2005¹⁴.

Taking into account these suppositions, rock types were chosen with a range of composition elements of metamorphic rock types. Slate was chosen as a foliated metamorphic rock type. Marble was also chosen as a metamorphic calcite rock.

Subsequent to choosing the above rock types further information was obtained via radar from the Cassini spacecraft¹³. This information conflicted with information previous thoughts that there were seas of hydrocarbons at the equator. Radar images revealed that these regions were in fact extensive plains covered in longitudinal sand dunes. As a result of this information sedimentary sandstone was also chosen for testing.

The rock types chosen had varying compositions, not only across the samples but inherently within the samples themselves. The samples are inevitably complex with non-uniformity in their composition, particularly so in the case of the slate sample. The thrust of this work is the feasibility of the LIBS analytical technique to analyse these samples in these environments. Consequently, account must be taken of the ambiguous composition of the rock types.

2. History and Uses

2.1 Scientific History of LIBS

LIBS was first published in the report by Brech and Cross in 1962, which observed emission spectra from a metal target using a ruby maser¹⁵. In 1963 the paper published by Debras-Guédon and Liodec¹⁶ described first analytical use of LIBS using a ruby laser to produce excited spectral emissions of the elements. In 1964 the first use of a Nd:YAG laser was reported by Geusic¹⁷ et al from Bell Labs. In the same year Maker, Terhune and Savage¹⁸ reported the first observation of optically-induced breakdown in a gas.

In the early 1970's Moenke-Blankenburg¹⁹ wrote a review on LIBS with cross-excitation, and in the late 1980's the same author produced the book 'Laser Microanalysis²⁰', which also provided another comprehensive review of the analytical applications of laser-target interactions.

The first people to use LIBS to determine the chemical composition of a substance were L. Radziemski and D. Cremers in the 1980's. In this century many papers were produced by this duo with collaboration from colleagues, some such papers are stated in the references²¹⁻²⁸. These papers varied from time-resolved techniques to chemical detection of gases, liquids, aerosols and solids. This work culminated in the book, *Laser-Induced Plasmas and Applications* written by L.J. Radziemski and D.A. Cremers in 1989²⁹.

In the 1980's only a handful of groups were working on LIBS; this number has increased exceedingly since then, as shown in figure 2.1.

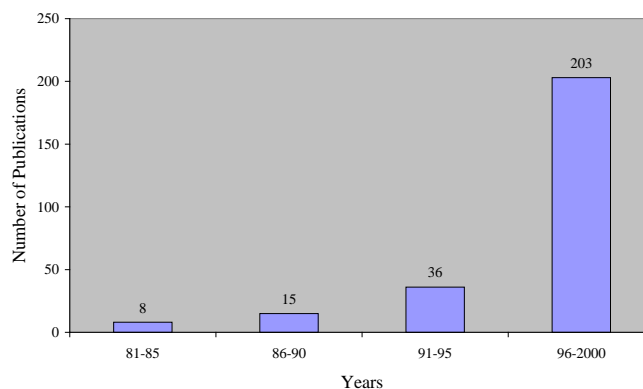


Figure 2.1: LIBS publications by year groupings³⁰

In the late 1990's, with the advent of high resolution spectrometers, the LIBS technique really took off. These detectors allowed multiple elements to be detected at once, with increased sensitivity compared to that of previous methods.

The first international conference on LIBS was held in 2000 in Pisa, Italy. Since this date conferences have been held yearly, each alternate year being an international meeting.

A comprehensive LIBS review paper was written by D. Cremers³¹ and L. Radziemski in 1987, and another was written in 2002 by L. Radziemski³², which provides a sense of the technique's development from inception to the year 2000.

Another thorough review focusing on the effects of experimental parameters on LIBS analytical performance was provided by E. Tognoni³³ et al, early in 2002. This paper refers to literature of experimental studies from 1988 to 2001.

Lastly, a useful source for the all-inclusive history of LIBS is the Handbook of Laser Induced Breakdown Spectroscopy³⁴, which provides a broad review from 1960 – 2002.

2.3 Uses, Types and Divisions

LIBS analysis is extremely versatile and can be used in many different fields of research. The LIBS technique offers: rapid analysis - one measurement per laser pulse; sampling of solids, gases or liquids; simultaneous multi-element detection; a spatial resolving power of ~1-500 μm ; remote analysis capabilities; depth-profiling of layered structures and surface coatings; detection limits of 1-100 ppm, depending on sample composition and instrumental characteristics; all with little or no sample preparation.

Some of the disadvantages of LIBS range from poor shot-to-shot stability; matrix effects; poor signal to noise ratio; loss of weaker lines and difficulty in obtaining quantitative analysis.

There are many different applications of the LIBS technique in numerous different fields. These wide ranging applications include: archaeological analysis of Minoan dagger history³⁵, elemental composition of artworks to characterise pigments in a Byzantine work layer by layer³⁶, analysis of bobsleigh runners in the 2002 winter Olympics to ensure they meet with the Olympic standards in having a homogeneous metallic composition throughout³⁷, various different varieties of coating analysis such as Lademann's investigation into the stability of coated titanium microparticles used in sunscreens³⁸, dentistry applications, utilizing the high spatial resolutions possible with LIBS, to identify the transition from carious (unhealthy) tissue to healthy tissue³⁹, and in the nuclear industry for remote chemical analysis, exploiting the ability of LIBS to work in submerged remote environments^{40,41}. These several uses mentioned are just a small selection that have so far been explored using the LIBS analysis technique.

Most of the above mentioned applications are at atmospheric pressure with terrestrial gaseous environments. Some research has been undertaken in different pressure regimes and environments, such applications are useful to ascertain the uses of LIBS in space exploration.

A cross section of papers written by Los Alamos national laboratory (LANL) on LIBS publications for planetary science are stated in Appendix [B] some reference summaries are stated here:

LIBS Operation on Airless Bodies^{4,42}, a study undertaken to characterise the changes to the LIBS plasma spark in different pressure regimes.

LIBS Operation on Venus^{4,43}, these studies concentrate on the hostile environment of Venus with atmospheric pressures ~90Bars.

*Investigation of LIBS feasibility for in situ planetary exploration: An analysis on Martian rock analogues*⁴⁴

This latter study focuses on volcanic rock analysis in an environment similar to a Martian one, using the calibration free LIBS (CF-LIBS) method at wavelengths of 355 nm. It suggests that the technique can be used to allow elemental qualitative and quantitative identification on the silicate minerals studied in the Martian environment. The CF-LIBS technique was shown to be accurate within the range 1-30% for the major constituents, but this depended heavily on the element and its concentration. The accuracy would be reasonable for first line identification but could be questionable when used in precise analytical measurements.

*LIBS application for analyses of Martian crust analogues: Search for the optimal experimental parameters in air and CO₂ atmosphere*⁴⁵.

This study compares a Terrestrial environment to a Martian environment, with particular attention paid to the optimal experimental parameters such as emission intensity, temperature and electron density. It found that the acquisition window where local thermodynamic equilibrium (LTE) holds is much shorter in Martian environments due to low electron density and fast plasma cooling and decay, the latter giving a short interval for maximizing signal to noise ratios.

Further analysis of studies relevant to the work in this thesis are described in the theory, section's 3.5, 3.6 & 3.7.

3. Theory

The following section will concentrate on each of the processes involved in LIBS analysis. In order to facilitate easy categorisation of the development of the theory, it has been broken down into subsections entitled; Laser; Induced; Breakdown; and Spectroscopy. Following this a thorough investigation of other features in LIBS analysis is undertaken.

3.1 Laser

Theodore Maiman invented the first laser in May 1960⁴⁶. Laser action is initiated by exciting the electrons of the atoms in a laser medium from the ground state into a higher energy level using optical amplification⁴⁷, producing a population inversion⁴⁶. This is achieved by pumping⁴⁸ the laser medium via the application of a large amount of energy in the form of broadband light.

As the electrons make transitions back to the ground state they emit radiation. Most energy transitions emit a phonon, but some transitions result in the emission of a photon. When a photon is emitted it is trapped within the laser cavity. This photon passes through the medium and stimulates further emissions from the population inversion.

There are many types of lasers that can be used in LIBS experiments, examples being Nd:YAG, Excimer, CO₂ and Microchip lasers. The majority of LIBS measurements use a flashlamp pumped Nd:YAG laser, which is the laser used in this work.

The Neodymium-YAG (Nd:YAG) laser rod is a doped insulator laser that uses a Nd³⁺ ion to dope a yttrium-aluminum-garnet host crystal⁴⁷.

Nd:YAG lasers operate via a four energy level system with the lasing transition taking place between the ⁴F_{3/2} and ⁴I_{11/2} states⁴⁸ resulting in infrared light emission of wavelength 1064 nm. The energy levels involved in the laser transitions are those of the impurity ions. The electrons relax via phonon

interactions from the third level into the second level of this system which is known as a metastable state, meaning that it can return to a less excited state only via a highly inhibited transition. As such, electrons remains in this state for an appreciable fraction of a second rather than for the lifetime of a typical transition rate of $\sim 10^{-8}$ s. It is this long lifetime that provides the mechanism by which a population inversion can be achieved.

The Nd:YAG laser is a popular choice for laser ablation experiments as it displays a high spatial coherence and has high output energies⁴⁹.

Converting the 1064 nm laser output to shorter wavelengths is achieved by passing the laser beam through a non-linear crystal. This produces harmonics obtained from phase matching⁴⁸. The conversion efficiency is approximately 50% and reduces with each harmonic. The crystal used to produce green light of wavelength 532nm, used in this work, is KTP (potassium titanyl phosphate).

The light emitted by a laser will have different optical frequencies associated with different modes of the optical resonator. These resonator modes are known as longitudinal and transverse modes. The longitudinal modes of a laser govern the spectral characteristics, such as line width and coherence length. The transverse modes govern the beam divergence, beam diameter and energy distribution.

A laser that operates in its fundamental transverse mode, or TEM₀₀ mode, emits light with a Gaussian intensity profile. This light will propagate as a directional parallel beam for a distance given by $\pi d^2/\lambda$, the Rayleigh range, (where d is the laser output coupler diameter). Beyond this range the beam will expand with a divergence of $\Delta\theta = d/\lambda$, known as the beam divergence.

3.2 Induced (Laser Ablation)

R. Srinivasan and V. Mayne-Banton of IBM Research first reported the laser ablation phenomenon to produce thin films in 1982⁵⁰. Laser ablation is a process whereby the short, intense burst of energy delivered by a laser pulse is used to vaporise a material that would often be impossible to vaporise by conventional methods^{51,52}. Lasers are advantageous in many ways. Because of their high spatial coherence they may be focused onto a very small area and this can result in intense local heating without neighbouring areas being affected. The majority of the laser energy is deposited near the surface of the target, allowing surface regions to be ablated without affecting the bulk. It is also relatively easy to control a laser's energy density or fluence⁵³.

$$\text{Fluence (Jcm}^{-2}\text{)} = \text{laser pulse energy (J)} / \text{focal spot area (cm}^2\text{)} \quad (3.1)$$

$$\text{Radiant Power or Flux (W)} = \text{pulse energy (J)} / \text{pulse duration (sec)} \quad (3.2)$$

$$\text{Intensity or Irradiance (Wcm}^{-2}\text{)} = \text{peak power (W)} / \text{focal spot area (cm}^2\text{)} \quad (3.3)$$

It is almost impossibly complicated to carry out a detailed theoretical analysis of the ablation process, especially when the substrate melts or vaporises⁵⁴. However it is possible, making simple assumptions, to adopt models that enable important parameters to be identified and orders of magnitude estimated. Appendix [C] lists some of the most representative theoretical models of the laser-solid interaction, and a brief description of each.

Laser intensity thresholds necessary to produce ablation are sensitive to surface parameters and the purity of the material. Typical reported³⁴ threshold values for LIBS type plasmas on solids are in the range of 10^8 - 10^{10} Wcm⁻². A paper by Semerok *et al*⁵⁵ discusses the thresholds and ablation rates of copper in air for a 532nm, 6ns, Nd:YAG laser.

Laser ablation results in heating and damage to the surrounding area, the degree of which is determined by the rate of energy absorption and the rate of energy loss through thermal conduction in the substrate. In general three types of absorption must be taken into account, volume absorption by the electrons and phonons in the lattice, free carrier absorption at the surface and absorption by the plume.

For ablation to take place there needs to be sufficient heating of the substrate to take it through to the vapour phase. The vaporised material will expand in the form of a plume, the plume being plasma-like, consisting of molecular fragments, neutral particles, free electrons and ions, and chemical reaction products⁵³. The laser energy will continue to heat this partially ionised evaporated material while part of the energy continues to the substrate surface. As the energy increases the plume can become opaque and shield the surface.

The ability of a material to absorb laser energy limits the depth to which that energy can perform useful ablation. Generally, reflectance decreases with decreasing wavelength⁴⁸. This would tend to suggest that shorter wavelengths would be optimum for ablation, but the reflectance of most surfaces reduces during a laser pulse as the temperature rises. Therefore the initial advantage of a shorter wavelength is not necessarily maintained. For a more detailed study refer to Anisimov *et al*⁵⁶ who have taken the reflection of light from substrates and the temperature dependence of the reflectance into consideration.

It should also be noted that after the initial pulse, subsequent laser pulses are incident upon a 'new' surface, which could have been melted, recondensed, have suffered surface reflectivity changes or be covered with re-deposited material of a composition that differs from that of the original substrate.

In general one can estimate the minimum power density needed to produce vaporisation using the Moenke-Blankenburg⁵⁷ equation:

$$I_{\min} = \frac{\rho L_v \kappa^{1/2}}{\Delta t^{1/2}} \quad (3.4)$$

Where:

I_{\min} = minimum power density (W.cm^{-2}) ρ = density of substrate (kg.m^{-3})

L_v = latent heat of vaporisation (kJ.kg) Δt = laser pulse length (s)

κ = thermal diffusivity of specimen ($\text{W.m}^{-1}.\text{K}^{-1}$)

The ablation depth per pulse can be calculated using equation³⁴:

$$A_d = \frac{f(1-R)}{[C_p(T_b - T_0) + L_v]\rho} \quad (3.5)$$

Where:

A_d = ablation depth per pulse (m) R = fractional surface reflectivity

C_p = specific heat ($\text{J.kg}^{-1}.\text{K}^{-1}$) T_b = boiling point (K)

f = fluence (J/m^{-2}) T_0 = room temperature (K)

There will be a significant change in ablation rate when working in different pressure environments, a decrease in pressure producing an increase in ablation rate, due to reduced shielding of the sample surface from the incident laser pulse. Work by Multari *et al*⁵⁸, Vadillo *et al*⁵⁹ and Semerok *et al*⁶⁰, studied factors related to ablation rate, such as fluence, laser pulse length, pressure, lens to surface distance (LTSD) and angle of incidence.

Ionisation of the plume emitted from the sample can occur by multiphoton absorption or by avalanche (impact) ionisation. Breakdown thresholds for longer (ns) pulses are usually determined by avalanche ionisation⁶¹.

Multiphoton absorption^{62,63} is a process that was predicted theoretically by Maria Göppert-Mayer in 1929, but was unable to be experimentally verified until the advent of the laser in 1960. In this process an atom may absorb two or more photons simultaneously, (or within less than a nanosecond), in some cases allowing it to be ionized by photons with an energy less than that of the threshold energy due to possible transitions to virtual states.

Avalanche breakdown is the process whereby an energetic carrier creates a carrier pair after colliding with the lattice. These new carriers are then energised by photon absorption and accelerated until the process repeats and an avalanche develops. A study of avalanche breakdown in air has been completed by Kroll and Watson⁶⁴.

Avalanche breakdown requires the presence of some “priming” free electrons which can be provided by dust particles, by multiphoton ionisation of a gas atom in the beam path or by absorbed impurities in the substrate which are evaporated and ionised below the bulk substrate threshold.

The vapour particles escaping the substrate surface have a Maxwell velocity distribution with vectors pointing away from the surface⁶⁵. These vectors are changed by collisions with the vapour particles themselves producing a region known as the Knudsen layer⁶⁶. Within this layer the plume reaches internal equilibrium and rapidly moves away from the sample surface. If the vapour pressure of the plume within this layer exceeds the ambient pressure, the flow velocity becomes supersonic and forms a shock front. Anisimov *et al*⁶⁷ has produced a detailed discussion of vapour expansion and condensation.

At low irradiance most of the pulse energy is spent in heating the substrate surface. As the irradiance increases the energy and temperature of the plume increases, thus reducing the efficiency with which energy is imparted to the surface. This increase leads to more absorption creating a positive feedback loop; much of this energy goes into dissociation and ionisation of the plume particles. Thus the incident irradiance reflects the behaviour of the degree of absorption.

When the plume is partially ionised laser light is absorbed via two methods; by thermally excited atoms (bound-free absorption), and by ions (Bremsstrahlung absorption)⁶¹. The Bremsstrahlung phenomenon was discovered by Nikola Tesla in research between 1888 and 1897^{68,69}. Bremsstrahlung or ‘braking radiation’, also known as free-free radiation, is the process whereby electromagnetic radiation is produced by the deceleration of a charged particle, in this case an electron, when it has collided with another charged particle, in this case an ion. When this process is reversed, and produces an acceleration of the charged particle, is known as inverse-Bremsstrahlung.

Transitions, (radiation or absorption) that an atom or ion can undergo can be summarised using the following diagram:

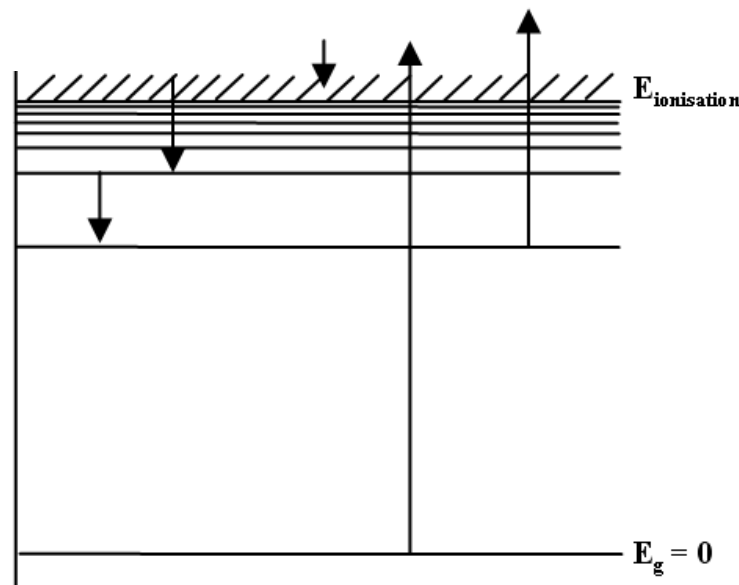


Figure 3.3: Illustration of possible transitions of electrons
(Composite drawn from many sources)

Where, from left to right we have:

- bound-bound
- free-bound (Avalanche)
- free-free (Bremsstrahlung)
- Ionisation from the ground state
- Ionisation from an excited state

Once the plume is fully ionised light absorption is dominated by Bremsstrahlung absorption. In this scenario the plume absorbs all or part of the incident radiation and the energy provided is converted into internal energy of the plume. This energy is consumed as hydrodynamic motion or radiated away as thermal radiation. As mentioned, the plume rapidly expands away from the surface, but this plume also remains confined to a channel formed by the incident light due to interaction of this light with the plume³⁴. This phenomenon is commonly referred to as a Laser-Supported Absorption Wave (LSAW). This wave propagates in three zones, plume front, shock front and absorption front as shown in figure 3.3^{34,70,71}.

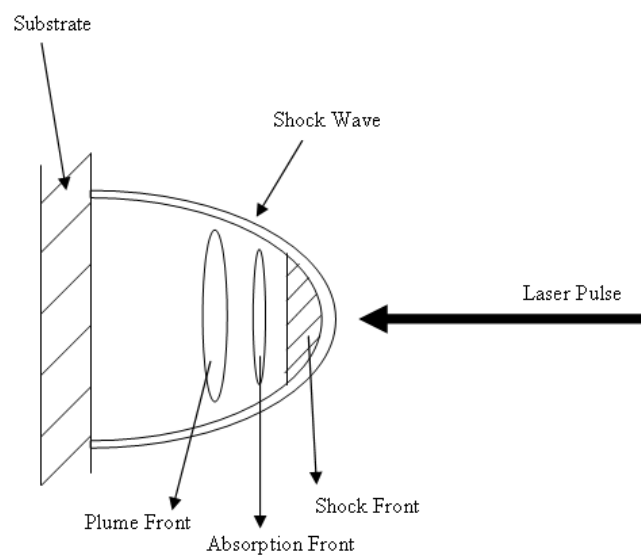


Figure 3.4: Schematic diagram of plasma propagation³⁴

This LSAW can be divided into two classes depending on the incident irradiance, optical density and internal energy of the plume. The first class, known as a Laser-Supported Combustion Wave (LSCW), is a weakly absorbing subsonic wave, the theory of which was formulated by Raizer in 1970⁷².

The layers of cold gas in the plume front are heated by conduction and thermal radiation from the absorption front until they themselves start producing their own radiation. In this regime a fraction of the light absorbed produces the chemical reaction and the propagation is limited to the laser beam channel, both towards and away from the laser source. The wave is also optically thin so the

laser radiation can still reach the surface. The velocity of the LSCW scales with the square root of the irradiance and vanishes at critical irradiance⁶¹.

The second class of an LSAW is known as a Laser-Supported Detonation Wave (LSDW). In this class the irradiance increases and in consequence there are increases in the temperature, pressure and velocity of the absorption front. The increased irradiance also results in a larger proportion of the beam flux being absorbed, which in turn contributes to preheating and ionization, and ultimately results in the dominating mechanism of plume expansion becoming compression rather than conduction so that the plume front becomes optically thick. The velocities increase and the wave becomes a supersonic shock wave. The plume is also shown to propagate cylindrically along the beam path due to its mechanism being supported by the laser beam.

At even higher irradiances the wave class changes to what is known as a Laser-Supported Radiation Wave (LSRW), or breakdown wave. In this regime the plasma itself is emitting enough radiation to enable the atmosphere in front of it to become absorbing³⁴. This couples the absorption zone to the plasma front. The propagation of this wave relies on avalanche breakdown, with the avalanche first developing at the focal point (region of highest flux) and then transferring that propagation to areas of lower flux.

A one dimensional approximation study of velocities, pressure, temperature and densities for all classes of laser supported waves has been carried out by Root⁷³ in 1989 and a further study modelling ablation mechanisms, rates and analytical considerations is reported by Bogaerts et al⁷⁴.

All regimes will be altered with a change in ambient pressure producing a change in the plume size. A higher pressure will slow down and confine the plume whereas at low pressures there will be reduced trapping of the absorbed energy, and as such a plasma lifetime decrease, but there will also be an increase in ablation rate due to less plasma sheilding⁵⁹.

Review papers have been written by Bogaerts et al⁷⁴ and Russo et al⁷⁵, which review the many models of the ablation process with varieties of laser and sample parameters. Papers by Aguilera and Aragon⁷⁶, Wood et al⁷⁷, Iriarte et al⁷⁸, Capitelli et al⁷⁹ and Gizzi et al⁸⁰ also provide a good understanding of the ablation/plume process within a LIBS plasma.

3.3 Breakdown (Plasmas)

'After termination of laser pulse plasma loses energy and decays. Mechanisms include recombination, radiation and conduction...'³⁴

Plasmas produced by laser ablation will expand rapidly and show large density and temperature gradients along the axis of the incoming beam. Typically, plasmas produced in LIBS experiments initiate with high ionisation but after recombination and relaxation the plasma becomes weakly ionised. Throughout this process there is broadband background radiation due to Bremsstrahlung radiation that decays early in the plasma lifetime. The plasma lifetime is only of interest for LIBS experiments when it reaches the later stages, where the recombination radiation is emitted.

LIBS plasmas should preferably be optically thin: an optically thin plasma is a plasma in which the radiation that has been emitted escapes without noteworthy absorption or scattering.

Ideally LIBS plasmas should have an elemental composition identical to that of the substrate. This is not always the case due to the differing volatilities of the constituent species of the substrate producing preferential ablation rates.

When analysing the intensity of different elemental spectral lines it has been shown⁸¹ that there is a fractionation or matrix effect inherent in substrates composed of a different matrix of elements.

For example, figure 3.4 shows that, although the concentration of lead in the sample is constant, its LIBS analysis shows an incongruent quantity, depending on the matrix composition of lead and sand.

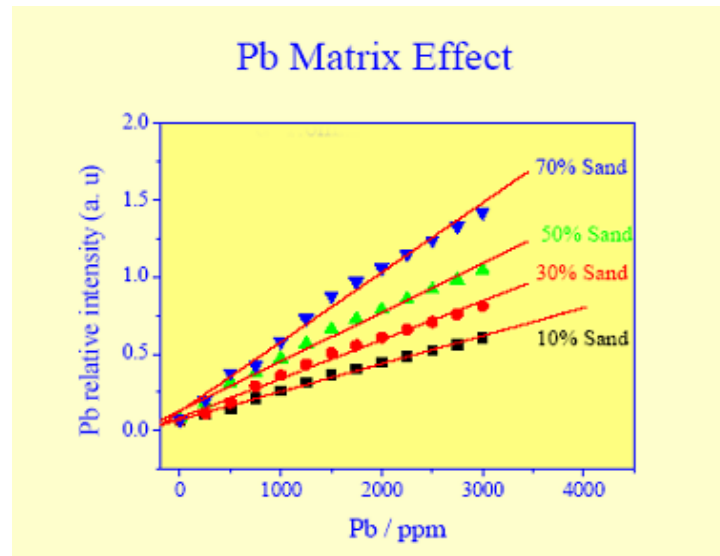


Figure 3.5: Graph showing matrix effect evident in samples containing both sand and lead⁸⁰.

Many factors influence the degree of fractionation such as laser wavelength, pulse duration and irradiance, fluence and atomic mass of the constituents, as have been extensively studied by Russo *et al*^{75,82}, Mao *et al*⁸³, Figg and Kahr⁸⁴, Jeffries *et al*⁸⁵, Eggins *et al*⁸⁶, Gunther *et al*^{87,88} and Singh and Narayan⁸⁹. It has been indicated⁴² that matrix effects are less prominent at lower pressures, due to the reduced proximity of the plasma species resulting in increased interaction between the laser pulse and the sample.

In order to maximise stoichiometry all constituents should be completely vaporised and removed. This can be done by ensuring the energy deposited into the substrate is greater than the latent heat of vaporisation for all matrix constituents. It has been noted by Ready⁹⁰ that if the irradiance is $<10^6 \text{Wcm}^{-2}$ with microsecond pulse lengths then thermal effects will influence the process allowing differential ablation, but for nanosecond laser irradiances $>10^9 \text{Wcm}^{-2}$ the ejected material should be close to the sample composition due to the thermal properties no longer playing a major role. Bogaerts *et al*⁹¹ provide a review of the laser ablation/plume process with varying models and sample parameters.

When an electron undergoes a transition to a state of lesser energy it can emit a photon. These photons produce spectral lines characteristic of the atom, ion or molecule. Spectral lines emitted from a plasma have widths, shapes and intensities that depend on the temperature, pressure and electron density of the plasma. Therefore spectral lines can give information about the conditions in the plasma itself. Lines that have been emitted from a ground level transition are in most cases the strongest lines, known as resonance lines.

If a spectral line has changed from its expected value in some way this suggests a perturbation in the medium. This could be a spectral line broadening or shifting mechanism due to the plasma parameters. There are many broadening and shift varieties, the most important in LIBS conditions being Doppler and Stark broadening, described in section 3.3.1. The interference from these mechanisms in LIBS plasmas will only be apparent if the spectrometer and detector system has sufficient optical and spectral resolving power. Natural line widths can be neglected in LIBS experiments as they are negligible when considering the resolution of LIBS apparatus.

Table 3.1 illustrates Doppler and Stark widths for some lines of interest to LIBS experiments:

Element	Wavelength (nm)	Atomic Mass	Temperature (K)	Doppler FWHM (nm)	Stark width FWHM (nm at 10^{17}.cm^{-3})
C	193.1	12	10000	0.004	0.0044
C	247.9	12	10000	0.005	0.0072
O	777.3	16	10000	0.014	0.0630
Na	589.2	23	10000	0.009	0.0314
Mg	285.2	24	10000	0.004	0.0082
Al	309.2	27	10000	0.004	0.0520
Si	288.1	28	10000	0.004	0.0128
Si	390.5	28	10000	0.005	0.0234
Si	181.4	32.1	10000	0.002	0.0044
K	766.5	39.1	10000	0.009	0.0830
Ca	422.6	40	10000	0.005	0.0126

Table 3.1: Doppler and Stark widths from literature³⁴, with electron densities of 10^{17}.cm^{-3} .

A summary of the different broadening mechanisms will now be given:

3.3.1 Conditions Local to Emitting Particle

Natural Broadening, (no line shift)

The process whereby the same excited level in an individual atom will have slightly different energy from that same level in a different atom. This method can be described by a Lorentzian distribution.

Thermal (Doppler) broadening, (no line shift)

This phenomenon is due to the relative velocity of photons with respect to the observing framework, the photons emitted will be red or blue shifted due to the Doppler effect, producing a Gaussian profile. The distribution of velocities within the plasma will depend on the plasma temperature, the higher the temperature the greater the distribution of velocities and, as such, the broader the spectral line emitted. The Doppler width is given by:

$$\lambda_D = \lambda_0 \left(\frac{kT}{mc^2} \right)^{1/2} \quad (3.6)$$

Where:

λ_D = Doppler width (nm)

c = speed of light (ms^{-1})

λ_0 = Central wavelength of spectral line (nm)

m = mass of the atom (Kg)

k = Boltzmann constant (J/K)

T = absolute temperature (K)

Pressure broadening

Pressure plays an important role in plasmas, the higher the pressure the more particles in a selected range which will affect the emitted radiation. There are many types of pressure broadening, described here:

Impact (line shift possible)

Impact pressure broadening is, as it suggests, due to impact of the emitting particle with other particles in its emission path. The more particles in

its path the more impacts; thus this process is affected by the temperature and density of the plasma. Broadened lines can be describes by a Lorentzian profile.

Quasistatic (line centre can be shifted)

This mechanism is due to nearby particles shifting the energy levels and therefore the emission frequencies of the emitting particle, and thus is dependent on plasma density. The line profile is affected by the distance between the emitting particle and the perturbing particle⁹².

Linear Stark Broadening (can cause line shift)

This interaction is due to the interrelation of the emitting radiation with an electric field. The shift in energy is linear with field strength given by:

$$\Delta E \propto \frac{1}{r^2} \quad (3.7)$$

Resonance Broadening

This is the process whereby the emitting particle undergoes an energy exchange with an identical particle. It can be described by a Lorentzian profile and the relation:

$$\Delta E \propto \frac{1}{r^3} \quad (3.8)$$

Van der Waals Broadening

This process occurs when Van der Waals forces perturb an emitting particle. This mechanism can be described in the centre of the plasma by a Van der Waals profile and at the edges by the Lennard-Jones Potential^{93,94}:

$$\Delta E \propto \frac{1}{r^6} \quad (3.9)$$

3.3.2 Conditions Along Entire Emission Path

Opacity broadening

Plasma opacity is the re-absorption of an emitted photon. It can be so great as to cause self reversal, whereby the centre of the emitted spectral line is inverted. The re-absorption will be greater the more interactions there are along the emission path. As such it is more apparent with emissions from the centre of the plasma than those at the edges. This difference in re-absorption broadens the spectral lines.

All of the above broadening mechanisms can be prevalent in a plasma, some in isolation and some in combination. If these mechanisms are in fact working in combination they can yield profiles which are a convolution of the individual line profiles. Such a convolution is shown when a Gaussian and a Lorentzian broadening mechanism are combined to produce a Voigt Profile. The Gaussian dominating at the line centre and the Lorentzian dominating in the line wings⁹⁵.

The purpose of LIBS analysis is primarily to discover the chemical composition of a substrate. Qualitatively this is an easy procedure, shown by the presence of a characteristic spectrum. To obtain quantitative results one must be able to interpret the intensity of spectral lines, giving the number density of the species in question. In order to undertake such a task one must determine the state of the plasma, namely its temperature and density.

If a plasma displays thermodynamic equilibrium its temperature can describe conditions of the plasma, such as distribution of particle speed and the relative populations of energy levels. This state is rarely found and as such one can only approximate with local thermodynamic equilibrium (LTE), applying to a local sector rather than the whole plasma.

When a LIBS plasma extends to a LSDW or LSRW the energy in the plasma is distributed across the whole volume, producing LTE at times several hundred nanoseconds after the initial laser spark. This can be implied from work in this

field addressed by Salzmänn⁹⁶ (1998), Griem⁹⁷ (1997) and Sobelman⁹⁸ et al (1981).

If in fact LTE does exist, the relative populations of energy levels can be given by the Boltzmann distribution.

$$\frac{N_j}{N_0} = \frac{g_j}{U} \exp\left(\frac{-E_j}{kT}\right) \quad \text{with respect to the ground state.} \quad (3.10)$$

Where: N_j = population of the level E_j
 N_0 = Total species population
 g_j = Statistical weight of the level ($2J + 1$)
 U = Partition function (statistical weight of the ground state)

$$\text{Or:} \quad \frac{N_j}{N_i} = \frac{g_j}{g_i} \exp\left(\frac{-(E_j - E_i)}{kT}\right) \quad \text{for relative populations.} \quad (3.11)$$

This information tells us that the ground state is most populated but as the temperature increases the population moves to the excited states. This method can be used to calculate the temperature of the plasma by measuring the wavelengths and relative intensities of spectral lines, if their transition probabilities and the statistical weights of the levels are known.

LTE within the plasma can also lead to a knowledge of the relative populations among ion stages, if the electron density is known, by using the Saha Equation to obtain temperature:

$$\frac{N(U,0)n_e}{N(U-1,0)} = \frac{2g(U,0)}{g(U-1,0)\left(\frac{mkT}{2\pi\hbar^2}\right)^{3/2} \exp\left(\frac{-\Delta E}{kT}\right)} \quad (3.12)$$

Where: $N(U,0)$ = population of ground state of ion stage U
 $N(U-1,0)$ = population of ground state of ion stage $U-1$

m = electron mass

n_e = electron density

ΔE = ionisation energy of stage U relative to stage $U-1$

This equation only holds for weakly ionised plasmas. In terms of relative intensities:

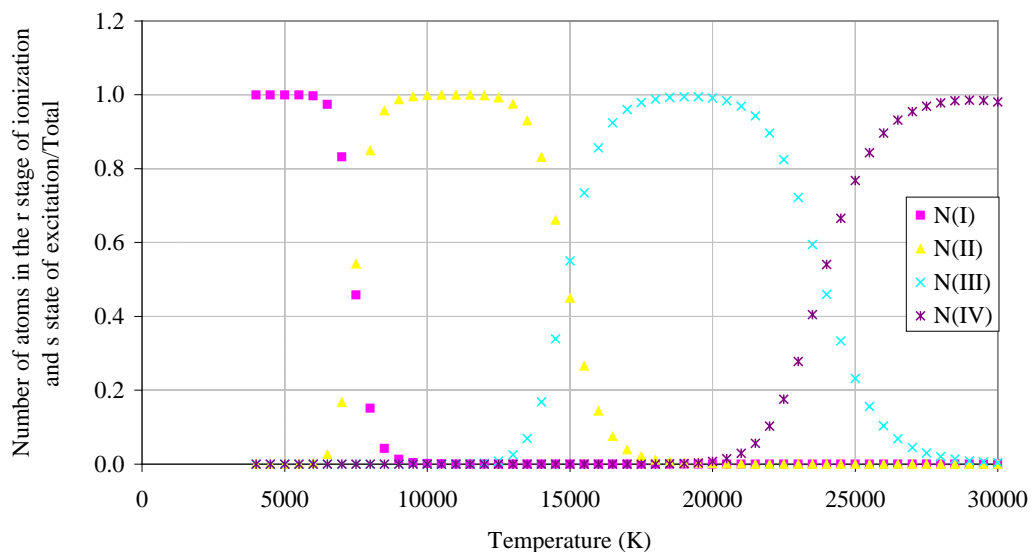
$$\frac{I'}{I} = \frac{\lambda g' A' N(U)}{\lambda g A N(U-1)} \quad (3.13)$$

The Saha equation describes the degree of ionization of this plasma as a function of the temperature, density, and ionization energies of the atoms.

This method involves measuring the relative intensities of lines from different ion stages and is known as the temperature of the ionisation equilibrium. The results inform us as to which ionic species is dominating at which temperature range. Increasing temperature causes higher ionic species to dominate.

Shown in figure 3.5 are results of the Saha calculation for nitrogen⁹⁹. It can be seen that only one or two ionisation stages need to be taken into account at certain plasma temperature ranges.

Figure 3.6: Saha factors applied to nitrogen⁹⁹ (pressure = 0.1 Pa)



LIBS plasmas of irradiances of $>10^8 \text{Wcm}^{-2}$ have been shown^{34,100} to have electron densities of $N_e \geq 10^{16} \text{cm}^{-3}$ and temperature ranges of $kT \geq 1\text{eV}$ at several hundred ns after initiation, which classifies them as cold dense plasmas. These electron densities will be highest at the initiation of plasma formation and will decrease with plasma lifetime as shown in³⁴.

Conversion of temperatures into electron volts is often undertaken in plasma physics:

$$\frac{1\text{eV}}{k_B} = T(\text{kelvins}) \quad \frac{1.60 \times 10^{-19}}{1.38 \times 10^{-23}} = 11604.50\text{K} \quad (3.14)$$

Where: k_B = Boltzmann constant

If undertaking LIBS experiments at atmospheric pressure it is useful to note the densities of molecular oxygen and nitrogen, the prevalent background species, which are of the order of $2 \times 10^{25} \text{m}^{-3}$. If LIBS is undertaken under different pressure regimes it should be noted that plasma and background electron densities will be orders of magnitude different.

Plasma properties such as line shape and width can provide us with much useful information for LIBS analysis, such as quantitative information on the electron densities, electron temperature and relative concentrations of the elements present.

3.4 Spectroscopy

‘An optical spectrum consists of radiative transitions between stationary states of an atom or molecule.’¹⁰¹

When an electron within an atom undergoes a transition to a state of lesser energy it can emit a photon. These photons produce spectral lines of the atom, ion or molecule, known as an emission spectrum.

Optical spectroscopy is the analysis of spectral lines emitted or absorbed from atoms, ions or molecules and the use of this information to ascertain the identity, structure and/or environment of such species. These lines represent the energy levels of the emitting species.

Spectrochemical analysis is the search for characteristic emission line patterns from an atom, molecule or ion. Analysis of their wavelengths, intensities, widths, shifts and spectral distribution can provide further information. Analysis of the emission spectra can be made quantitative if one can determine the relative intensities of such spectra to determine the abundance of that species in the substrate.

Plasma spectroscopy can be used to analyse electron densities, temperatures, pressures, velocities and relative abundances. A plasma's physical properties can be shown to affect the emission spectra in many ways. Studying these effects has been covered in section 3.3, many of these effects are produced by line shifts and broadening mechanisms as a result of plasma properties. A plasma's properties, such as temperature and electron density, can be determined from the emission lines themselves.

The link between line wavelength and individual atom emissions/absorptions was first discovered in 1860 by Kirchhoff and Bunsen. The foundations of spectroscopy and atomic structure are covered in quantum mechanics.

Quantum theory states that energy is quantised; it can only exist in discrete packets of energy which satisfy the relation:

$$E = nh\nu \quad (3.15)$$

Where

- E = total energy
- n = quantum number
- h = Planck's constant
- ν = frequency of oscillations

The energy quantisation can be found for the one electron atom from the time-independent Schroedinger equation. An energy level diagram for such a system is shown below:

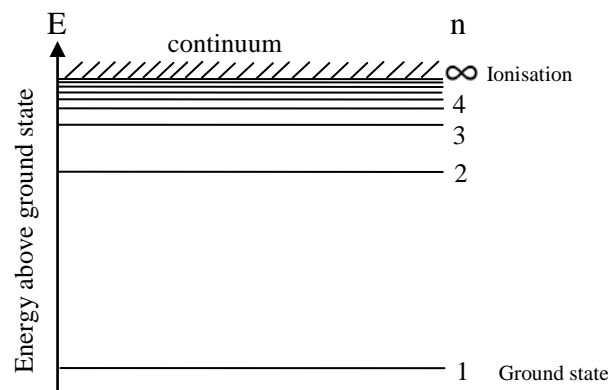


Figure 3.7: Energy level diagram for one electron atom.
(composite drawn from many sources)

Although this theory has been developed for a one-electron atom, and as such an energy level is only dependent on the quantum number n , the theory also holds when applied to multielectron atoms but the energy of the system, due to the levels having sub-levels and the electrons having spin, then depend on three quantum numbers n , l and m_l .

It can be seen that there are situations where a single energy value E_n can actually depend on a few different configurations of energy in the system, this

corresponds to atomic states that have different behaviour but the same total energy, known as degeneracy.

The energy level diagram above should actually be a lot more complicated than shown due to the degeneracy mentioned and also due to perturbations of the energy levels from interactions such as electrostatic interactions, magnetic interactions, nuclear mass/volume, and spin. This results in energy level splitting as shown in figure 3.8.

A suitable simplified version of a multielectron atom can be explained by the Hartree¹⁰² theory, predicting that:

*'the total energy of an electron in the outermost populated shell of any atom is comparable to that of an electron in the ground state of hydrogen.'*¹⁰²

This prediction is based on the fact that the outer electrons of a multi-electron atom are shielded from the strong nuclear charge by the inner shell electrons. This theory holds well but corrections are needed to allow for the weaker interactions mentioned above. These weaker interactions result in the fine structure of the energy levels of atoms. Such interactions are:

Splitting:

- Residual Coulomb interaction, (Spin coupling and Orbit coupling)
 - Adds corrections for electron spin-orbit interactions and relativistic dependences of mass on velocity, the Dirac theory.

Fine-structure splitting:

- Spin-Orbit interaction, the fine-structure splitting of degenerate levels,
 - known as LS coupling and JJ coupling for atoms with large Z, Quantum electrodynamics and the Lamb Shift.

Hyperfine splitting:

- Interaction of the intrinsic magnetic dipole moment of the nucleus and the magnetic field produced by atomic electrons.
 - smaller than spin-orbit interactions by 3 orders of magnitude

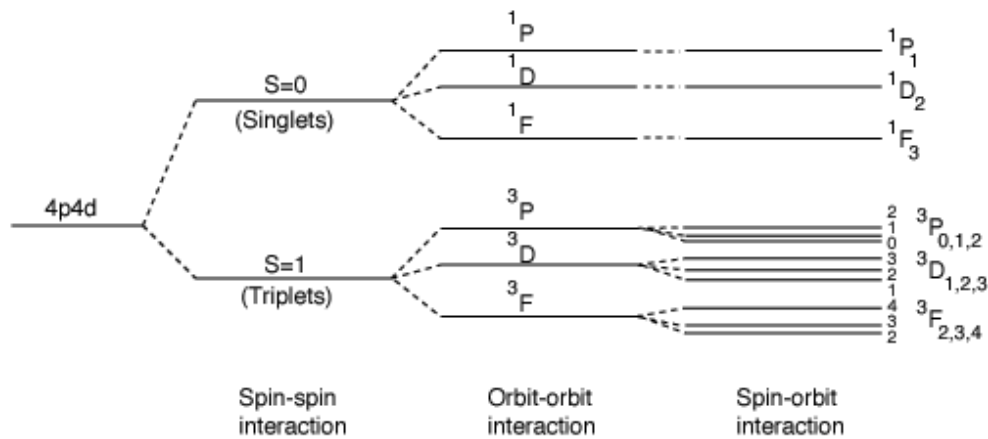
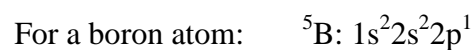


Figure 3.8: Influences on atomic energy levels¹⁰³.

The Hartree theory yields information on ordering, according to energy, of the outer filled subshells of multi-electron atoms.

Spectroscopic notation can be explained using standard notation, as shown:



The principle quantum number n is represented by the integer before the letter; the azimuthal quantum number, or subshell, is represented by the spectroscopic notation in table 3.2; the superscript on the subshell designation specifies the number of electrons which it contains; the superscript on the chemical symbol specifies the number of electrons in the atom.

The filling of subshells is governed by the Pauli exclusion principle, whereby:

'In a multielectron atom there can never be more than one electron in the same quantum state'

The first subshell may contain two electrons and not violate the exclusion principle as one electron may have spin ‘up’ and one spin ‘down’.

Energy levels are often listed as wavenumbers (cm^{-1}) where the ground state is zero, allowing the wavenumber of a transition to be interpreted from the energy level difference:

$$\text{wavenumber, } \sigma \text{ (cm}^{-1}\text{)} = \frac{\Delta E}{hc} \quad (3.16)$$

Derived from:

$$\Delta E = h\nu \quad (3.17)$$

$$c = \nu\lambda \quad (3.18)$$

$$\sigma = \frac{1}{\lambda} \quad (3.19)$$

Where: E = Energy difference of two levels (J)
 ν = frequency (Hz)
 c = speed of light (ms^{-2})
 λ = wavelength (nm)

The ionization energy, the energy required to remove an electron from the atom, varies with the number electrons in the outer shells of each atom.

For example a noble gas, in which the *p* subshell is completed, is much harder to ionize than an alkali which has a single weakly bound electron in an *s* subshell. These alkali elements have correspondingly high chemical activity due to their energetic favourability to interact with other elements to produce a more stable arrangement.

An element’s chemical properties and its ability to interact with other atoms depend on the number of electrons in the outer subshell of the atom, as these are the electrons that govern the electric and magnetic fields of that element.

Modern quantum theories are also able to give very satisfactory treatments of the transition rates and selection rules observed in the measurements of the spectra emitted by atoms.

3.5 Pressure Related Processes

LIBS measurements are influenced by the ambient conditions. Pressure alters the plasma characteristics affecting the emission intensity, width and resolution of spectral lines¹⁰⁴⁻¹⁰⁷.

In different pressure environments the temporal process of plume dynamics is changed, because of a difference in the mean free path of particles in the surrounding medium. There is also a discontinuity in the amount of mass ablated from the sample due to these same changes in confinement of the plasma volume.

Mean Free Path:

$$\ell = \frac{RT}{\sqrt{2}\pi d^2 N_A P} \quad (3.20)$$

Where:

- ℓ = mean free path
- R = universal gas constant = 8.31J/mol K
- T = temperature
- d = molecular diameter, nominal approximation value = 0.3nm
- N_A = Avogadro's number = $6.0221 \times 10^{23} \text{ mol}^{-1}$
- P = pressure

Leading to mean free path calculations of:

Pressure (Pa)	Pressure (mb)	Mean Free Path (m)
160×10^3	1600	63.8×10^{-9}
150×10^3	1500	68.1×10^{-9}
101×10^3	1013	100.8×10^{-9}
78×10^3	780	130.7×10^{-9}
53×10^3	530	192.6×10^{-9}
30×10^3	297	0.34×10^{-6}
9900	99	1.03×10^{-6}
5	5×10^{-2}	2.04×10^{-3}
0.03	3×10^{-4}	0.34
1×10^{-3}	1×10^{-5}	10.21
400×10^{-6}	4×10^{-6}	25.53

Table 3.4: Pressure values and corresponding mean free paths. (calculated from equation 3.20)

This table shows pressure measurements in both the S.I. units of Pascal and millibar, as millibar are the pressure units used in this work. From this table one can see the huge difference in the mean free path of the particles that the plasma volume is expanding into, from 64 nm to 26 m!

There may also be a change in the intensity of a spectrum due to the influence of the surrounding medium. Such interference from the ambient gases may be due to absorption or emission of spectral lines of interest. Much work has been done in the area of low pressure LIBS systems^{104,105,107,108} but less has been covered on high pressure systems^{106,109,110}. However parallels can be drawn from papers on Laser Emission Spectroscopy (LES) under high pressures in liquids. A paper in this area reveals that “*pressure has little effect on the early-stage plasma evolution, but as the plasma cools, solution pressure begins to play a major role*”¹¹¹

Low pressures result in reduced confinement of the plasma volume, allowing it to dissipate more quickly and thus resulting in reduced excitation within the plasma due to fewer collisions of the plasma species. In contrast to this, the mass

of the ablated sample may increase due to the reduced shielding of the sample surface by the plasma.

At pressures just below atmospheric pressure the plasma has been shown to be larger than at atmospheric pressure¹⁰⁸. These results show that the increase in line intensity peaks at 1.3 kPa and then decreases beyond this point with no further decrease below 0.4 Pa. The peak has been attributed to reduced confinement of the plasma to the surface compared with that at atmospheric pressure and increased mass ablation of the target, with the lack of further decrease being ascribed to a steady state of ablation.

A different study undertaken at low pressures has shown greater than a 1 order of magnitude increase in ablation rate when changing from atmospheric pressure (101.3 kPa) to a pressure of 1.3 kPa¹⁰⁵. This has been attributed to the reduced shielding of the surface at these lower pressures.

The same study also showed a signal increase by a factor of 3-4 when reducing the pressure from 78.6 kPa to 9.3 kPa¹⁰⁵, and that continued reduction in pressure resulted in a reduced line intensity. These results are expected due to plasma dissipation in lower pressure regimes, but the loss in signal could also be due to a misalignment or defocusing of the optics collecting the signal as the plasma size changes.

At higher pressures one would expect the plasma confinement to increase producing a small plasma volume. It has been shown in one account that this is not the case due to the plasma having an extremely high pressure in the early stages of its lifetime¹⁰⁶. However, a contrasting investigation shows that the plasma size does decrease with increasing pressure¹¹⁰.

There are documented accounts of high pressure environments causing some spectral lines to broaden, occasionally resulting in self absorption due to increases in confinement¹⁰⁶. This would be expected with some spectra when increasing the pressure due to the low lying upper levels in some species¹¹⁰. This draws the conclusion that there is some increase in confinement, but it is

minimised when the plasma is in initiation due to the plasmas internal pressures. This argument is backed up by research undertaken by Arp et al¹⁰⁶ (2004), stating that *“a steady state is reached at which increased pressure does not produce decreased ablation.”*

This study is also linked to discussions on plasma shielding under increased pressures. It has been inferred that *“above a certain pressure, once the plasma is established, plasma shielding becomes so strong that further increases in the pressure do not significantly increase shielding.”* Having said that, these measurements were done at very high pressures, 0.078 MPa – 9.1 MPa, and the paper states that *“The majority of change occurred as the pressure was increased from atmospheric to 4.5 MPa”*, so it is still of interest to study these affects in our research.

In high pressure environments the ambient gas is also an important aspect. This gas may absorb some of the emitted plasma species if the emission lies within the absorption coefficient of the surrounding medium. The ambient gas may also become excited itself, emitting at a possible wavelength of interest, (e.g. CH₄ atmosphere interfering with possible C emissions from sample).

Data taken in a different piece of research done by Arp et al¹¹⁰(2004) shows that in different pressure environments, when changing the delay time or laser power, one observes a change in line intensity of these emissions but within the same elemental spectra.

With all these factors to take into account when analysing LIBS in different pressure environments one needs to consider the influences of; pressure; temporal delays; power requirements and wavelength interferences.

3.6 Power Related Processes

Power, or laser pulse energy, is important in LIBS research as it affects the amount of ablated material and the plasma size in measurements. It is of particular importance in this study as space driven applications often have power limits, and a knowledge of the minimum power needed in order to produce a reproducible plasma is crucial.

Measurements in lower pressures, carried out by Radziemski et al¹⁰⁴, have determined that the minimum energy at which a reproducible plasma can be formed is 17mJ/pulse, and that there is a significant difference in results when changing the pressure in the experiments. Another study, but for high pressure systems, by Zane et al¹⁰⁶ shows that increases in pulse energy from 30-50 mJ/pulse produce an increase in emission intensity. This research study will examine those values and ascertain if this is also the case in the pressure and gaseous environmental conditions of Titan, together with the changes that are apparent in other pressure and gas regimes.

3.7 Gas Related Processes

The ambient gas in LIBS measurements plays an important role, as interference from spectral lines and absorption of spectral emissions by the ambient gas can occur. Titan has a methane nitrogen mix in its atmospheric composition. Variations of these mixes were chosen for the study, together with pure gas fills of nitrogen and methane. Nitrogen is known¹¹⁰ to be relatively inert and has few atomic emission lines, minimizing interference. Methane is known to be predominant on Titan in its atmospheric composition, precipitation and possibly methane seas. It is of interest to study how much these gases and their absorption at the higher pressures of Titan's atmospheric conditions affect the LIBS plasma and its emission properties.

Methane is known^{112,113} to have absorption bands in the infrared portion of the electro-magnetic spectrum. These bands range from approximately 600+ nm.

(619 nm, 727 nm, 890 nm being the lowest bands), the bands ranging from 750 nm can be seen in figure 3.8.

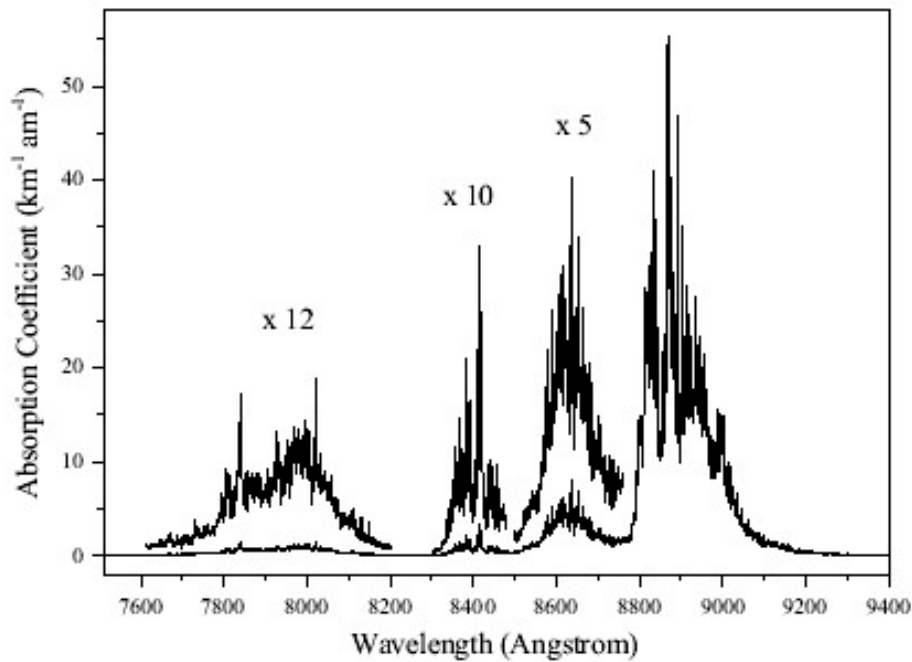


Figure 3.9: Absorption bands of methane from 750-940nm¹¹⁴

Methane is known¹¹⁵ to dissociate with the incidence of solar photons. Methane plasmas contain many reactant products, species present incorporating¹¹⁵⁻¹¹⁹ many ions, radicals and molecules such as hydrocarbons, the most abundant being: C_2H_6 (ethane) and C_2H_2 (acetylene), with others such as: C_2H_4 (ethylene), C_3H_8 (propane), CH_3 (methyl, free radical), CH_2 , CH , H , and H_2 .

Titan's atmosphere contains predominantly nitrogen. The nitrogen radicals can react with these methane radicals producing more complex materials such as HCN (hydrogen cyanide), C_2N_2 (cyanogens), HC_3N (cyano acetylene), C_2H_3CN (ethyl cyanide) and HCN polymers. These products are known as tholins which form the reddish-brown powder producing Titans haze.

3.9 Optical Fibres

Many LIBS systems also make use of optical fibres (FO). A optical fibre utilises the phenomenon of total internal reflection, whereby a ray hits the cladding at an angle greater than the critical angle, θ_c , and as such is reflected back into the core, as shown in figure 3.10:

$$n_i \sin \theta_c = n_r \sin 90 \quad (3.24)$$

from Snell's Law

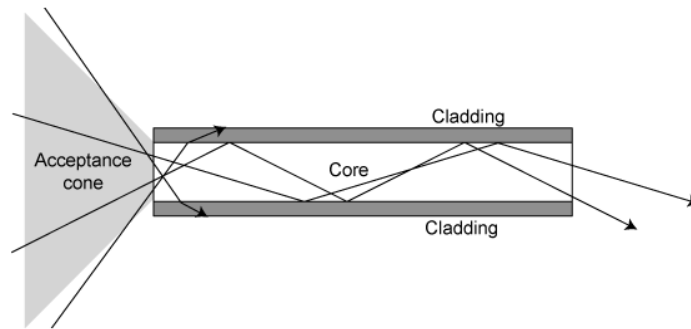


Figure 3.10: Image of total internal reflection inside a optical fibre.

The acceptance cone angle for optical fibres of numerical aperture 0.22 is 25° - 26° .

Derived from:

$$\text{Acceptance angle, } a \quad \sin a = \frac{1}{n_0} \sqrt{n_1^2 - n_2^2} \quad (3.25)$$

Where: n_2 = refractive index of cladding
 n_1 = refractive index of core
 n_0 = refractive index of external medium

if $n_0 = 1$ then:

$$NA = \sin a = \sqrt{n_1^2 - n_2^2} \quad (3.26)$$

3.10 Spectral Resolution/Diffraction

Spectrometers used in LIBS experiments utilize diffraction gratings to disperse the light.

The grating equation for such a system is:

$$a \sin \theta = \lambda m \quad (3.27)$$

Where:

θ = angle between normal to the grating and the diffracted beam

a = ruled spacing

m = the integer of the order of the maximum.

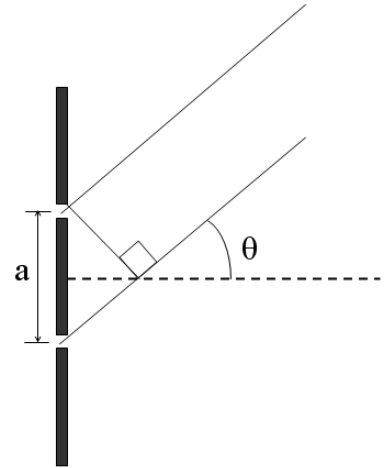


Figure 3.11: Illustration of diffraction parameters for a grating.

From this equation one can derive the angular dispersion, $d\theta/d\lambda$:

$$\frac{d\theta}{d\lambda} = \frac{m}{a \cos \theta} \quad (3.28)$$

The ruled spacing is the reciprocal of the number of lines per unit length, so for a $150 \text{ grooves mm}^{-1}$ grating, a is $6.7 \mu\text{m}$.

In most modern spectrometers ruled gratings are used, the angle of which is adjusted to enhance a particular diffraction order¹²⁰. These gratings are blazed gratings as shown in figure 3.12:

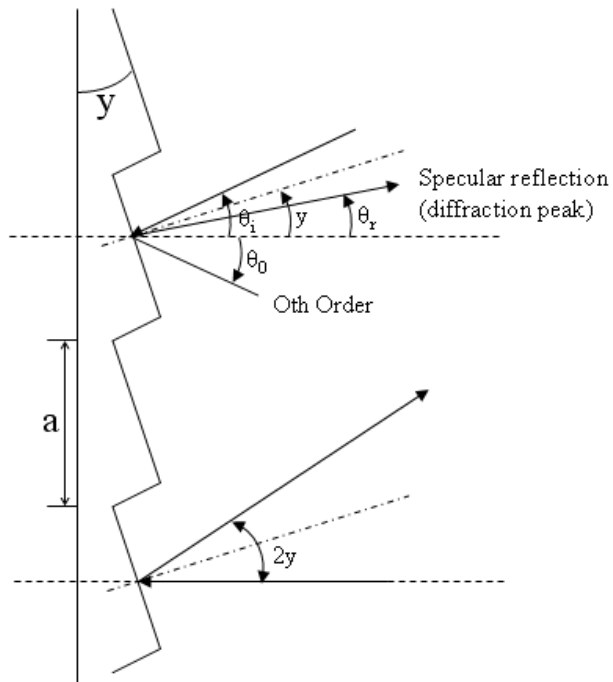


Figure 3.12: Illustration of diffraction parameters for a blazed grating.

The angular positions of the nonzero orders, θ_m , are determined by a , λ and θ_i . The location of the diffraction peaks is governed by the blaze angle, y .

The second illustration shows the incident wave normal to the plane of the blazed reflection grating: $\theta_i = 0$

For specular reflection:

$$\theta_i - \theta_r = 2y$$

Therefore the diffraction peak is at:

$$\theta_r = -2y.$$

or:

$$\theta_m = -2y,$$

in other words:

$$a \sin(-2y) = \lambda m \quad (3.29)$$

3.11 Detectors

The LIBS detection system is based on an Intensified Charged-Coupled Device (ICCD). The ICCD works by coupling a CCD detector to a micro-channel plate (MCP) to increase the gain in the system. The MCP is closely related to a photomultiplier tube, increasing the electron cascade as shown in figure 3.13:

Photons incident on the photocathode are absorbed and electrons are released, which are then multiplied into a charge cloud by a cascade in the MCP and finally are incident on the fluorescent screen. The MCP can be gated with short time constants by controlling the voltage across the system.

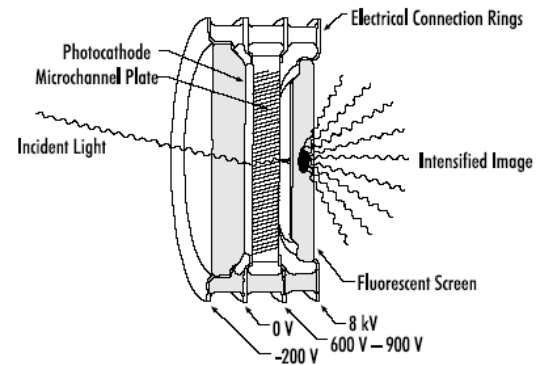


Figure 3.13: An image intensifier tube

The CCD works as an image sensor via the integration of an array of photoactive capacitors. In reading the device each capacitor transfers its charge to a coupled capacitor and so on until the charge is transferred to the last capacitor in the system. This then transfers the charge to an amplifier to be converted into voltage for the line by line reading of the array.

3.12 Timing

Timing considerations are extremely important in LIBS experiments. A gated detector needs to capture the image of the plume when it displays the recombination radiation emitted in the later relaxation stages; which is after both the laser pulse and the background continuum have diminished, as shown in figure 13.14.

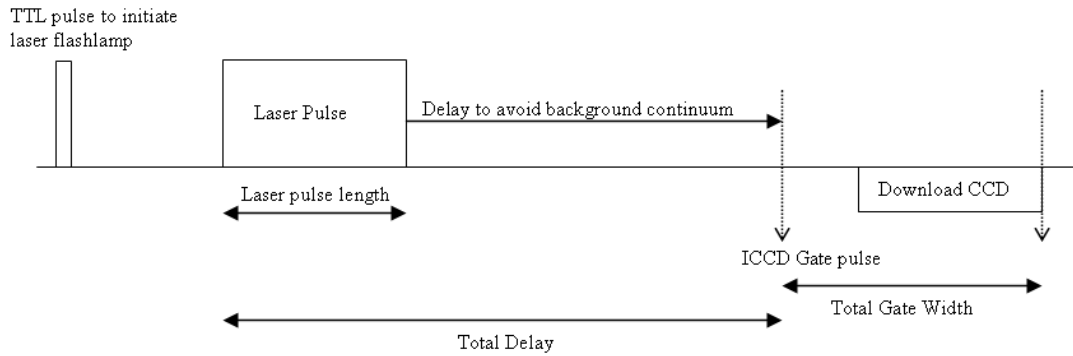


Figure 3.14: Illustration of timing requirements for LIBS experiments.

Typically the plume signal decays over an interval of one to several microseconds, dependent on the energy deposited and the pressure regime, (with reducing pressure the temporal process is shortened due to reduced confinement). After approximately $1\mu\text{s}$ from the incident laser pulse the discrete spectral lines begin to form from the recombination radiation emitted from the plume. This is the spectral window of interest and as such the ICCD gate pulse needs to be triggered within this period.

3.13 Limit of Detection

LIBS analysis brings with it many restrictions when undertaking qualitative and quantitative analysis. These limitations are commonly known as ‘Limits of Detection’ (LOD) and can take many forms.

Apparent in every LIBS system are integral shot to shot variations, these can be the result of many factors such as; laser intensity fluctuations, laser light scattering due to surface effects and changes, geometrical and optical parameters, ambient atmosphere attributes and dust particles. Also relevant are substrate composition variations including, reflectivity changes, re-deposition from the plume, integral composition incongruities and matrix effects.

These effects can be minimised but not eliminated. Known methods for reduction of these influences are calibration, integration, analysis of ratios rather than true intensities and background elimination.

4. Development of LIBS

4.1 Experimental Apparatus

Salford University obtained a LIBS system in the summer of 2001 which was an Acton Research Corporation, SpectraPro 500i, 0.500m, F/6.5, imaging triple grating spectrograph, in a Czerny-Turner configuration [Appendix D]. The three gratings incorporated are a 2400g/mm ruled grating blazed at 240nm a 600g/mm ruled grating blazed at 1 micron and a 150g/mm ruled grating blazed at 300nm. The spectral responses of the gratings are shown in [Appendix E].

The system also incorporates a Princeton Instruments Inc. PI-MAX Intensified CCD (ICCD) camera with its intensifier photocathode working in the wavelength range of 190 - 900nm. The synchronous operation of this camera and its computer interface is accomplished via a ST-133 controller. To facilitate time-resolved measurements involving gating operations, the ST-133 has a built-in Pulse Timing Generator (PTG) card, with 2ns width and 1.6ns delay gating capabilities possible at a maximum repetition rate of 10Hz.

The camera uses a proximity focused microchannel plate (MCP) image intensifier, which delivers light via a fused fibre-optic bundle, optically coupled to a CCD array¹²¹. This intensifier acts both as an electronic shutter which is controlled by the PTG and also as the gain medium for exposure. Integral to this camera is the thermoelectrically cooled CCD detector with an active area of 26.6 x 6.6mm.

The software used to control the system's gratings, PTG/ICCD and mirror and also to capture the images was WinSpec/32¹²² with a Thermo Galactic™ GRAMS/32® interface. Also, the SpectraPro software provided with the equipment was used to re-calibrate the EPROM in the system.

The ablation source was a Continuum Surelite SLI – 10, Q-switched, Nd:YAG laser, frequency doubled to run at 532nm, with a maximum power output at this wavelength of 260mJ.

4.2 Laser Optimisation

The laser was not in operation when it was first commissioned, so a full optimisation was undertaken.

Before the laser would operate a new flashlamp was purchased and installed, the laser's printed circuit board (PCB) was repaired. An assessment of any other problems was then undertaken to optimise the laser output. This was done by checking if the laser was free running, the power output was at full capacity with optimum oscillator alignment, the beam shape was satisfactory and whether the optics in the system were damaged.

The laser voltage was reset to read 1.06kV, (original 1.26kV). This enabled a free running verification. This optimisation was done with an oscilloscope set up to take readings from a photodiode circuit incorporating a silicon photo-detector (bpx65) with a rise time of ~3.5ns.

Readings were taken by imaging a business card placed between the pockel cell and the $\frac{1}{4}$ wave plate while the shutter was open. The curve on the oscilloscope was analysed, free running being apparent when spikes showed in the output curve.

Voltage readings were scanned, checking for free running spikes apparent in the oscilloscope reading. After full characterisation had been fulfilled the laser voltage was set to 1.38kV.

The beam shape was checked using photographic paper and the alignment adjusted accordingly.

Lastly the beam profile was analysed. Initially this was attempted using an image of the beam profile as shown in figure 4.1:

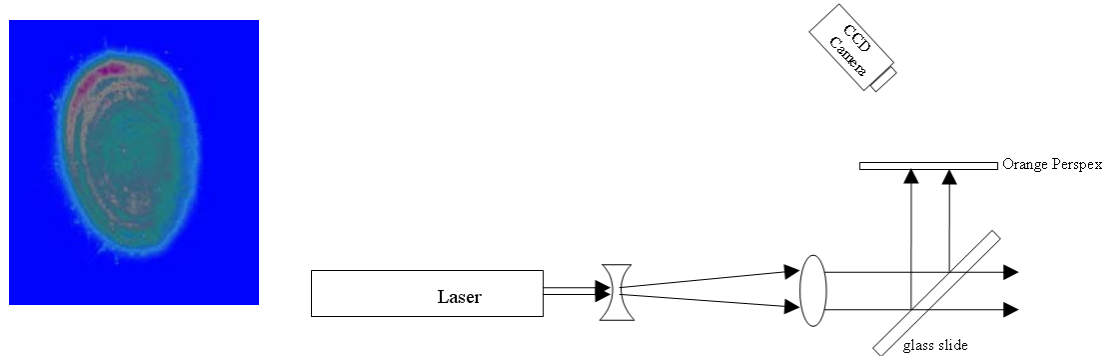


Figure 4.1: Setup and image of beam profile capture using CCD camera

This was unsatisfactory because, in order to capture the image with the CCD available, the beam needed to be diverged and attenuated. This changed the beam profile and added aberrations to an unknown extent and as such this could not be used as viable information. Consequently a photodiode was set up as shown:

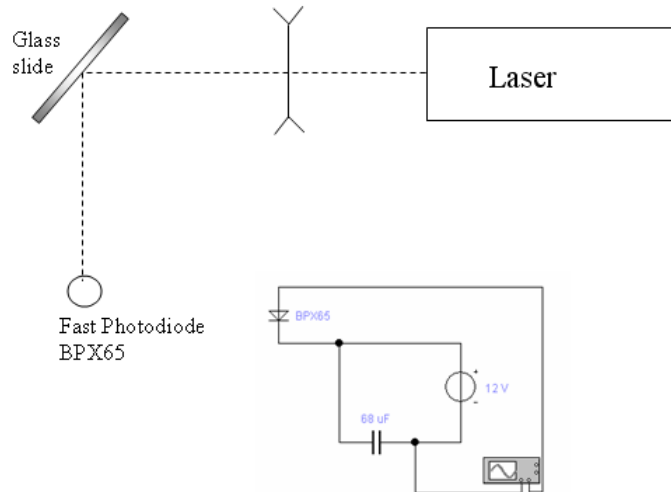


Figure 4.2: Setup and circuit diagram of beam profile capture using photodiode

The beam profile was taken using voltage readings from the photodiode. The results are shown here:

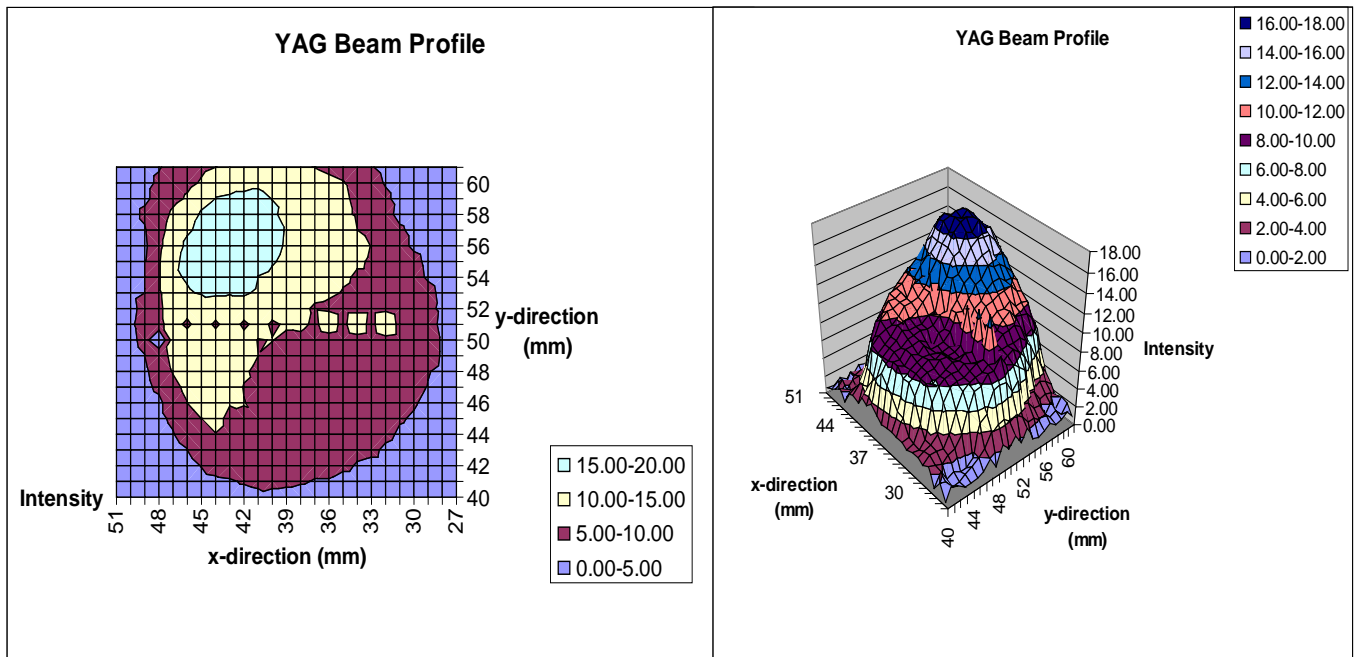


Figure 4.3: Charts showing beam profile from photodiode capture, the different colours represent the beam intensity

As can be seen, the profile was far from 'true' Gaussian. To combat this, the less intense section of the beam was masked out to produce a near homogeneous beam output at the high intensity range.

Once the laser had been fully reconditioned the new spectrometer system was evaluated. This was initially done using known wavelength emissions from a constant source; a cadmium (Cd) lamp, with the wavelength emissions; 361.0508nm, 479.9912nm and 508.5822nm used for calibration.

4.3 Light Coupling Optics

An optics system was developed to couple the light to the spectrometer. This delivered the light from the Cd lamp, (and subsequently the laser ablated plume), to the spectrometer at an observed focal length of 0.5m. The software used to optimise this lens setup was OSLO LT developed by Sinclair Optics¹²³. After careful consideration of the possible parameters, using the lenses available, the setup shown in figure 4.4 was finalised. The lens database, and OSLO parameters are attached in [Appendix F].

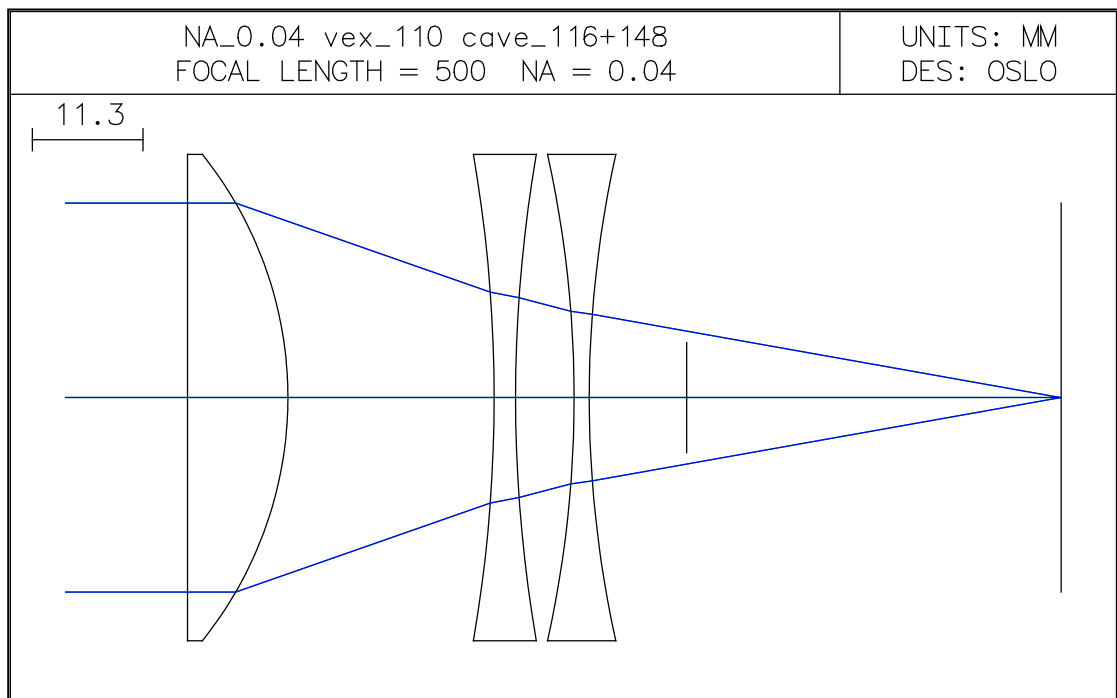


Figure 4.4: Light coupling optics lens setup diagram

This setup takes parallel light into the spectrometer at a distance of 89mm but with an observed distance of 500mm. The incident light first has to be collimated. This is done using a simple convex lens placed in front of the above lens system, set at the focal point of the lens from the light source.

4.4 System Malfunction Evaluation

The LIBS suffered from a number of malfunctions that had to be addressed before the experimental work could commence. This proved to be very time consuming.

However, as each problem was successively removed, the evaluation of subsequent problems became easier. Unfortunately, it was approximately 2 years before all the problems had been resolved. While this evaluation and solution of the problems was inevitably time consuming, a full appreciation of the capabilities and limitations of the system was acquired over the period. The problems, together with their solution, are detailed below.

4.4.1 EPROM:

The EPROM was programmed with an incorrect code which caused faulty return settings of the grating turret and incorrect software readings indicating which grating was currently active. For example, when the turret was on 2400g/mm the software read that it was on 150g/mm, the actual grating that was active was ascertained by the spectral window present in each capture.

This problem was solved by using SpectraPro software in Terminal Mode and HyperTerminal, available from Windows98. The status of the EPROM was read using the mono-eestatus dialogue box within HyperTerminal. These settings were found to be faulty and so the EPROM was restored by 'flashing' it with original factory settings.

4.4.2 Stepper Motor:

The stepper motor problems were highlighted when erroneous wavelength readings were observed, as they were shifting beyond acceptable tolerances. The accepted wavelength reproducibility of each grating is stated in the system specification [Appendix D]. The wavelength reproducibility fell outside these accepted values. For example, a shift of 12nm occurred on the 150g/mm grating where the specification for this grating quotes a wavelength reproducibility of +/-

0.4nm. These faults highlighted a problem and a new stepper motor was installed. The data is shown in the tables below:

Table 4.1: Table showing wavelength reproducibility errors, Grating 2400g/mm.

Wavelength reproducibility = +/-0.025nm, resolution for ICCD based on 4 pixels = 0.085nm

Test Number	Peak wavelength value	Wavelength change (with previous test number)
2	576.9805	
3	576.5762	-0.4043
12	576.9935	0.4173
15	576.5762	-0.4173
18	576.5892	0.013
28	576.5761	-0.0131
31	576.7308	0.1547
60	576.9935	0.2627
64	576.9672	-0.0263
67	576.5975	-0.3697
68	576.9670	0.3695

Table 4.2: Table showing wavelength reproducibility errors, Grating 600g/mm.

Wavelength reproducibility = +/-0.1nm, resolution for ICCD based on 4 pixels = 0.34nm

Test Number	Peak wavelength value	Wavelength change (with previous test number)
0	579.1869	
4	576.4671	-2.7198
13	579.2855	2.8184
16	576.4638	-2.8217
23	576.6306	0.1668
33	576.6302	-0.0004
39	576.6302	0
51	579.5115	2.8813

Table 4.3: Table showing wavelength reproducibility errors, Grating 150g/mm.

Wavelength reproducibility = +/-0.40nm, resolution for ICCD based on 4 pixels = 1.36nm

Test Number	Peak wavelength value	Wavelength change (with previous test number)
1	545.3674	
5	534.6346	-10.7328
14	545.9348	11.3002
17	533.613	-12.3218
24	533.9536	0.3406
34	533.613	-0.3406
40	534.2941	0.6811
52	546.6258	12.3317

4.4.3 Mirror:

It was found that the diverting mirror on the entrance slit was not always returning to the settings set in the software, (front or side position). This was ascertained when captures that should have produced a strong signal output were only producing noise. After all other possibilities were ruled out it was deduced that the mirror must not be returning to its correct alignment. The spectrometer was opened up and it was found that the returning spring had become detached, this was re-attached and no further problems manifested themselves.

4.4.4 PTG Cable:

The manufacturers discovered a problem with all their serial cables which relayed the signal from the spectrometer camera to the PTG card. They were all recalled and replaced.

4.4.5 Software:

There were many other WinSpec software problems that became apparent while running tests to optimise the system. Each was reported to the manufacturers and most were corrected with the advent of new software. Some of these problems are listed below, a selection of sweeps are detailed in [Appendix G]:

Continuous cleans

With continuous cleans set 'on' there was no signal able to be captured, (with continuous cleans 'off' the system worked satisfactorily). A solution was not provided and as such the system cannot be run with continuous cleans on.

Burst mode

This facility is available to take multiple shots from a single trigger pulse, allowing analysis of the plume temporally. This mode never worked and as such this facility was unavailable.

View width/delay sequence

This button is meant to show the user the width and delay sequence for sequential timing. Each time it was pressed the software crashed. This was also true if one attempted to save these values to file. This was resolved by reverting to a previous version of the software.

4.4.6 PTG Card/Timing:

Only after all the faults that were apparent using a constant source Cd lamp had been discovered, could the timing for the LIBS system be appraised. This revealed further problems.

The theory section covers the parameters to be taken into account when considering timing in a LIBS system. In the LIBS system used in this work the Nd:YAG pulse at 532nm lasts for ~6ns. A further delay in the system must also be implemented due to the initial background continuum of the laser induced plasma.

In setting up the timing considerations it is essential not to capture the laser pulse accidentally as its high intensity would damage the ICCD. Materials were characterised using a spectrophotometer and a blocking filter was employed, (orange perspex) shown in figure 4.5, that cut out the laser light wavelength:

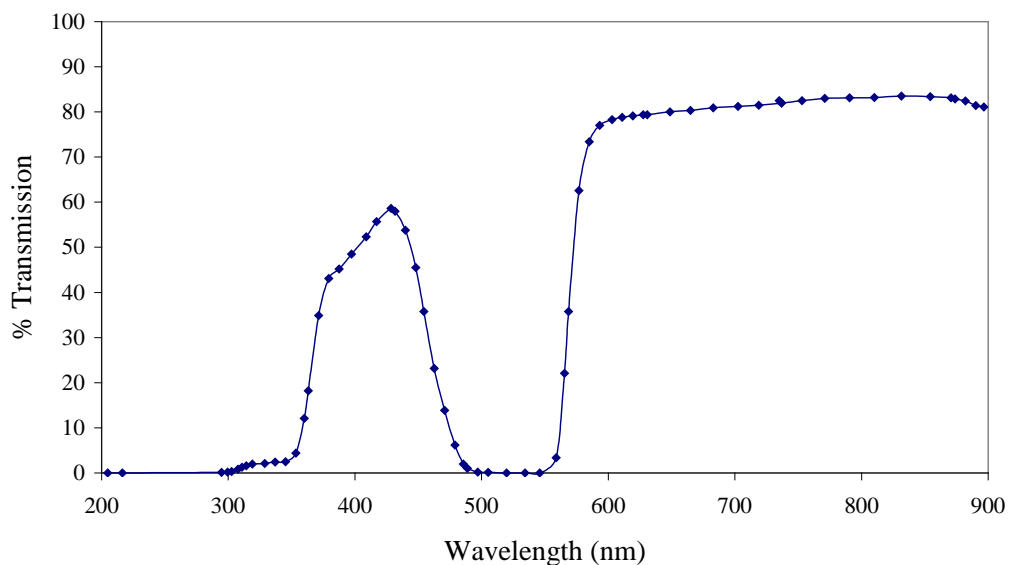


Figure 4.5: Transmission response of orange perspex.

This was placed in front of the entrance slit of the LIBS spectrometer to ensure no stray laser light could enter the system.

The timing for the system was originally set using a Pulse Generator in the following setup:

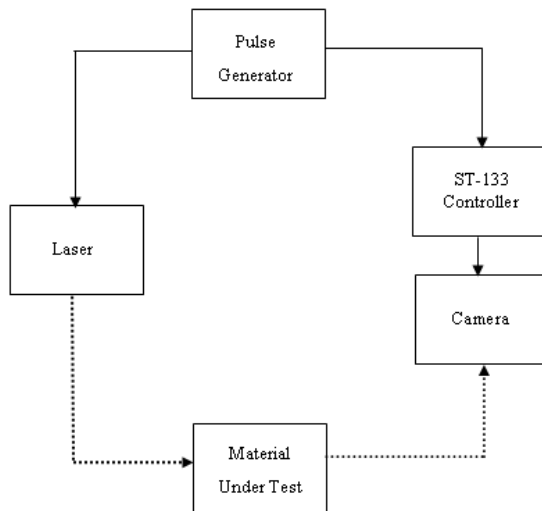


Figure 4.6: Schematic of the system timing using pulse generator

This setup however was found not to work satisfactorily. The laser fired correctly when receiving an input pulse, but the ST-133 controller did not send the signal to the camera. It was found that the controller was not in fact receiving the pulse as there was an impedance mismatch.

In order to match the output of the pulse generator, (15V), to the external sync input, (5V), of the ST133 controller an in-house impedance matching circuit was needed. This was developed using Electronics Workbench¹²⁴ software as a guide. The circuit below was devised utilizing a TL071CP fast Op-Amp. (Originally an LM741 Op-Amp was used but this was found not to respond fast enough to the 10Hz input signal.)

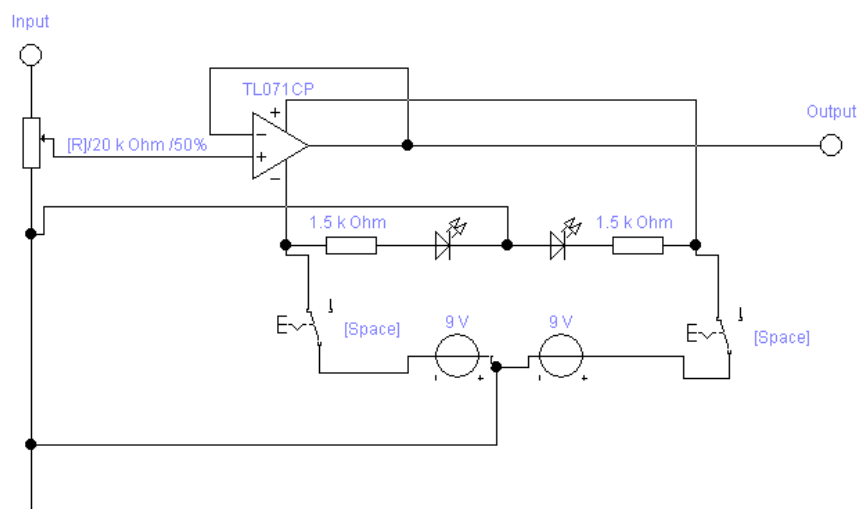


Figure 4.7: Circuit diagram of impedance matching circuit

With the new system the camera was now able to capture a signal, but this signal was found to consist only of noise. This was thought to be a result of the timing in the system. A delay could be introduced via the software for the PTG, but no matter how much this delay was varied, no LIBS signal was captured.

After careful investigation it was found that the inherent delays in the system itself, (such as device and wiring delays), were much larger on the controller side of the system layout than on the laser side, causing the camera to capture the event after the LIBS signal had completely died away. A timing circuit was developed to produce a delay on the laser side of the system. It was hoped that the PTG software should then be able to introduce a sufficient delay to match the camera shot to the plume output. The following circuit, figure 4.8, was formulated which produced a delay of 49.4ms

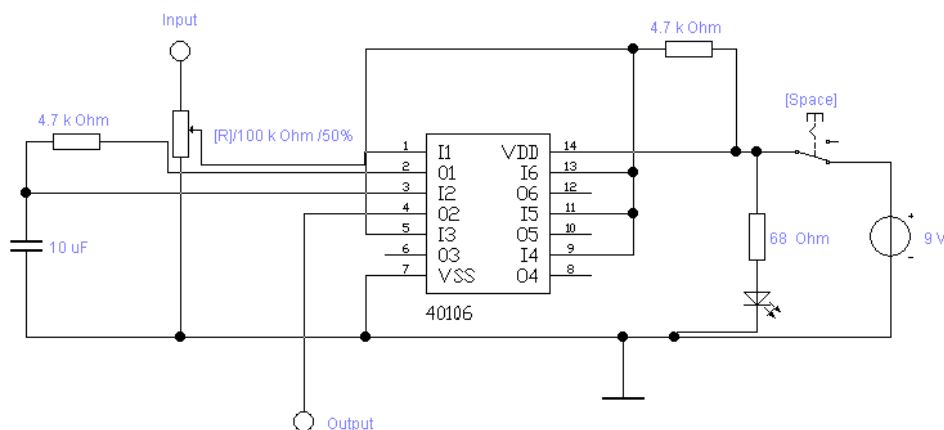


Figure 4.8: Circuit diagram of delay circuit

The system was setup accordingly, as shown in figure 4.9:

Timing was calculated using:

$$\text{Cable Delays} = 1.5\text{ns/ft} = 4.92\text{ns/m}$$

$$\text{Speed of light} = 3 \times 10^8 \text{ ms}^{-1}$$

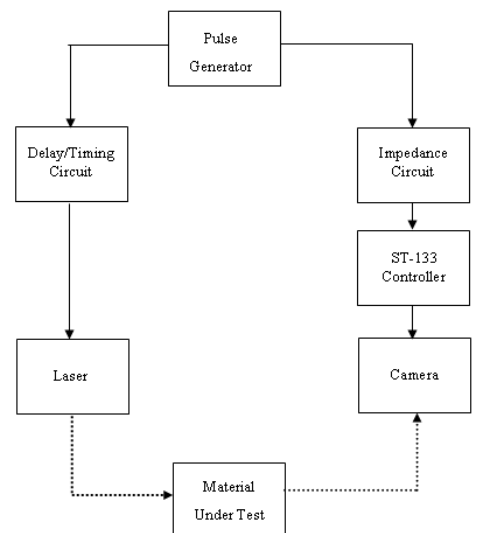


Figure 4.9: Schematic of the system timing using delay and impedance circuit.

After exhausting a wide range of PTG software delay possibilities and still getting no LIBS signal the circuit was re-analysed and it was found that the capacitor in the circuit did not respond quickly enough to the input signal. This capacitor was replaced but unfortunately this still did not produce a LIBS capture.

It was decided to remove all unknowns from the system to ascertain if any of the faults were due to a malfunction in the hardware or PTG software, as the schematic shows in figure 4.10.

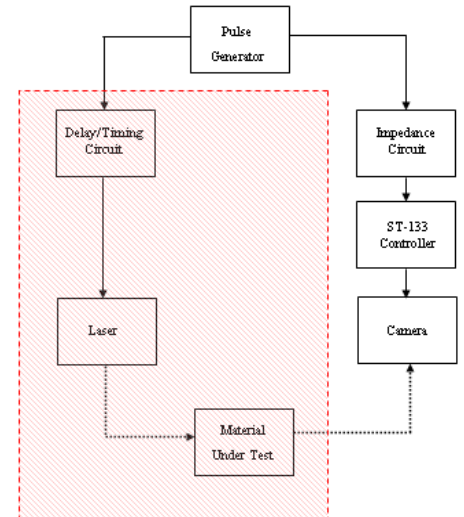
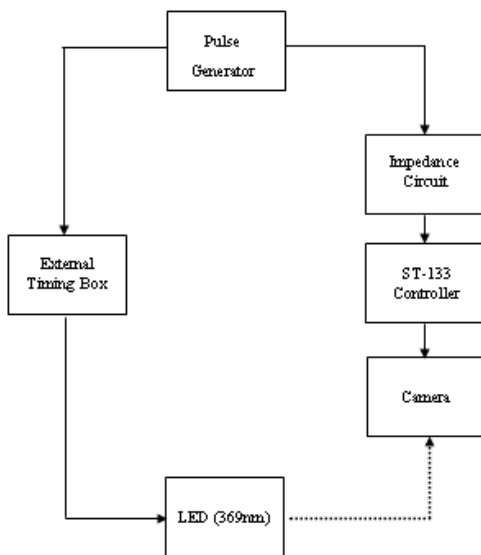


Figure 4.10: Schematic of the system timing, showing redundant parts of system to be removed for calibration.

Figure 4.11: Schematic of the system timing, showing setup with external timing box.



The PTG settings were cross referenced with an external timing box connected to a light emitting diode (LED) emitting at 369 nm, the schematic is shown in figure 4.11.

This box was set to turn on the LED after a 1s delay from its trigger-in and keep it on for 0.5s, (timing latency = $\pm 1\mu\text{s}$). The pulse generator sends a trigger to the timing box and a concurrent signal to the ‘external trigger in’ on the back of the PTG card, via the impedance circuit.

With the setup shown in figure 4.11 there was still no signal captured. The manufacturers were informed and they took the PTG card and repaired it. This

still did not solve the problem, so a new controller was provided. With the new controller a signal was finally captured.

Although a signal was captured it was found, following cross referencing with the known delay time on the LED and the delay time on the PTG software, that in fact the software had a problem. It was evident that the PTG width and delay parameters, set on the software, were 3 orders of magnitude in error.

This manifested itself when observing the file information after a shot was taken. For example if the parameters on the software were set to 1msec, (width and delay) and following the capture of the image the file information for that shot was observed, the information showed that the width and delay were captured at 1µsec. This discrepancy was cross referenced with the LED timing known to be correct and it was found that although the file information obtained after the capture was correct. the software settings were incorrect. The manufacturers were informed and a new version of the software was provided. After checking this software it was found that the problem still existed, but after further analysis it was found that the problem only existed when using repetitive timing mode on the PTG settings of the software. If sequential mode was used instead no similar problem existed. This was done by setting sequential mode in ‘repetitive’ mode, by setting the start and end settings on width and delay as the same.

The final arrangement for the timing system was set using the laser as the master trigger. The setup is shown in figure 4.12:

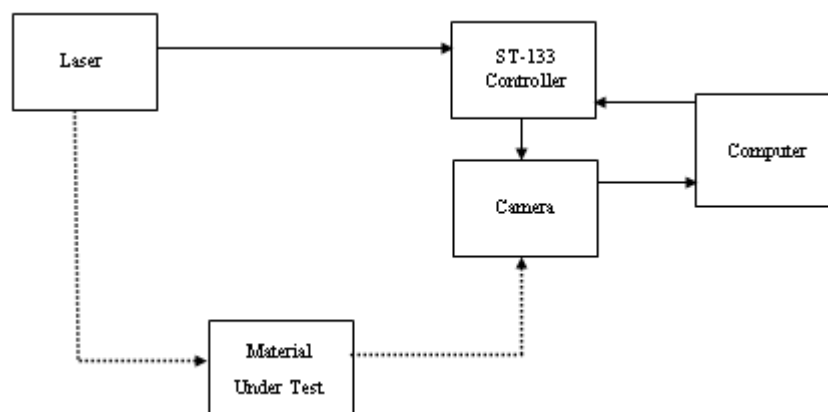


Figure 4.12: Schematic of the final arrangement for the timing setup of the LIBS system

The laser sends a signal to the controller via its fixed sync out, the laser fires 108.4 ± 1^{125} ns after the fixed sync out signal leaves. The laser light travels to the material under test (MUT) in 13.2ns. The signal takes 22.63ns to travel from the laser fixed sync 'out' to the external sync 'in' on the controller. There are internal delays in the controller, PTG and camera system which take 62.26ns. The software delays the ICCD camera shot until required. The light from the plume takes 10.7ns through the optical fibre of refractive index 1.6 to the spectrometer entrance slit, the light then takes 1.67ns to travel from the entrance slit to the ICCD.

The delays are summarised here:

Light travel to Camera = 134ns

Signal travel to Camera Capture (plus variable delay) = 85ns

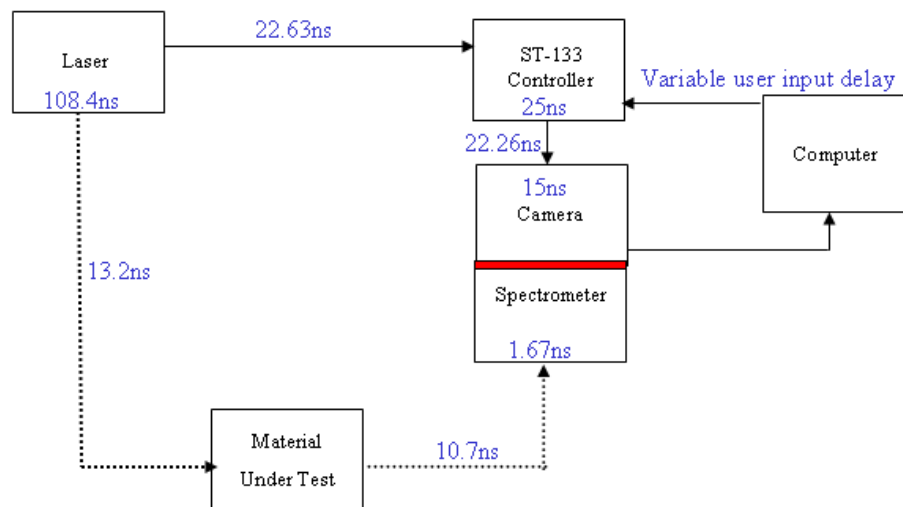


Figure 4.13: Schematic of the final arrangement for the timing setup of the LIBS system, with inherent delays shown.

4.5 Grating Efficiencies

Following the system timing setup described above, a check of the system's gratings efficiencies was undertaken and dummy's guides were written on the LIBS system's operation and setup parameters.

Intensity information at four wavelengths was obtained for each grating using spectral emissions from a mercury lamp, as shown in figure 4.14. This data was cross referenced with the National Institute of Standards and Technology¹²⁶ (NIST) values.

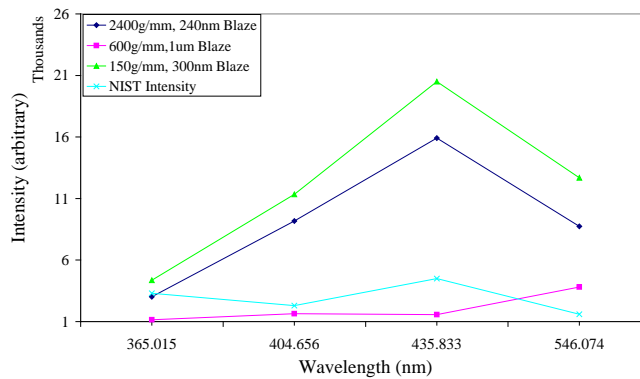


Figure 4.14: Intensity versus wavelength chart for mercury lamp emissions obtained from spectrometer captures and NIST values.

The trend differences are due to the grating efficiencies and should be taken into account when analysing results.

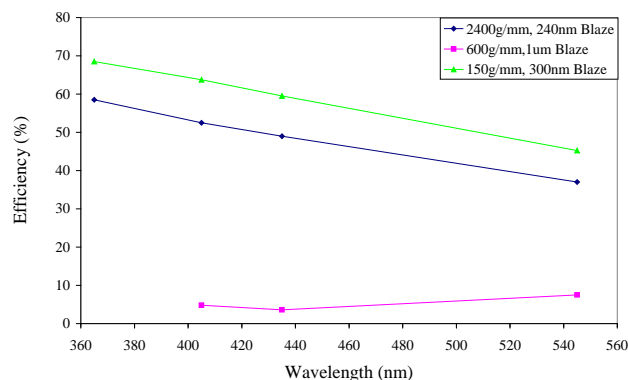


Figure 4.15: Grating efficiencies versus wavelength

Taking into account the percentage efficiency of each grating when plotting the intensity of each spectral line, the intensity versus wavelength chart fits more closely with measured NIST values.

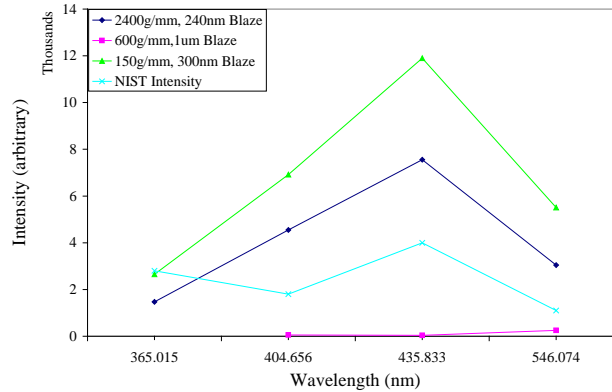


Figure 4.16: Intensity versus wavelength for gratings corrected for their efficiency wavelength response.

As can be seen, the 600g/mm grating in this wavelength bandwidth is not efficient, and as such was ruled out for future experiments. The optimum gratings to use for the wavelength range to be investigated are the 150g/mm and 2400g/mm.

4.6 Dummy's Guides

A number of simple manuals have been written to facilitate a new user's operation of the LIBS system – the so-called “dummy's guides”. The first dummy's guide to be written was Basic Spectrometer System Use, [Appendix H]. A manual was written for the use of the spectrophotometer, [Appendix I] and one was also written for the Conversion from WinSpec to Grams & Multifile Building, [Appendix J].

Together with the dummy's guides, computer programs were written by the author of this thesis in order to analyse the spectral lines obtained and match them to elements' spectral emissions. This was done using an astronomical catalogue and data table provided by NASA's now terminated Astronomical Data Centre (ADC). This catalogue [Appendix K] was obtained from their now discontinued ftp site: <ftp://adc.gsfc.nasa.gov>, in .dat format, last updated by Paul

Kuin [NASA/ADC] 07-Oct-1996. It appears that this information can possibly now be obtained from http://www.maa.agleia.de/Cat/sac_v_2.html#list quoting that the original data was: 6016 Line Spectra of the Elements (Reader, Corliss 1980-1981), see also catalogue 6086.

The format of the data was changed and prepared for use. A software program was then written in Pascal, (attached in [Appendix L]), to take spectral lines and search the database for matches, dependent on the wavelength accuracy for the grating which obtained the data.

After successive use of this program it became apparent that an update was needed. The process of acquiring the information was too laborious: it involved running the Pascal program, which then put the data into text files. Following this the text files needed to be compiled into one file, usually in Excel.

To facilitate quicker analysis a new database was set up in Access, (attached in [Appendix M]), which had queries to interrogate the data. This also output the spectra data into text files, which would need to be compiled into one file for viewing, but it did interrogate the data much more quickly than the previous Pascal program.

Lastly this database was advanced with Visual Basic for Applications (VBA) programming, (attached in [Appendix N]), to enter the data directly into Excel on separate sheets in one workbook. This program saved much time with analysis and so many other programs were written to assist the analysis process. All programs are listed here, and the full code is added to the appendices.

VBA Programs:

VBExcel Modules

A single workbook was used to contain all relevant programs and macros used for data analysis, correlation and formatting. A selection are added to [Appendix O].

Pascal Programs:

Wavefini

Original program built to interrogate the spectra at wavelength and grating specifications, attached in [Appendix L]

Peakshot

Program built to analyse the intensity of selected emission peaks, attached in [Appendix P]

Relstddev

Pascal program used to find average, standard deviation and relative standard deviation of a dataset, attached in [Appendix Q]

There was also a dummy's guide written to facilitate the use of some of the programs that are used in depth profiling, attached in [Appendix R]

5. Development of Pressure Apparatus

5.1 Experimental Apparatus

In order to facilitate the application of LIBS in different pressure environments suitable high pressure/vacuum apparatus (HPVA) was developed from existing hardware. The main experimental chamber consisted of a base unit and chamber, as shown in the working drawings shown as figure 5.1.

5.2 Dome Window

The dome had an optical window. Its transmission curve was analysed in a spectrophotometer to ensure satisfactory transmission for the laser input (532 nm), shown in figure 5.2:

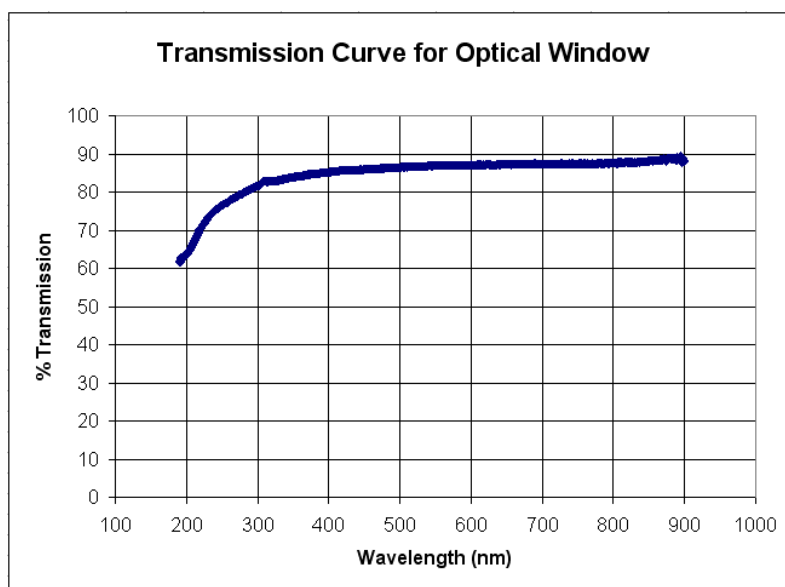
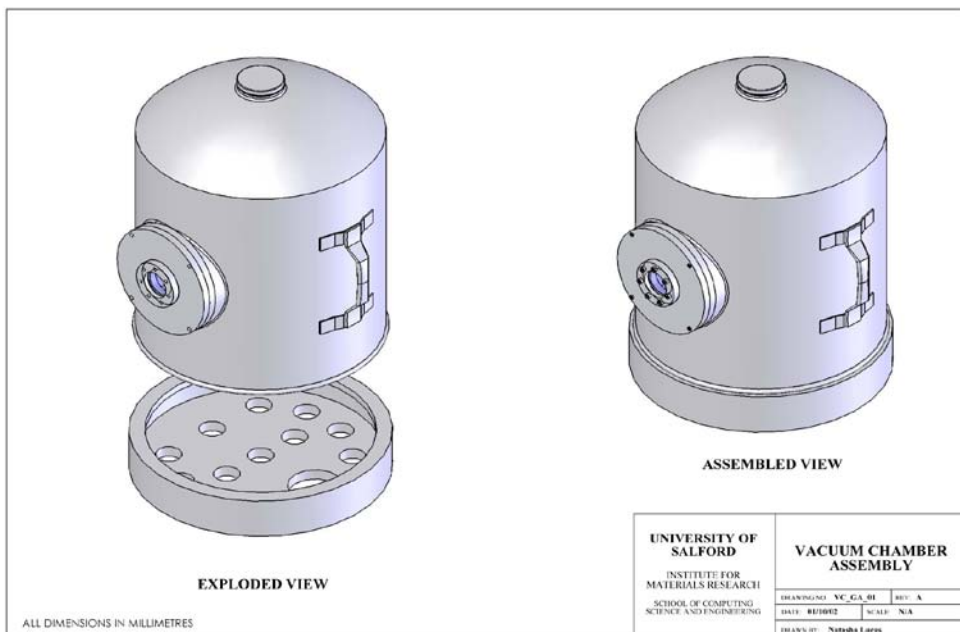
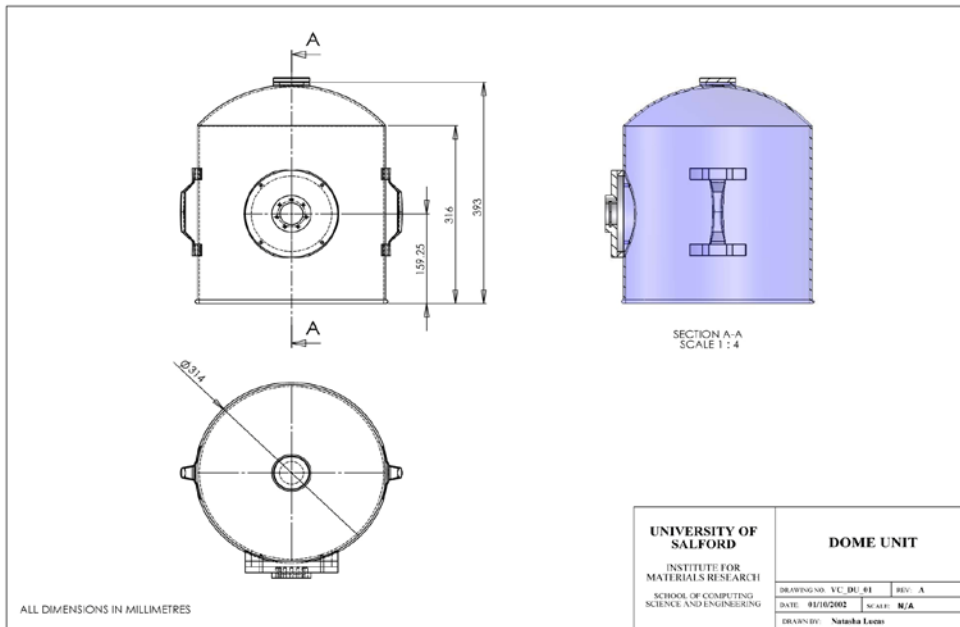
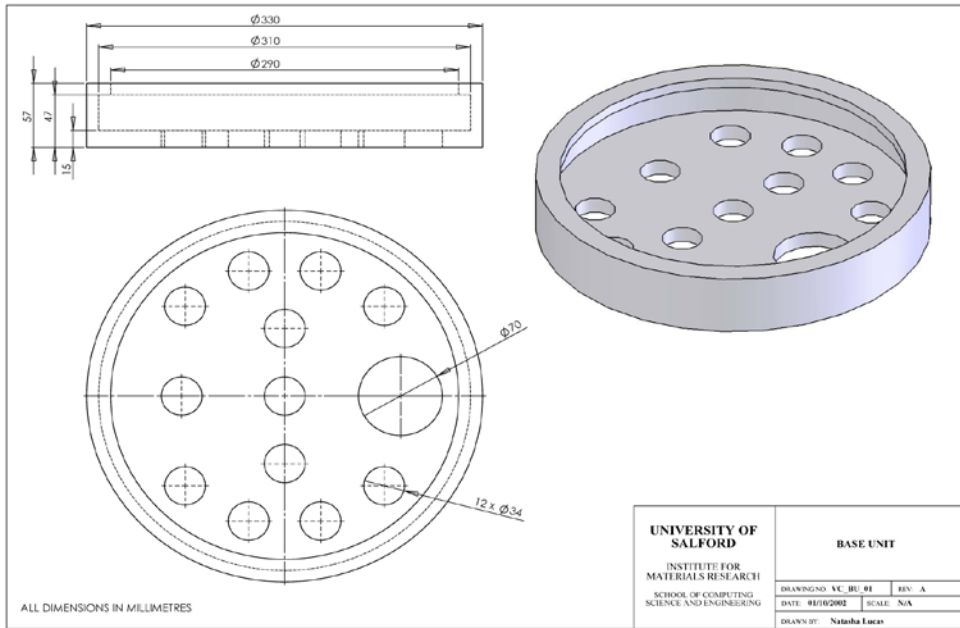


Figure 5.2: Chart showing transmission curve for the HPVA dome.

Figure 5.1 Working drawings of HPVA chamber



5.3 Sample Stage

A sample stage was developed from an old Scanning Electron Microscope (SEM) stage, which originally worked in a horizontal position. The capability to run vertically was solved by changing the stage's runners and adding a constant force spring of force 2N, kindly donated by Kern-Liebers¹²⁷.

A bracket was designed and developed¹²⁸ to couple the adapted SEM stage to the HPVA with feedthroughs for the micrometer movement rods of the stage, as shown in figures 5.3 & 5.4.



Figure 5.3: Image to show micrometer feedthroughs of sample stage on the HPVA

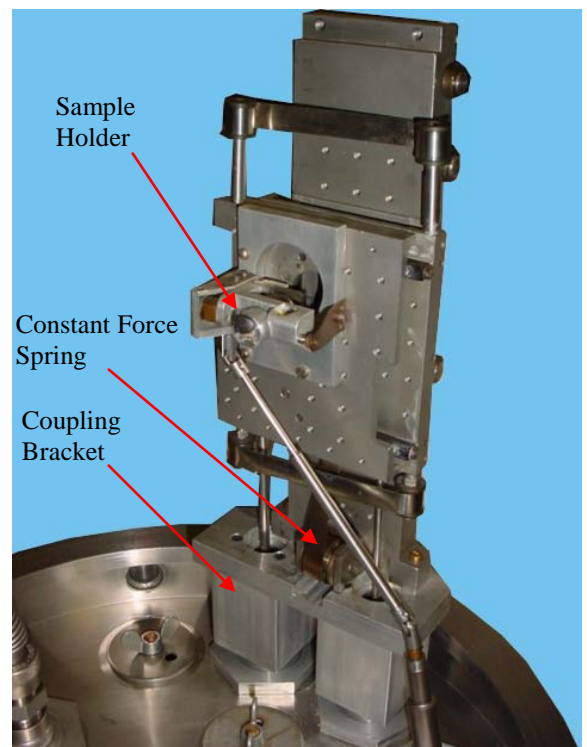


Figure 5.4: Image to show sample stage and coupling bracket

5.5 Optical Fibre

In order to couple the output from the laser plume to the external spectrometer optical fibre coupling was used.

This consisted of a UV-VIS optical fibre bundle, 2 metres long with a quartz core transmitting at 190nm to 1100nm. It contains a single row of 200 micron fibres terminating in 10mm diameter ferrules, as shown in figure 5.5.

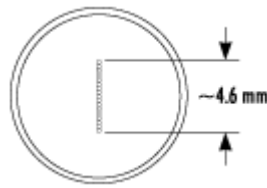
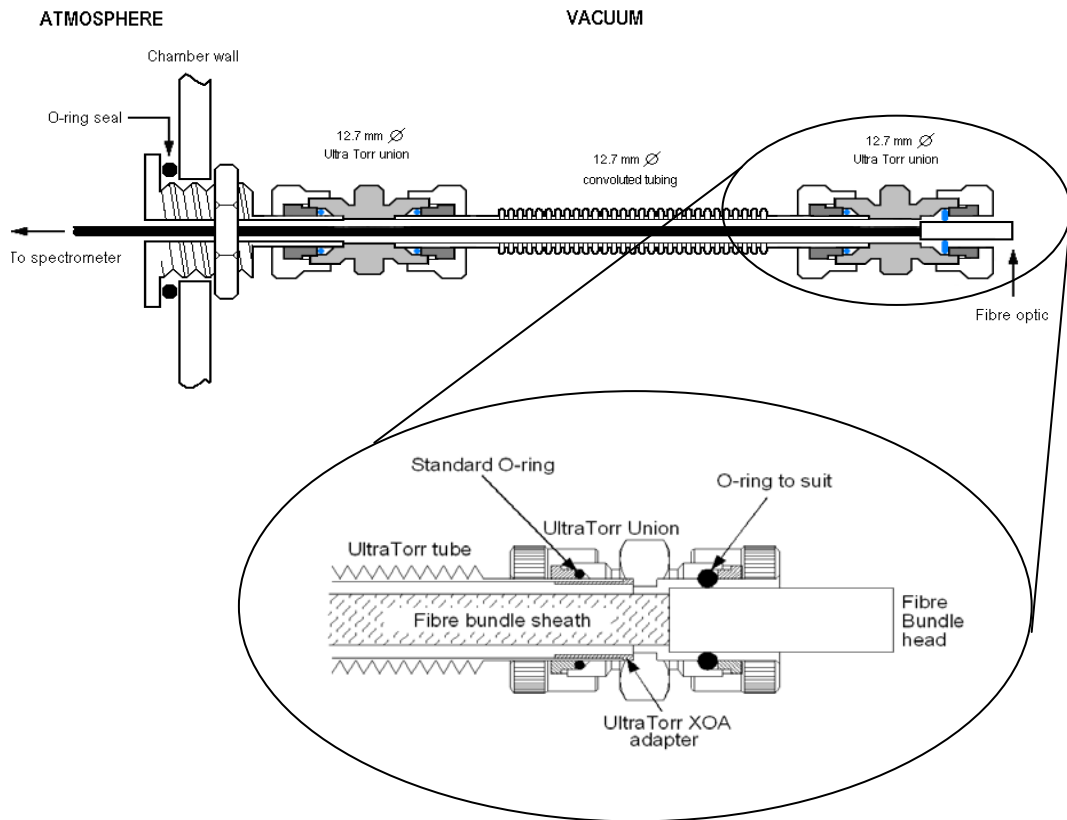


Figure 5.5: Image of configuration of fibre bundle at the spectrometer end

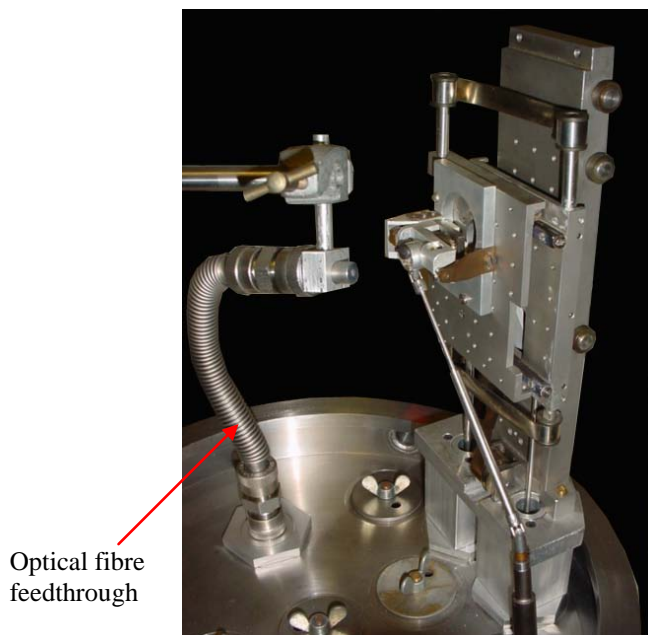
An imaging fibre adapter was also included, designed specifically for imaging spectrometers. *“The all-reflective design eliminates chromatic aberrations and the aspheric mirror cancels astigmatism, allowing precise imaging of fibres at the spectrograph entrance slit”¹²⁹.*

To pass the optical fibre through the HPVA chamber wall, a unique feedthrough was designed, as shown in fig 5.6:

Figure 5.6: Drawing of optical fibre feedthrough, courtesy of John Cowpe and Richard Pilkington



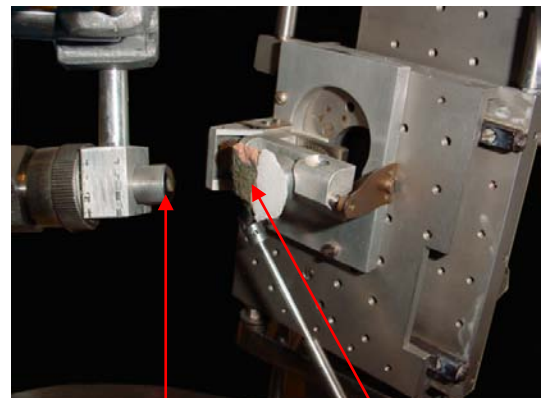
The optical fibre was set up to directly image the plume as shown in images 5.7 & 5.8, particular attention being paid to the angle of the optical fibre, to ensure it imaged a good cross section of the plume



Optical fibre feedthrough

Figure 5.8: Image showing optical fibre feedthrough

Figure 5.7: Image showing alignment of fibre end



Fibre end

Sample

5.4 Vacuum Apparatus

The vacuum apparatus was used for measurements below roughing pressures of 5×10^{-2} mb (the units of pressure given throughout this work are those taken from the gauges used) was set up as shown in figure 5.9. All other pressure measurements were taken using the setup shown in the next section.

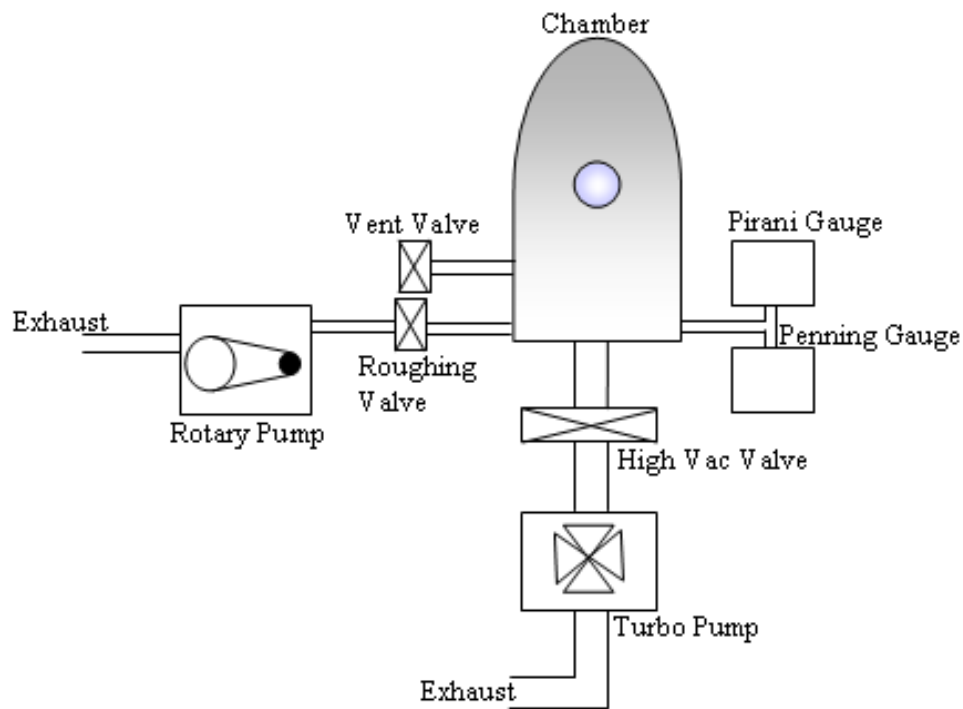


Figure 5.9: Schematic of vacuum apparatus setup

5.5 General High Pressure/Vacuum Apparatus

The vacuum system for the majority of measurements was set up as shown in figure 5.10, allowing capability to run the system at high pressure or vacuum.

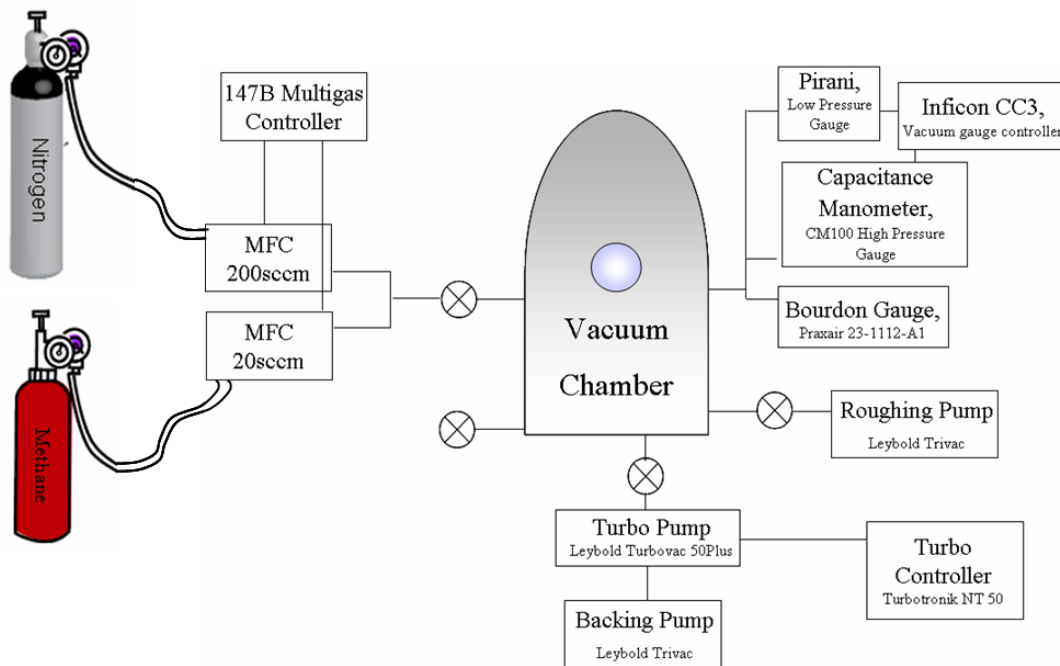


Figure 5.10: Schematic of high pressure/vacuum apparatus setup

5.6 Leak Detection and Calibration

Both systems were leak checked before experimental work commenced. The Mass Flow Controllers (MFC) were calibrated against accurate Transfer Standards as shown in figures 5.11 & 5.12 Results are presented in figures 5.13 & 5.14:

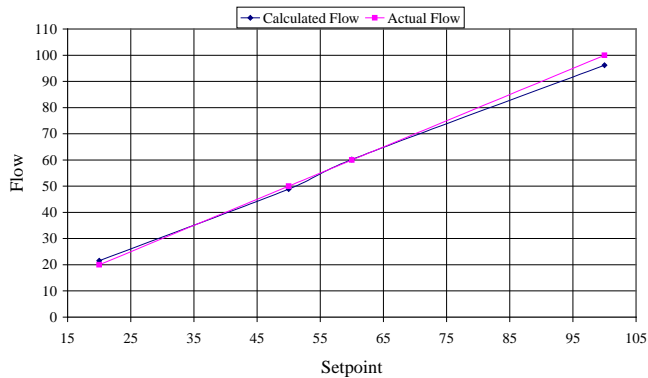


Figure 5.11: Calibration of 100sccm MFC

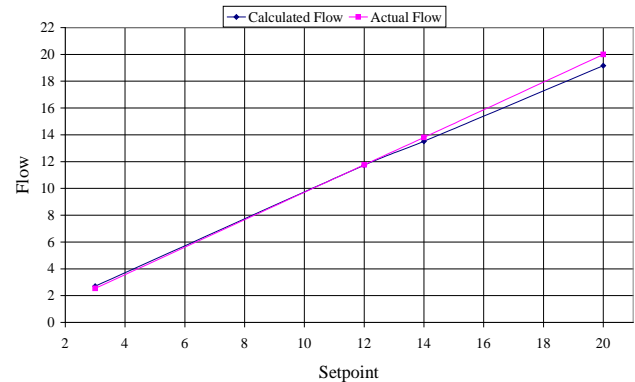


Figure 5.12: Calibration of 20sccm MFC

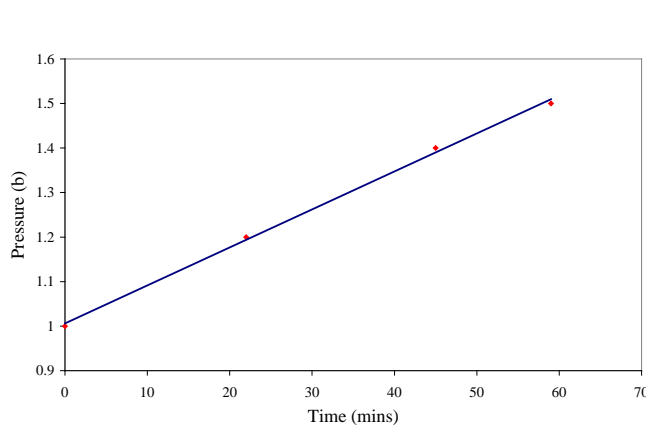


Figure 5.13: Rate of fill of HPVA

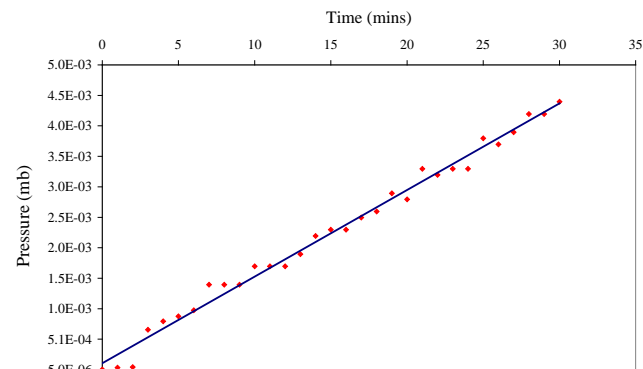


Figure 5.14: Leak rate of vacuum apparatus

In high pressure experiments, rather than using and running the possibility of damaging the vacuum gauges, the Bourdon high pressure gauge, as shown in figure 5.15, was calibrated for its repeatability and usefulness at determining pressures below atmospheric.



Figure 5.15: Image of Praxair Bourdon gauge

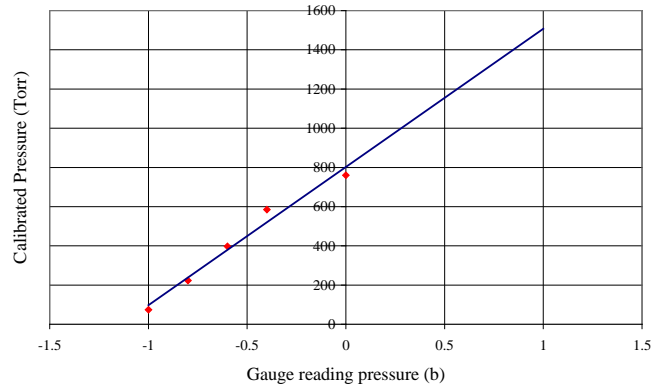


Figure 5.16: Average of three sets of measurements for calibration of the Bourdon gauge when used at pressures below atmospheric

It was found, as shown in figure 5.16, that the gauge showed good repeatability in this range and was utilised in experiments where high pressure and vacuum analysis was undertaken in one sweep.

5.7 Optical Bench Layout Incorporating Vacuum Chamber

The optical bench was setup as shown in figure 5.17, As can be seen in this setup, the optical coupling system, described in section 4.3, was replaced with the optical fibre system outlined above.

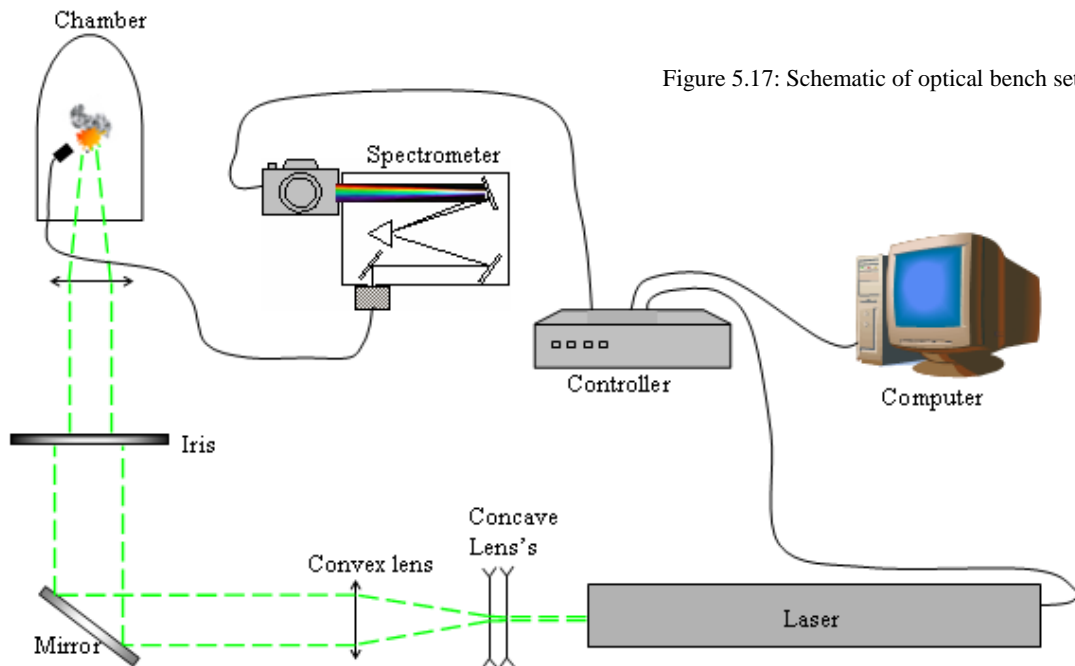


Figure 5.17: Schematic of optical bench setup

6. Experimental Results

6.1 Development of Experimentation Techniques

6.1.1 General Experimental Parameters

All experiments unless otherwise stated were undertaken with a power 0.29 W giving a laser pulse power of 57 mJ/Pulse. To compensate for the loss of signal achieved with reducing power, the fluence in the pressure experiments was set near to the maximum obtainable value of 14 mJ.cm⁻². Although this does have the drawback of poor shot to shot stability as discussed previously, it does increase the signal which is a requirement when compensating for the reduced intensity with reduced pressures.

All delays unless stated otherwise were set to 0.6 μ s as this has been found, as shown in chapter 10, to be a suitable delay to obtain a signal under all pressure regimes investigated. It is important to bear in mind that a signal will show a loss at higher or lower than atmospheric pressures due to the delay not being optimised for these settings.

Widths were set at 0.8 μ s after analysis of the optimum setting for the experiments undertaken, described in section 6.6.

6.1.2 Characterisation/Calibration

Characterisation of the LIBS system's capabilities, calibration of these capabilities and error analysis was undertaken once the system was working within acceptable tolerances. Calibration was undertaken using a cadmium (Cd) and/or mercury (Hg) lamp as a reference source. Shown here in figure 6.1 are the intensity fluctuations of the Cd lamp over time, the marker curves showing in red every 5 shots.

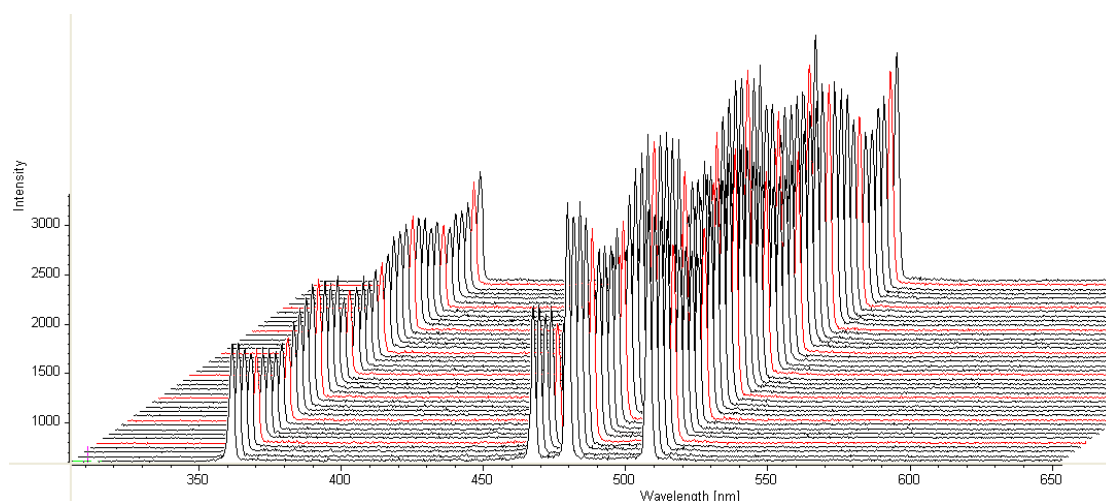


Figure 6.1: Graph showing fluctuations in cadmium lamp intensity over time

Also shown are three representative calibration plots, figures 6.2, 6.3 & 6.4, taken with a mercury lamp using each grating. Each spectrum obtained was within the error for that grating.

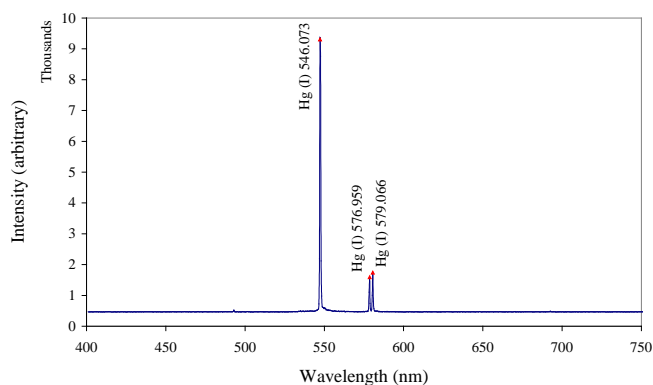


Figure 6.2: Calibration using mercury lamp, 150grooves/mm grating

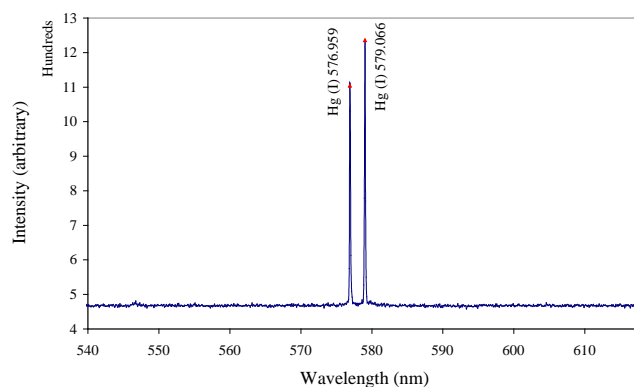


Figure 6.3: Calibration using mercury lamp, 600grooves/mm

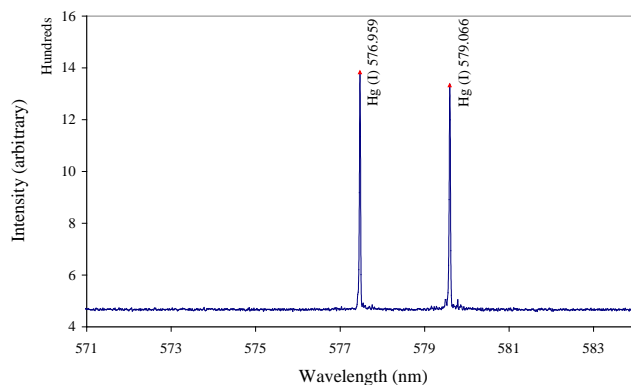


Figure 6.4: Calibration using mercury lamp, 2400grooves/mm

Following calibration, a comprehensive spectral line search was commenced using several different samples; namely, dysprosium, lead, zirconium, indium, silicon, copper, carbon, glass and tin. These results were found to be in good agreement with NIST data of spectral lines, verifying the LIBS setup and calibration.

An example using a copper sample is shown. All lines fitted with NIST data results within the margin of error; some of the main emissions are marked.

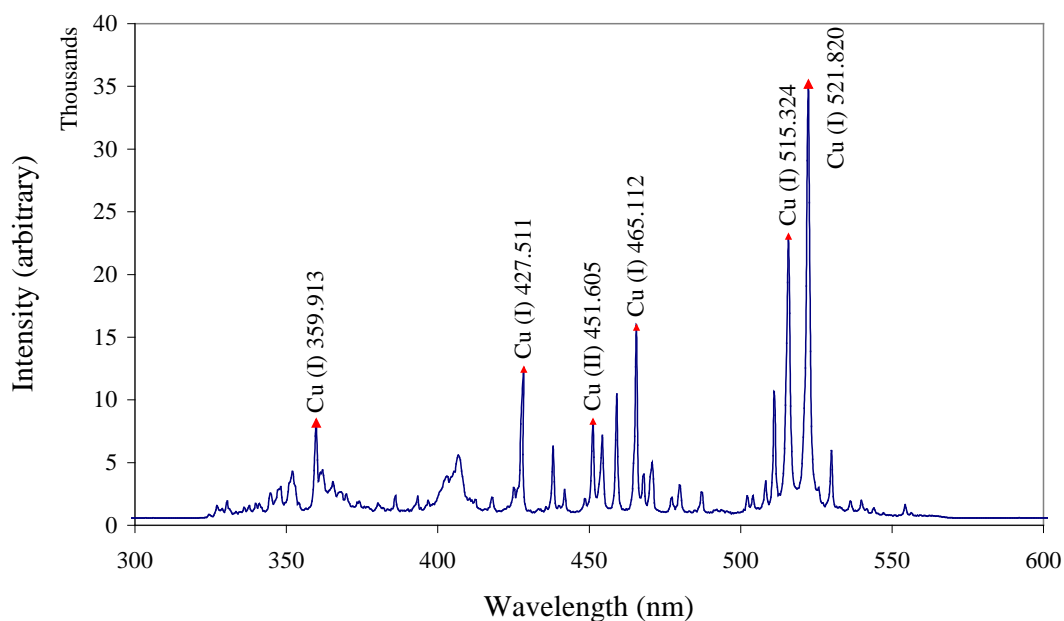


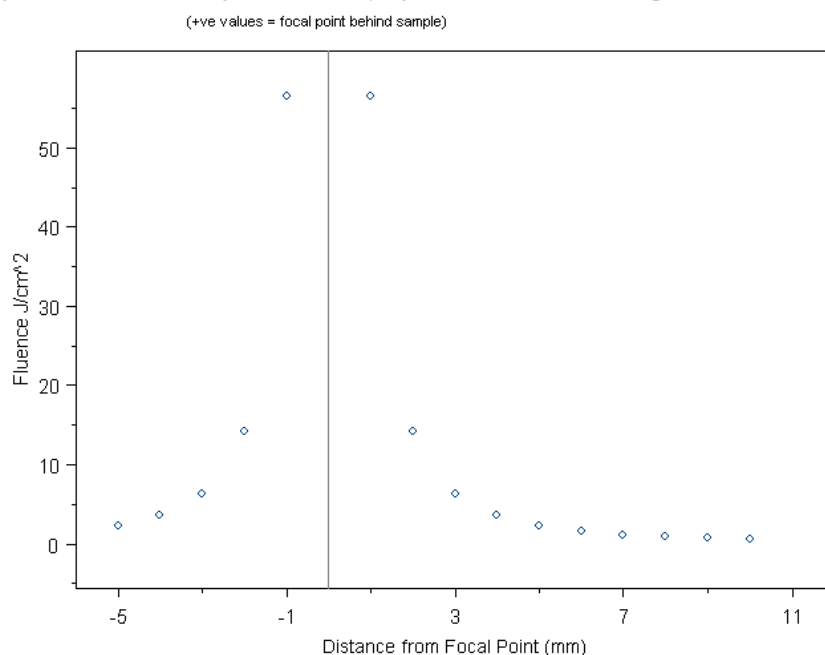
Figure 6.5: Copper emission spectrum

6.1.3 Optimum Fluence

Analysis was undertaken to ascertain the optimum fluence value for experimentation. This value is known to be critical³⁴ in LIBS measurements and is often quoted as lens to sample distance or LTSD.

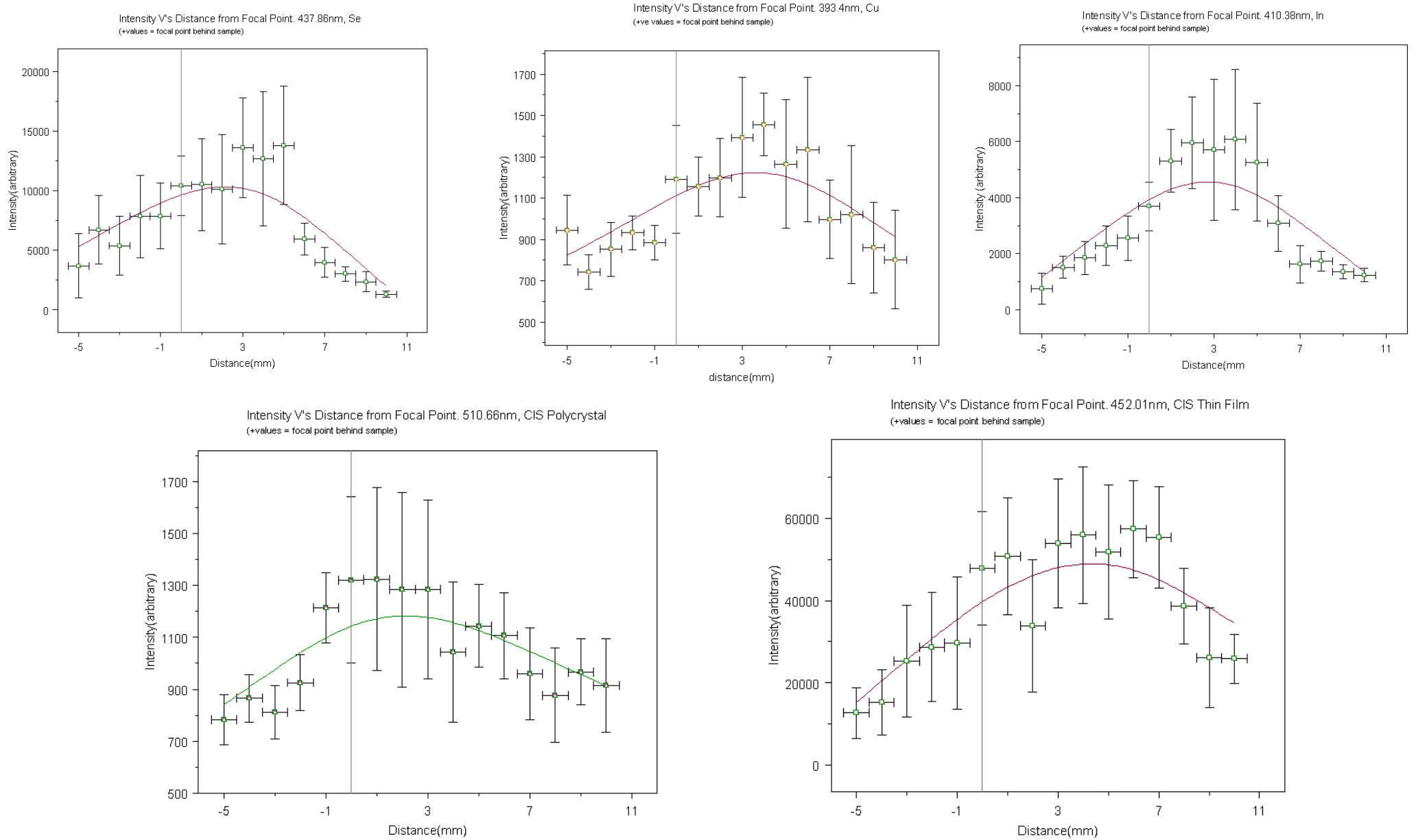
High intensity output was considered in conjunction with shot to shot variation of this intensity. Varying intensities of different elements' and compounds' spectral emissions at set distances from the focal point of the lens were analysed. These were cross referenced with their fluence values which show, in figure 6.6, an asymptotic relation to a sample's distance from focal point.

Figure 6.6: Chart showing fluence at varying distances from the focal point of the final lens



An optimum distance, (i.e. fluence), was then ascertained considering the signal output against losses incurred in shot to shot stability. In order to test this parameter fully, many samples were tested encompassing: silicon, dysprosium, lead, copper, indium, selenium, and copper indium diselenide (CIS) (both thin film and polycrystalline). Shown in figure 6.7 are the results obtained from the constituents of CIS, and the compound CIS itself, both analysed to ensure that no significant changes occur when an element is bound to a compound.

Figure 6.7: Emission intensity versus distance from focal point for CIS and its constituents



It was found generally that at higher fluence values a higher intensity of signal is obtained, but this comes with the drawback that the standard deviation of this intensity is large. It is therefore more prudent to choose a lower fluence value to ensure that the shot to shot stability is more uniform.

As such, samples in future experiments will generally be placed at approximately 6-7mm in front of the focal point of the final convex lens. Although positioning of the sample behind the focal point does appear to be more experimentally sound, the results do not take into account the losses incurred due to the laser 'spark' as the power is high enough to break down the air at the focal point. This in itself would interfere with LIBS measurements and for this reason positioning behind the focal point was ruled out.

6.1.4 Imaging

Imaging mode was utilised in order to establish the full height of the slit image on the chip. This parameter is useful for the possible manufacture of an in-house optical fibre coupler.

A cadmium lamp was imaged using each grating, an example image from the 150grooves/mm grating is shown in figure 6.8:

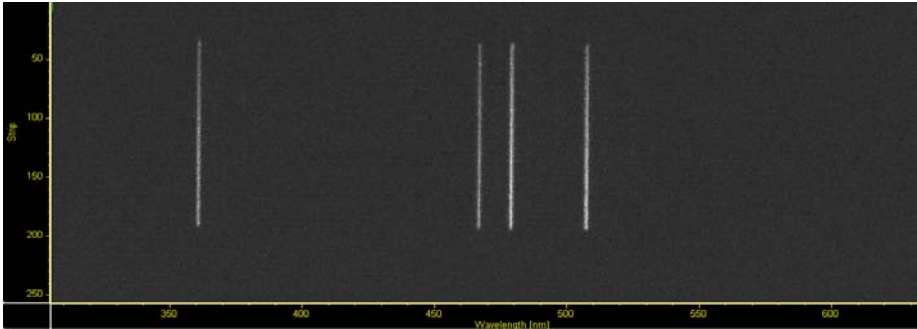


Figure 6.8: Spectrometer image of cadmium emission lines

The input from the source was blocked at the entrance slit of the spectrometer with a vernier attached to two blocks above and below the slit. The image height in pixels was cross referenced with the vernier reading on the blocks. An observable image of 6.5 mm within the slit height was established:

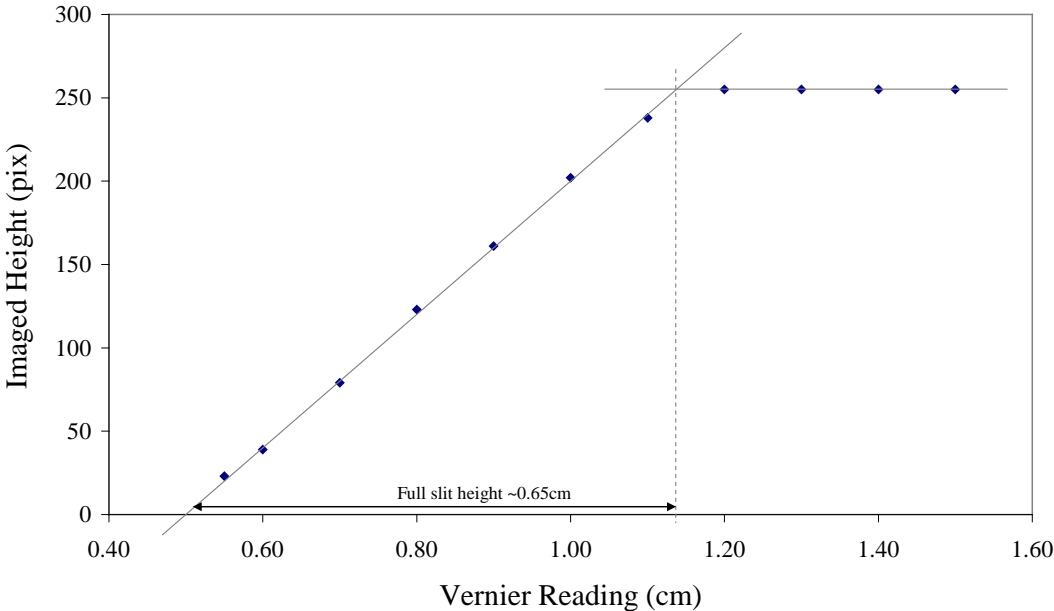


Figure 6.9: Imaged size of spectrometer entrance slit versus actual vernier reading

6.1.5 Matrix Identification

A technique used to optimise the equipment and validate its calibrations was undertaken by experiments of spectral line elimination from constituent parts of a matrix sample. The samples used to facilitate these measurements were solder and its constituent species.

The known constituents of the solder^{A30} are tin 48.5%, lead 47%, rosin flux 3% and copper 1.5%. To isolate the flux the solder was heated with a soldering iron, the flux then flows out of the solder, this yellow residue was analysed. The company providing the solder, (HLA Multicore), informed us that the flux was naturally occurring pine tree sap called abietic acid.

The first case scenario was to analyse the raw data, each spectrum was taken over 10 accumulations:

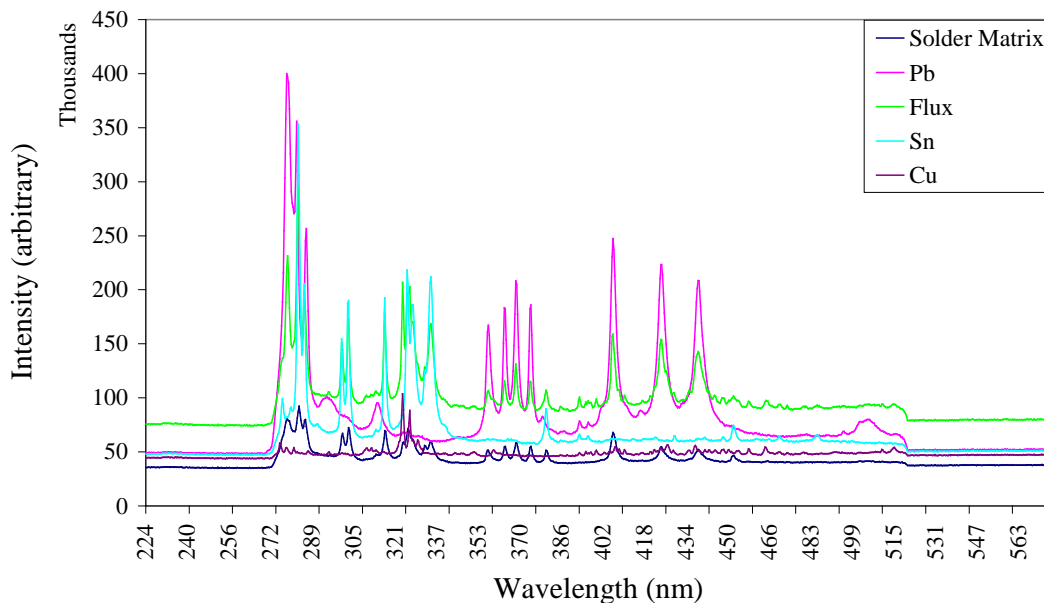


Figure 6.10: Spectral responses of solder matrix and its constituent parts

It can be seen that each of the constituent parts is found in the matrix of the solder. Also shown is the large shot to shot instability found with LIBS measurements resulting in varied baselines. It was also apparent that there was a large error in the wavelength accuracy of the grating, 150 grooves/mm, of ± 1.6 nm.

To minimise these problems each of the spectra was baselined and normalised. In addition to this each of the spectra was corrected to account for the wavelength efficiency of the grating and the signal from the unused edges of the detector was removed. This processing allowed for the constituent parts to be more easily differentiated.

The resulting spectra were obtained:

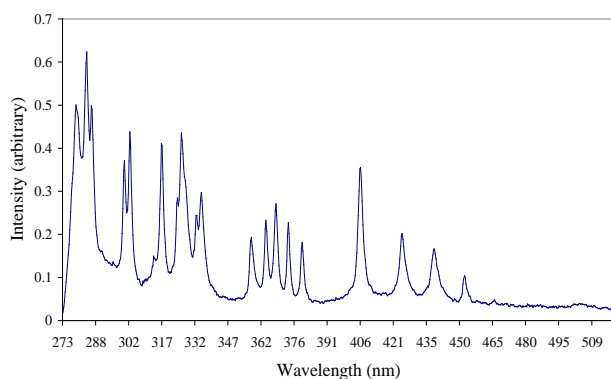


Figure 6.11: Solder emission spectrum

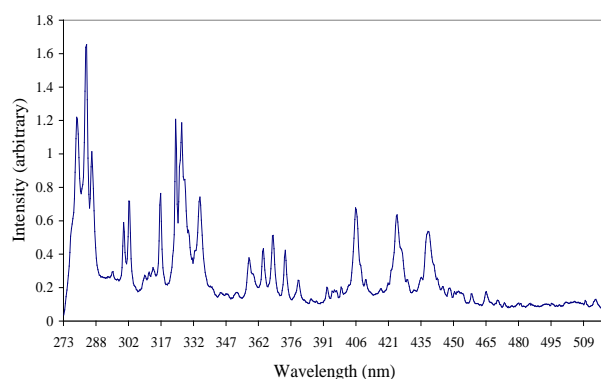


Figure 6.12: Addition of constituent species emission spectra. (Sn, Pb, Cu, rosin flux)

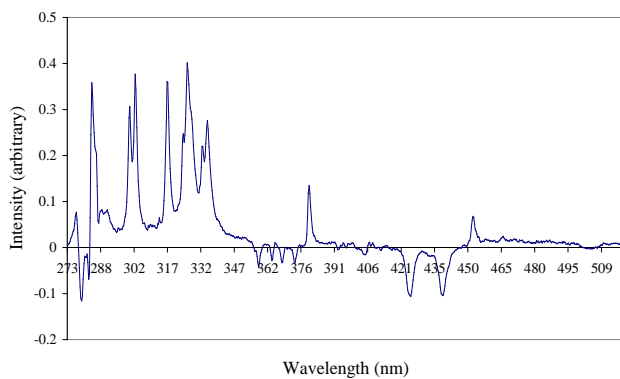


Figure 6.13: Solder emission spectrum minus lead emission spectrum

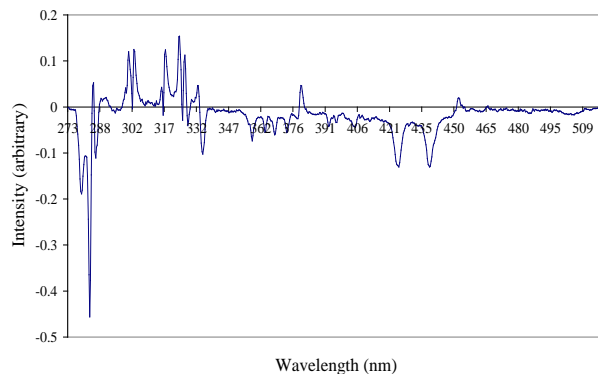


Figure 6.14: Solder emission spectra minus lead and tin emission spectra

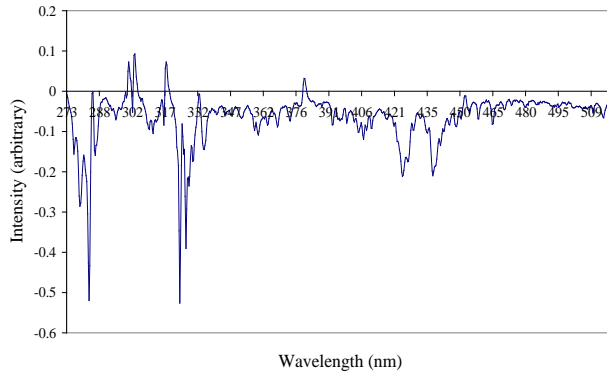


Figure 6.15: Solder emission spectrum minus lead, tin and copper emission spectra

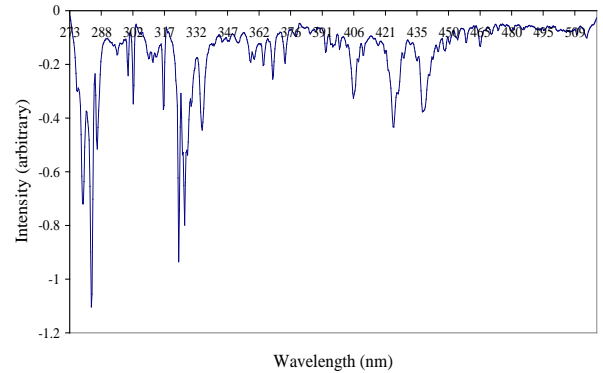


Figure 6.16: Solder emission spectrum minus lead, tin and copper emission spectra

If the experiment was dependent on quantitative work the type of corrections would be varied and calibration curves would be established. This experiment was aimed at optimising the equipment and validating its calibrations and as such just a cursory glance at line elimination was pursued.

It can be seen that there is a good correlation between the raw solder and the addition of the spectra of the constituent parts. Also, each of the spectra subtracted from the raw solder illustrates the spectral responses of each element.

The data analysis can give a satisfactory interpretation for validation of constituent parts, but accuracy is far from satisfactory due to inherent errors in wavelength of emissions. This in turn is due to the low resolution grating and intensity variations with each constituent spectrum. The process did however validate the satisfactory working operation of the instrument and experimental parameters.

6.2 Depth Profiling

As depth profiling was of interest to the project this was the first area to be covered by experimentation. The major parts of this work have already been published at the Photon06 conference in Manchester, 2006 and added in [Appendix A]. The thin film deposition, SIMS and RBS part of this work was undertaken by J Hisek. The LIBS, micrographs and SEM portion of this work was completed by N. Lucas.

Depth profiling of a material known as CIS, (copper indium diselenide), was undertaken. This material is of particular interest to the photovoltaic industry and a close working relationship was built with another research team who were working to produce thin film CIS samples. Depth profiling of these samples was of particular interest to them to ascertain if their depositions were uniform.

CIS thin films grown on silicon and glass were ablated using a frequency doubled Nd:YAG laser at a wavelength of 532 nm and at fluences between 0.8 Jcm^{-2} to 0.15 Jcm^{-2} , removing approximately 95 nm to 1300 nm of material with each shot. Typical depth resolution for LIBS depth profiling is in the range of 100-500 nm per shot, but in certain cases average depth per shot values below 10 nm have been reported^{130,131}.

A series of single shot laser pulses were focused at a single point on the sample and selected spectral emission lines; Si: 390.55 nm; In: 451.13 nm; Cu: 521.82 nm, relating to the elements present in the films and substrate were recorded and plotted in figure 6.17. Selenium was not plotted here as no spectral response was available for selenium in this spectral range. All plotted lines were normalised to remove emission intensity variations.

The beam profile of this laser is pseudo Gaussian (not 'top hat') and as a result it is not possible to produce a clear cut off between substrate and deposited material.

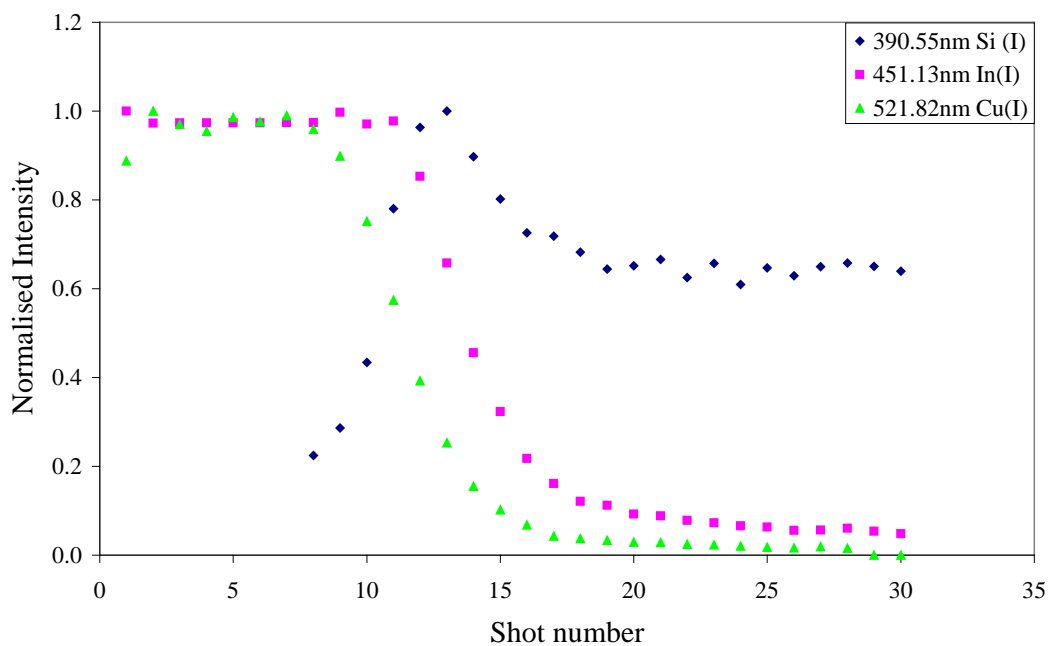


Figure 6.17: Shot versus intensity plot to illustrate removal of CIS on silicon substrate, $1.33 \times 10^8 \text{Wcm}^{-2}$

CIS thin films grown on glass were ablated using the same parameters as those above and are shown in figure 6.18. CIS and glass lines were analysed over a number of shots, again there was no clear cut off between the two interfaces due to the beam shape.

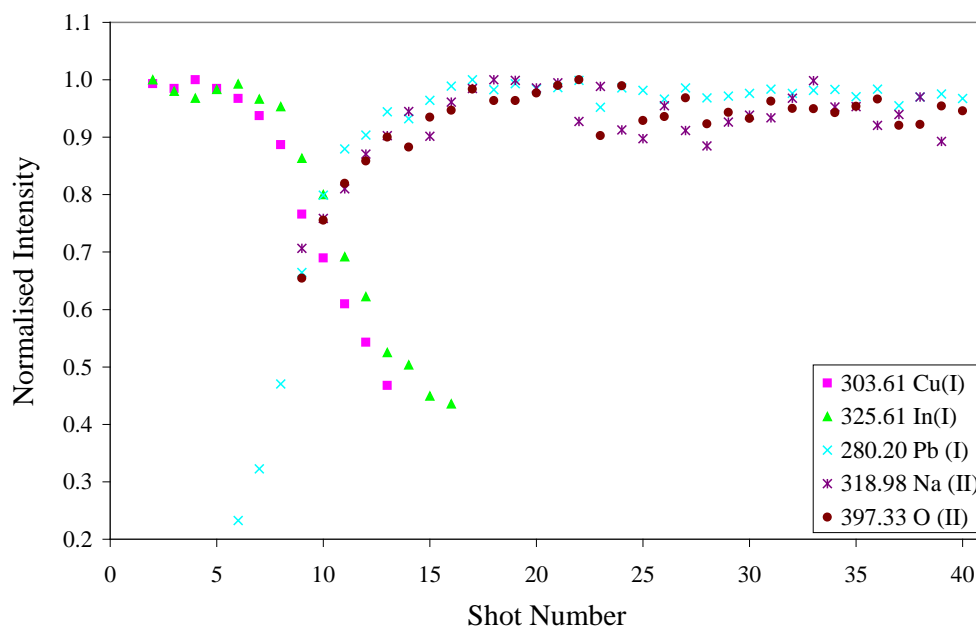


Figure 6.18: Shot versus intensity plot to illustrate removal of CIS on glass substrate, $1.33 \times 10^8 \text{Wcm}^{-2}$

Assumptions have been made in order to obtain these results.

- 1) There is a constant removal rate through the sample and substrate.

This is assumed but can be liable to dispute as there are changes in the laser beam shape and irradiance from shot to shot, (as shown with the non-perfect intensity distribution in the beam profile). There will be re-deposition of the sample and subsequent re-ablation. Also, account must be taken of the complex nature of the laser/surface interaction.

- 2) The boundary between the substrate and the deposited material is clear and defined.

The LIBS spectra obtained are supported by Secondary Ion Mass Spectrometry (SIMS), figure 6.19, and Rutherford Backscattering (RBS), figure 6.20, data, showing that the composition of the CIS films is uniform throughout.

SIMS was used to determine compositional changes throughout the thickness of the films. As there are several isotopes of these elements (i.e. ^{63}Cu and ^{65}Cu) their ratios were recorded and compared. The measured and normalised ratios were identical for all films and close to the nominal values¹³².

The observed signal intensities for Cu, In and Se were at a constant level throughout the entire thin films, indicating compositional uniformity. The films analysed were deposited with different biasing voltage waveforms (sample P122: rf; sample P127: dc; sample P130: pulsed dc) and the signal intensities of each of these species were compared. The following figures illustrate that no relevant variations of composition with thickness could be detected.

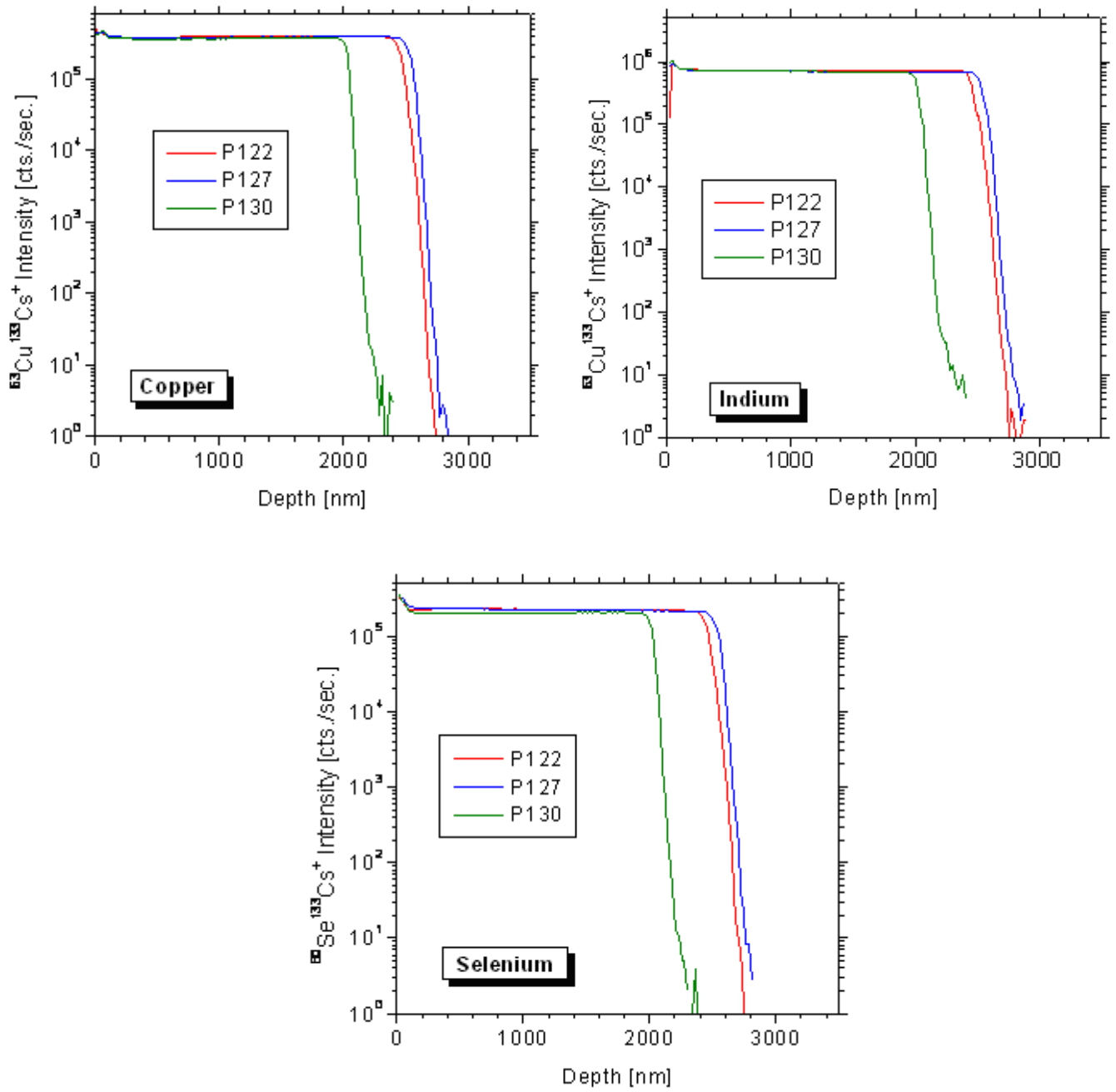
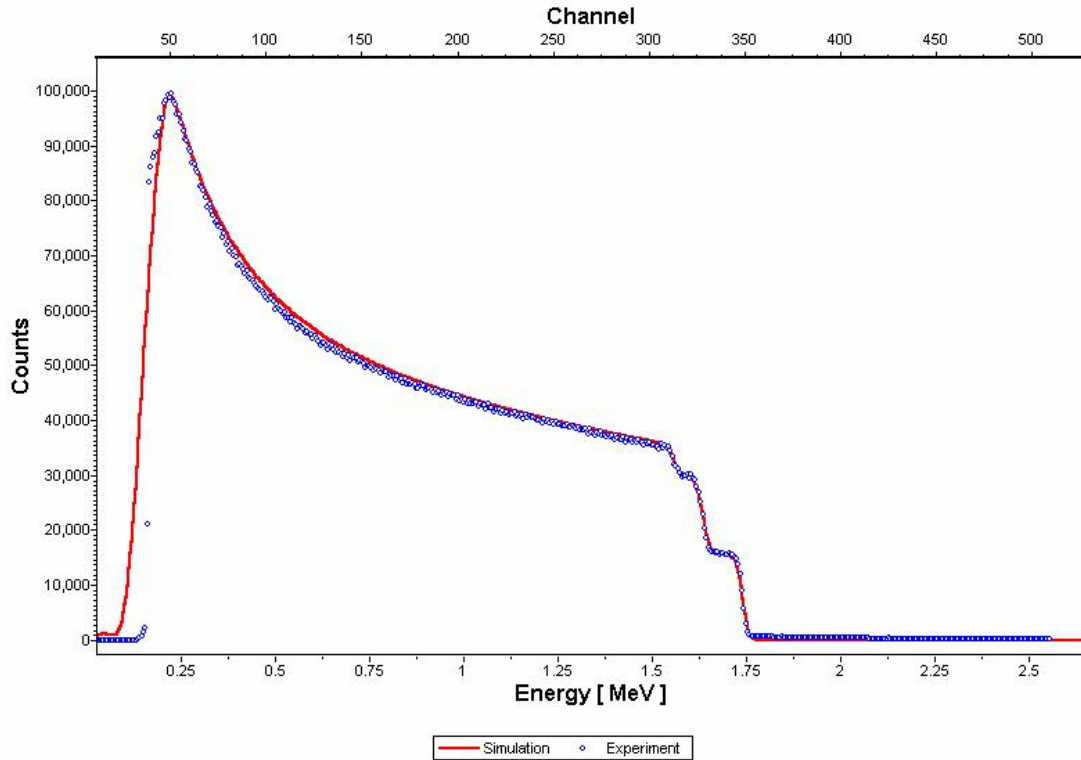


Figure 6.19: SIMS comparison of copper, indium and selenium depth distributions

Rutherford backscattering results also showed direct correlation between the simulated compositional uniformity and the experimental composition, again suggesting the composition of the CIS films is uniform throughout and verifying the LIBS depth profile results obtained.

Figure 6.20: RBS plot showing experimental results cross referenced with simulated results



These photographic images of ablated CIS on a silicon substrate, figure 6.21, clearly show the exposed silicon substrate in the centre of the ablated region, together with evidence of re-deposition.

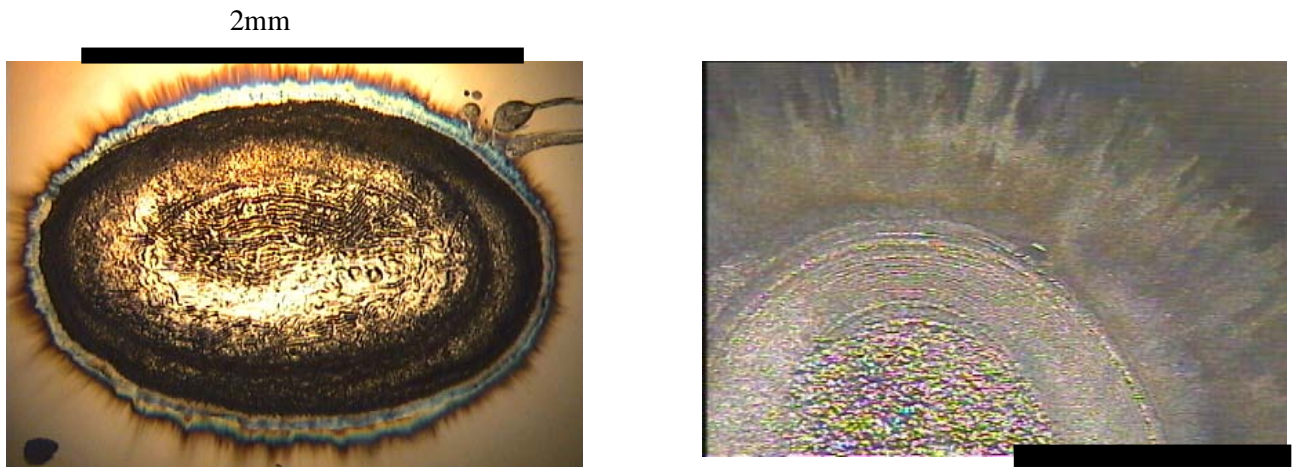


Figure 6.21: Images of ablation crater's on thin film CIS sample deposited on silicon.

The SEM cross section, shown here in figure 6.22, is illustrative of the depth and formation of the ablation crater. It is visually apparent that the beam is non homogeneous and pseudo Gaussian.

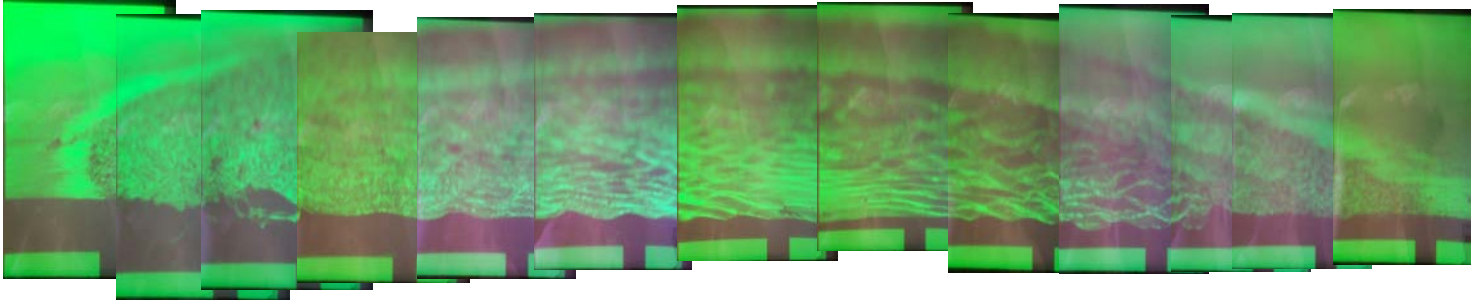


Figure 6.22: SEM image showing an ablation crater

It has been found that depth profiling with LIBS is indeed possible and valid. Optimisation could be brought about by using optics to change the beam profile to a ‘top hat’ profile, thus allowing for a clear cut off between sample and substrate to be ascertained.

6.3 Samples

The samples used for experimentation were varied to provide a good base of results.

6.3.1 Silicon

An unpolished Silicon wafer, figure 6.23, was chosen as a pure sample which provided a good reference for changes in pressure and environment which was independent of matrix effects or sample incongruities. The wafer was unpolished in order to reduce reflectivity changes from the wafer compared to the rock samples.

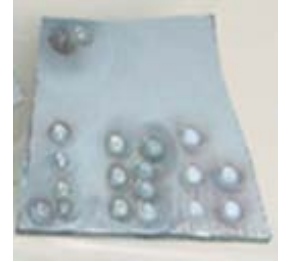


Figure 6.23: Image of silicon sample after laser ablation, the circles are ablation craters.

The spectrum shown in figure 6.24, used the 150g/mm grating and was taken to define the prime wavelength region to employ with the 2400g/mm grating, 10 accumulations were taken. It was established that the prime wavelength region to study would be the high density of singly ionized ion emissions around 250nm, shown in figure 6.25.

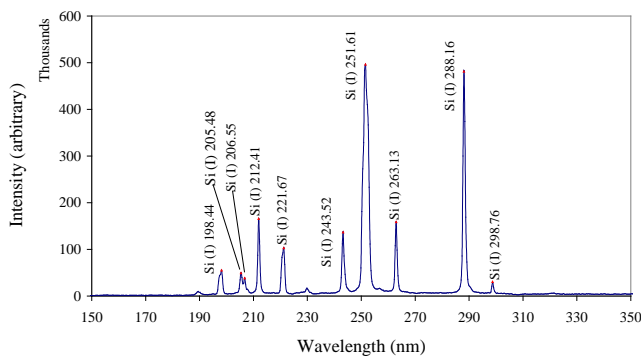


Figure 6.24: Silicon sample in atmospheric conditions, 150g/mm grating

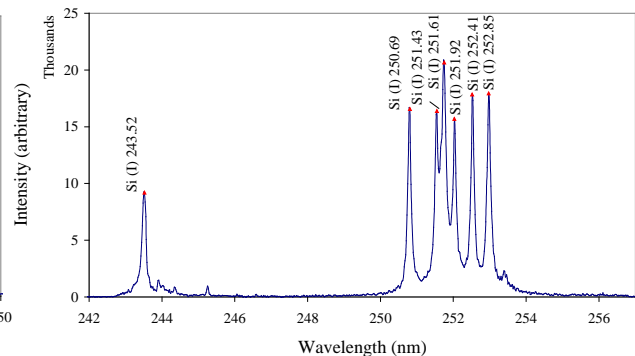


Figure 6.25: Silicon Sample in atmospheric conditions, 2400g/mm grating

6.3.2 Sandstone

Sandstone, which contains predominantly silicon, was chosen as a sedimentary rock type. Two sandstone samples were used, the first being weathered sandstone taken from the local (Manchester) area, the second being the same sample but without the weathered surface. All are shown in figure 6.26.



Figure 6.26: Images of sandstone samples, with ablation craters clearly visible. Both were taken from a larger block shown on the left, where organic residues can be seen building up on the surface, the clean stone visible underneath.

It was important to study both types because weathered layers may well be predominant in samples to be studied in the field and consequently it was of interest if the results in the two cases varied. As mentioned, sandstone is predominantly silicon, but traces of iron in this sample were evident, as would be suggested by its colouring. The spectrum from the sample is shown in figure 6.27.

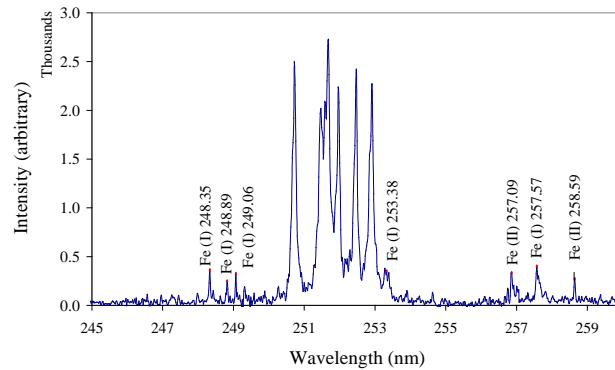


Figure 6.27: Sandstone sample emission spectrum in atmospheric conditions, 2400g/mm

6.3.3 Slate

Slate was chosen as a representative of a homogenous foliated metamorphic rock¹³³. It is composed primarily of silicon, iron and aluminium with traces of other elements.

Slate is often the colour of the minerals contained within it,¹³⁴ for example; red, purple or brown containing iron oxides and grey or black containing organic matter. It was of interest to find samples with different colourings to reflect these differences. A single sample, shown in figure 6.28, was chosen from North Wales that incorporated two distinct regions of colour, one pale the other dark.



Figure 6.28: Slate sample showing ablation craters and re-deposition of material around the crater.

These regions for future reference will be called 'Pale Slate' and 'Dark Slate'. The colouration could be due to different mineral types and/or concentrations or due to weathering of one side of the sample.

Two wavelength regions were studied with the slate samples, 245-259 nm, figures 6.29 & 6.30, and 269-282 nm, figures 6.31 & 6.32. The second range being employed as there are fewer spectral lines in that region and hence less spectral interferences from lines close to those studied.

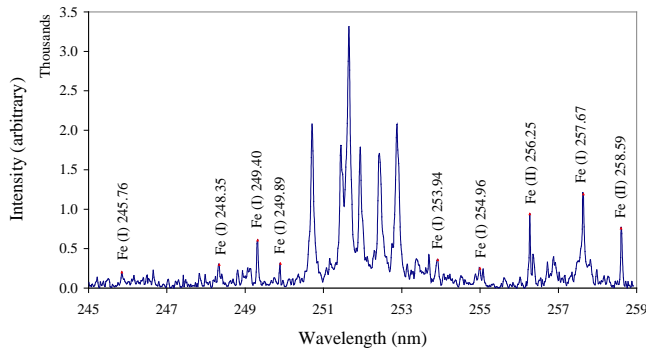


Figure 6.29: Pale slate sample in atmospheric conditions, 2400g/mm grating

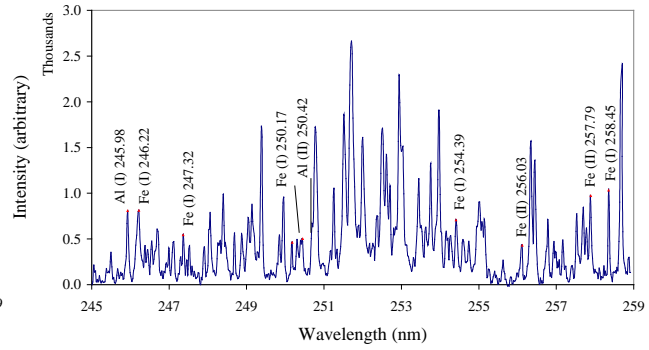


Figure 6.30: Dark slate sample in atmospheric conditions, 2400g/mm grating

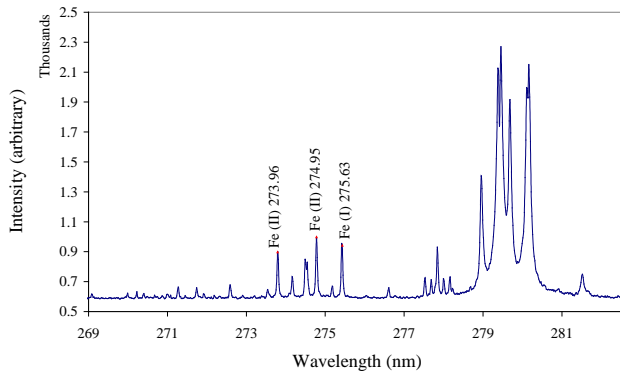


Figure 6.31: Pale slate sample in 1 bar nitrogen fill, 2400g/mm grating

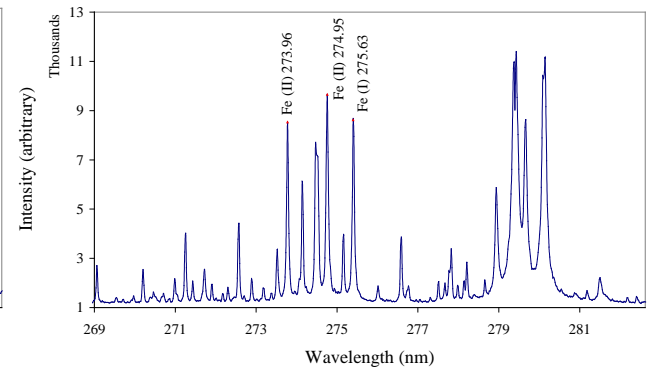


Figure 6.32: Dark slate sample in 1 bar nitrogen fill, 2400g/mm grating

6.3.4 Marble

The last sample is the metamorphic rock, marble, shown in figure 6.33. This rock is known to contain calcium carbonate or calcite^{133,134}.



Figure 6.33: Images of marble samples, the one on the left showing the crystalline structure, the one on the right showing the ablation craters and in some cases the re-deposition from a partial or full methane content atmosphere.

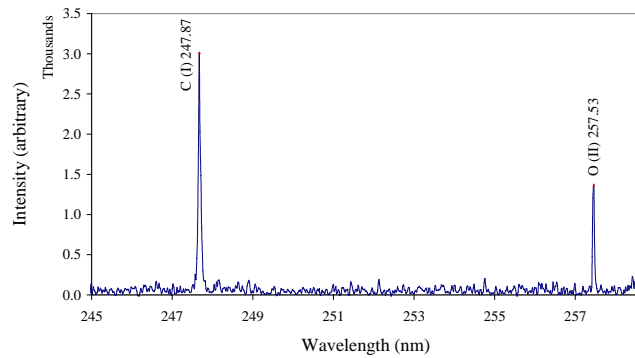


Figure 6.34: Marble sample in atmospheric conditions, 2400g/mm grating

The wavelength region shown in figure 6.34 has few spectral lines, but the region shown does contain a first ionisation stage of carbon which was important for experimental results in order to ascertain the interferences of the carbon content in the gaseous environment with carbon emission lines from the sample.

Also studied with the marble sample was the wavelength region 368-378 nm, figure 6.35, and 390-402 nm, figure 6.36. These ranges contain strong calcium emissions, the second range displays the effects of self reversal at pressures above roughing vacuum, which is common with calcium emissions³⁴. This effect is shown in detail in section 6.9.3.

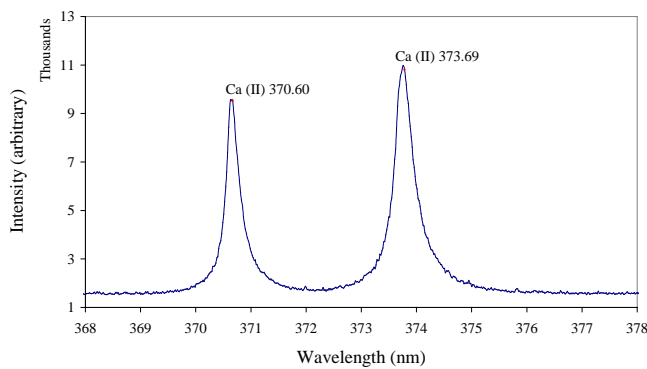


Figure 6.35: Marble sample emission spectrum, 1 bar nitrogen fill, 2400g/mm grating

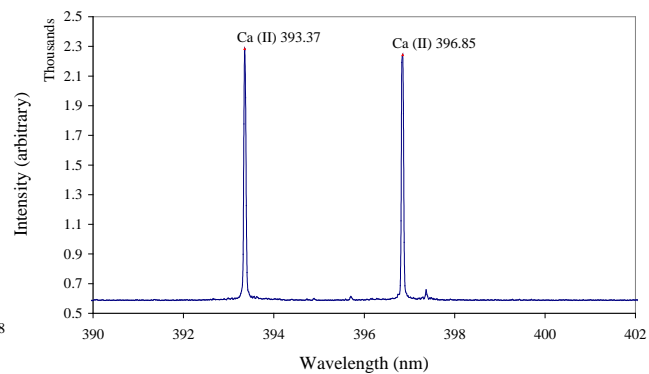


Figure 6.36: Marble sample emission spectrum, in vacuum as emission lines exhibit self-reversal at other pressures, 2400g/mm grating

6.4 Energy-dispersive X-ray spectroscopy (EDX)

X-Ray Dispersive Analysis (EDX) analysis was performed on the samples to apply an internal standardisation to LIBS results obtained in this study.

Gain calibration of the EDX apparatus was applied with a cobalt K line, seen on the left hand side of the images shown in figures 6.37 - 6.42. Results are subject to an inherent error due to the samples being non-conductive and becoming charged from the incident electrons of the Scanning Electron Microscope (SEM). The samples could have been coated in gold to minimise this problem, but this would have introduced a different error due to attenuation of the signal from the gold film; consequently this procedure was not utilized.

Sample elements were analysed to obtain a ratio of their percentage weight concentrations in the substrate matrices. The tables 6.1 – 6.4 show the elemental ratios and the images, shown in figures 6.37 - 6.42, show the EDX emission spectra. The images are poor due to the limited ability to extract the data from the system.

Sandstone			
Element	% Weight	error	% Atomic
	of Element	(+/-)	Weight
Na	<1.038	0.519	
Mg	1.674	0.819	1.944
Al	20.53	1.024	21.474
Si	72.383	1.247	72.719
K	3.933	0.621	2.838
Fe	1.104	0.483	0.558
Totals	99.624		100

Table 6.1: Elemental ratios of constituents in sandstone

Weathered Sandstone			
Element	% Weight	error	% Atomic
	of Element	(+/-)	Weight
Na	<0.739	0.37	
Mg	<0.334	0.167	
Al	21.434	2.303	22.151
Si	69.953	2.58	69.437
K	2.976	1.371	2.123
Fe	<0.102	0.051	
Totals	94.636		100

Table 6.2: Elemental ratios of constituents in weathered sandstone

Pale Slate			
Element	% Weight	error	% Atomic
	of Element	(+/-)	Weight
Na	4.344	0.889	5.303
Mg	2.505	0.522	2.893
Al	27.14	0.747	28.236
Si	59.098	0.877	59.055
K	4.796	0.409	3.443
Fe	2.131	0.306	1.071
Totals	100.014		100

Dark Slate			
Element	% Weight	error	% Atomic
	of Element	(+/-)	Weight
Na	5.082	0.799	6.276
Mg	2.831	0.471	3.306
Al	23.961	0.673	25.212
Si	59.108	0.785	59.738
K	4.043	0.362	2.936
Fe	4.983	0.403	2.533
Totals	100.008		100

Table 6.3: Elemental ratios of constituents in pale slate

Table 6.3: Elemental ratios of constituents in dark slate

Due to interference of carbon emissions with the cobalt calibration line, the ratio of peaks of carbon could not be determined. The oxygen peak could not be investigated in the ratio measurements either, as the system was not calibrated to account for this line. Due to these restraints the ratios of marble peaks were omitted and the concentration of the other samples analysed should take account of the inability to ratio these lines in the results.



Figure 6.37: Sandstone EDX image

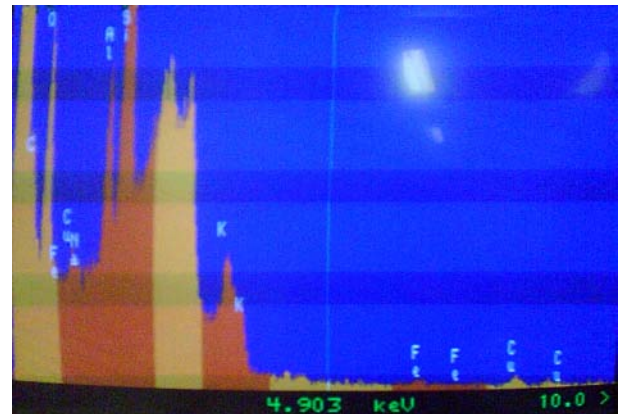


Figure 6.38: Sandstone EDX image, 4* original magnification to resolve iron and copper peaks.

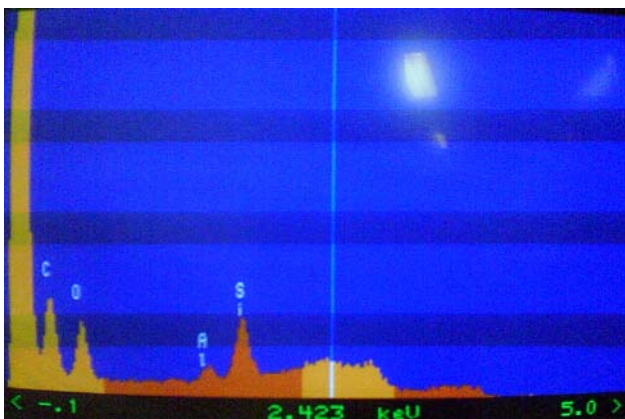


Figure 6.39: Weathered sandstone EDX image

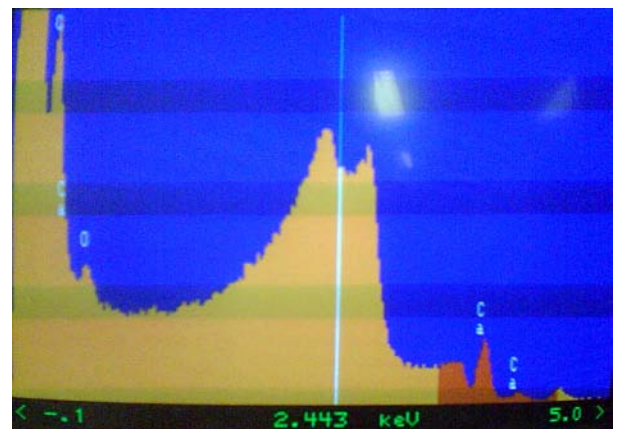


Figure 6.40: EDX image of marble sample

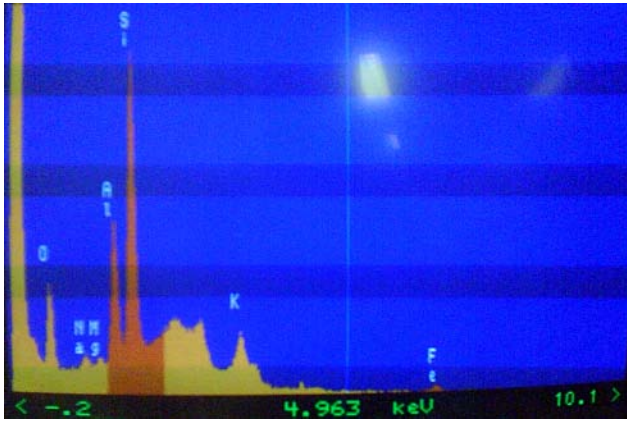


Figure 6.41: Pale slate EDX image

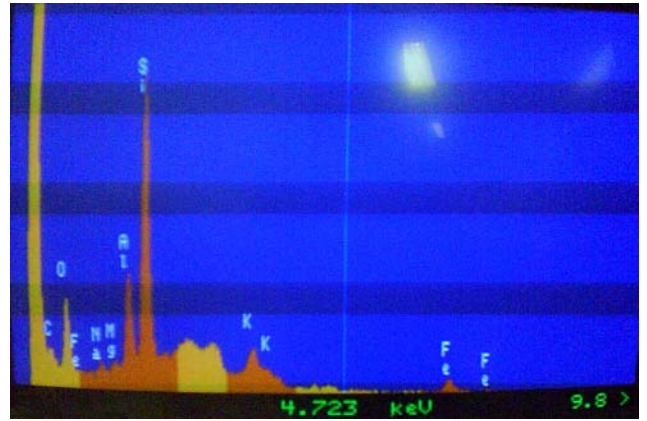


Figure 6.42: Dark slate EDX image

There was an error in the system which resulted in the false double peak at approximately 2.4 KeV, seen predominantly in the marble samples results. This false double peak is apparent in all measurements and can be excluded from the results.

The results are in good agreement with the data obtained from LIBS measurements. Good correlation is shown firstly by the differences in pale slate and dark slate, in that dark slate is shown to contain more carbon and iron in its matrix. Also, the clearly defined carbon peak in weathered sandstone is visible, due to the surface weathering emissions. In this result the decrease in silicon emission is also apparent, which is thought to be due to attenuation by the weathered surface.

6.5 Temporal Delay

Temporal delays in LIBS experiments affect the emission line resolution, width, intensity and signal to noise ratio. These values are further affected by changes in pressure, where under different pressure regimes different delay times will be optimal due to the mean free path of particles changing under different pressures, bringing about a change in the speed of dissipation of the plume.

A calculation of best possible delay parameters was undertaken. Optimum delays were ascertained for samples under atmospheric conditions. Further delay experiments were carried out in different pressure regimes to determine to what extent the variations in plume dynamics change the optimal delay setting.

For many of these experiments, not being able to use burst mode adversely affected the results. If burst mode had been working, delays from a single plasma could be ascertained and as such one would expect less deviation from plasma and laser output intensities. Without this mode, the delay experiments were taken at different delays from different plasmas, (different laser shots). This resulted in large variations in shot to shot stability, from background noise to output signal intensity. Although this was less than ideal, good approximations could still be obtained from the relative intensities of peak to peak measurements.

Analysed are delay sweeps for silicon samples at different pressures. It can clearly be seen that the optimum delay for a given set of parameters depends on the pressure of the system. This, as mentioned, is due to the change in the mean free path in each pressure regime.

Figure 6.43 shows the spectral information under different delays in atmospheric temperatures, pressures and gases. The spectra have not been baselined so the large reduction in background noise with increasing delay can be seen. At 0.2 μs the resolution of the peaks is not apparent, the signal being dominated by the background continuum. With the delay set to 0.27 μs and above the charts reveal the spectral lines of silicon at 288.158 nm, 385.602 nm and 431.089 nm respectively within the error of the 150 g/mm grating used. The optimum delay

in atmospheric conditions with these experimental parameters was found to be $\sim 0.6 \mu\text{s}$.

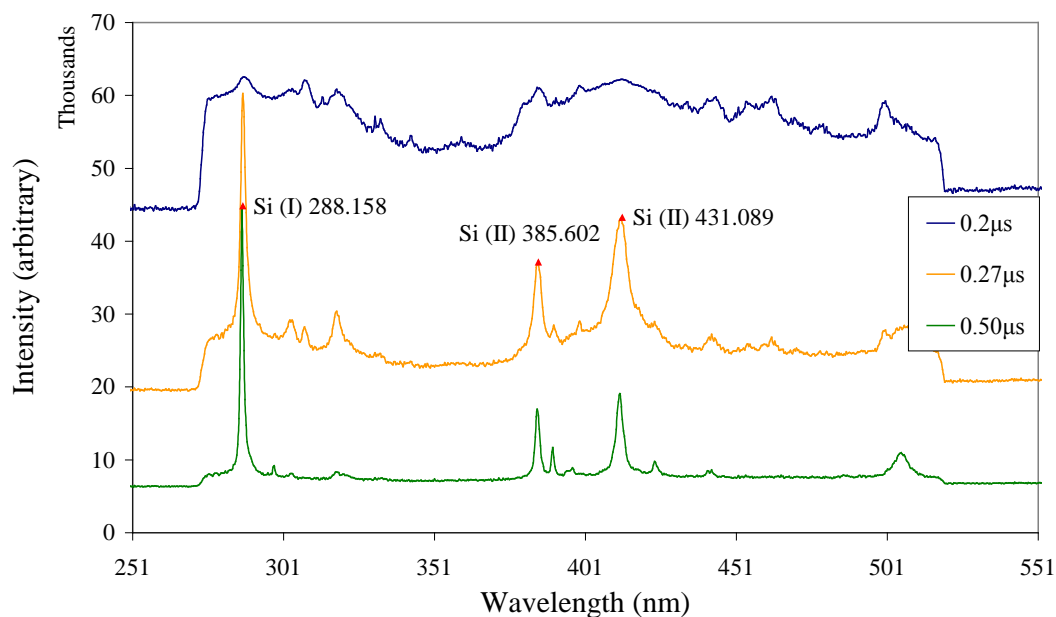


Figure 6.43: Delay variation, silicon sample, atmospheric pressure

Displayed in the next set of measurements, figures 6.44 & 6.45, using a silicon sample in an high pressure mix of nitrogen and methane, is the resolution of the peaks with increased delays, particularly the silicon (I) double peak at 251.432 nm and 251.611 nm.

It can be seen that a further increase of delay from $0.8 \mu\text{s}$ to $1.1 \mu\text{s}$ achieves no greater reduction in noise or resolution of peaks, just a loss in spectral signal intensity. The measurements also reveal that with increasing delay in this pressure environment the width of the peaks reduces.

There is an obvious trade off with signal, width and noise. If just analysing the intensity to pressure, as in figure 6.45, one could deduce that $0.35 \mu\text{s}$ would be the optimum delay setting at 1.5 bar pressure, but when analysing the width and noise also one can see that the optimum actually lies at approximately $0.8 \mu\text{s}$.

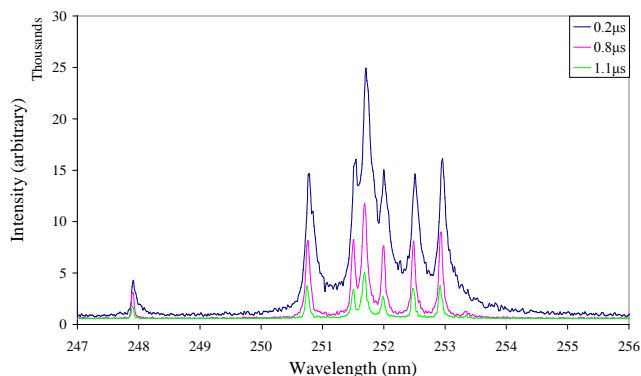


Figure 6.44: Delay variation, silicon sample, 1.5 bar pressure of gas mixture 94%N₂ 6%CH₄

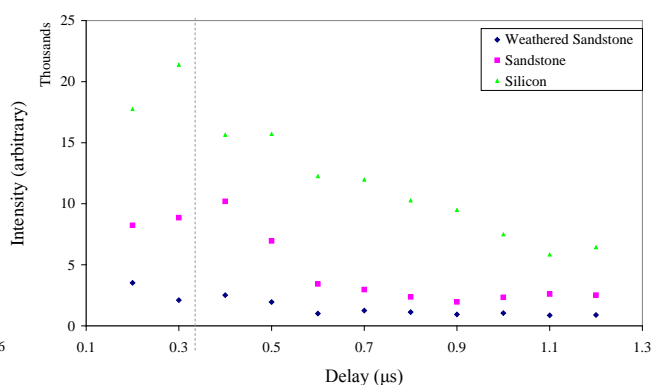


Figure 6.45: Delay versus emission intensity of the silicon emission line at 251.61 nm in different samples. Averaged over 15 shots, 1.5 bar pressure with gas mixture 94%N₂ 6%CH₄

The next chart, figure 6.46, shows more clearly the situation where the baseline noise reaches a minimum, but the signal intensity keeps decreasing with further delay, particularly between a delay setting of 1.2-1.8 μs. There is also a slightly different gas mixture from the last chart, but there is no significant change in optimal delay settings for such mixtures, it being optimum at approximately 0.8 μs. This suggests that the gas mixture does not affect the optimum delay setting whereas the pressure does quite remarkably.

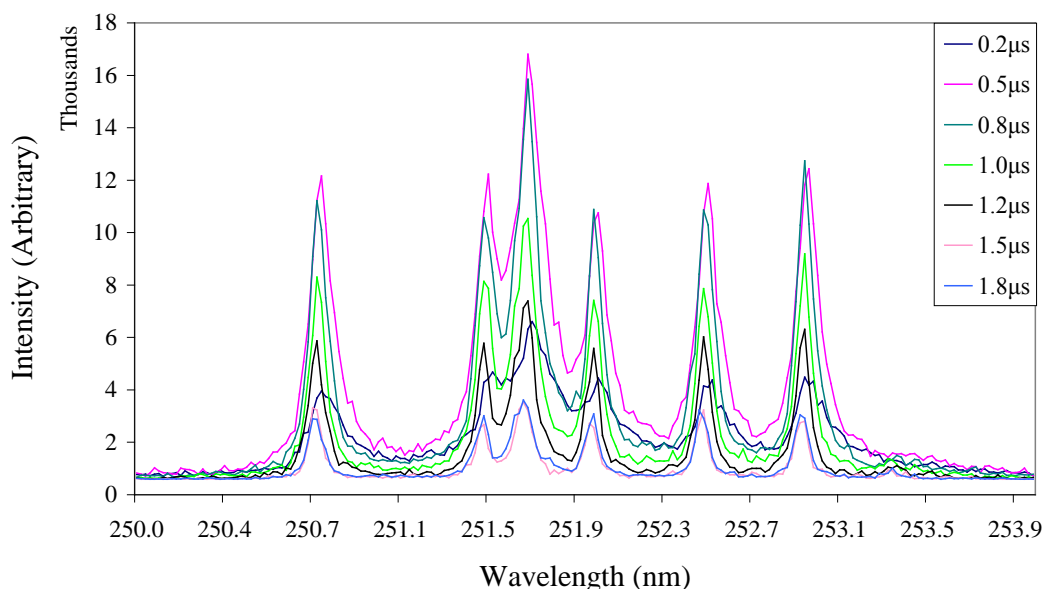


Figure 6.46: Delay variation, silicon sample, 1.5 bar pressure of gas mixture 93%N₂ 7%CH₄.

In the next set of measurements the system was set up in a reduced pressure environment. These measurements (figure 6.47) reveal that the background noise dies away more quickly than in high pressure systems due to previously mentioned pressure effects such as a lower mean free path leading to a quicker reduction in plasma temperature and electron density due to a faster dissipation time of the plume, requiring the signal to be captured earlier, before it has had time to diverge.

It can also be seen in figure 10.5 that much narrower lines can be obtained in low pressure environments compared with atmospheric or high pressure systems. This would be expected from the theory on line broadening mechanisms described in section 3.3.1, stating that as the pressure increases so do the broadening mechanisms due to an increase in electron density. It is apparent that if the delay is increased only slightly, from 0.4 μs to 0.6 μs , the signal loss is significant but no gain in signal to noise ratio is achieved, the parameters being much more sensitive than in high pressure environments.

Also shown is the resolution of spectral lines at delays as short as 5 ns! The background continuum under this delay setting is still significantly large, but the noise to signal ratio is noteworthy compared with high pressure or atmospheric systems. This clearly shows the implication of the changes in plume dynamics in such pressure environments.

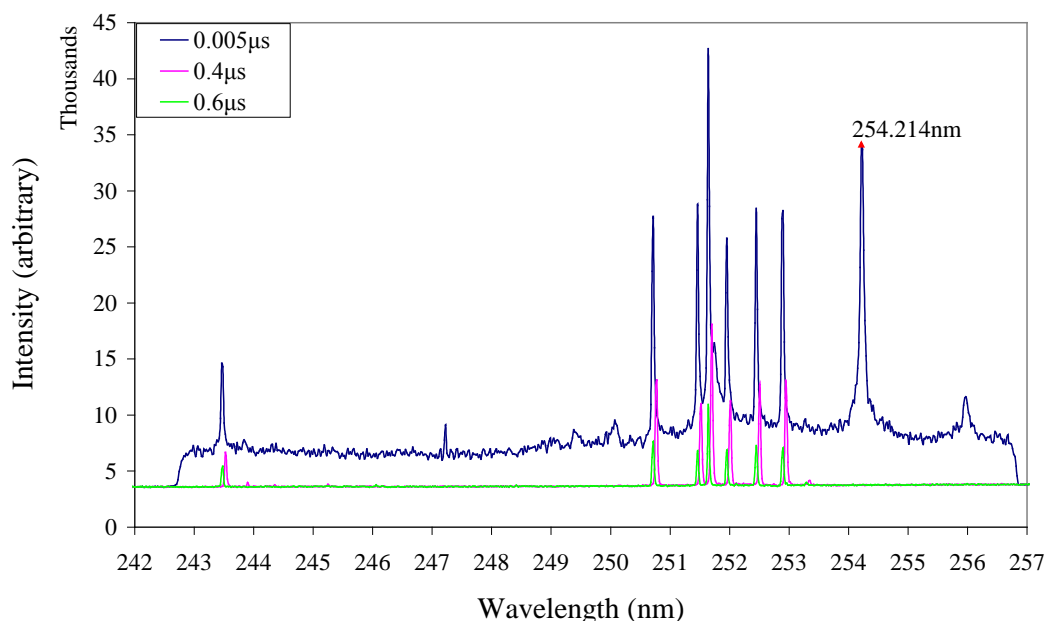


Figure 6.47: Delay variation, silicon sample, under vacuum pressure of 3×10^{-4} mb.

The spectral line showing at 254.214 nm, only appears at a detector delay of 5 ns. Within the error of the grating, (0.1 nm for 2400 g/mm), this can be attributed to either Si(III) 254.182 nm or O(III) 254.264 nm. The line disappears at later stages because early in the plasma lifetime the plasma temperature will be higher, and thus a higher ionic species will dominate. As the plasma cools and the thermal activity decreases, the higher ionic species prevalent in the plasma will also diminish, as discussed in section 3.3.

This next set of experiments cross referenced previous results with a different matrix material, containing predominantly silicon, rather than a pure silicon sample. This material was sandstone rock.

This set of experiments, figure 6.48, was done under a roughing vacuum of approximately 5×10^{-2} mb. The delay settings in this experiment was varied to cover all previously obtained optimal settings for vacuum, atmospheric and high pressure systems.

It can be seen that delay settings optimised for air and high pressure produce minimal signal intensity at vacuum, as would be expected. Its is of use to note the low noise in these results, apparent in all vacuum measurements.

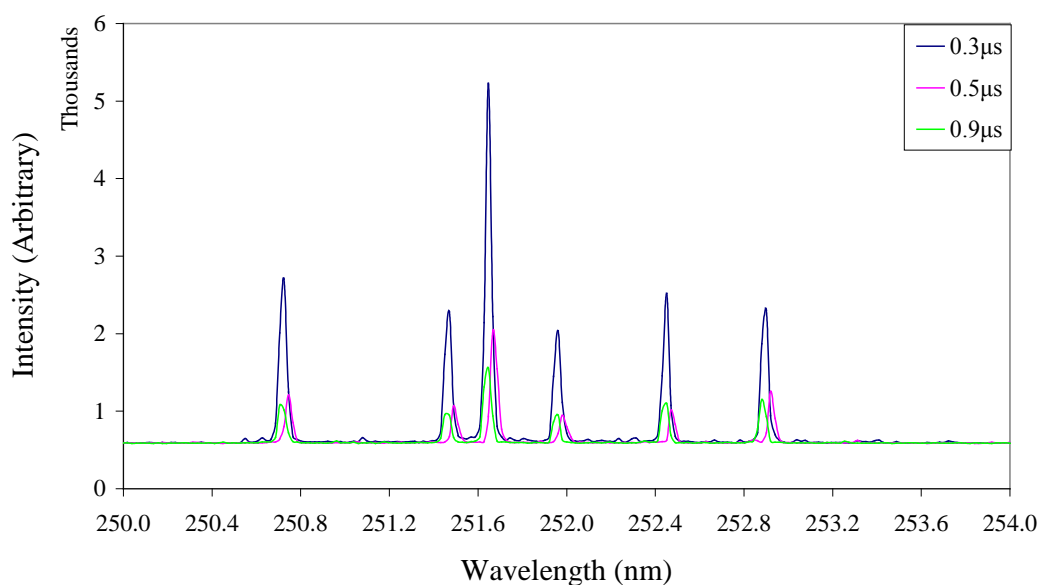


Figure 6.48: Delay variation, sandstone sample, under vacuum pressure of 5×10^{-2} mb.

Figure 6.49 shows baselined spectra of the silicon line, Si (I) 288.158 nm, where the delay time is kept constant and the pressure is reduced. It can be seen that in order to optimise intensity of signal the delay time must be reduced in decreasing pressures because if the delay time is kept constant and the pressure is reduced, the signal also reduces.

It can also be seen that with reducing pressure the line width decreases. This is a result of the increased mean free path of particles in the low pressure medium, decreasing pressure broadening mechanisms and opacity broadening.

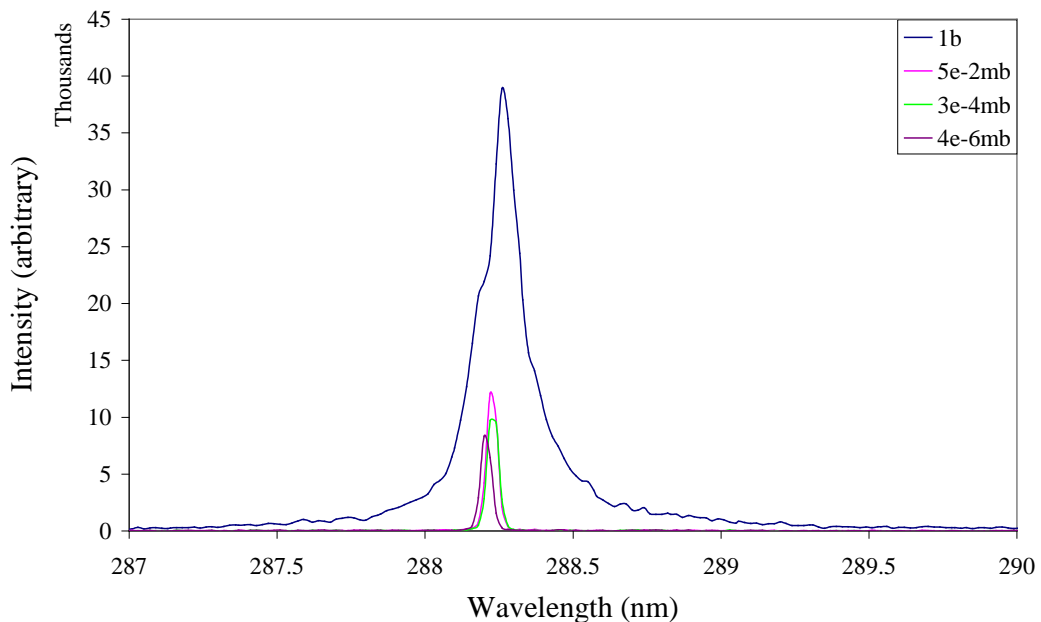
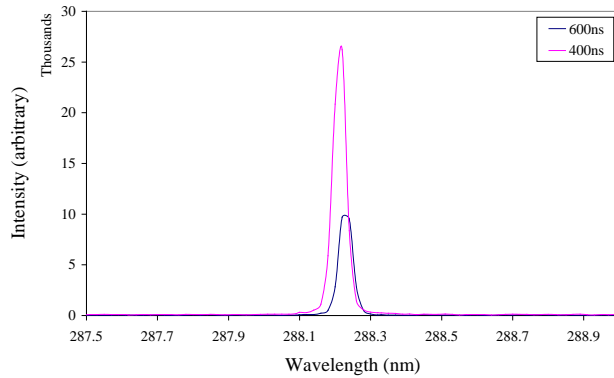
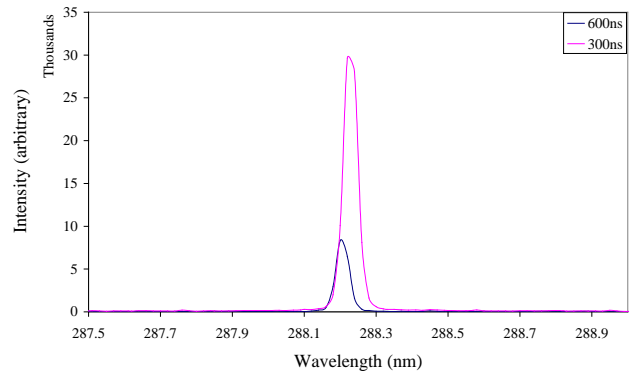


Figure 6.49: Silicon pressure variations, delay 600 ns

In the following charts, (figures 6.50 and 6.51), the pressure was constant and the delay time decreased. It is apparent that at pressures of 3×10^{-4} mb a reduction of $0.2 \mu\text{s}$ in delay produces a 63% increase in signal to noise, (results are baselined).

To remain near to that signal intensity at a reduced pressure of 4×10^{-6} mb, the delay needed to be reduced by $0.3 \mu\text{s}$. This increased the signal by 72% but doubled the line width. The line width increases because earlier in the plasma lifetime there is a higher electron density and temperature, increasing the broadening mechanisms.

Figure 6.50: Silicon delay variations, pressure 3×10^{-4} mbFigure 6.51: Silicon delay variations, pressure 4×10^{-6} mb

It is observed that there is a general trend of approx $0.2 \mu\text{s}$ change in the optimum delay for these experiments, from high pressure optimum delays at $\sim 0.8 \mu\text{s}$, atmospheric at $\sim 0.6 \mu\text{s}$ and vacuum at $\sim 0.4 \mu\text{s}$.

It is possible to see a trend in the percentage difference in intensity. The ‘true’ intensities are in fact very different, but the percentage loss of signal intensity under similar delay changes is comparable in the different experiments undertaken here.

In the vacuum experiments the observed percentage intensity change for a constant pressure is, for an increase in delay of $\sim 0.6 \mu\text{s}$, approximately a 73% loss in signal.

For the high pressure experiments the percentage loss of signal for a $\sim 0.6 \mu\text{s}$ delay change is 50% increasing to a loss of 80% when increasing this delay again to $0.9 \mu\text{s}$. However, increasing the delay further does not bring about a significant decrease in signal.

6.6 Gate Width Variations

Width variations for gated detection of silicon samples and sandstone samples were taken to ascertain the optimum value required to obtain high emission intensity but not forsaking the width and resolution.

Data was obtained for the comparable pressures and gases of a Titan environment, namely 1.5 bar, with gas combinations of:

5% CH₄ 95% N₂

6% CH₄ 94% N₂

7% CH₄ 93% N₂

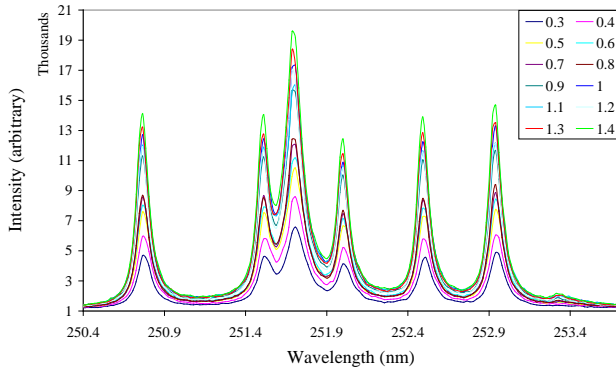


Figure 6.52: Width variation in microseconds at 1.5 bar with 6% CH₄ 94% N₂ gaseous mixture, silicon sample

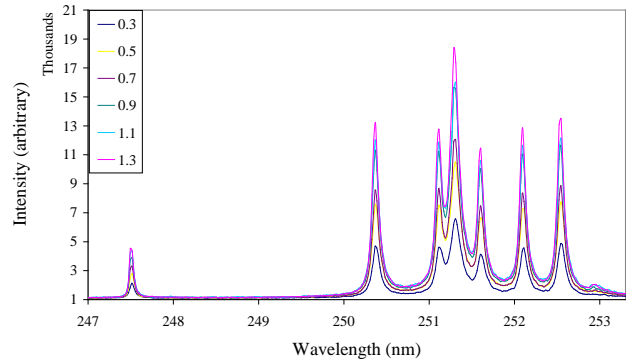


Figure 6.53: Width variation in microseconds at 1.5 bar with 6% CH₄ 94% N₂ gaseous mixture, silicon sample

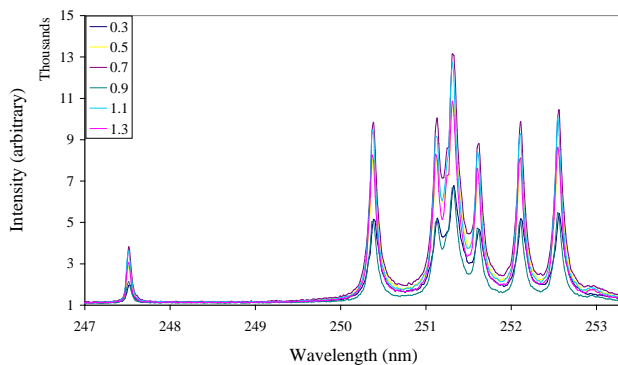


Figure 6.54: Width variation in microseconds at 1.5 bar with 5% CH₄ 95% N₂ gaseous mixture, silicon sample

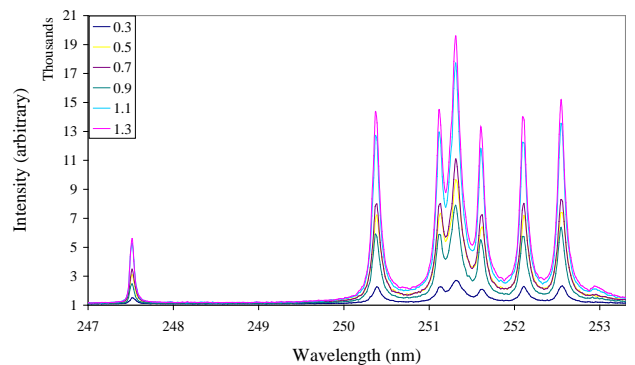


Figure 6.55: Width variation in microseconds at 1.5 bar with 7% CH₄ 93% N₂ gaseous mixture, silicon sample

It has been shown, in figures 6.52 – 6.55, that a greater intensity output can be achieved at longer widths of gate detection as expected, but there is also a trade off with noise and resolution as was found with the temporal delays.

Generally with these gaseous environments at 1.5 bar pressure the optimum width has been shown to be around 0.8 μs . This allowed for a high signal intensity while still achieving good resolution of the peaks.

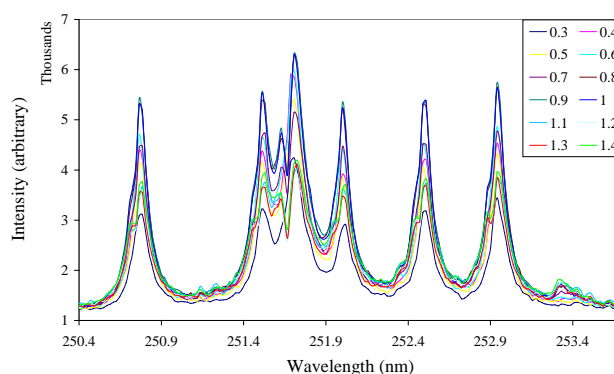


Figure 6.56: Width variation in microseconds at 1.5 bar with 6% CH₄ 94% N₂ gaseous mixture, sandstone sample

It can be seen in figure 6.56 that there was no significant difference when bound to a matrix compound. If anything, the variation is less than that of pure silicon.

6.7 Power Variations

It is advantageous to ascertain the dependence of LIBS on laser pulse energy or power, especially for space missions where available power may be limited. The laser power affects the mass of material ablated and therefore the plume size, as described in section 3.6.

Power was varied by changing the size of an iris in the beam path, as shown in figure 6.57:

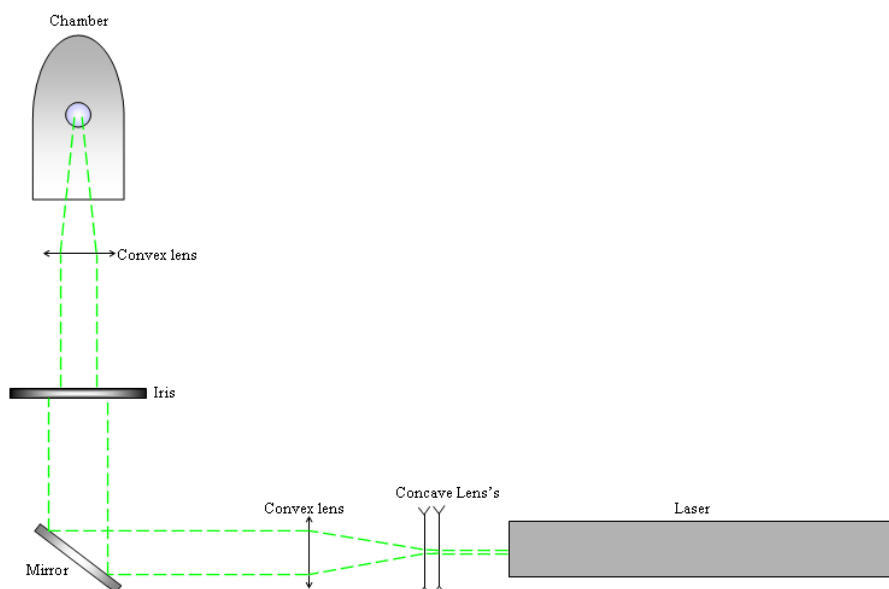


Figure 6.57: Schematic diagram of optical bench setup for power variations

Iris size with respect to power output is plotted in figure 6.58.

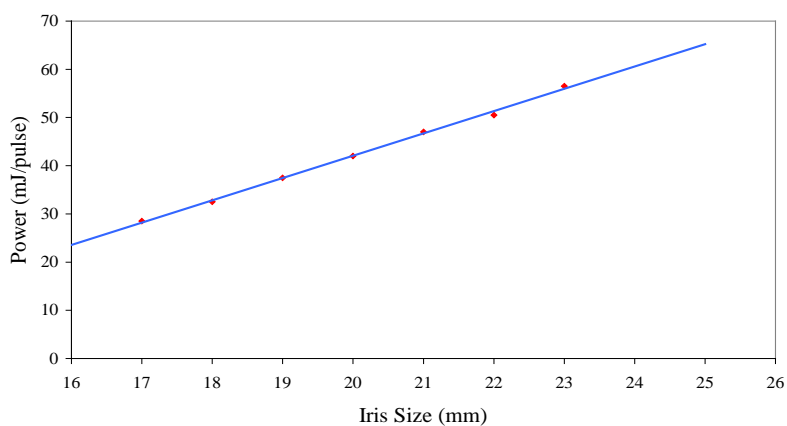


Figure 6.58: Power output with relation to iris size

Data was obtained for the comparable pressures and gases of a Titan environment, namely 1.5 bar, with gas combinations of:

5% CH₄ 95% N₂

6% CH₄ 94% N₂

7% CH₄ 93% N₂

The samples used were silicon and sandstone. The silicon provided a clean reference point and the sandstone showed how the spectral response changes when the element is bound to a compound in a matrix.

The differences seen in these two charts, figures 6.59 & 6.60 silicon and sandstone at 1.5 bar, are mainly due to iron content in the sandstone, except for the C (I) line which is representative of the ambient gas.

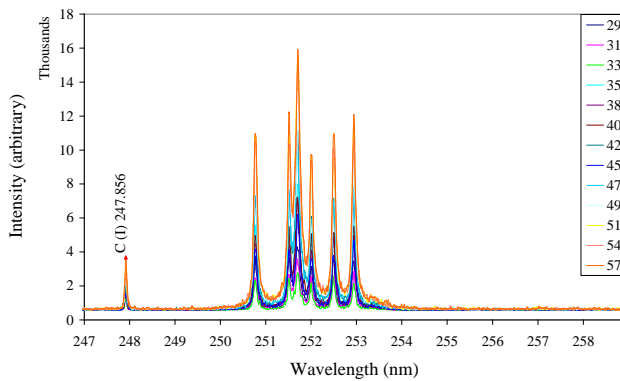


Figure 6.59: Power variation (mJ/pulse) on silicon sample, gas composition: 5%CH₄ 95%N₂

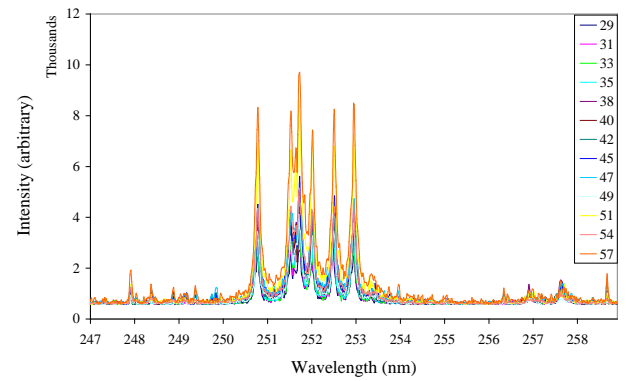


Figure 6.60: Power variation (mJ/pulse) on sandstone sample, gas composition: 5%CH₄ 95%N₂

With the next chart, silicon at 1.5 bar; figure 6.61, one can see more clearly how the power variation affects the line intensity.

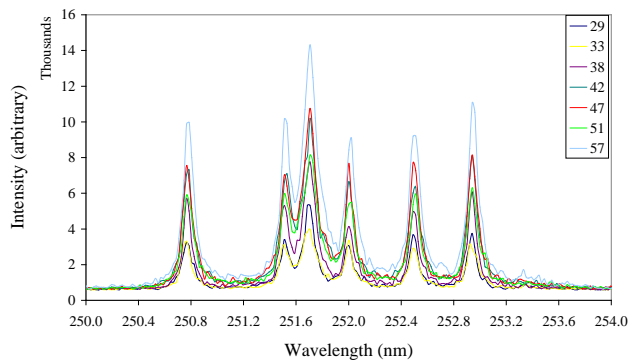


Figure 6.61: Power variation (mJ/pulse) on silicon sample, gas composition: 7%CH₄ 93%N₂

It can be seen that the variation in line width and background continuum is not as apparent as was shown in delay variations. As such it is useful to plot power versus intensity to ascertain the changes of intensity with laser power.

Plotted here are the emission intensities of constituent elements of the sandstone sample and the ambient gas. The increase in intensity with respect to power is evident in both cases.

Figure 6.63 is taken over an average of 15 shots per measurement. When comparing this with single shot output, figure 6.62, (single shot taken from 7th shot in a series of 15 to eliminate initial shot instability), it can be seen that the averaging does not produce a significant change in results and as such this technique was not employed for subsequent measurements.

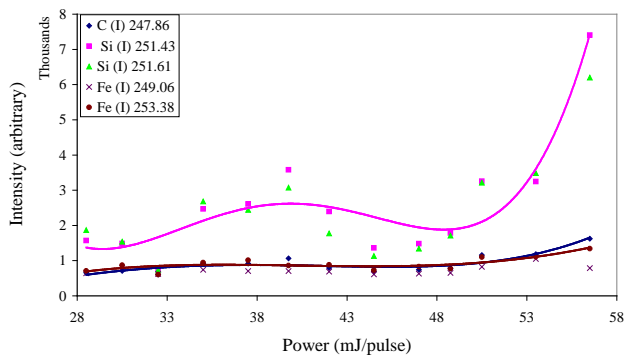


Figure 6.62: Power Variation on Sandstone Sample, gas composition: 6%CH₄ 94%N₂

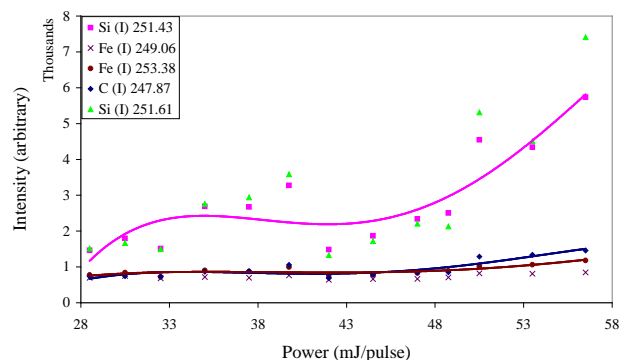


Figure 6.63: Averaged over 15shots, Power Variation on Sandstone Sample, gas composition: 6%CH₄ 94%N₂

All curves here fit with a 4th order polynomial trendline. It can be seen that initially an increase in power produces an increase in intensity, but the intensity increase then flattens off until the power is increased to approximately 51mJ/pulse whereafter the line intensity increases exponentially up to the highest value taken in these experiments.

There is an observed plateau between 33 and 51 mJ/pulse which suggests that an increase in power in this region does not produce a significant increase in emission intensity, which for space-driven applications could prove useful when power may be limited.

In order to see the changes more clearly due to the large differences in emission intensity, figure 6.62 was plotted on a logarithmic scale, figure 6.64.

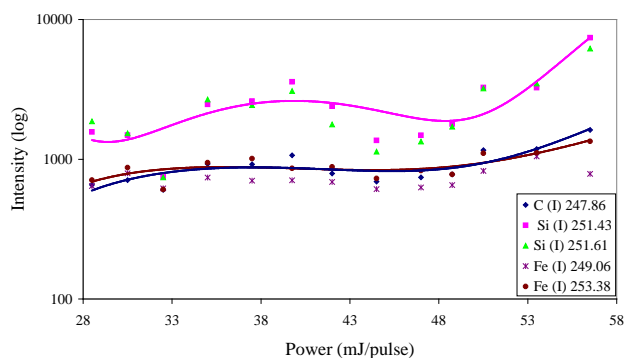


Figure 6.64: Logarithmic plot of power variation, sandstone sample, gas composition: 6%CH₄ 94%N₂

In the next plot, figure 6.65, the silicon sample was used as a control. The silicon sample contains no iron content, so the plot of iron increase with power should remain constant, as is observed. This line therefore represents the background continuum.

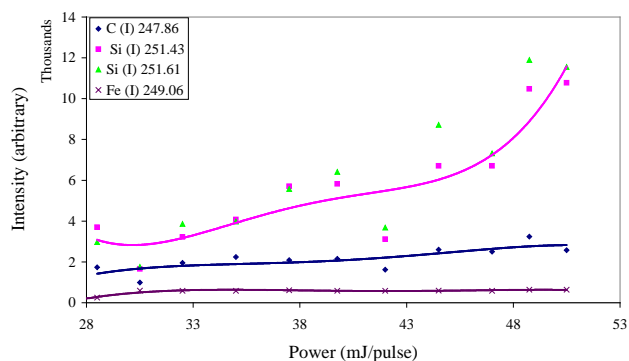


Figure 6.65: Power variation on silicon sample, gas composition: 6%CH₄ 94%N₂

When using a pure sample such as the silicon used here one can see more of a linear increase in intensity with laser power. This could be due to matrix effects in the sandstone sample.

Lastly, weathered sandstone was analysed to see how much the weathered surface affects the emission intensities with varying laser powers, shown in figure 6.66. The increase in emission intensity in this sample is more linear than that of ‘clean’ sandstone. This would be expected due to the weathering masking the output of the first few shots, which is discussed in detail in section 6.8.

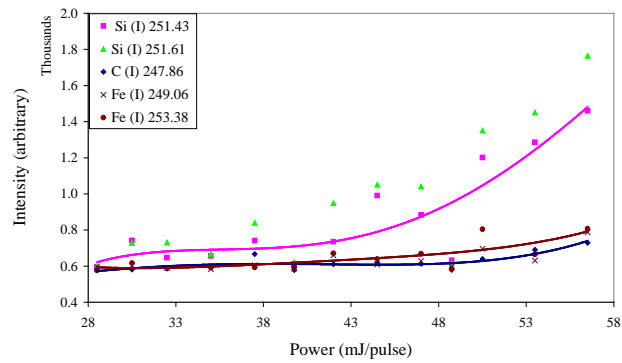


Figure 6.66: Power variation on weathered sandstone sample, gas composition: 6%CH₄ 94%N₂

6.8 Surface Weathering

As part of this study an investigation was undertaken to examine what influence weathering has on experimental results. Weathering is apparent in most naturally occurring external rocks faces, dependent on many factors such as pollution and ambient conditions. It is important to know if it is possible to gain good experimental results with or without weathered surfaces. It has already been shown, in section 6.2, that depth profiling using LIBS is indeed possible. Application of these techniques to rock samples will now be undertaken.

The emission spectrum of the weathered surface was analysed with 15 laser shots at a power of 57mJ/pulse, shown in figure 6.67.

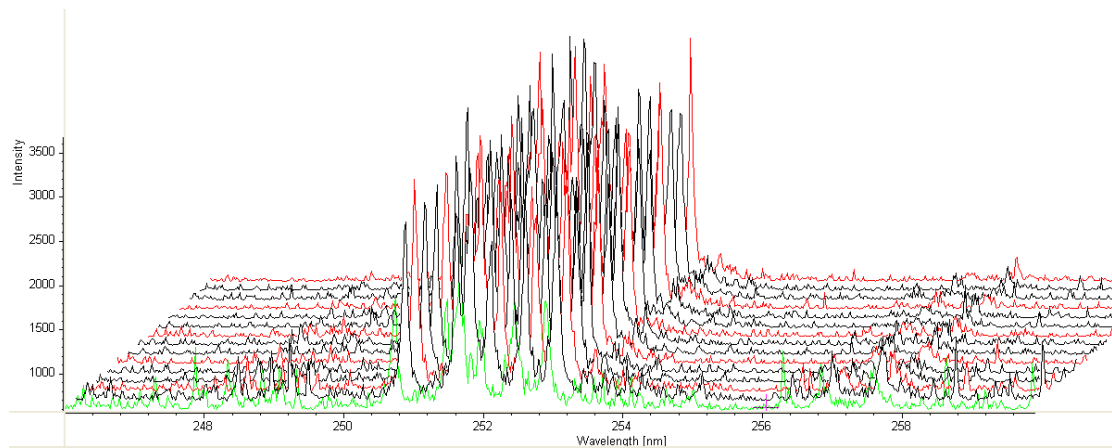


Figure 6.67: Weathered sample 3D emission spectra, 15 shots

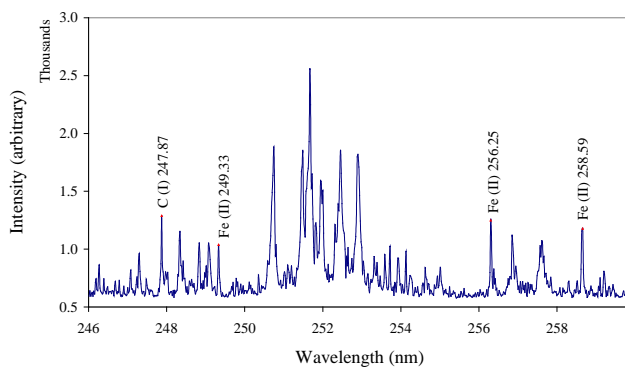


Figure 6.68: Weathered sample spectrum, first shot

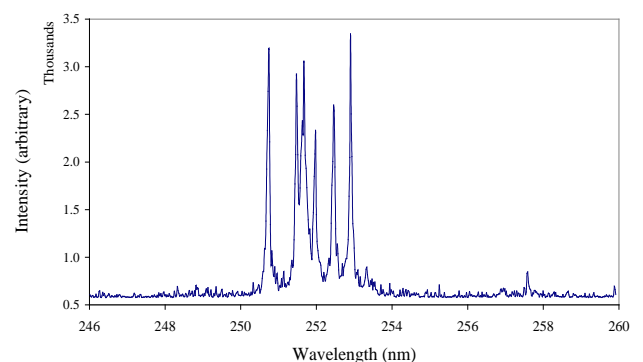


Figure 6.69: Weathered sample spectrum, fifteenth shot

A strong weathering constituent in this sample is carbon, C (I) 247.87 which can be seen visually in green algae on the surface of the sandstone, shown in figure 6.70.



Figure 6.70: Image of weathered sandstone sample, showing green algae build-up

This carbon line was plotted against shot number together with that of Fe (II) 249.33 nm, Fe (II) 256.25 nm, and Fe (II) 258.59 nm to observe the weathering layer decreasing. Also plotted was the silicon line at Si (I) 251.61nm as this was observed to show an emission increase in conjunction with the decrease in carbon and iron lines.

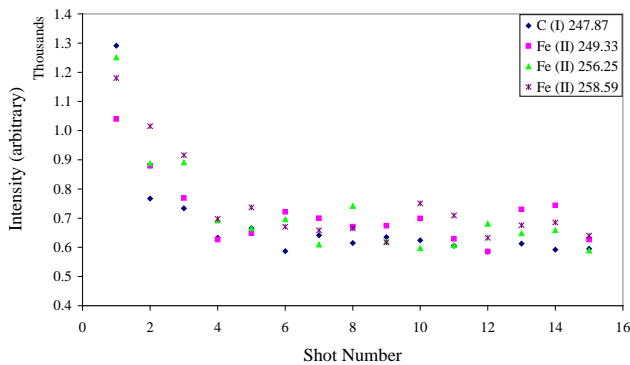


Figure 6.71: Weathered surface emission intensity reduction with shot number in atmospheric conditions

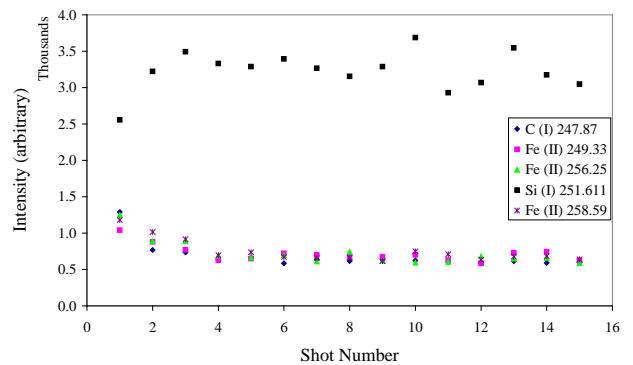


Figure 6.72: Comparison of silicon line emission intensity increase with shot number in atmospheric conditions

It can be seen from these results that the weathered surface is removed after approximately 5 shots in atmospheric conditions.

Further interest lies in how this weathered surface removal is affected by the different pressure and gaseous environments due to the plasma changes and possible re-deposition of materials. Shown here are the weathered surface lines emission spectra under different pressures and with different fill gases.

The first sets of data, figures 6.73 & 6.74, were taken at pressures of 5×10^{-2} mb:

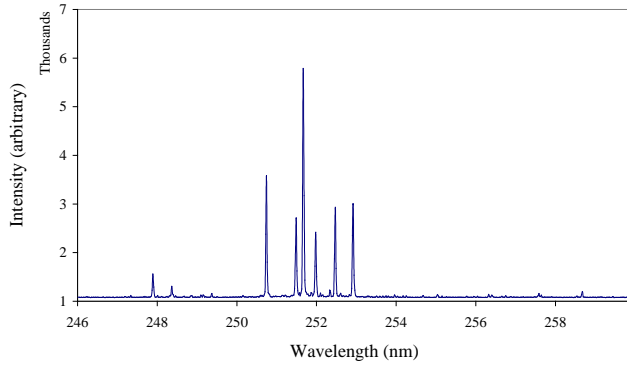


Figure 6.73: Weathered sample spectrum, first shot at 5×10^{-2} mb

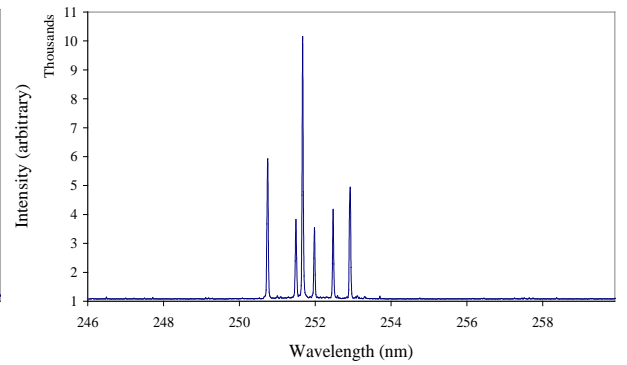


Figure 6.74: Weathered sample spectrum, fifteenth shot at 5×10^{-2} mb

Quite clearly there is a large difference in the emission spectrum at low pressures compared with that at atmospheric pressures. The second ionisation stages of iron are not apparent in these spectra due to the reduced pressure bringing about a reduction in plasma temperature and as such a loss of higher ionisation species. However the carbon emission line is still evident. All are plotted in figures 6.75 & 6.76.

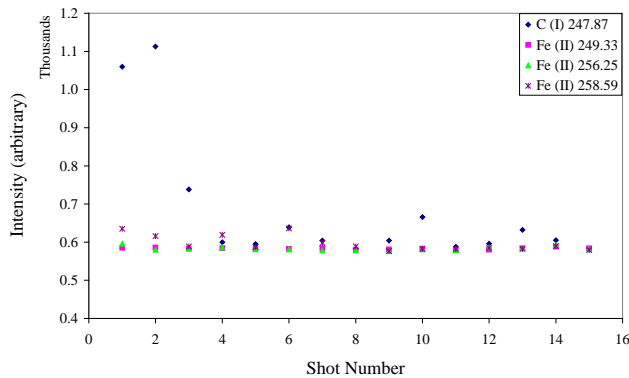


Figure 6.75: Weathered surface lines emission intensity reduction with shot number at 5×10^{-2} mb

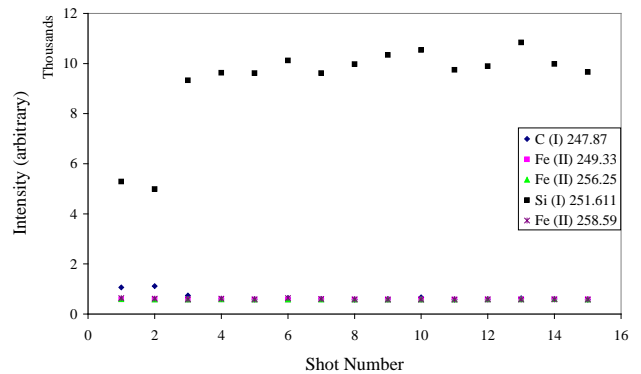


Figure 6.76: Comparison of silicon line emission intensity increase with shot number at 5×10^{-2} mb

Although the iron lines do not show a large change in emission intensity the carbon and silicon emission lines exhibit the same characteristic as those in atmospheric conditions. This suggests that although the same emission lines cannot be studied in both environmental conditions, careful selection of emission lines produces similar results. The difference in shielding of the sample surface under reduces pressures is apparent, as the surface coating appears to be removed at approximately 3-4 laser shots, 1-2 shots less than that at atmospheric pressure.

Results, shown in figures 6.77 & 6.78 were also obtained for weathering removal at a pressures of 1.5 bar, the pressure found on Titan's surface. Initially the filling gas used was nitrogen, as this is known to produce little interference at this spectral range.

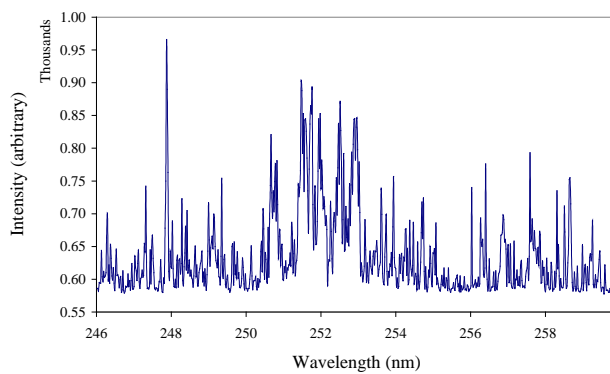


Figure 6.77: Weathered sample emission spectrum, first shot at 1.5 bar nitrogen fill

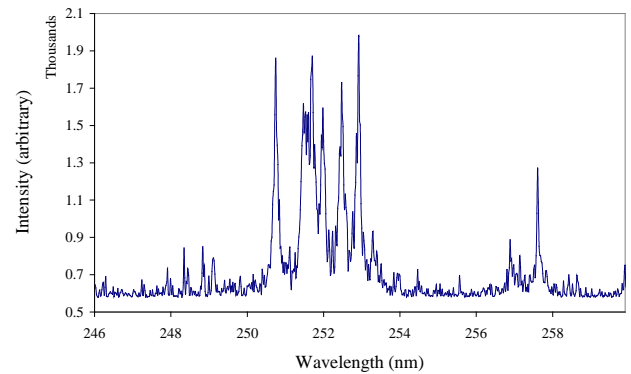


Figure 6.78: Weathered sample emission spectrum, fifteenth shot at 1.5 bar nitrogen fill.

Again, a large variation in spectral emissions at these pressures is apparent. The high pressure measurements producing much less clarity of emissions and a reduced signal to noise ratio when compared to that of atmosphere or vacuum.

With this being the case, the iron lines did not show a significant change in emission intensity even though the higher temperatures in the plasma should allow for second ionisation lines to be apparent. The carbon and silicon emission lines produced a similar variation to that of atmospheric and vacuum systems. All emission lines are plotted in figures 6.79 & 6.80.

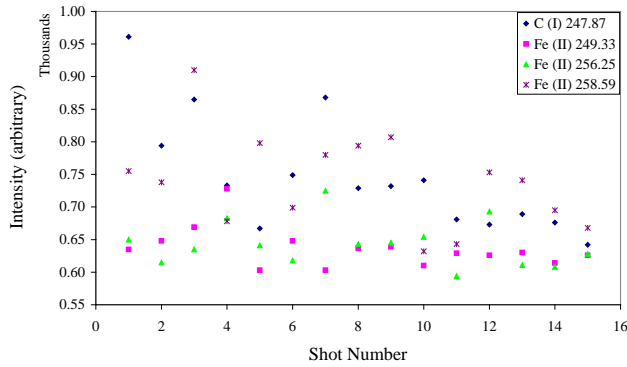


Figure 6.79: Weathered surface lines emission intensity reduction with 1.5 bar nitrogen fill

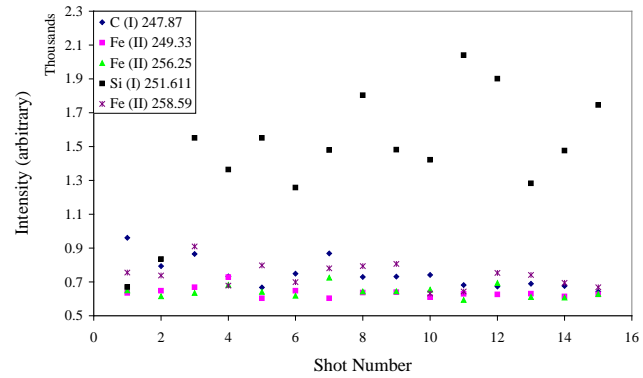


Figure 6.80: Comparison of silicon line emission intensity increase with shot number at 1.5 bar nitrogen fill

As shown in figures 6.79 and 6.80, the silicon emission lines show the same trend of increase as those in vacuum and atmospheric conditions. The carbon emission does exhibit the same trend although there is much more noise and shot to shot instability with these measurements taken at 1.5 bar pressure. This would suggest that when analysing the surface conditions in these pressure regimes it would be better to analyse the increase and levelling off of silicon rather than the decrease in carbon.

It is evident that high pressures bring about more sample surface shielding, so it will take longer to remove the weathered coating. Interference and shot to shot instability make it hard to ascertain a true value of shots needed to remove the weathered coating, but it can be deduced that the surface is removed after approximately 6-7shots.

In the next set of results, shown in figures 6.81 & 6.82, taken with methane as a filling gas at 1.5 bar, it was observed that there is very little increase in emission intensity of silicon lines from the first shot to the 15th shot.

As with the nitrogen fill at these pressures, there is a loss of signal to noise ratio, but it was not improved after 15 shots as was observed in the nitrogen environment.

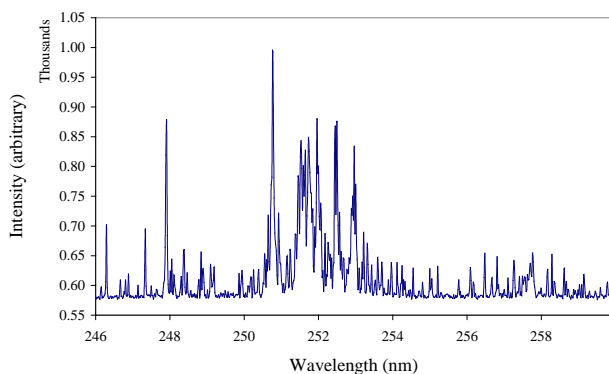


Figure 6.81: Weathered sample emission spectrum, first shot at 1.5 bar methane fill

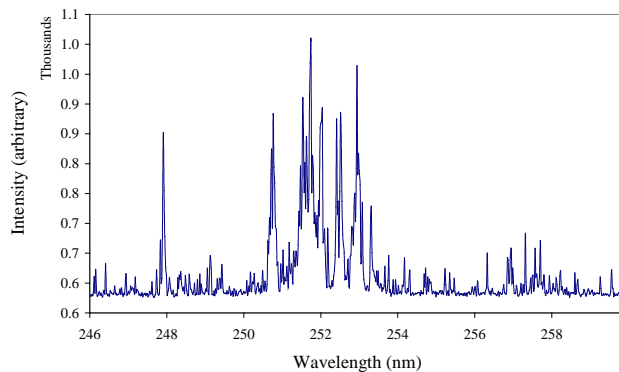


Figure 6.82: Weathered sample emission spectrum, fifteenth shot at 1.5 bar methane fill

The carbon emission line does not significantly decrease in these measurements because there is carbon content in the filling gas. As was found with nitrogen filling gas at 1.5 bar, the iron emissions show little change in emission intensity for shot number, as shown in figures 6.83 & 6.84.

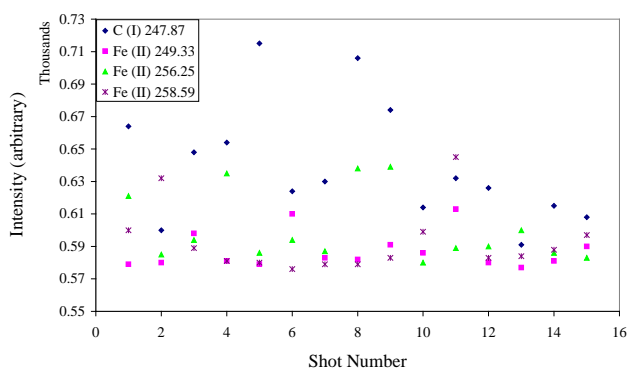


Figure 6.83: Weathered surface lines emission intensity reduction with a 1.5 bar methane fill

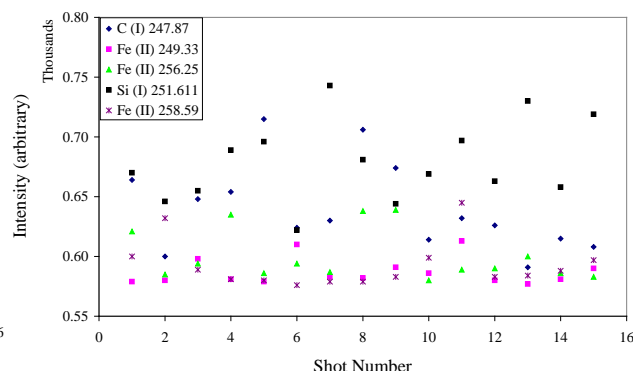


Figure 6.84: Comparison of silicon line emission intensity increase with shot number with a 1.5 bar methane fill

With methane as a filling gas it is harder to ascertain the removal of the coating at this wavelength range. A loss in carbon emission intensity is apparent, but there is no clear cut off as to when this change levels off. In addition, there is an observed re-deposition of carbon onto the surface of the samples in the form of black soot, seen in the sample pictures, section 6.3, figures 6.23, 6.28 and 6.33. This could cause interference with the results obtained.

In order to obtain surface weathering results with methane as a filling gas one would have to either take more shots in order to ascertain the ambient carbon

content without interference from the weathered surface or look at an alternative spectral range, where different emission lines may produce a clearer cut off.

Alternative wavelength ranges were analysed to see if this trend could be reproduced. Two emission lines were found, namely Si (I) 243.52 nm and Fe (II) 263.16 nm, that displayed the same characteristics, verifying the results in methane environments. It can be seen in figure 6.85 that the weathered surface is removed in a methane environment after approximately 8 shots, although more variation from shot to shot after this point is apparent as with other high pressure measurements.

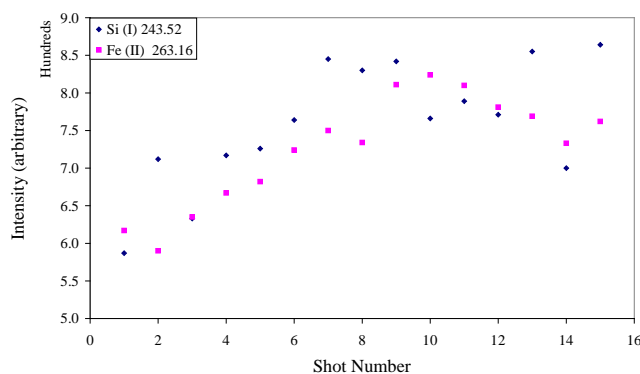


Figure 6.85: Silicon and iron emission line intensity increase with shot number

Methane is seen to bring higher emission intensity damping than that of nitrogen at comparable pressures, as will be discussed in section 6.9. As such there would be an expected increase in the number of laser shots before the weathered coating is removed due to the laser power reaching the sample surface being attenuated by the plume and gaseous content. This effect can be observed in the results obtained.

The gaseous mixture on Titan is thought to be in the region of 6% methane and 94% nitrogen. This filling mixture was used to establish if the surface weathering removal could be seen in these conditions. The results are plotted in figures 6.86 - 6.89. The pressure was again set to 1.5 bar.

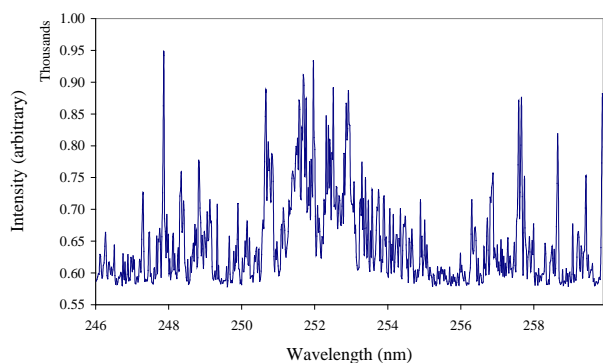


Figure 6.86: Weathered sample emission spectrum, first shot at 1.5 bar, 6%CH₄ 94%N₂ fill

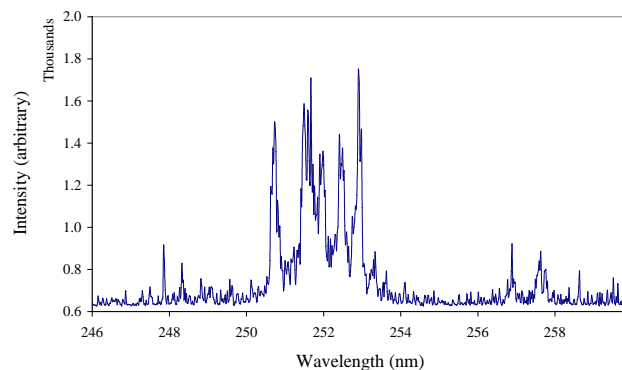


Figure 6.87: Weathered sample emission spectrum, fifteenth shot at 1.5 bar, 6%CH₄ 94%N₂ fill

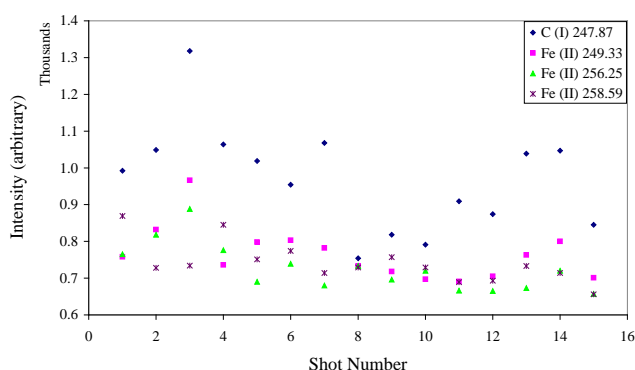


Figure 6.88: Weathered surface lines emission intensity reduction with shot number, 1.5 bar 6%CH₄ 94%N₂ fill

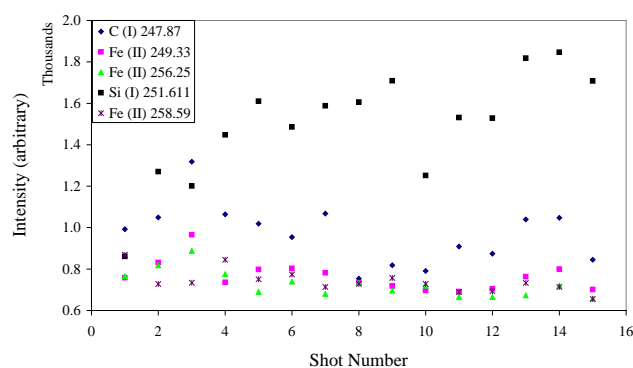


Figure 6.89: Comparison of silicon line emission intensity increase with shot number, 1.5 bar 6%CH₄ 94%N₂ fill

With this filling gas one can observe the increase in silicon emissions as was apparent in the nitrogen fill under both atmospheric and vacuum regimes. The observed loss in the carbon emission line is again less apparent due to the interference from the atmospheric gases.

In this pressure and gaseous mixture there is a drop off in intensity of the iron emission lines as was apparent in atmospheric conditions, but there is less clarity in response. Although this is true, there remains the capability to observe the removal of the surface weathering with Titan's atmospheric pressures and gases.

The shots needed to remove the weathered coating with this fill mixture should lie somewhere in between that of pure nitrogen and methane. The removal of the coating is observed to be complete at approximately 7 laser shots, showing direct correlation with pressure, fill and surface removal speed of the other results obtained.

Utilising equation 3.5 from page 16 one can determine the ablation depth per pulse for the weathered samples. This derivation will be dependent on inherent errors in the results, as mentioned in section 3.2, due to composition and reflectivity changes of the sample and as such the depths extracted are quoted with an approximate $\pm 20\%$ uncertainty.

$$A_d = \frac{f(1-R)}{[C_p(T_b - T_0) + L_v]\rho} \quad (3.5)$$

Using the parameters from the EDX measurements of constituent species from the weathered sandstone, 69% silicon and 22% aluminium, and then weighting the results for these species, the ablation depth per pulse in atmospheric conditions is calculated to be approximately 22 nm per pulse. This fits with ablation depth measurements taken by Vadillo et al¹⁰⁷ in 1999.

This can then be used to estimate the depth of the weathered coating, which is calculated to be approximately 110 nm, with 5 shots being needed to remove the coating in atmospheric conditions.

6.9 Pressure and Gaseous Content Variations

6.9.1 Pressure Variations

The next study undertaken was to establish how much the pressure affects the emission intensity, width and resolution of the spectra. As mentioned already in section 3.5, pressure affects the plasma due to many factors. A difference in the mean free path of particles in the ambient gas leads to a difference in the dissipation speed of the plume, bringing about a discontinuity in the amount of sample material ablated due to reduced shielding by the plasma. As the plasma size changes in the different pressure environments a misalignment of the optical fibre may occur resulting in a difference in captured signal.

Higher pressures can induce pressure broadening mechanisms due to increased confinement of the plume, discussed in section 3.3.1, which can increase the line width of spectral emissions, sometimes resulting in self absorption. Lastly, the ambient gas may affect results due to absorption of the plasma's emission signal or ionisation of the gas molecules themselves.

In order to measure from pressures below atmospheric up to pressures above atmospheric a 'filling' gas was used. The apparatus was first evacuated to roughing pressures of $\sim 5 \times 10^{-2}$ mb for 30 minutes to ensure that little ambient atmospheric gas remained. Following this the apparatus was slowly filled with the backing gas, measurements being taken at pressure intervals after the apparatus was at maximum pressure, with the pressure being reduced after each measurement. Earth's atmospheric pressure is at 1 bar, Titan's is at 1.5 bar.

It should be noted that the delay on these experiments was set at 0.6 μ s. Although this parameter will allow for a spectral signal at each pressure regime, there will be observed signal intensity losses at lower and higher pressures, compared to atmospheric pressure, due to the value not being optimised for all pressure measurements.

Another factor to take into consideration is the plasma size change in each pressure regime inducing a factor of alignment of the optical fibre into the possible intensity outputs. The work done in these measurements shows the same characteristic line pattern as that of the work done by Knight et al¹⁰⁵, where they cross referenced the optical fibre alignment with their pressure analyses. Their results showed that the changes were due to pressure artefacts themselves and not to misalignments of the optical fibre. As the results here are comparable the same assumption was made.

Analysed first was the change in width and resolution of the spectral results with changes in the pressure. The silicon sample was used initially for these results as any interference from other spectral lines would be minimal. As with the power measurements, a single shot analysis of silicon, with nitrogen as a filling gas, was compared with data averaged over 15 shots as shown in figures 6.90 & 6.91

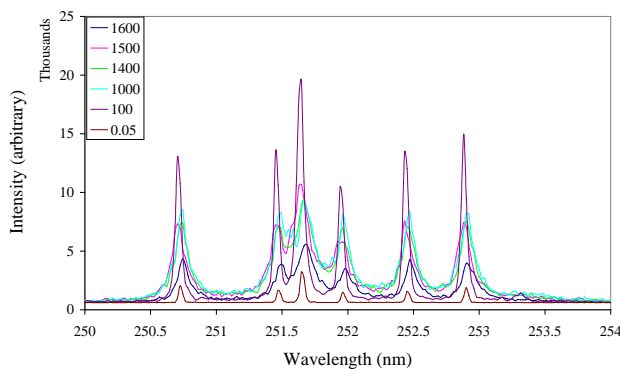


Figure 6.90: Single shot emission spectrum of silicon sample showing intensity change with pressure, with N₂ as filling gas

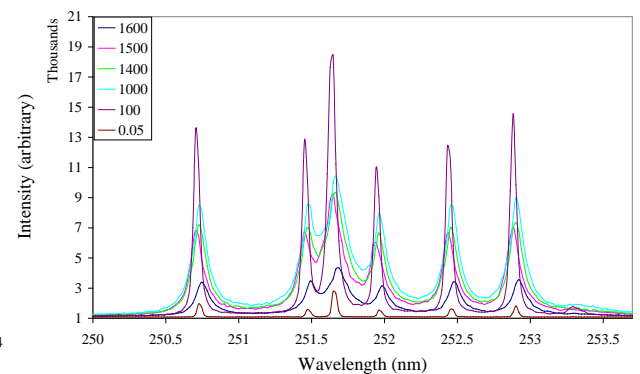


Figure 6.91: 15 shot average, silicon sample, intensity change with pressure, with N₂ as filling gas

In this instance a difference in results from the averaged to non-averaged data can be seen. As such the following pressure charts are all averaged over 15 shots.

Different filling gases were then used to discover the expected variations in line intensity and to ascertain if there are any influences on width and spectral resolution with varying gaseous mixtures. Measurements were taken with a silicon sample under four other gas regimes, namely;

5% CH₄ 95% N₂,

6% CH₄ 94% N₂,

7% CH₄ 93% N₂,

pure CH₄,

The results are shown in figures 6.92 – 6.96.

As the main area of interest for this study is the different gaseous mixtures, in order to obtain a better picture of the change with pressure against intensity more data was collected for these measurements. Also shown in figure 6.94 is a simplified chart of the 6%/94% mixture for comparison with other charts.

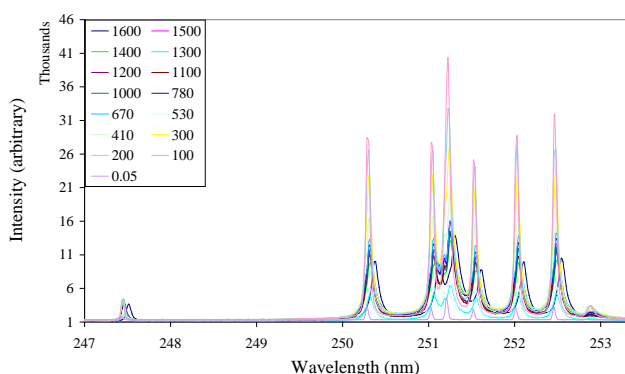


Figure 6.92: Silicon sample emission intensity change with pressure, with 5%/95% mixture as filling gas. variation in millibar

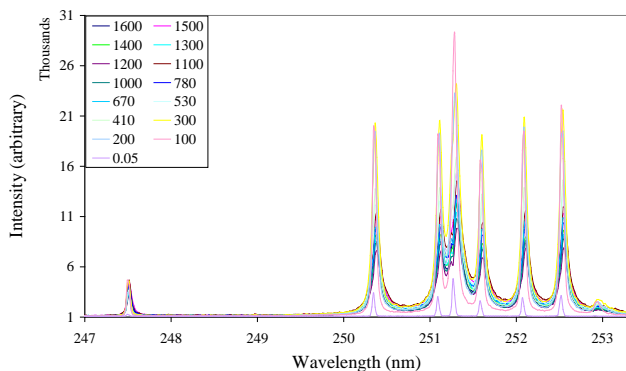


Figure 6.93: Silicon sample emission intensity change with pressure, with 6%/94% mix as filling gas. variation in millibar

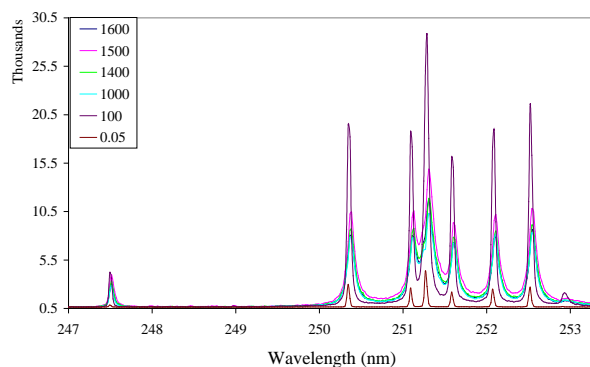


Figure 6.94: Simplified silicon sample emission intensity change with pressure, with 6%/94% mix as filling gas. variation in millibar

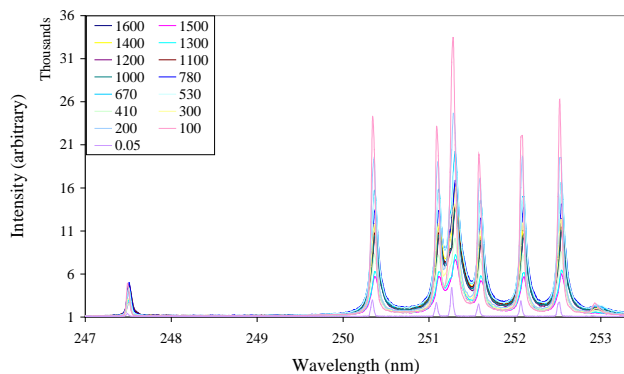


Figure 6.95: Silicon sample emission intensity change with pressure, with 7%/93% mixture as filling gas. variation in millibar

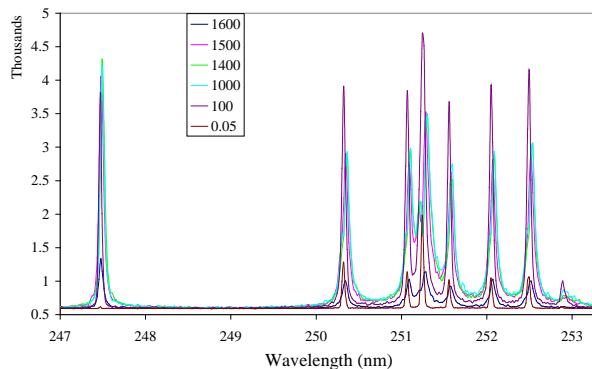


Figure 6.96: Silicon sample emission intensity change with pressure, with CH₄ as filling gas, variation in millibar

The results support the supposition that the width and resolution of the spectral lines are pressure dependent. There is the largest variation at high pressures (1600 mb) or low pressures (300-0.05 mb) but the other pressures measured appear to fit to a mean value.

It can clearly be seen that the carbon content is dependent on the ambient atmospheric gas in these samples, the content increasing with fill ratio. This phenomenon will be explored more later in section 6.9.2.

The spectrum of the sandstone sample was analysed to ascertain if the width and resolution results found in the previous measurements with a pure silicon wafer are changed when the element is bound to a matrix compound, the results are shown in figures 6.97 – 6.100.

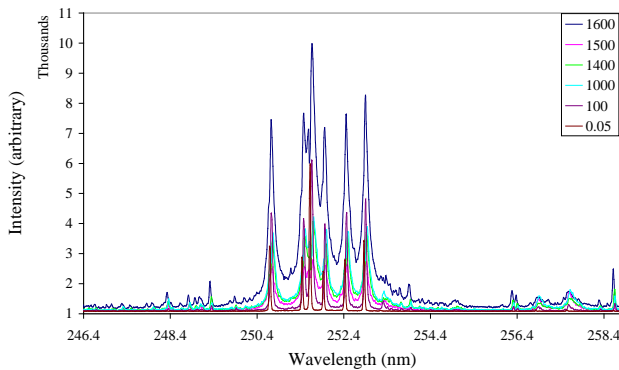


Figure 6.97: Sandstone sample emission intensity change with pressure, with N₂ as filling gas, variation in millibar

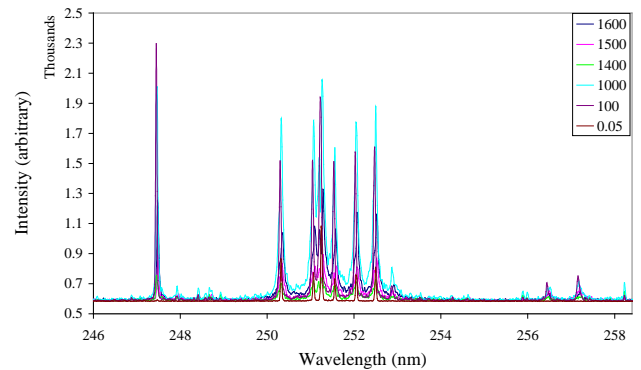


Figure 6.98: Sandstone sample emission intensity change with pressure, with CH₄ as filling gas, variation in millibar

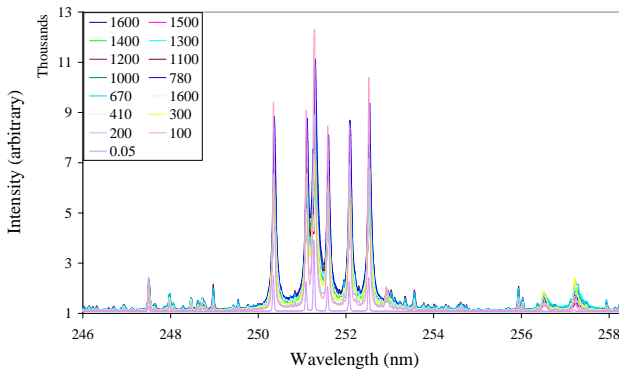


Figure 6.99: Sandstone sample emission intensity change with pressure, with 6%/94% mix as filling gas, variation in millibar

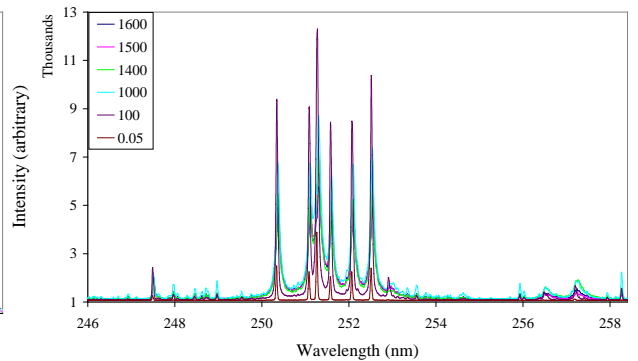


Figure 6.100: Simplified sandstone samples emission intensity change with pressure, with 6%/94% mix as filling gas, variation in millibar

It is apparent that there is no great variance from a pure silicon sample to that of a sandstone with respect to pressure variations and the width and resolution of the spectral lines. Both studies portray a trend where at lower pressures the width is at its narrowest and the resolution is optimum. As the pressure increases the width increases and loss of resolution of the spectral lines is observed.

The next study was undertaken to ascertain the emission intensity change with pressure which, as can be seen from the last set of charts, is quite significant. Pressure was plotted against emission intensity for certain spectral lines, namely C (I) 247.86 nm, Si (I) 251.43 nm, Si (I) 251.61 nm and Fe (I) 249.06 nm, all measurements were averaged over 15 shots.

The first filling gas used was nitrogen, as this is the main constituent gas in both the Earth and Titan atmospheres.

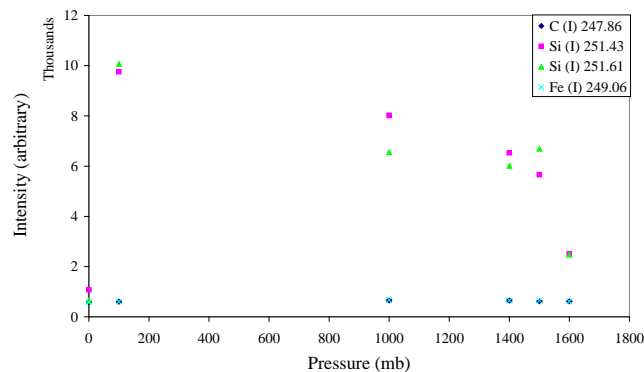


Figure 6.101: Chart showing emission intensity change with pressure, with N_2 as filling gas, silicon sample.

As the silicon sample was analysed first as shown in figure 6.101, there is no emission from the iron line at 249.06 nm, there is also no emission from the carbon line as nitrogen was used as a filling gas. As such these lines represent the background continuum.

It can be seen from the carbon and iron line emissions that the background response is nearly linear across these pressure regimes with this filling gas, even though the delays were set at $0.6 \mu s$. This is a good indication that the pressure versus intensity response is not affected greatly by the static delay setting used.

The procedure was repeated with methane as the filling gas. Methane has a high carbon content and as such the carbon emission intensities should be affected by this filling gas. Shown in figure 6.105 is the methane influence on the measurements.

Measurements were also obtained for the other gaseous mixtures used in previous experiments. The results are presented here in figures 6.102 – 6.105.

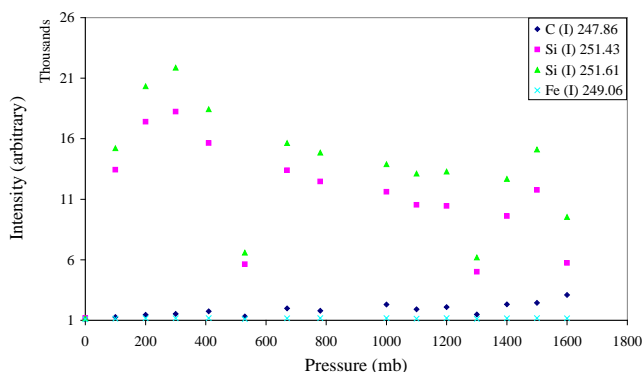


Figure 6.102: Change in emission intensity with pressure variations, 5/95 mix as filling gas, silicon sample

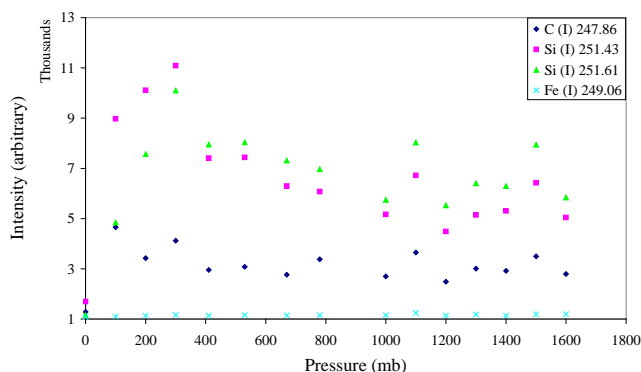


Figure 6.103: Change in emission intensity with pressure variations, 6/94 mix as filling gas, silicon sample

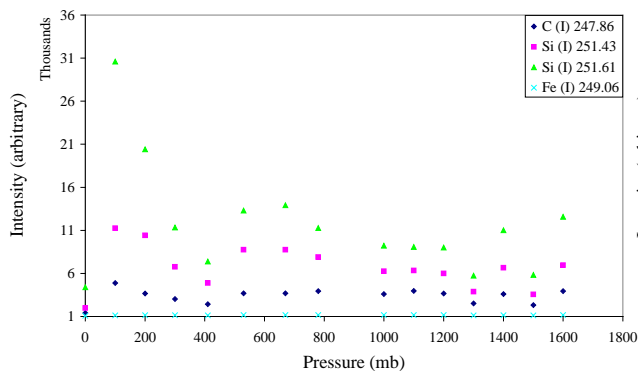


Figure 6.104: Change emission intensity with pressure variations, 7/93 mix as filling gas, silicon sample

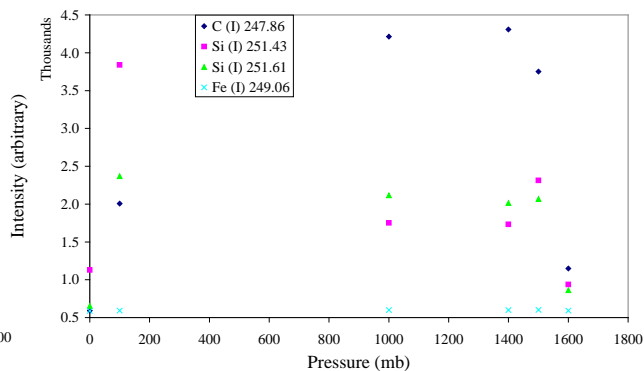


Figure 6.105: Change emission intensity with pressure variations, CH₄ as filling gas, silicon sample.

As with the other measurements, iron is not found in the sample so it can be used as a guide to the background continuum intensity changes with pressure.

As the methane content increases in the ambient gas the carbon emission line starts to fit the trends of the other lines. When pure methane is used, the carbon emission line is observed to increase with increasing pressure, but an intensity drop off is observed at pressures higher than 1400 mb.

Initially one can see that there is a reduced intensity at vacuum pressures of 0.05mb in all cases. This can be attributed to the increase in mean free path of the particles and as such a reduction in confinement of the plume. The loss in confinement will bring about a loss in emission intensity two-fold, firstly there will be less species to emit due to dissipation, secondly there will be less re-excitation due to reduced collisions.

Three body processes, or inverse Bremsstrahlung, are more likely at higher pressures than lower pressures and could account for the observed increase in the number of ionisation states at the lower pressure, as observed in the studies mentioned in *The Handbook of LIBS*³⁴, page 120.

At approximately 250 mb one can see an increase in emission intensity in all studies. This is a result of the increase in pressure bringing about an increase in confinement of the plume. In unison with that the amount of ablated material will decrease with an increase in pressure, as the plasma produced will act to shield the sample surface from the laser pulse. At approximately 250 mb an optimum is reached whereby a trade off between confinement, shielding and excitation is achieved. This phenomenon has also been reported in similar studies under these pressure regimes. One such study is that by Vadilo et al¹⁰⁷ in 1999, where it is noted that an increase in average ablation rate is observed with decreasing air pressure from 1000 to 250 mb.

When analysing the intensity versus wavelength at these pressures (250 mb) one can also observe that there is an optimum line width and resolution reached, whereby the confinement of the plume is sufficient to produce a large emission signal but it is not too great as to significantly affect the line width due to pressure broadening mechanisms.

After 250 mb there is a drop off of emission signal, with this reduction process being quicker the more methane content there is in the ambient atmosphere.

The reduction in emission signal as the pressure is increased from 250 mb can be attributed to the increase in re-combination at higher pressures. Three body

processes, (inverse Bremsstrahlung), are more likely at higher pressures than lower pressures. The re-combination would result in less emissions and as such a reduced emission intensity. Concurrently, the plasma would be more optically thick, thus shielding the surface more effectively from the incoming laser pulse bringing about a reduction in the amount of sample ablated and as such a reduction in the emission intensity. In parallel with this, an optically thick plasma is more likely to bring about self reversal of the emissions which would result in a reduced intensity.

The study reveals an increase in the damping of the optical emissions with higher methane content in the ambient atmosphere.

Methane plasmas contain many reactant products, as discussed in section 3.7, species present incorporating¹¹⁵⁻¹¹⁹ many molecules, ions and radicals. The quenching effect observed could be due to these many reaction species reducing the optical emissions by radiationless transitions, 3 body collisions, and re-absorption. As such the more methane content in the ambient gas the higher the damping effect.

The increase in reaction species in the ambient gas will allow for a larger number of de-excitation process in the plasma, especially when compared with that of the relatively inert nitrogen gas.

Some such de-excitation processes could be losses due to ionisation when the electron is in resonance with another state, or simply due to the greater number of levels available in methane and its constituent reaction products. Alternatively they could be due to the fact that rotational and vibrational de-excitation processes are more readily available in the methane than the nitrogen, these de-excitation processes obeying the conservation rule that electron and phonon energy loss mechanisms are preferential to the emission of a photon.

This hypothesis is supported by the appearance of a singly ionised emission of carbon from the gaseous environment. This must be due to the methane content,

(as no carbon is available in the silicon sample), and as such validates the supposition that the methane dissociates in the plasma into its constituent species.

After the intensity drop off, observed with an increase in pressure above 250 mb, the emission intensity reaches a steady state or plateau region, generally falling between 500 – 1400 mb.

As the pressure increases so does the thermal conductivity of the plasma, partly being due to the phenomenon of ambipolar diffusion, whereby as the electrons, (faster moving than the ions), leave the plasma an imbalance in charge is observed. This causes an attraction on the escaping electrons, slowing the escape processes. This would produce a reduced emission intensity at higher pressures

In contrast to the ambipolar diffusion process, the increase in pressure will bring about an increase in the number of ions in the plasma via electron-photon-ion collisions, yielding a higher probability of further electron multiplication and a higher energy and temperature of the electrons. The greater the electron density the more likelihood of a cascade of electron multiplication due to Bremsstrahlung and multiphoton radiation processes.

Electron densities are known¹³⁵ to change with distance from the sample surface. The optical fibre alignment in this study was positioned so as to reduce the discontinuities of this effect. Electron densities were estimated to be approximately $1 \times 10^{16} \text{ cm}^{-3}$ from similar investigations^{34,135}.

Under different pressures electron densities and temperatures will be orders of magnitude different. Laser irradiance also plays an important role, the higher the irradiance, the higher the electron temperature and density. Ascertaining the changes in electron densities and temperatures in LIBS plasmas at varying pressures would be an intriguing area for further study.

Another factor that will affect the emission intensity is, as mentioned earlier, the de-excitation processes available in the plasma. As the pressure is increased the proximity of the constituents will increase, producing an increase in de-excitation

processes, reducing the signal intensity. This phenomenon can be used to explain why a greater loss is observed in the environments that contain more methane content and why the difference in the peak emission to that of the plateau region is less when analysing the samples with greater methane content in the atmosphere.

Not to be forgotten is the effect of self reversal, which can be seen in the calcium emissions of marble covered in section 6.9.3. This effect is due to the close proximity of the plasma constituents in the increased pressure regime, resulting in greater losses due to collisions with species, in this case re-absorption of the emitted species.

Generally there will be a trade off in this plateau region; increases in emissions being brought about by the reduction in dissipation of the plume, increasing density and ambipolar diffusion. This together with the number of collisions and re-excitation of constituent species results in a noise and width increase from the increased energy in the system.

Decreases in emission will be the result of the same increase in confinement of the plume, but in contrast to this bringing about an increase in emissions the trade off is more likely to produce a decrease in emissions. In this instance the decreases are due to increased sample shielding, higher probability of self reversal, increase in the number of de-excitation processes other than photon emission and an increase in re-combination at higher pressures.

Not forsaking the factors mentioned on plasma processes, account should be taken for the possibility of species present in the path from the plasma to the optical fibre absorbing or deflecting the optical emission.

The following chart, figure 6.106, plots certain emission lines from all samples, with observations of emission intensity and pressure. The dotted line represents the approximate level of background continuum.

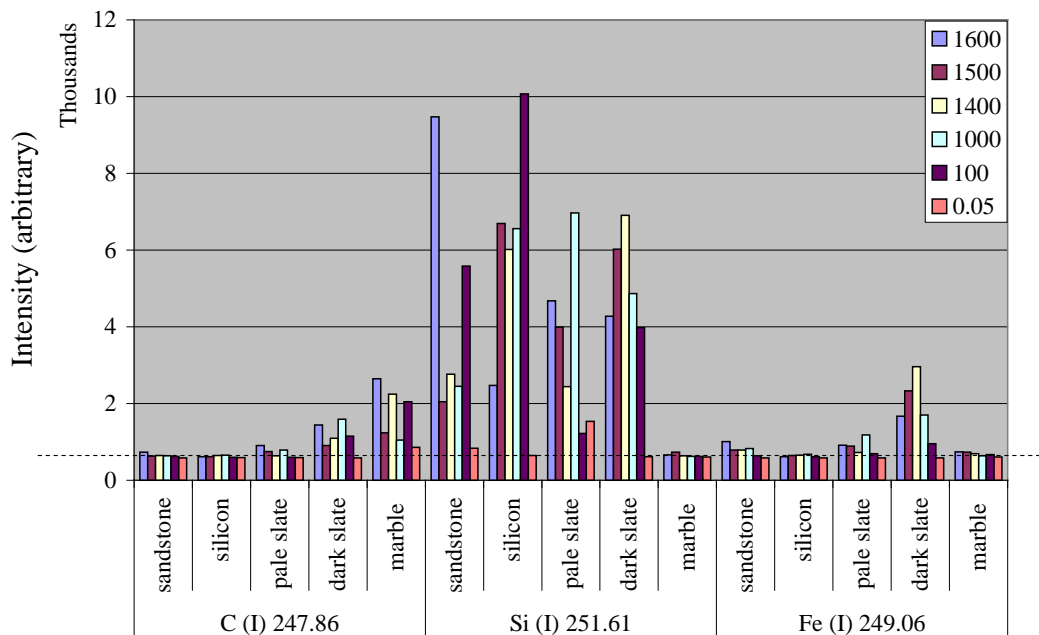


Figure 6.106: Plot of specific emission line intensity variations from each sample with respect to pressure.

From this chart one can see the elemental constituents of each sample. It is useful to ascertain the differences between dark and pale slate. For all measurements the pressure value of 0.05 mb shows a significant loss in signal, but from the intensity versus wavelength charts shown previously, it can be seen that these pressures do produce a good trade off with signal to noise and resolution. For this research study the main pressures of interest are around 1500 mb and one can see that generally a good signal is obtained for these pressures.

6.9.2 Ambient Gas Interference

It has been shown that methane adversely affects the emission intensities of the optical signal by quenching the emissions. Samples were analysed to reveal to what extent the carbon emission line intensity changes due to ambient gaseous conditions and if this result is obscured when carbon is a constituent of the sample itself. Results were obtained at pressures of 1.5 bar with all gaseous mixtures previously studied, namely; CH₄, N₂ and mixtures of 5/95, 6/94 & 7/93 percent methane and nitrogen respectively.

In order to be able to compare signal to noise ratio, baselines of the data were taken. The resulting chart still exhibits the resolution characteristics of the non – baselined data, but signal to noise ratio is accounted for, as shown in figures 6.107 & 6.108.

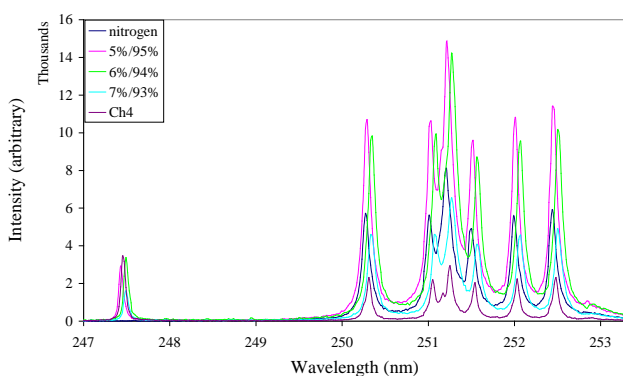


Figure 6.107: Silicon sample, emission signal with different gaseous content at 1.5 bar

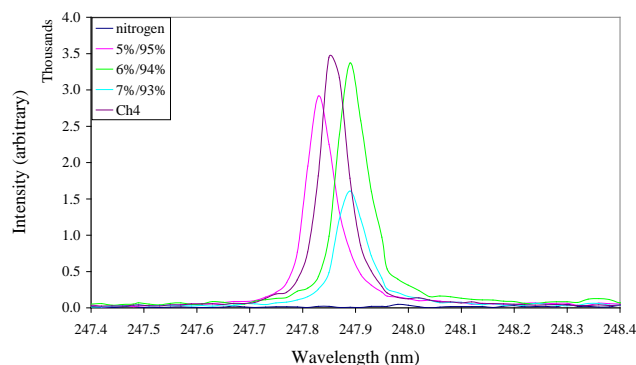


Figure 6.108: Silicon sample, carbon line emission signal with different gaseous content at 1.5 bar

The carbon content was analysed from the baselined data and plotted, shown in figure 6.109. It was then plotted simultaneously with a silicon emission line, figure 6.110, to illustrate how the gaseous environment changes all emission intensities, as discussed in section 6.9.3.

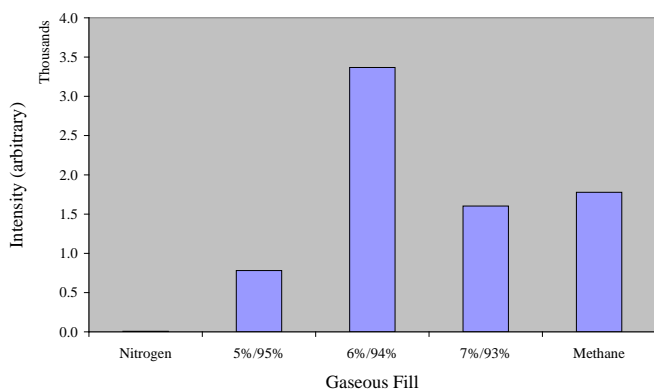


Figure 6.109: Silicon sample, carbon emission intensity for various gas fills

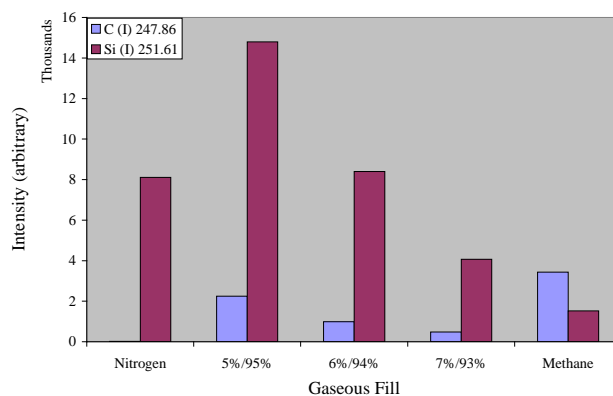


Figure 6.110: Silicon sample, carbon and silicon emission intensities for various gas fills

In figure 6.110 it is quite obvious how the emission intensity is quenched with the increase in methane content in the atmosphere. The assumption is made that silicon content and therefore silicon emission intensity is approximately the same throughout all measurements. Figure 6.110 was normalised to the silicon intensity at each regime thereby enabling elimination of effects due to gaseous quenching. The carbon emission intensity changes with gaseous content can then be observed as shown in figure 6.111.

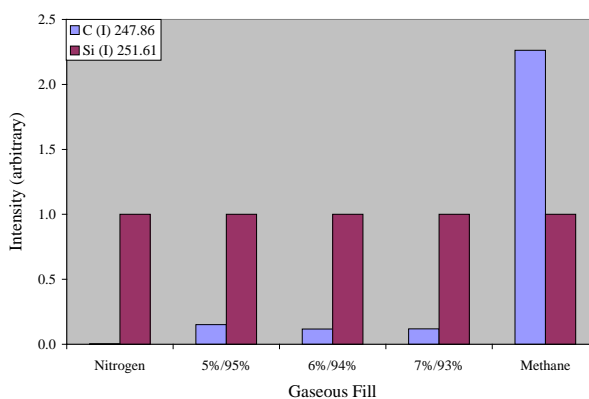


Figure 6.111: Plot of silicon and carbon emission intensities from silicon sample, normalised to silicon.

Once normalised it can clearly be seen that the carbon emission line intensity does in fact change with gaseous content.

These results were cross referenced with sandstone samples to ascertain any affects apparent due to sandstone being a matrix compound.

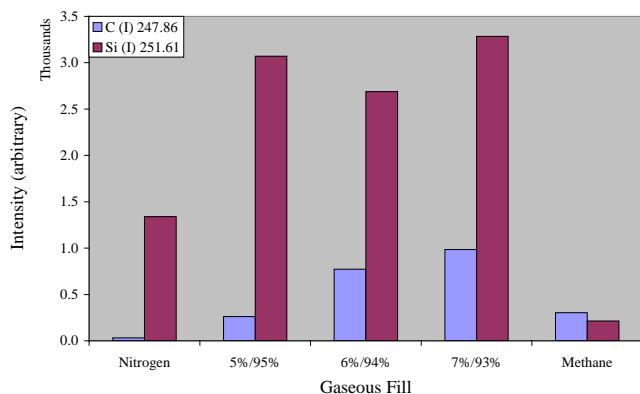


Figure 6.112: Sandstone sample, carbon and silicon emission intensities for various gas fills

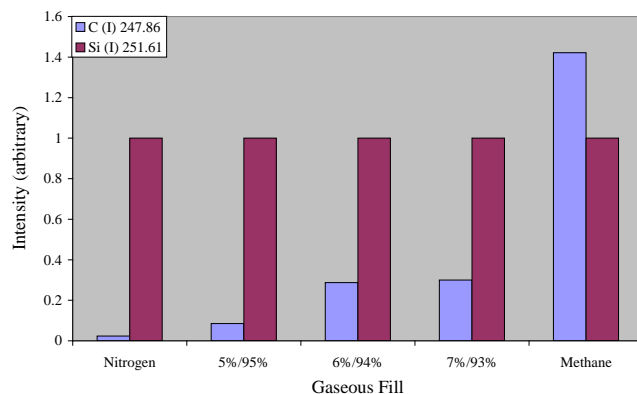


Figure 6.113: Plot of silicon and carbon emission intensities from sandstone sample, normalised to silicon

It is shown that the matrix compound, sandstone, produces a fit closer to expected values, with carbon emission intensity increasing with methane fill percentage.

Finally the results were cross referenced with marble, which contains carbon in its matrix.

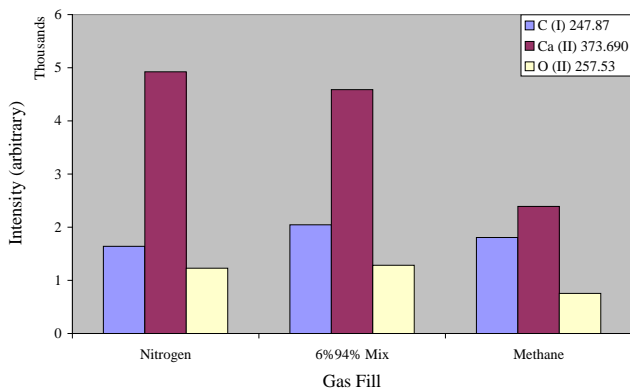


Figure 6.114: Marble sample, carbon, silicon and oxygen emission intensities for various gas fills

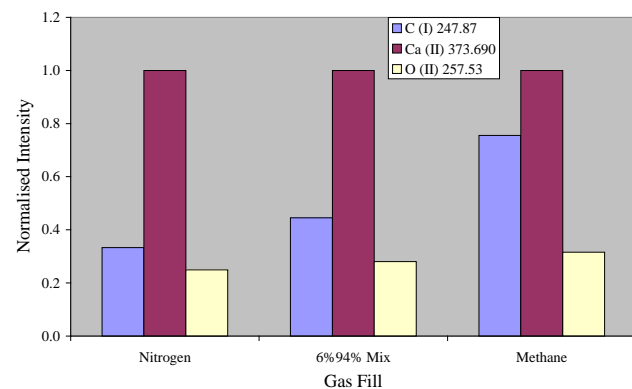


Figure 6.114: Plot of silicon, carbon and oxygen emission intensities from marble sample, normalised to silicon

The charts show good correlation with previous results, the carbon emission intensity is shown to increase with methane content in the atmosphere, as is found with samples not containing carbon.

In the results from the marble sample, an oxygen emission line is also plotted to cross reference the data obtained with an emission line that should remain constant, much like silicon. Although this oxygen emission line is shown to

increase slightly in the normalised chart with increase methane content in the atmosphere, the trend of carbon emission intensity increase far outweighs the trend of oxygen emission intensity increase, suggesting that the methods are valid.

These results suggest that it is possible to analyse atmospheric carbon and therefore methane content with LIBS measurements, even when the samples themselves contain carbon.

6.9.3 Wavelength Variations

As mentioned when evaluating the samples in section 6.3, the main species of the constituent elements of interest can be detected in the wavelength range 245-259 nm. As such the main research study was directed at this range. Although this is the main range of interest, in some samples it is worthwhile to look at other wavelength ranges and ascertain interferences due to pressure and gas influences.

Marble

Marble emission lines were plotted against each gaseous content with varying pressures, illustrated in figure 6.115.

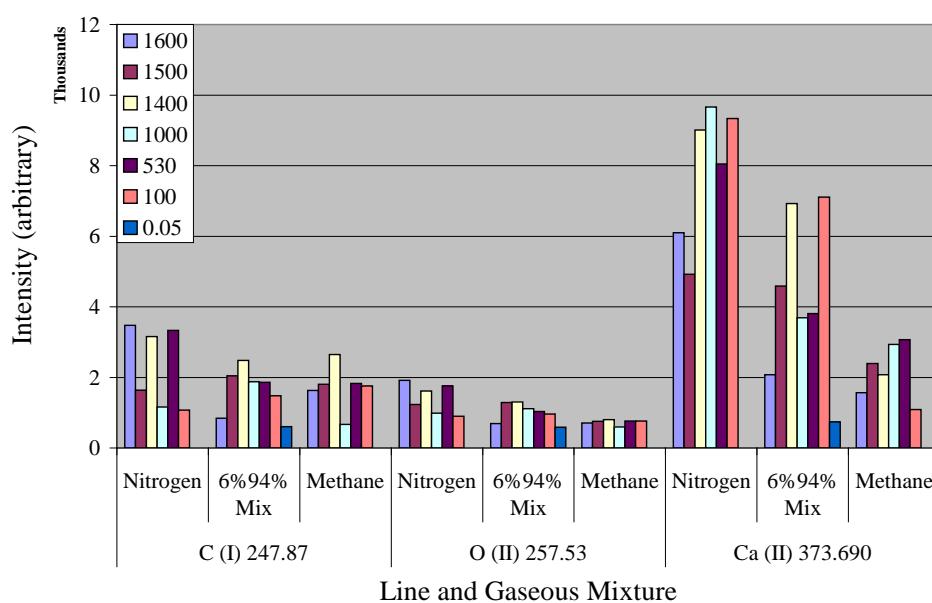


Figure 6.115: Emission intensities of various marble emission lines showing variations due to pressure and gaseous content

A general trend is observed where the emission intensities are reduced with increased methane content in the ambient atmosphere, validating results obtained previously.

It is also shown that the results from the carbon emission line that should be constant from the carbon content in the sample are skewed by the atmospheric content of methane. This suggests that the true changes of emission line intensity with gaseous content must be observed from the calcium and oxygen emission lines, with the highest intensity outputs being at approximately 1400 mb.

Self reversal is evident at a different wavelength region in the marble sample, as shown in figures 6.116 & 6.117.

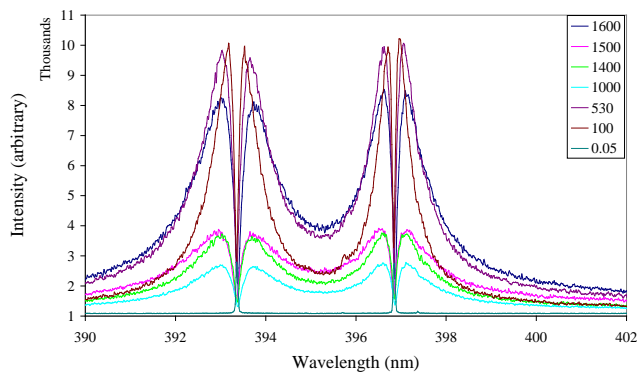


Figure 6.116: Pressure variation of Ca(II) 393.37nm and Ca (II) 396.85nm in marble, with N_2 fill. Showing self reversal due to pressure.

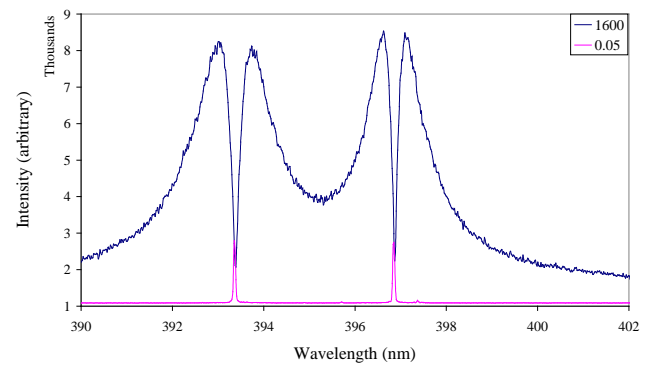


Figure 6.117: Simplified Pressure variation of Ca(II) 393.37nm and Ca (II) 396.85nm in marble, with N_2 fill. Showing self reversal due to pressure.

When plotting pressure versus intensity for the above plots, figure 6.118, it becomes apparent that a difference in emission intensity with respect to pressure is observed when compared with previous intensity versus pressure plots. Reduced loss in emission intensity is evident at lower pressures than has previously been observed, and at higher pressures the emission intensity increases.

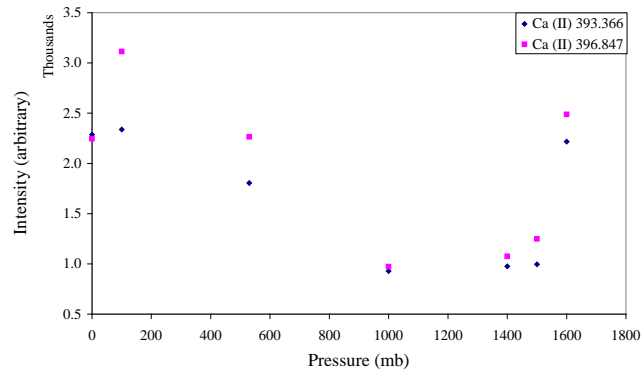


Figure 6.118: Pressure versus intensity variation of calcium emission lines from marble sample, with nitrogen filling gas.

These effects are a result of a loss of emission intensity due to self reversal at the higher pressures and a lack of self-reversal at lower pressures, producing skewed results.

A loss of emission intensity is observed with increased pressure as the self-reversal becomes more prominent, shown by a wider gap at what would be the peak of the emission intensity.

As the pressure is increase further an observed increase in emission intensity is seen. A mechanism that could be affecting this is the large difference in signal to noise ratio at different pressures that is seen in these self-reversal emissions plotted in figure 6.116.

This effect quite obviously can change intensity versus pressure results considerably and as such should always be checked for before commencing analysis.

Slate, Pale and Dark.

Slate samples were analysed using the same techniques as those used previously in order to ascertain any changes to results from different rock types.

Pressure versus intensity charts for slate are quite different from the samples previously analysed. Using nitrogen as a filling gas, the emission lines; Fe (II) 247.95 nm, Fe (I) 275.63 nm, C (I) 247.86 nm, Si (I) 251.43 nm & Si (I) 251.61 nm, were analysed under varying pressures.

The differences in slate emissions could be due to compositional changes. Shown in image 6.119, there are spots on the sample which can be attributed to ferrous reduction spheres^{133,136} that have formed around iron nuclei. Differences such as these throughout the sample could account for the variations in spectral lines emissions, more so than found in non metamorphic rocks such as sandstone.



Figure 6.119: Image of dark slate sample showing ferrous reduction spheres.



Figure 6.120: Image of slate sample showing 'sooting' of the surface from re-deposition at the ablation craters.

Results were taken with the experimental conditions kept constant for all measurements. A new part of the sample was analysed with each new pressure measurement. As a result the new part of the sample may have in fact been different from the last analysis spot and as such may have affected the results. Metamorphic slate is also a foliated rock which may have layers of minerals associated with its structure. One can also see the variations in the pale slate composition with bands of darker slate evident in the composition, shown in figure 6.120.

In this second image, figure 6.120, the re-deposition of matter onto the surface of the sample when ablated in methane environments can be seen. Pure methane fills, and percentages of methane as low as 5%, produce this ‘sooting’ of the sample surface. This phenomenon was also observed on all the other samples.

Within the wavelength range 246–258 nm slate has many emission lines, particularly dark slate. In order to reduce the spectral interferences, the wavelength range 269–282 nm was analysed. This range has strong emissions from iron that are not influenced by other spectral lines. The results are shown in figures 6.121 – 6.124.

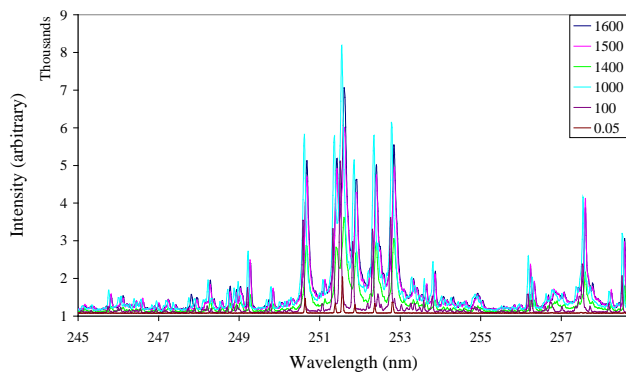


Figure 6.121: Pale slate, emission intensity change with pressure variations, nitrogen filling gas, wavelength centre at 252nm.

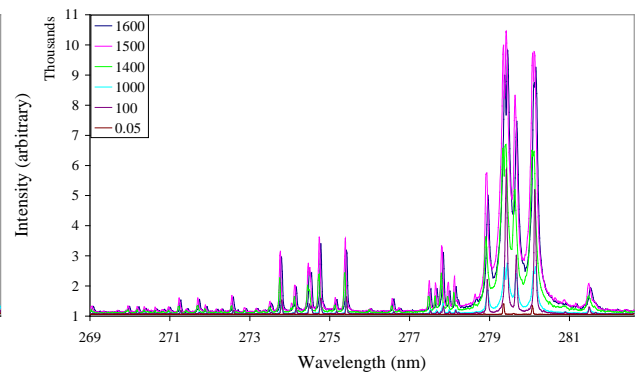


Figure 6.122: Pale slate, emission intensity change with pressure variations, nitrogen filling gas, wavelength centre at 276nm.

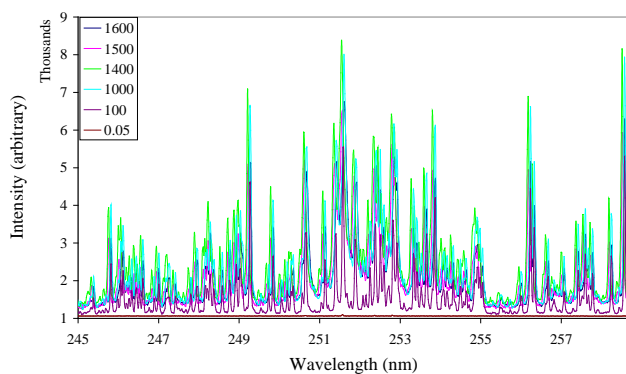


Figure 6.123: Dark slate, emission intensity change with pressure variations, nitrogen filling gas, wavelength centre at 252nm.

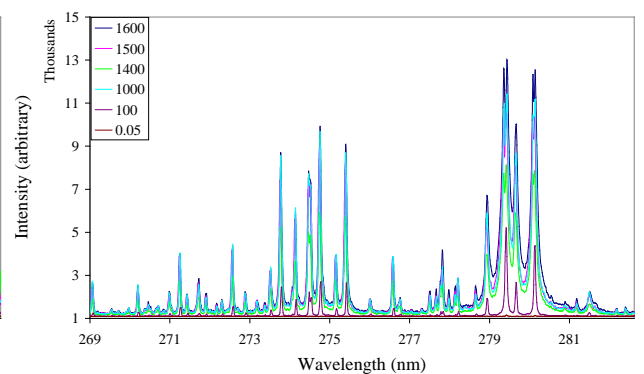


Figure 6.124: Dark slate, emission intensity change with pressure variations, nitrogen filling gas, wavelength centre at 276nm.

Dark slate has the majority of the anomalous results and, as can be seen from the spectral output, dark slate has the most spectral lines and as such the highest possibility of interference from other spectral emissions. Slate by its nature is

composed of many different minerals which are known to change the pigmentation of the material. This would suggest that the darker the slate the more minerals it contains, and as such the more spectral interferences that are possible.

Picking the lines with less interference in the 276 nm region of the spectra and plotting with the originally analysed lines in the 252nm region the differences become apparent, shown in figures 6.125 & 6.126. The width and resolution of the spectra produce the same trends as with other samples, as shown in figures 6.121 – 6.124, but the intensity versus pressure measurements produce a different curve from that of other samples, which can be attributed to the variations of sample composition mentioned.

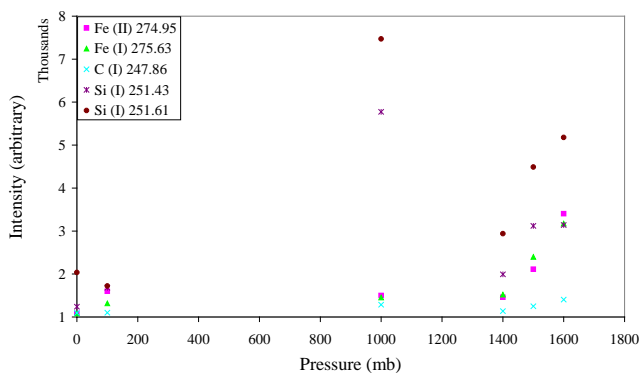


Figure 6.125: Pale slate, pressure versus intensity variations with nitrogen filling gas

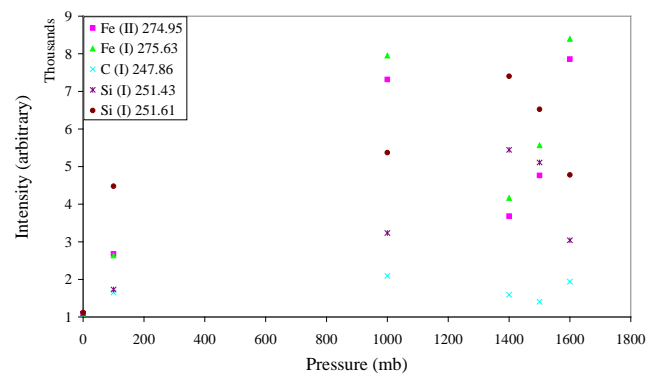


Figure 6.126: Dark slate, pressure versus intensity variations with nitrogen filling gas

As can be seen from the dark slate results, one gets a very different pressure versus intensity plot for the silicon and iron measurements taken near 276 nm, compared with the measurements taken near 252nm, where the spectral interferences are most prominent. At higher wavelengths, where less interference is apparent the pressure versus intensity curve is similar to that of pale slate.

These results show that care needs to be taken when analysing rocks of varying composition. As expected, results are skewed by the changing composition of metamorphic rocks with high mineral content when compared to that of sedimentary rock or pure silicon.

7. Errors, Conclusions and Further Work

7.1 Errors

As mentioned in section 3.13, LIBS analysis brings with it many restrictions on measurement precision. Such limitations vary from pulse to pulse intensity variations of the laser, geometrical and optical parameter changes, integral composition incongruities and matrix effects.

Pulse to pulse variations can produce limitations in ascertaining the incident surface parameters such as surface profile changes, reflectivity changes, re-deposition of plume particulates and possible interference due to dust particles causing laser light scattering.

Along with inherent errors in LIBS measurements, the experimental parameters used in this study introduced their own measurement precision inaccuracy. Inherent errors associated with the use of rock samples, particularly slate, as stated in section 6.9.3, were apparent. These errors arose from the integral composition incongruities. Errors are also associated with the differences in the ambient atmosphere attributes and pressure variations.

These parameters were minimised or eliminated where possible by the use of calibration, integration and ratio analysis where possible. Of course these effects can only be minimised and will always be associated with LIBS results.

Error bars were included where this inclusion did not serve to obscure the results and benefited interpretation. A representative sample of results are shown in figures 7.1 – 7.5:

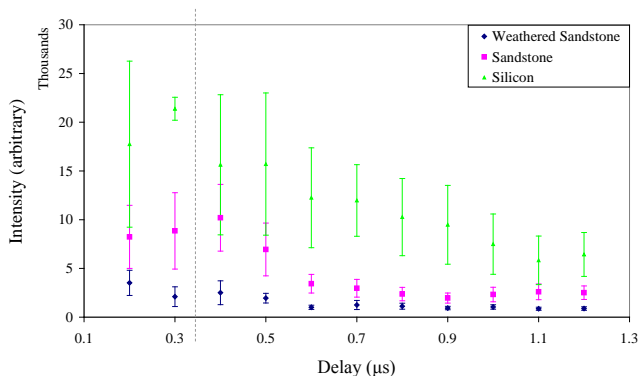


Figure 7.1: One standard deviation of delay versus emission intensity of the silicon emission line at 251.61 nm in different samples. Averaged over 15 shots, 1.5 bar pressure with gas mixture 94%N₂ 6%CH₄

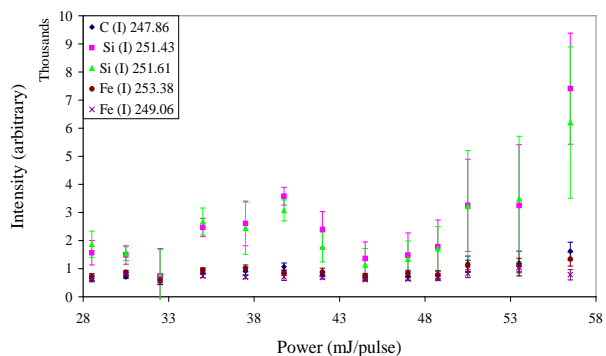


Figure 7.2: One standard deviation of power versus intensity variations on sandstone sample, gas composition: 6%CH₄ 94%N₂

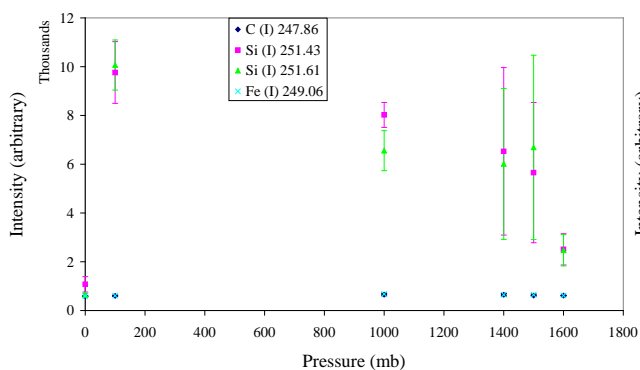


Figure 7.3: One standard deviation of change in intensity with pressure, with N₂ as filling gas, silicon sample.

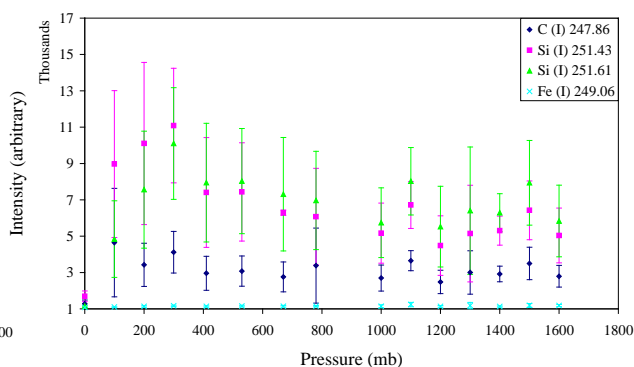


Figure 7.4: One standard deviations of change in intensity with pressure, with 6/94 mix as filling gas, silicon sample

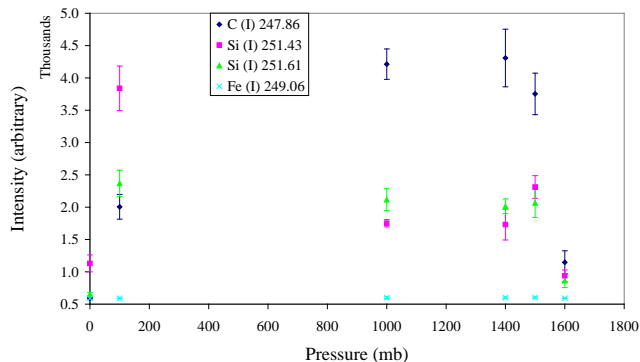


Figure 7.5: One standard deviation of change in intensity with pressure, with CH₄ as filling gas, silicon sample.

Analysis of the errors reveals that in LIBS measurements, generally the higher the intensity of an emission the larger the error associated with that measurement.

7.2 Conclusions

The aim of this study was to fully commission a LIBS system, building in the capability to analyse LIBS in varying pressure and gaseous environments. Once commissioned, work was to be undertaken to ascertain if LIBS analysis was possible in the pressure and gaseous environments of Titan and other possible planetary atmospheres. This benchmarking of LIBS capabilities in such environments has been undertaken and results have been shown to be successful.

The samples chosen provided good references to many different rock types, including that of a pure 'control' sample. In general, it has been shown that LIBS has sufficient sensitivity to monitor the majority of elements of interest to geologists at useful concentrations.

A better understanding has been gained into the effects of ambient atmosphere and pressure on LIBS measurements with the low power requirements that are stringent for space applications.

Temporal considerations in varying pressure regimes were analysed. It was found that delay limitations on signal intensity were apparent, as has been established in previous studies. In these experiments a value of 0.6 μs was found to be sufficient to achieve a reliable emission intensity across the pressure ranges used, showing that it is possible to obtain a satisfactory LIBS emission signal even when the atmospheric pressure in the field application may change, such as in asteroid mineral identification experiments. For field applications where the pressure is known in advance this work could be used to set the temporal delay for optimum emission intensity at that pressure regime.

Optimal gate width values were found for the parameters used in these experiments. It was ascertained that a value of 0.8 μs would allow for high emission intensity without neglecting optimum width and resolution of the spectral lines.

Power limitations are prevalent in space applications, consequently this work studied the effects of laser pulse power on emission intensity. Previous studies

have found that a reproducible plasma can be formed with powers as low as 17 mJ/pulse but that there was a significant difference when changing the pressure in the experiments.

This study found that at 1.5 bar pressure the lower powers of 28.5 – 33 mJ/pulse did produce a reproducible emission signal but with low signal to noise ratio. It was found that between 33 and 51 mJ/pulse there was a plateau region of low gradient where an approximate linear increase in intensity was attained. After 51 mJ/pulse, up to the maximum of 56.5 mJ/pulse, the intensity increase tended towards the exponential.

Any power range used in this study would form a reproducible plasma but the lower laser pulse powers should be avoided where possible to achieve higher signal to noise ratios. If the power available for an application was limited, the small gain in emission intensity achieved over the plateau region may not warrant an increase in power, but for powers in excess of 51 mJ/pulse there is sufficient gain in emission intensity to warrant a small increase in power.

If a field sample possesses a weathered surface, the gain in emission intensity with respect to power is more linear across the power range studied. This is due to a damping of the underlying rock's emission spectra from the contaminants of the surface. If this effect is to be minimised, careful consideration of which emission lines to analyse in the experiment should be undertaken.

The weathered surface of a sandstone sample was analysed to see if LIBS analysis could distinguish between the two interfaces and if this removal was affected by varying the pressure as would be expected. This work followed on from previous work done at atmospheric pressures on thin film CIS deposited on silicon and glass substrates.

It was found that the emission signal from constituents of the weathered surface could be identified and that an approximate depth of weathered coating could be ascertained. Weathered surfaces in field applications will vary in thickness and

constituents dependent on their orientation to the elements and variety of contamination sources.

If an emission line from a constituent of the weathered surface could not be differentiated, for example when there is interference from emission lines arising from the planetary atmosphere, as found in this study with the carbon emission line, useful results were still obtainable from other emission lines such as the increase in emission intensity coming from the underlying rock constituents.

Also analysed was the variation in the number of shots needed to remove the sample in varying pressure and gaseous environments. It was verified that with increasing pressure an increasing number of laser shots was needed to remove the surface coating. This can be attributed to the increased shielding of the sample surface as the pressure is increased and the plasma becomes more confined.

An interesting result was discovered whereby at comparable pressures of 1.5 bar, the higher the methane content in the atmospheric gas the more laser shots were needed to remove the surface coating. This effect can be attributed to the greater number of dissociation products existing in the methane plasma bringing about a greater shielding of the surface when compared to that of nitrogen.

Variations of emission signal with pressure were studied, initially with a view to changes in width and resolution of spectral lines, followed by a study on the emission intensity changes with pressure.

The variations due to pressure, as stated in section 6.9.1, could be due to a change in the size of the plasma and as such the amount of optical signal incident on the optical fibre. The study by Knight¹⁰⁵ observed the same characteristic line pattern as was found in this study, but their study undertook to ascertain if this was in fact due to a misalignment of the optical fibre and it was suggested that this was not the case. As such, with careful selection of the optical fibre alignment, this effect was discounted.

This study found that at vacuum pressures one could achieve a greater resolution and reduction in width of the spectral lines, as would be expected due to the reduced number of line broadening mechanisms coming into effect at these reduced pressures. This increase in resolution was at the expense of emission intensity, but the signal to noise ratio on such measurements was optimal.

Between pressures of 670-1600 mb a steady state was achieved, (except in pure methane fills), whereby the width and resolution of spectral emissions at different pressures was comparable; only a small gain/loss was achieved at the lower/higher pressures. At these values a steady state was also found in emission intensity. These effects can be attributed to a trade off between inverse Bremsstrahlung, optical shielding of the plasma, and self reversal of the emission species.

At the highest pressures analysed in this study, 1600 mb, it was established that with a pure methane fill one achieves a considerable loss in width and resolution, and a reduced emission intensity. This difference, when compared to that of nitrogen or mixed fills, can be accounted for with the higher number of reaction products in the methane plasma quenching the optical signal at the higher pressures by radiationless transitions and shielding of the sample surface from the incident laser pulse.

This quenching of the optical signal was found across the board when analysing emission intensities in methane fills when compared to comparable pressures of nitrogen fills.

Generally a pressure of 250 mb was found to be optimum for emission signal, while still achieving a good width and resolution. This result fits with the study under similar pressure regimes undertaken by Vadilo¹⁰⁷. This effect can be attributed to the optimum balance achieved at these pressures whereby the pressure is low enough to bring about reduced shielding of the sample surface, allowing for a greater ablation of the sample surface, but high enough to allow for sufficient confinement of the plume, producing a high emission signal.

After analysis of the interference of emission lines emitted from the ambient atmosphere and the sample, it was found that it is indeed possible to analyse atmospheric content with LIBS measurements even when there is a difficulty in separating these two media's emission signals. By accounting for the emission from the sample, the quenching from the ambient gases and the elimination of these factors from the results it was found that the proportion of signal due to the gas could be ascertained.

If LIBS analysis is to be undertaken in a variety of space-driven applications careful thought will need to be taken as to the gaseous content of the chosen application, particularly if that gaseous content contains methane as this adversely affects LIBS spectral emission intensities and signal to noise ratios. Titan's atmosphere contains approximately 6% methane which has been shown to give deleterious signal to noise ratios by damping the optical emission signal. Nevertheless it is possible to obtain a viable LIBS signal, so LIBS could be recommended for future space missions to Titan.

Considered selection of the emission lines to be analysed will also need to be undertaken, firstly to ensure no interference is apparent from possible weathered coatings, and secondly due to the phenomenon of some emission lines exhibiting self reversal at the higher pressures.

7.3. Further Work

All results obtained in this study were undertaken at atmospheric temperatures of 259K. The temperature on Titan is 94K, this temperature difference would affect the plasma characteristics considerably by changing parameters such as mean free path, absorption, and ionization stages prevalent in the plasma.

It would be of interest to analyse the salient points of this work in the temperature environment of Titan to ascertain the probable influence on results obtained.

Another area for further work, and of particular interest to this study, would be the analysis of the electron densities and electron temperatures of the plasma under different pressure and gas parameters. This information would prove valuable for the verification of results obtained in this study and the reasons for the possible causes of the optical quenching.

A top hat profile would have allowed for greater accuracy in the depth profiling measurements. Further work in this area could be aided by the use of specialised optics in the beam path of the Nd:YAG laser, or by use of an Excimer laser which has a top hat profile and generally a bigger beam area.

References

- 1 W A. Arnett, (2006 Aug 25). <http://www.nineplanets.org/>
 2 NASA Official: Marilyn Lindstrom, (NASA).
<http://solarsystem.nasa.gov/planets/index.cfm>
 3 European Space Agency, (2007). <http://sci.esa.int/science->
www/area/index.cfm?fareaid=7
 4 (NASA/ JPL operated by the California Institute of Technology).
<http://libs.lanl.gov/Environments-Venus.html>
 5 NASA, (<http://saturn.jpl.nasa.gov/multimedia/images/image->
[details.cfm?imageID=1105](http://saturn.jpl.nasa.gov/multimedia/images/image-))
 6 G. Schwehm, *Status Reports to the Solar System Working Group on*
Planetary Missions and the Planetary Science Archive (15th April 2005).
<http://saturn.jpl.nasa.gov/>
 7 R. Lorenz, *The Glitter of Distant Seas* Science **302**, 403-404 (2003).
 8 F. Sohl, W.D. Sears, and R.D. Lorenz, *Tidal dissipation on Titan* Icarus
115, 278-294 (1995). <http://www.arcetri.astro.it/volt05/lunine3.ppt>.
 9 F. Sohl, H. Hussmann, B. Schwentker, T. Spohn, and R.D. Lorenz,
Interior structure models and tidal Love numbers of Titan J. Geophys.
 Res. **108** (2003).
 10 G. Tobie et al., *Titan's internal structure inferred from a coupled*
thermal-orbital model Icarus **175** (2), 496-502 (2005).
 11 B Arnett, (2000).<http://www.exeter.ac.uk/Mirrors/nineplanets/titan.html>
 12 G. Tobie, O. Grasset, J. I. Lunine, A. Mocquet, and C. Sotin, *Titan's*
internal structure inferred from a coupled thermal-orbital model Icarus
175, 496-502 (2005).
 13 Lorenz R et al., *The sand seas of Titan: Cassini RADAR observations of*
longitudinal dunes Science **312**, 724-727 (2006).
 14 ESA/NASA/Univ. of Arizona, (January 14, 2005).
http://www.nasa.gov/mission_pages/cassini/multimedia/pia07232.html
 15 F Brech and L Cross, *Opticalmicr oemission stimulated by a ruby laser*
 Appl. Spectrosc. **16**, 59 (1962).
 16 J. Debras-Gue'don and N. Liodec, *De l'utilisation du faisceau d'un*
amplificateur a ondes lumineuses par e'mission induite de rayonnement
(laser a´ rubis), comme source e´nerge´tique pour l'excitation des
spectres d'e´mission des e´le´ments C.R. Acad. Sci. **257**, 3336 (1963).
 17 J.E. Geusic, H.M. Marcos, and L.G. Van Uitert, *Laser oscillations in Nd-*
doped yttrium aluminum, yttrium gallium, and gadolinium garnets, App.
 Phys. Lett. **4** (1964).
 18 P.D. Maker, R.W. Terhune, and C.M. Savage; *Vol. 2*, edited by Paris.
 Proceedings of Third International Conference on Quantum Electronics
 (Columbia University Press, New York, Vol. 2, 1559 1964), p. 1559.
 19 L. Moenke and Moenke-Blankenburg, *Laser Micro-Spectrochemical*
Analysis, Chapter 2 (Crane, Russak & Co, New York, 1973., 1973)
 20 Moenke-Blankenburg, *Laser Microanalysis* (Wiley, New York, 1989)
 21 T.R. Loree and L. J. Radziemski, *Laser-induced breakdown*
spectroscopy: time integrated applications. **1**, 271-280 (1981).

- 22 L. J. Radziemski and T. R. Loree, *Laser-induced breakdown spectroscopy: time-resolved spectrochemical applications*. Plasma chem.. plasma proc **1**, 281-293 (1981).
- 23 L. J. Radziemski, D. A Cremers, and T.R. Loree, *Detection of beryllium by laser-induced breakdown spectrometry of aerosols* Anal. Chem **55**, 1246-1251 (1983a).
- 24 L. J. Radziemski, T. R. Loree, D. A. Cremers, and N. M. Hoffman, *Time-resolved Laser-induced breakdown spectrometry of aerosols*. Anal. Chem **55**, 1246-1251 (1983b).
- 25 D. A. Cremers, L. J. Radziemski, and T. R. Loree, *Spectrochemical analysis of liquids using the laser spark* Appl. Spectrosc. **38**, 721-726 (1984).
- 26 D. A. Cremers and L. J Radziemski, *Detection of chlorine and fluorine in air by laser-induced breakdown spectrometry* Anal. Chem **55**, 1252-1256 (1983).
- 27 D. A. Cremers and L. J. Radziemski, *Laser plasmas for chemical analysis* Ch. 5 (Marcel Dekker. New York, 1987)
- 28 D. A Cremers, *The analysis of metals at a distance using Laser-induced breakdown spectroscopy*. Appl. Spectrosc. **41**, 572-578 (1987).
- 29 David A. Cremers and Leon J. Radziemski, *Laser-Induced Plasmas and Applications* (CRC Press, Technology & Industrial 1989)
- 30 U Panne, C. Haisch, H. Fink, and I. Radivojevic, *Neue Entwicklungen in der laserinduzierten plasmaspektroskopie (LIPS)* (Institute of Hydrochemistry, Technical University Munich, Germany, 2001)
- 31 D.A. Cremers and L.J. Radziemski, *Laser plasmas for chemical analysis*, Ch. 5 (MarcelDekker, New York, 1987)
- 32 L J. Radziemski, *From LASER to LIBS, the path of technology development* Spectrochimica Acta Part B **57**, 1109–1113 (2002).
- 33 E. Tognoni, V. Palleschi, M. Corsi, and G. Cristoforetti, *Quantitative micro-analysis by laser-induced breakdown spectroscopy: a review of the experimental approaches* Spectrochimica Acta Part B **57** 1115–1130 (2002).
- 34 David A. Cremers and Leon J. Radziemski, *Handbook of Laser-Induced Breakdown Spectroscopy* (John Wiley & Sons Ltd, 2006)
- 35 *LIBS reveals Minoan dagger history*, (Optics.org, IOP Publishing Limited,, 30 May 2002). <http://optics.org/articles/news/8/5/32/1>
- 36 *Two laser techniques combined to probe artwork* (Optics.org, IOP Publishing Limited,, 26 May 2000). <http://optics.org/articles/news/6/5/19/1>
- 37 Shelley Thompson, *Los Alamos News Letter; Vol. 3* (April 18, 2002). <http://www.lanl.gov/news/newsletter/041802.pdf>
- 38 J Lademann, H Weigmann, H Schäfer, G Müller, and W Sterry, *Investigation of the stability of coated titanium microparticles used in sunscreens*, Skin Pharmacology And Applied Skin Physiology **13**, 258-264 (September - October 2000).
- 39 O Samek, H H Telle, and D C S Beddows, *Laser-induced breakdown spectroscopy: a tool for real-time, in vitro and in vivo identification of carious teeth* BMC Oral Health **1:1** (2001). <http://www.biomedcentral.com/1472-6831/1/1/>

- 40 A.I. Whitehouse, J. Young, I.M. Botheroyd, S. Lawson, C.P. Evans, and
J. Wright, *Remote material analysis of nuclear power station steam
generator tubes by laser-induced breakdown spectroscopy*
Spectrochimica Acta, Part B **56**, 821-830 (2001).
- 41 A I. Whitehouse, *Spectroscopy Europe*; **Vol. 18** (2006), p. 14-21.
[http://www.appliedphotonics.co.uk/PDFs/Spectroscopy%20Europe%20ar
ticle.pdf](http://www.appliedphotonics.co.uk/PDFs/Spectroscopy%20Europe%20article.pdf)
- 42 B Salle, D A Cremers, S Maurice, and R C Wiens, *Laser-induced
breakdown spectroscopy for space exploration applications: Influence of
the ambient pressure on the calibration curves prepared from soil and
clay samples* Spectrochimica Acta Part B **60**, 479-490 (2005).
- 43 Z A Arp, D A. Cremers, R D. Harrisa, D M. Oschwaldc, G R. Parker Jr,
and D M. Wayne, *Feasibility of generating a useful laser-induced
breakdown spectroscopy plasma on rocks at high pressure: preliminary
study for a Venus mission* Spectrochimica Acta Part B **59**, 987– 999
(2004).
- 44 F. Colao, R. Fantonia, V. Lazica, A. Paolina, F. Fabbria, G.G. Orib, L.
Marinangelib, and A. Balivab, *Investigation of LIBS feasibility for in situ
planetary exploration: An analysis on Martian rock analogues* Planetary
and Space Science **52**, 117-123 (2003).
- 45 F Colao, R Fantoni, V Lazic, and A Paolini, *LIBS application for
analyses of martian crust analogues: Search for the optimal experimental
parameters in air and CO₂ atmosphere* Applied Physics A **79**, 143-152
(2004).
- 46 Jeff Hecht, *Understanding Lasers*, 2 Sub edition ed. (Wiley-IEEE Press
1993)
- 47 W. Koechner, *Solid-State Laser Engineering*, 1 (Springer, 5th edition,
1999)
- 48 J Wilson and J.B.F Hawkes, *Lasers: Principles and Applications* Prentice
Hall International Series in Optoelectronics (1987).
- 49 D. B. Chrisey and G. K. Hubler, *Pulsed Laser Deposition of Thin Films*
(Wiley-Interscience)
- 50 Srinivasan and V. Mayne-Banton, *Self-Developing Photoetching of
Poly(ethylene terephthalate) Films by Far-Ultraviolet Excimer Laser
Radiation* Appl. Phys. Lett. **41**, 576-578 (1982).
<http://www.research.ibm.com/journal/rd/411/doany.html>
- 51 J. C. Miller, *Laser Ablation*, 28 (Springer-Verlag, 1994)
- 52 J. C Miller and R. F Haglund, *Laser Ablation and Desorption*, 30
(Academic Press, 1998)
- 53 C Friedrich, *Laser Ablation* (1998).
<http://www.me.mtu.edu/~microweb/chap4/ch4-2.htm>
- 54 N. Rykalin, A. Uglov, and A. Kokora, *Laser Machining and Welding*
(Mir Publishers, Moscow)
- 55 Alexandre F. Semerok, Beatrice Salle, Jean-Luc Lacour, and J.-F.
Wagner, *Femtosecond, picosecond, and nanosecond laser microablation:
laser plasma and crater investigation* ECLIM 2000: 26th European
Conference on Laser Interaction with Matter, CEA-Saclay (France)
(Proceedings of SPIE -- Volume 4424)

- 56 S. I. Anisimov, B. I. Dmitrienko, and L. V. Leskov, *Effect of Reflectivity of Surface on Vaporization of Metals by High-Intensity Light Flux* *Fizika I khimiya obrabotki materialov* **4**, 10-14 (1972).
- 57 L. Moenke-Blankenburg, *Laser Micro Analysis*, 25 (1989).
- 58 R. A. Multari, R. E. Foster, D. A. Cremers, and M. J. Ferris, *The effects of sampling geometry on elemental emissions in LIBS* *Appl. Spectrosc.* **50**, 1483-1499 (1996).
- 59 J. M. Vadillo, J. M. Fernandez-Romero, C. Rodriguez, and J. J. Laserna, *Effect of plasma shielding on laser ablation rate of pure metals at reduced pressure* *Surf. Interface Anal* **27**, 1009-1015 (1999).
- 60 A. Semerok, B. Salle, J. F. Wagner, and G. Petite, *Femtosecond, picosecond, and nanosecond laser microablation: laser plasma and crater investigation* *Laser Part. Beams* **20**, 67-72 (2002).
- 61 Martin von Allmen, *Laser-beam interactions with materials*, 2 (Springer-Verlag, 1987)
- 62 John Robertson and Robin S. Marjoribanks, *Multiphoton Absorption and the Evolution of Green Plants* *Canadian Undergraduate Physics Journal* **Volume 1** (2002).
- 63 Davidson, *Multi-Photon Absorption and Ionization* (<http://webphysics.davidson.edu/alumni/jimn/Final/Pages/FinalMPA.htm>)
- 64 N. Kroll and K.M. Watson, *Theoretical Study of Ionization of Air by Intense Laser Pulses* *Phys. Rev.* **5**, 1883 - 1905 (1972).
- 65 Y. V. Skorovab and H. Rickmanc, *Gas Flow and dust acceleration in a cometary Knudsen layer* *Planetary and Space Science* **47** 935-949 (1999).
- 66 K. Aoki, C. Bardos, and S. Takata, *Knudsen Layer for Gas Mixtures* *Journal of Statistical Physics* **Volume 112, Numbers 3-4**, pp. 629-655(27) (August 2003).
- 67 S. I. Anisimov, Y.A. Imas, G.S. Romanov, and Y.U. Khodyko, *Effects of High-Power Radiation on metals* (1970).
- 68 David J. Griffiths, *Introduction to Electrodynamics*, 3rd edition, pages 463–464.
- 69 S. Ichimaru, *Basic Principles of Plasmas Physics: A Statistical Approach*, p. 228
- 70 *Laser Induced Plasma Spectroscopy*, (Institute of Hydrochemistry, Technische Universitat Munchen.http://www.ws.chemie.tu-muenchen.de/laser/LIPS_set_Start.htm)
- 71 D. Breitling, et al., *Shadowgraphic and interferometric investigations on Nd:YAG laser-induced vapor/plasma plumes for different processing wavelengths* *Appl. Phys. A*, 1999 69, S505-S508 (1999).
- 72 Y. P. Raizer, *Subsonic Propagation Of A Light Spark And Threshold Conditions For Maintenance Of A Plasma By Radiation* *Sov. Phys. JETP* **31**, 1148-1154 (1970).
- 73 R.G. Root, *Laser-induced Plasmas and Applications, Modeling of post-breakdown phenomena* (Marcel Dekker, New York, 1989)
- 74 A. Bogaerts, Z. Chen, R. Gijbels, and A. Vertes, *Laser ablation for analytical sampling: what can we learn from modelling?* *Spectrochim Acta Part B* **58**, 1867-1893 (2003).
- 75 R. E. Russo, X. L. Mao, H. C. Liu, J. Gonzalez, and S. S. Mao, *Laser ablation in analytical chemistry – a review* *Talanta* **57**, 425-451 (2002).

- 76 J.A. Aguilera and C. Aragon, *Characterization of a laser-induced plasma by spatially resolved spectroscopy of neutral atom and ion emissions. Comparison of local and spatially integrated measurements.* Spectrochimica Acta Part B **59**, 1861– 1876 (2004).
- 77 R. F. Wood, K. R. Chen, * J. N. Leboeuf, A. A. Puretzky, and D. B. Geohegan, *Dynamics of Plume Propagation and Splitting during Pulsed-Laser Ablation* physical review letters 25 august 1997 **79** (1997).
- 78 D.I. Iriarte, J.A. Pomarico, and H.O. Di Rocco*. *Non-LTE and opticaldepth effects to be considered in quantitative spectroscopy of cold and dense plasmas.* Spectrochimica Acta Part B **58**, 1945–1957 (2003).
- 79 M Capitellia, U F Capitellie, and A Eletskiid, *Non-equilibrium and equilibrium problems in laser-induced plasmas.* Spectrochimica Acta Part B **55**, 559-574 (2000).
- 80 L.A. Gizzi, C.A. Cecchetti, M. Galimberti, A. Giulietti, D. Giulietti, L. Labate, y S. Laville, and P. Tomassini, *Transient ionization in plasmas produced by point-like irradiation of solid Al targets.* Physics of Plasmas **10** (2003).
- 81 Valery Bulatov, Rivie Krasniker, and Israel Schechter, *Environmental Analysis by Laser Induced Breakdown Spectroscopy*, www.technion.ac.il/~chr21bv/Libs.PPT
- 82 Richard E. Russo, Xianglei Mao, and Samuel S. Mao, *The Physics of Laser Ablation in Microchemical Analysis* volume **74**, pp 70 A-77 (February 1, 2002).
- 83 X. L Mao, A. C Ciocan, and R. E Russo, *Preferential Vaporization during Laser Ablation Inductively Coupled Plasma Atomic Emission Spectroscopy* Appl. Spectrosc. **52**, , 913-918 (1998).
- 84 D Figg and M. S Kahr, *Elemental Fractionation of Glass Using Laser Ablation Inductively Coupled Plasma Mass Spectrometry* Appl. Spectrosc. **51**, 1185-1192 (1997).
- 85 T. E. Jeffries, S. E. Jackson, and H. P. Longerich, *J. Anal. At. Spectrom* **13**, 935 (1998).
- 86 S. M. Eggins, L. P. J. Kinsley, and J. M. G Shelley, *Appl. Surf. Sci* **129**, 278–286 (1998).
- 87 D.; Günther, Frischknecht, R.; Heinrich, and H. J. C. A.; Kahlert, J. *Anal. At. Spectrom.* **12**, 939 (1997).
- 88 D.; Günther and C. A. Heinrich, *J. Anal. At. Spectrom.* **14**, 1369 (1999).
- 89 R K. Singh and J. Narayan, *Pulsed-laser evaporation technique for deposition of thin films: Physics and theoretical model* Phys. Rev. B **41**, 8843 - 8859 (1990).
- 90 J. F. Ready, *Effects of High-power Laser Radiation* (Academic Press, New York, 1971)
- 91 A. Bogaerts, Z. Chen, R. Bijbels, and A. Vertes, *Laser ablation for analytical sampling: what can we learn from modeling?* Spectrochim. Acta Part B **58**, 1867-1893. (2003).
- 92 G. Peach, *Theory of the pressure broadening and shift of spectral lines* Advances in Physics **30**, 367 – 474 (1981).
- 93 L. D. Landau and E. M. Lifshitz, *Electrodynamics of Continuous Media*, (Pergamon, Oxford, 1960)
- 94 Lennard-Jones and J. E. Cohesion, *Proceedings of the Physical Society* **43**, 461-482 (1931).

- 95 B. H. Armstrong, *Spectrum Line Profiles: The Voigt Function*. **7**, 61-88
(1967).
- 96 D. Salzmann, *Atomic Physics in Hot Plasmas* (Oxford Univ. Press, New
York and Oxford, 1998)
- 97 H. R. Griem, *Principles of Plasma Spectroscopy* (Cambridge University
Press, New York. , 1997)
- 98 I.I. Sobelman, L.A. Vainshtein, and E.A. Yukov, *Excitation of Atoms and
Broadening of Spectral Lines* (Springer, Berlin, 1981)
- 99 Dr. J. E. Ross, *The Saha-Boltzmann equation* (2004).
<http://www.physics.uq.edu.au/people/ross/phys2080/ael/saha.htm>
- 100 D.I. Iriarte, J.A. Pomarico, and H.O. Di Rocco*, *Non-LTE and optical
depth effects to be considered in quantitative spectroscopy of cold and
dense plasmas* Spectrochimica Acta Part B 58 (2003) 1945–1957 (2003).
- 101 Anne Thorne, P, *Spectrophysics*, 2nd ed. (Chapman and Hall Press, 1988)
- 102 Robert Eisberg and Robert Resnick, *Quantum Physics of atoms,
molecules, solids, nuclei and particles*, 2nd ed. (1985)
- 103 Robert B Leighton, *Principles of Modern Physics* (McGraw-Hill,
1959).<http://hyperphysics.phy-astr.gsu.edu/hbase/atomic/atstruct.html#c1>
- 104 Leon Radziemski, David A. Cremers, Katharine Benelli, Cynthia Khoo,
and Ronny D. Harris, *Use of the vacuum ultraviolet spectral region for
laser-induced breakdown spectroscopy-based Martian geology and
exploration* Spectrochimica Acta Part B 60 (2005) 237– 248 (2004).
- 105 A.K. Knight, N.L. Scherbarth, D.A. Cremers, and M.J. Ferris,
*Characterization of laser-induced breakdown spectroscopy (LIBS) for
application to space exploration* Appl. Spectrosc. **54**, 331– 340 (2000).
- 106 Zane A. Arp, David A. Cremers, Ronny D. Harris, David M. Oswald,
Gary R. Parker Jr., and David M. Wayne, *Feasibility of generating a
useful laser-induced breakdown spectroscopy plasma on rocks at high
pressure: preliminary study for a Venus mission*, Spectrochimica Acta
Part B 59, 987– 999 (2004).
- 107 J.M. Vadillo, J.M. Fernandez Romero, C. Rodriguez, and J.J. Laserna,
*Effect of plasma shielding on laser ablation rate of pure metals at
reduced pressure*, Surf. Interface Anal. **27**, 1009– 1015 (1999).
- 108 R.D. Harris, D.A. Cremers, C. Khoo, and K. Benelli, *LIBS-Based
Detection Of Geological Samples At Low Pressures (<0.0001 Torr) For
Moon And Asteroid Exploration* Lunar and Planetary Science **XXXVI**
(2005).
- 109 S Iwasaki and M Horio, *Carbon Content Detection in High Temperature
and High Pressure Fields Using LIBS*, (2000)
- 110 Z. A. Arp, D. A. Cremers, and R.C. Wiens, *Preliminary Study Of Laser-
Induced Breakdown Spectroscopy (LIBS) For A Venus Mission* Lunar and
Planetary Science XXXV (2004).
- 111 M Lawrence-Snyder, S. M Angel, and W F. Pearman, *LIBS in Extreme
Environments: The Feasibility of Sequential-Pulse LIBS for Deep-Ocean
Analysis*, The University of South Carolina, 2006
- 112 J.J. O'Brien, *Methane Absorption Coefficients in the 750-940 nm region
derived from Intracavity Laser Absorption Spectral Measurements*, DPS
34th Meeting, Session 39. Laboratory Investigations, October 2002

- 113 V. Teifel and G. Kharitonova, *The seasonal trend of the methane*
absorption in Southern hemisphere of Saturn Geophysical Research
Abstracts **9** (2007).
- 114 O'Brien and Cao, *methane absorption bands* JQRST **75** 323-350
(2002).<http://vpl.ipac.caltech.edu/spectra/ch4obrienvisible.htm>
- 115 J Näränen, *The Atmosphere of Titan* Finnish Summer School on Planetary
Sciences (2002).<http://www.astro.helsinki.fi/~naranen/titan/titan.html>
- 116 J Clark, *Chem Guide*
(2004).<http://www.chemguide.co.uk/physical/catalysis/hydrate.html>
- 117 P. K. Sharma, D. Rapp, and N. K. Rahotgi, *Methane Pyrolysis And*
Disposing Off Resulting Carbon ISRU III Technical Interchange
Meeting <http://www.lpi.usra.edu/meetings/ISRU-III-99/pdf/8008.pdf>
- 118 G.S. Lane and E.E. Wolf, *Methane utilization by oxidative coupling. A*
study of reactions in the gas phase during the cofeeding of methane and
oxygen Journal of Catalysis **113**, 144-163 (1988).
- 119 S.C.P. Fraga, M.M. de Lima, E.P. Ferreira Marques, R. Policarpo,
A.J.P.L. Alves, M.A.F. Salet, and M. Leite, *Emission spectra of gaseous*
avalanches and their time structure Nuclear Science Symposium and
Medical Imaging Conference **vol.1**, 209-211 (1992).
- 120 Eugene Hecht, *Optics*, 4th ed. (Addison Wesley, 2002)
- 121 *Princeton Instruments PI-MAX Camera User Manual*, **4411-0069**,
Version 2.A (Oct 18 1999.).
- 122 *WinSpec/32 Version: 2.5.16.1* (2000-2003).
- 123 Lambda Research Corporation, *Sinclair Optics OSLO software*.
<http://www.sinopt.com/>
- 124 Interactive Image Technologies Ltd., *Electronics Workbench, V 5.1* ©
1992-1996,
- 125 *Surelite Operation Manual*, Rev.d 9/98
- 126 Yu. Ralchenko, F.-C. Jou, D.E. Kelleher, A.E. Kramida, A. Musgrove, J.
Reader, W.L. Wiese, and K. Olsen, *NIST Atomic Spectra Database*
version 3.1.2, (2007), <http://physics.nist.gov/asd3>
- 127 Address
- 128 S Hurst and M Clegg, *Salford University Workshop* (2003).
- 129 *Acton Research Spectroscopy Accessories; Vol. A0* (Roper Scientific,
Acton Research, 2002). www.roperscientific.com
- 130 D. G. Papazoglou, V. Papadakis, and D. Anglos, *J. Anal. At. Spectrom*
19 (2004).
- 131 D. Romero and J.J. Laserna, *Anal. Chem* **69** (1997).
- 132 R D Pilkington, J Hisek, N Lucas, A E Hill, J S Cowpe, and J S Astin,
Comparative study of laser induced breakdown spectroscopy and
secondary ion mass spectrometry applied to dc magnetron sputtered as-
grown copper indium diselenide (CIS), Photon06
- 133 Dr Robert Muir Wood, *On the rocks, a geology of Britain* (British
Broadcasting Corporation, 1978)
- 134 (Department of Geology and Environmental Science, James Madison
University, Harrisonburg, Virginia 22807,
2006).<http://csmres.jmu.edu/geollab/Fichter/MetaRx/Rocks/slate1.html>
- 135 N M Shaikh, B Rashid, S Hafeez, Y Jamil, and M A Baig, *Measurement*
of electron density and temperature of a laser-induced zinc plasma J.
Phys. D: Appl. Phys. **39**, 1384-1391 (2006).

- ¹³⁶ Harvey Blatt and Robert J. Tracy, *Petrology: Igneous, Sedimentary, and Metamorphic*, 2nd ed, 359-360 (1996).
- ¹³⁷ *Acton Research Spectroscopy Datasheet*, (Roper Scientific, Acton Research, 2002). www.roperscientific.com

Appendices

Appendix A:

Comparative study of laser induced breakdown spectroscopy and secondary ion mass spectrometry applied to dc magnetron sputtered as-grown copper indium diselenide (CIS)

R D Pilkington, J Hisek, N Lucas, A E Hill, J S Cowpe and J S Astin.

Institute for Materials Research, University of Salford, Salford, UK

Abstract

The University of Salford has led the way in the fundamental research that has underpinned the development of thin film copper indium diselenide (CIS) based photovoltaics. These devices have demonstrated exceptional energy conversion efficiencies (>19%) and a high tolerance to radiation damage and are thus leading researchers towards the 20% efficiency barrier. Conventional CIS thin film growth processes require a post-selenisation step to incorporate Se into the as-grown material. This helps to achieve stoichiometry, improves the crystallinity, controls the defect structure and also can be used to convert the semiconductor type. This paper will report the use of pulsed dc magnetron sputtering from a CIS powder target. This approach has resulted in as-grown stoichiometric thin films consisting of pinhole free, densely packed grains. An important consideration in the thin film growth of complex materials is that stoichiometry is maintained throughout the film. Conventionally, secondary ion mass spectrometry (SIMS) is used to depth profile thin films but it has been reported that laser induced breakdown spectroscopy (LIBS) can also be used. We will report the initial results comparing and contrasting these two techniques and show that LIBS can produce meaningful data.

Keywords: LIBS, CIS, depth profiling, SIMS, copper indium diselenide, photovoltaic

1. Introduction

In the early 1970's the Salford photonics group was the first in the world to publish data on CIS [1,2]. We have continued to enjoy several first's in this area which has ultimately led to the development of current world-record CIS solar cells

To date there is still a great performance discrepancy between laboratory produced CuInSe_2 / Cu(In,Ga)Se_2 (CIS/CIGS) cells and commercially produced modules [3-5] with commercial cells having an efficiency of approximately 12% and laboratory cells regularly nearing 20%. It is the aim of continued research to find simplified processes that will allow the deposition of stoichiometric CIS/CIGS thin films using a single stage process capable of producing large area device quality material.

Sputtering has been repeatedly used for manufacturing CIS/CIGS and related materials. In general there are two approaches: sputtering from a compound target using rf power [6-9] or sputtering from elemental or alloy metal targets followed by a selenisation process (Se-vapour, or H_2Se) [10,11].

The incorporation of a magnetron improves the plasma stability and allows the use of lower process pressures, resulting in decreased scattering of the sputtered particles. Due to increased ion bombardment, the thin films become denser and more uniform. The relatively new technique of Pulsed dc Magnetron Sputtering PDMS has transformed the deposition of insulating materials. Pulsing the supplied dc voltage suppresses destabilising discharges and removes many of the target preparation problems [8,12,13].

2. Pulsed dc Magnetron Sputtering (PDMS)

PDMS is widely recognised as a new technology for the deposition of dielectric materials [12]. The magnetron discharge is pulsed in the mid frequency range 50 – 350 kHz and this alleviates the main problem associated with continuous dc reactive sputtering of such materials, namely arc events at the target. The correct selection of the dc pulse parameters i.e. frequency, duty and reverse voltage, results in extended arc-free operating conditions, even during the deposition of highly insulating materials [14]. The pulsed sputtering technique is now commercially exploited in many applications, including glass coatings with low emissivity, packaging barrier layers, flat panel displays etc. The inherent process stability during depositions results in reduced structural defects, improved film properties and enhanced deposition rates [15].

The application of PDMS for the deposition of complex photovoltaic materials (such as copper indium/gallium diselenide) from a powder target is a new endeavour. There have been a number of studies related to standard dc magnetron sputtering of copper indium/gallium diselenide from elemental sources, but these systems have been complex in their nature and the produced films required post deposition selenisation [10,11].

3. Experimental

A single unbalanced magnetron source, with an approximate target diameter of 180 mm was used. The system is described in detail elsewhere [13]. CIS powder, crushed from polycrystalline ingots [1,17] was separated to a grain size ranging from 0.05 mm to 1 mm and slightly tamped into the target plate to a thickness of around 3 mm. Its composition as determined by EDX analysis showed that it was non-stoichiometric, having a surplus of Copper and Selenium and hence lacking Indium. The average composition was found to be 29% Cu, 17% In and 54% Se with an estimated error of $\pm 4\%$.

The magnetron was driven by an Advanced Energy pulsed dc power supply, that operated to a maximum frequency of 350 kHz with an adjustable duty cycle between 50 to 100%. A target-substrate separation of 150 mm was chosen for these initial runs. The pulsing frequency was varied between 100 to 350 kHz, and the duty cycle was between 50 and 80%. Cleaned glass microscope slides were chosen as the substrate.

4. Results and discussion

Using PDMS resulted in a very stable plasma without the occurrence of any arcing. Process conditions such as argon pressure, target-substrate-distance and input power combined with pulsing frequency, duty cycle and the substrate biasing were investigated.

A representative selection of results for films grown under a range of conditions is given below in table I. In general it was found that the final composition remained close to stoichiometric and was largely insensitive to the process parameters.

Table 1. Example deposition conditions including the resulting composition obtained by EDX.

Sample No	Frequency kHz	Bias	Cu %	In %	Se %
1.8	350	n.a.	23.5	24.8	51.7
1.16	170	rf	23.6	23.9	52.5
1.22	130	rf	24.8	24.1	51.1
1.30	170	p. dc	23.5	25.1	51.4
1.35	130	p. dc	24.5	24.9	50.6
1.42	220	rf	24.1	25.1	50.8

It was also noted that the composition of the target powder remained largely unchanged from run to run.

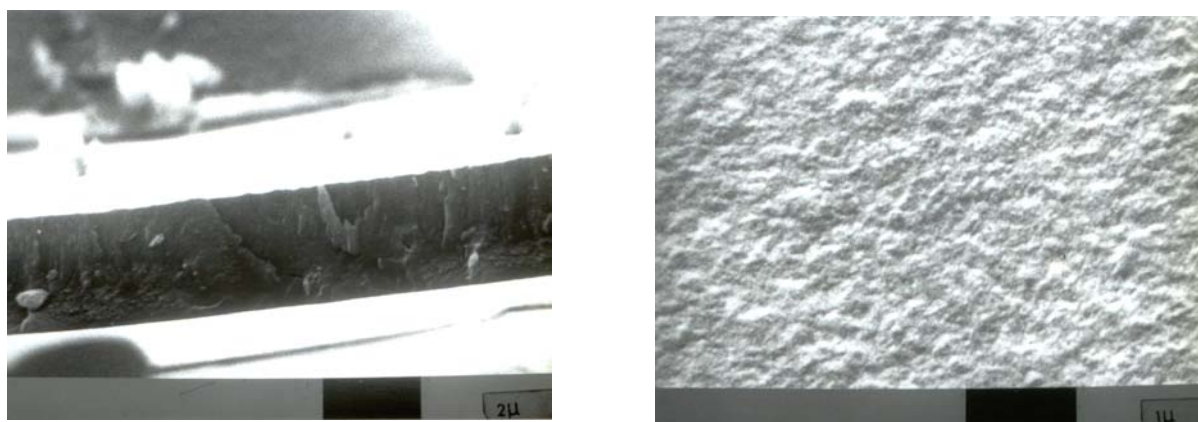


Figure 1 SEM images of as-grown 2 μ m thick CIS films

The major result of this study is that stoichiometric CIS thin films could be manufactured from a clearly non-stoichiometric powder target. The reasons for this are unclear, however this may be a feature of CIS when it is dc sputtered from a powder target.

The sputtering yields of Cu, In and Se are quite different from each other and it could be assumed that after an initial period an equilibrium state should be achieved, where the composition of the flux is identical to that of the target material. However, this would not seem to apply here or at least stands in contradiction with the results obtained. Until target powders with different overall compositions have been utilised and analysis of the plasma is undertaken, these conclusions are limited

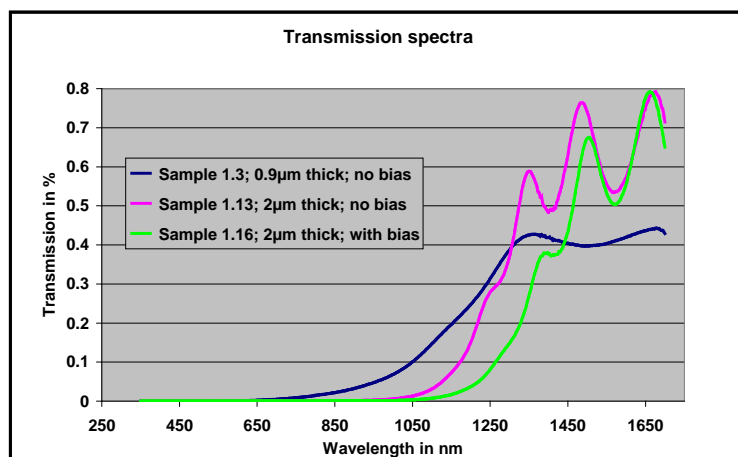


Figure 2
Representative transmission data

Optical measurements revealed that all films had almost 0% transmission in the 300 – 1050 nm range.

4.1. SIMS Profiling

Secondary ion mass spectrometry SIMS, was used to determine compositional changes throughout the thickness of the films. As there are several isotopes of these elements (i.e. ^{63}Cu and ^{65}Cu) their ratios were recorded and compared. The measured and normalised ratios were identical for all films and close to the nominal values.

Two major observations were evident from the recorded signals:

The compositional relation between the three constituents remained constant through the entire film thickness (Figure 3).

The intensity of the $^{80}\text{SeCs}^+$ signal was lower than expected for a corresponding real or nominal stoichiometric composition of CuInSe_2 - if compared to the Cu and In signal intensities. Therefore the actual ratio between the signals was the most likely to be incorrect. This is probably due to SIMS artifacts (i.e. instrument memory effects), as has been suggested by Guibertoni and Bersani [18].

The observed signal intensities for Cu, In and Se were at a constant level throughout the entire thin films, indicating compositional uniformity. The films analysed were deposited with different biasing voltage waveforms (P122: rf; P127: dc; P130: pulsed dc) and the signal intensities of each of these species were compared. Figure 3 illustrates that no relevant variations of composition with thickness could be detected.

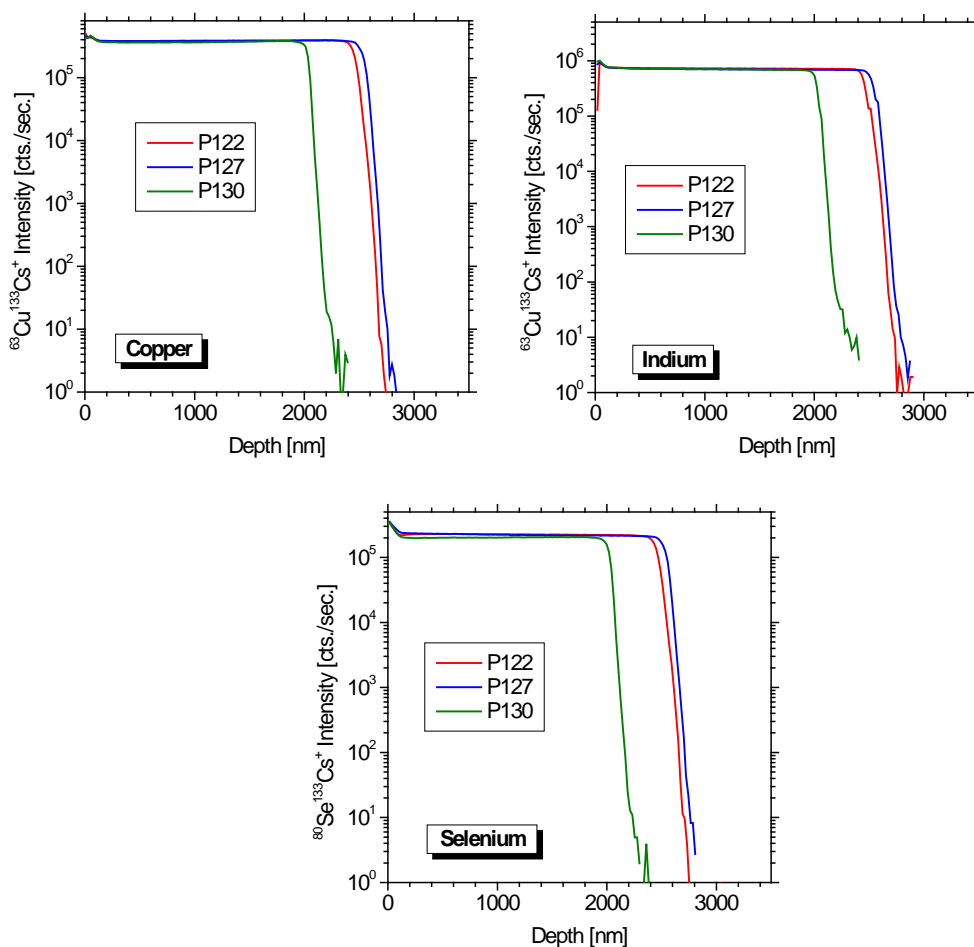


Figure 2 SIMS comparison of copper, indium and selenium depth distributions.

4.2. Laser induced breakdown spectroscopy (LIBS) depth profiling

CIS thin films grown on silicon were ablated using a frequency doubled Nd:YAG laser at a wavelength of 532nm and at fluences between 0.8 Jcm⁻² to 0.15 Jcm⁻², removing approximately 95nm to 1300nm of material with each shot. Typical depth resolution for LIBS depth profiling is in the range of 100-500nm per shot, but in certain cases average depth per shot values below 10nm have been reported [19,20]. A series of single shot laser pulses was focused at a single point on the sample and selected spectral emission lines relating to the elements present in the films and substrate were recorded; Si: 390.55nm; In: 451.13nm; Cu: 521.82nm. The beam profile of this laser is pseudo Gaussian (not 'top hat') and as a result it is not possible to produce a clear cut off between substrate and deposited material.

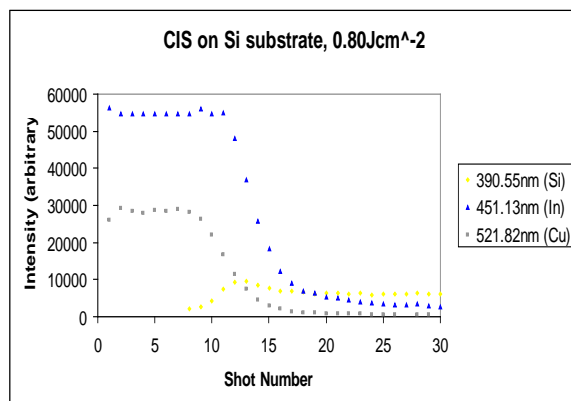


Figure 4 LIBS profiles



Figure 5 The ablated CIS region

1 mm

The LIBS spectra support the SIMS data, again showing that the composition of the CIS films is uniform throughout. This photographic image of ablated CIS on a Si substrate clearly shows the exposed silicon substrate in the centre of the ablated region, together with evidence of re-deposition.

5. Conclusions

The work described has shown that dc magnetron sputtering can produce close packed stoichiometric thin films of copper indium diselenide without the need for a post deposition selenisation step and using simple powdered targets with a non-stoichiometric composition. The optical transmission characteristics of the films indicate an unusually high degree of absorption at visible wavelengths. Conventional SIMS analysis showed the films to be of uniform composition throughout their thickness and this result was confirmed by laser induced breakdown spectroscopy measurements, suggesting that this technique could offer a useful additional method for compositional analysis.

Acknowledgements

The authors wish to thank Prof R.D. Tomlinson for being the originator of CIS research within the University of Salford and the world in general and Dr P.J. Kelly for his expert knowledge relating to PDMS.

References

1. J. Parkes, R. D. Tomlinson and M. J. Hampshire: *J. Appl. Cryst.* **6** (1973) 414.
2. J. Parkes, R.D. Tomlinson and M. J. Hampshire, *Solid-State Electron.* **16**, 773 (1973)
3. M. A. Contreras, B. Eggas, K.R. Ramanathan, J. Hiltner, S. Schwartzlander, F. Hasoon, R. Noufi, *Prog Photovolt.* **7**, (1999), 311
4. T. Negami, Y. Hashimoto, S. Nishiwaki, *Solar Energy Mat. & Sol. Cells* **67**, (2001), 331
5. M. Powalla, D. Hariskos, E. Lotter, M. Oertel, J. Springer, D. Stellbogen, B. Dimmler and R. Schöffler, *Thin Solid Films* **431-432**, (2003), 523
6. J. Piekoszewski, J. Loferski, R. Beaulieu, J. Beall, B. Roessler, J. Shewchun, *Procs. 14. IEEE Photov. Spec.* (1980), 980
7. T. Tanaka, T. Yamaguchi, A. Wakahara, A. Yoshida, *Thin Solid Films* **343-344**, (1999), 320
8. A.N.Y. Saman, PhD Thesis, 'The Fabrication and Characterisation of rf Sputtered CuInSe₂ and CuInS₂ Thin Films', University of Salford, (1984)

9. S.V. Krishnaswamy, A.S. Manocha, J.R.Szedon, J. Vac. Sci. Technol. A1, (1983), 510
10. J.A. Thornton, T.C. Lommasson, Solar Cells 16, (1986), 165
11. N. Nancheva, P. Docheva, N. Djourelov, M.Balcheva, Materials Letters 54, (2002), 169
12. S. Schiller, K. Goedicke, J. Reschke, V. Kirchhoff, S. Schneider, F.Milde, Surf. Coat. Technol. 61, (1993), 331
13. P.J. Kelly, Y.Zhou, A. Postill, Thin Solid Films 426, (2003), 111
14. P.J.Kelly, P.S.Henderson, R.D.Arnell, G.A.Roche, D.Carter, J. Vac. Sci. Technol. A18, 6, (2000), 2890
15. K.Suzuki, Thin Solid Films 351, (1999), 8
16. J. Parkes, R.D. Tomlinson, M.J. Hampshire, J. Cryst. Growth 20, (1973), 315
17. R.D. Tomlinson, Solar Cells 16, (1986),
18. D. Guibertoni, M. Bersani, The Center for Scientific and Technological Research (ITC-irst), Trento, Italy, personal communication.
19. D. G. Papazoglou, V. Papadakis, D. Anglos, J. Anal. At. Spectrom., 19, 483 (2004)
20. D. Romero and J.J. Laserna, Anal. Chem., 1997, 69, 2871.

Appendix B:

LIBS and Remote Raman Spectroscopy References By Los Alamos National Laboratory (LANL) and Collaborators

LIBS Publications for Planetary Science

Wiens R.C., Sharma S.K., Thompson J., Misra A., and Lucey P.G. (2005) Joint analyses by laser induced breakdown spectroscopy and Raman spectroscopy at stand-off distances. *Spectrochimica Acta A*, in press.

Sallé B., Cremers D.A., Maurice S., and Wiens R.C. (2005) Evaluation of a compact spectrograph for insitu and stand-off laser-induced breakdown spectroscopy analyses of geological samples in Martian missions. Manuscript in preparation for submission.

Radziemski L., Cremers D., Benelli K., Khoo C., and Harris R.D. (2005) Use of the vacuum ultraviolet spectral region for LIBS-based Martian geology and exploration. In press.

Sallé B., Cremers D.A., Maurice S., and Wiens R.C. (2005) Laser-induced breakdown spectroscopy for space exploration applications : Influence of ambient pressure on the calibration curves prepared from soil and clay samples. *Spectrochimica Acta B*, in press.

Sallé B., Lacour J.-L., Vors E., Fichet P., Maurice S., Cremers D.A., and Wiens R.C. (2004) Laser-induced breakdown spectroscopy for Mars surface analysis : Capabilities at stand-off distance and detection of chlorine and sulfur elements. *Spectrochim. Acta B* 59, 1413-1422.

Arp Z.A., Cremers D.A., Harris R.D., Oschwald D.M., Parker G.R., and Wayne D.M. (2004) Feasibility of generating a useful laser-induced breakdown spectroscopy plasma on rocks at high pressure: preliminary study for a Venus mission. *Spectrochim. Acta B*, 59, 987-999.

Arp Z.A., Cremers D.A., Wiens R.C., Wayne D.M., Salle B., and Maurice S. (2004) Analysis of water ice and water ice/soil mixtures using laser-induced breakdown spectroscopy: Application to Mars polar exploration. *Applied Spectrosc.*, 58, 897-909.

Brennetot R., Lacour J.L., Vors E., Rivoallan A., Vailhen D., and Maurice S. (2003) Mars analysis by laser-induced breakdown spectroscopy (MALIS): Influence of mars atmosphere on plasma emission and study of factors influencing plasma emission with the use of Doehlert designs. *Appl. Spectrosc.* 57, 744- 752.

Wiens R.C., Seelos F.P. IV, Ferris M.J., Arvidson R.E., Cremers D.A., Blacic J.D., and Deal K. (2002) Combined remote mineralogical and elemental identification from rovers: Field tests using LIBS and VISIR. *J. Geophys. Res. Planets.*, 10.1029/2000JE001439, 30 August.

Knight A.K., Scherbarth N.L., Cremers D.A., and Ferris M.J. (2000) Characterization of laser-induced breakdown spectroscopy (LIBS) for application to space exploration. *Appl. Spectrosc.* 54, 331-340.

Blacic, J.D., Pettit D.R., and Cremers D.A. (1992) Laser-Induced Breakdown Spectroscopy for Remote Elemental Analysis of Planetary Surfaces. Proceedings of the International Symposium on Spectral Sensing Research, Maui, HI, November 15-20.

Appendix C:

Theoretical Models of the Laser-Solid Interaction⁴⁹

The following table lists some most representative works, and a brief description of each.

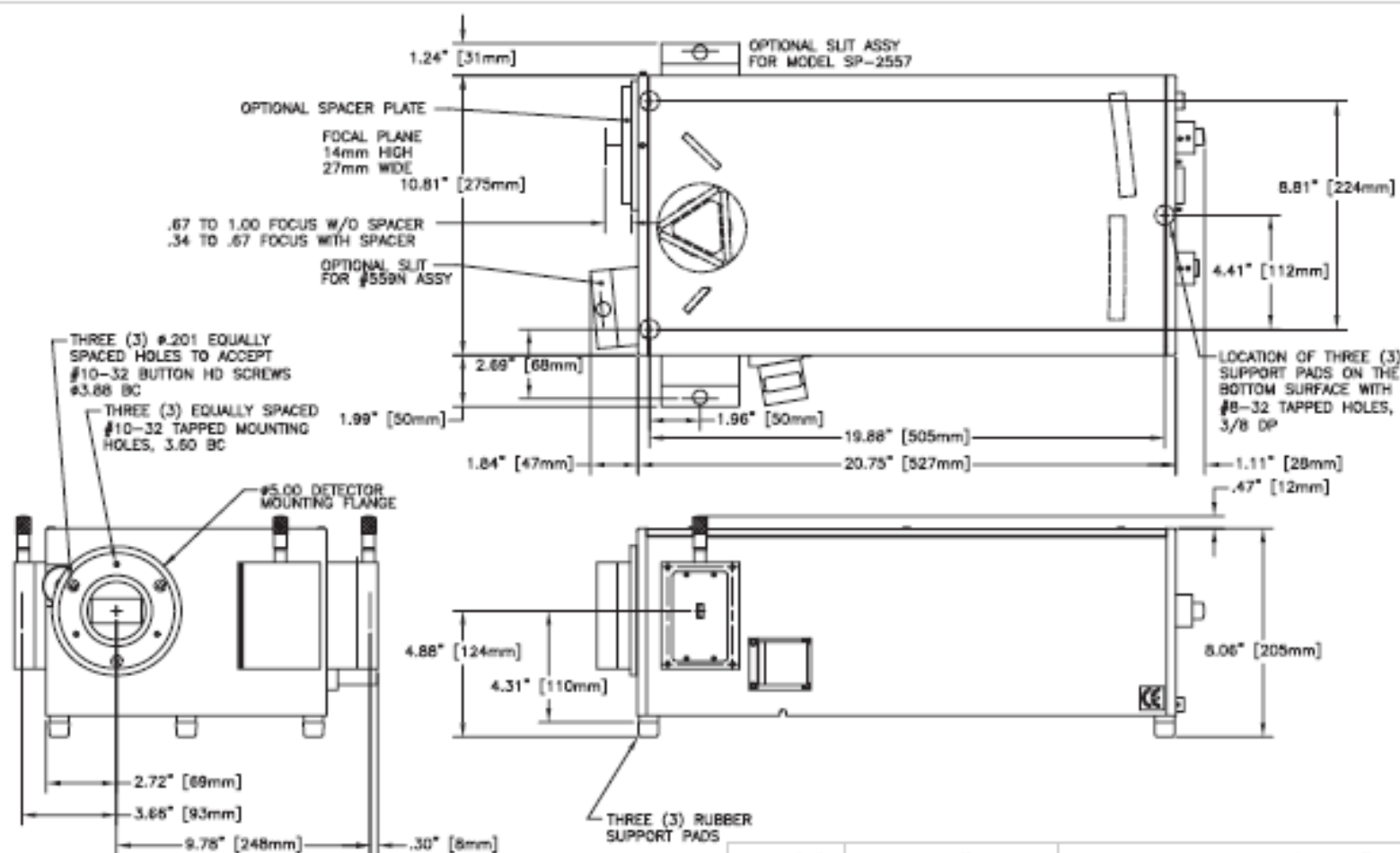
AUTHOR	YEAR	RESULT
Ready	1964, 1971	Material removal by evaporation
Von Allmen	1976	Material removal by evaporation and liquid expulsion
Andrews and Attey	1975	Material removal by evaporation and evaporation-controlled limit
Afanas'ev and Krohkin	1967	Vapour flow, pressure jump across Knudsen layer
Anisimov	1968	Temperature, pressure, and density discontinuity across Knudsen layer
Hassanein, Kulcinski, and Wolfer	1984	Material removal by vaporisation in vacuum
Olstad and Olander	1975	Nonequilibrium surface process
Kelly et al.	1985	Thermal-shock-induced exfoliation
Geohegan	1992	Phenomenological study

Appendix D:

Acton Research Corporation, SpectraPro 500i Specifications:

Grating groove density	2400g/mm, ruled grating, blazed at 240nm	600g/mm, ruled grating, blazed at 1 micron	150g/mm, ruled grating, blazed at 300nm
Spectral range (blaze wavelength)	190-700nm	650-2000nm	1700-7000nm
Dispersion	0.85nm/mm	3.4nm/mm	13.6nm/mm
Resolution, at 435.8nm slits 10microns x 4mm high	0.025nm	0.10nm	0.40nm
Wavelength accuracy	±0.1nm	±0.4nm	±1.6nm
Wavelength reproducibility	±0.025nm	±0.1nm	±0.04nm
Nominal spectral window for a 25mm wide detector	21.25nm	85nm	340nm
Resolution for an ICCD based on 4pixels (100microns)	0.085nm	0.34nm	1.36nm

Working Drawing¹³⁷ are shown on the next page:

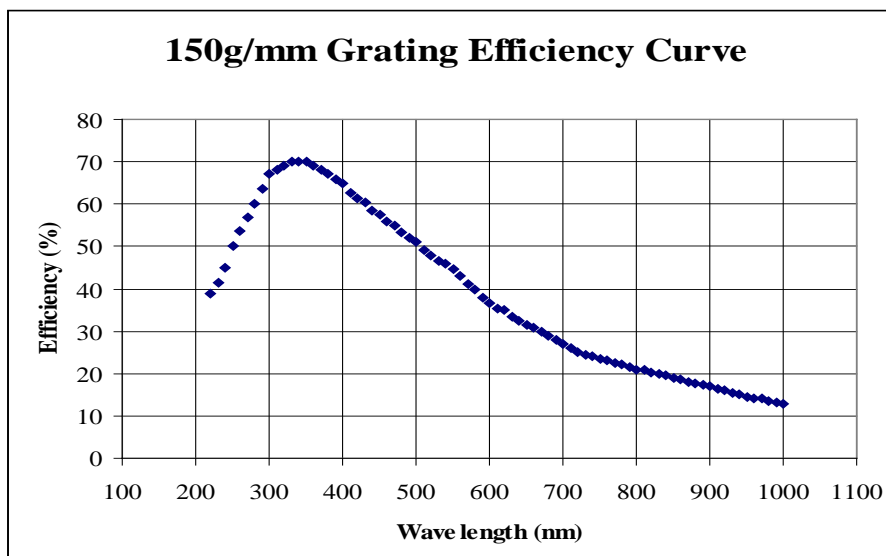
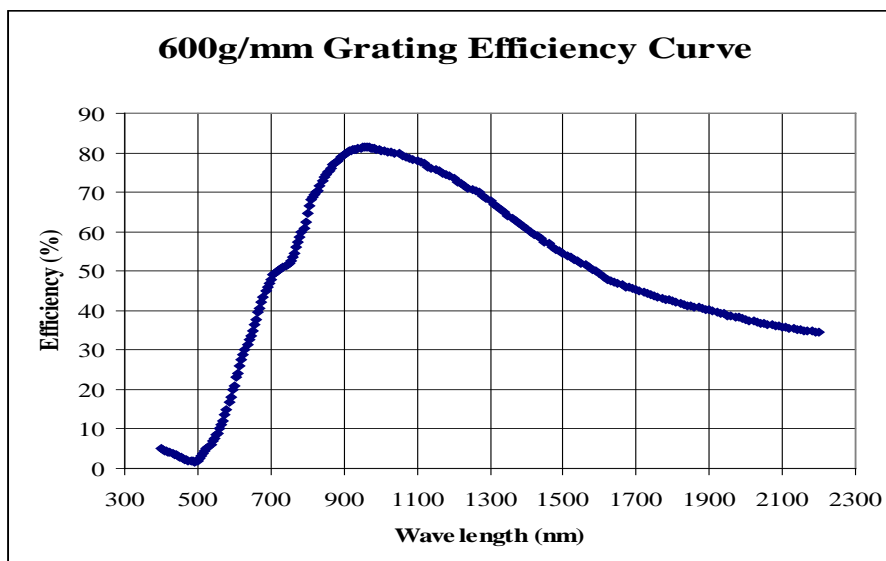
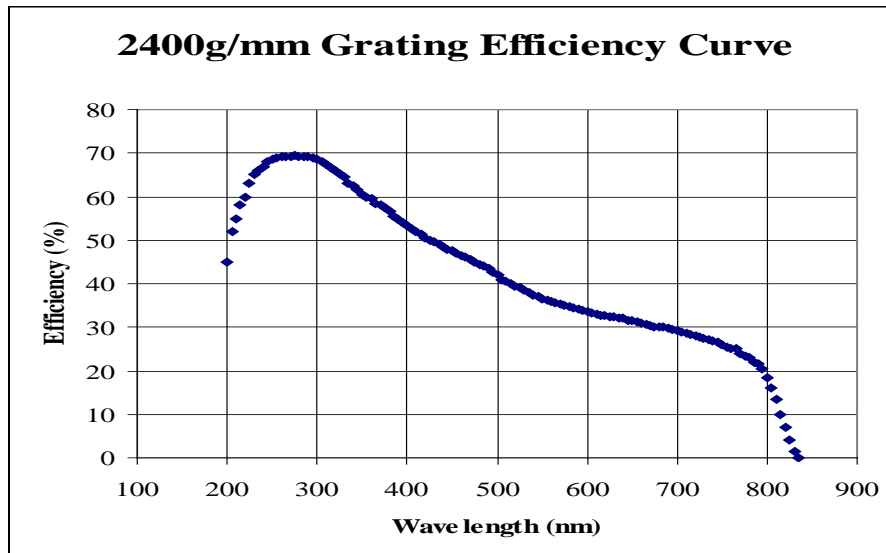


Model	Function	Port configuration	Optical path
SP-2555	Monochromator	Side Entrance Slit/Front Exit Slit	90°
SP-2556	Spectrograph	Side Entrance Slit/Front CCD Port	90°
SP-2557	Monochromator	Side Entrance Slit/Front Exit Slit/Side Exit Slit	90° and 180°
SP-2558	Spectrograph	Side Entrance Slit/Front CCD Port/Side Exit Slit	90° and 180°
SP-2560	Spectrograph	Side Entrance Slit/Front CCD Port/Side CCD Port	90° and 180°

Optional Motorized entrance slit available
Optional Front Entrance Slit available

Appendix E:

Grating Efficiency Curves

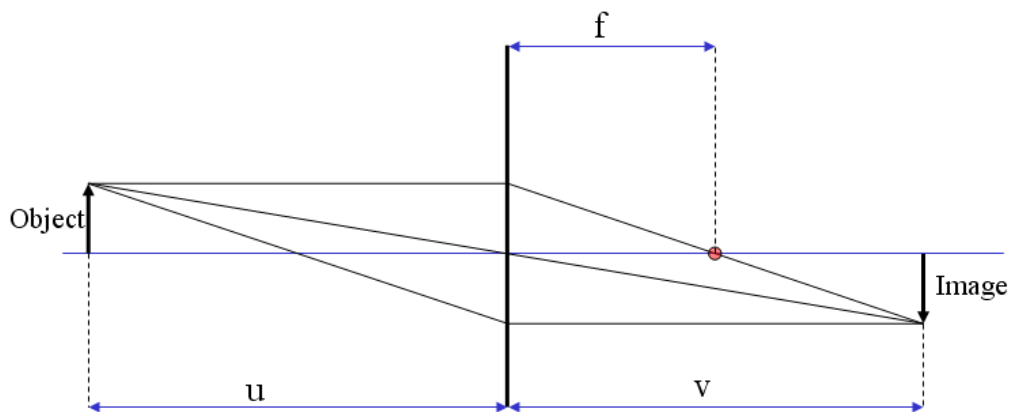


Appendix F:

Lens Database, compiled by N. Lucas:

In order to ascertain what lenses are available in the lab a lens database was compiled.

This summarised all the focal points of the lenses in the lab using two different methods to obtain their value. Method 1) rough guide measurement using room lights as source. Method 2) using the lens formula: $f = uv/(v+u)$ as shown:



$$f = uv/(v+u)$$

$$\text{set: } x = v + u$$

$$\text{therefore: } f = uv/x$$

$$\text{therefore: } \Delta f/f = \Delta u/u + \Delta v/v + \Delta x/x$$

$$\text{but: } x = v + u$$

$$\text{therefore: } \Delta x = \Delta v + \Delta u$$

$$\text{So: } \Delta f/f = \Delta u/u + \Delta v/v + \Delta v + \Delta u/u + v$$

The data obtained is shown overleaf. The information was first compiled using the flat edge of the plano-convex lens as a measuring point, this was later corrected as shown in the table.

Plano-convex original
measure point



Lens Number	u (mm) ± 3.5mm	v (mm) ± 3.5mm	f (mm)	error in f (mm)	Plano convex lens?	Light incident on flat surface?	Diameter (mm) ± 0.05mm	Thickness at optical axis (mm) ± 0.005mm
1	-117	219	76	-0.028	Yes	Yes	49.5	10.3
1	-130	213	81	-0.021	Yes			10.3
2	-130	351	95	-0.034	No	-	49.5	7.5
3	-130	189	77	-0.017	Yes	Yes	49.8	10.2
3	-130	202.5	79	-0.019	Yes			10.2
4	-130	500	103	-0.040	Yes	Yes	47.4	7.3
4	-130	634	108	-0.043	Yes			7.3
5	-928	1063	495	-0.001	Yes	Yes	50	4.6
5	-990	998	497	0.000	Yes			4.6
6	-990	1001	498	0.000	Yes	Yes	50	3
6	-1030	963	498	0.000	Yes			3
7	-400	535	229	-0.004	Yes	Yes	70	8
7	-500	425	230	0.002	Yes			8
8	-300	310		-0.001	No		60	meniscous: convex 1 side, concave other side.
8	-300	308.5		-0.001	Yes			
9	-250	91	67	0.049	Yes	Yes	67.9	24.1
9	-250	59	48	0.091	Yes			24.1
10	-100	77.5	44	0.020	Yes	Yes	49.7	21
10	-100	57	36	0.053	Yes			21
11	-100	277.5	74	-0.045	Yes	Yes	49.7	10.65
11	-100	450	82	-0.054	Yes			10.65
12	-500	441		0.002	No	-	90	9.4
13	-200	530	145	-0.022	Yes	Yes	38.3	4.4
13	-200	519	144	-0.022	Yes			4.4

Lens Number	Centre of lens y (mm)	new u/v value, accounting for centre of lens measurement		f (mm) Measured from centre of lens	Error in f (mm)	f (mm) measured from room lights
		Flat incident = u + y; otherwise = u-y u (mm)	flat incident = v-y, otherwise = v+y v(mm)			
1	5.15	122.15	213.85	78	0.066	80
1	5.15	124.85	218.15	79	0.064	
2				95		95
3	5.1	135.1	183.9	78	0.067	95
3	5.1	124.9	207.6	78	0.066	
4	3.65	133.65	496.35	105	0.044	110
4	3.65	126.35	637.65	105	0.042	
5	2.3	930.3	1060.7	496	0.011	600
5	2.3	987.7	1000.3	497	0.011	
6	1.5	991.5	999.5	498	0.011	600
6	1.5	1028.5	964.5	498	0.011	
7	4	404	531	229	0.023	250
7	4	496	429	230	0.023	
8						155
8						
9	12.05	262.05	78.95	69	0.078	75
9	12.05	237.95	71.05	55	0.087	(42)
10	10.5	110.5	67	42	0.123	50
10	10.5	89.5	67.5	38	0.136	
11	5.325	105.325	272.175	76	0.065	90
11	5.325	94.675	455.325	78	0.057	
12				234		250
13	2.2	202.2	527.8	146	0.034	140
13	2.2	197.8	521.2	143	0.034	

error
because
lights
not at ∞

thin lens
formula
doesn't
hold

Lens Data:

SRF	RADIUS	THICKNESS	APERTURE RADIUS	GLASS	SPECIAL
OBJ	0.000000	1.0000e+20	1.0000e+14	AIR	
1	0.000000	10.300000	25.000000	BK7	C
2	-40.000000	21.147586	25.000000	AIR	
3	-148.000000	2.200000	25.000000	BK7	C
4	148.000000	6.000000	25.000000	AIR	
5	-116.000000	1.550000	25.000000	BK7	C
6	116.000000	10.000000	25.000000	AIR	
AST	0.000000	38.400000	5.662505	AIR	F
IMS	0.000000	0.000000	20.000000		F

Paraxial Constants:

Effective focal length:	500.0000	Lateral magnification:	-5.0000e-18
Numerical aperture:	0.0400	Gaussian image height:	0.0005
Working F-number:	12.5000	Petzval radius:	509.9980
Lagrange invariant:	-2.0000e-05		

Appendix G:

Controller/Software Sweeps, Author N. Lucas

Submitted: 31/7/03

PTG/Software Problems

Detailed below is my method and details of a WinSpec Parameters Sweep to find problem with PTG/Software.

Notes: setup LED (369nm) with timing box (external) to turn on LED after 1s delay for 0.5s, (timing latency = $\pm 1\mu\text{s}$). Pulse generator starts timing box and also sends signal to 'external trig in' on PTG.

Experimental Setup

NB: exposure time set to 1s, slit width 10 μm , gain 20

Timing

External sync: - no capture

Internal sync: -

Continuous cleans: On – does not capture image from trigger (just sits and waits, have to press stop button on tool bar to resume)
Off – works fine

Shutter Control:

Normal, Pre Open on – works fine

Pre open off – does not capture image from trigger

Disabled Closed: Pre Open on – takes image but is noise only, no matter what set exposure time to.

Pre Open off – does not capture image from trigger

Disabled Open: Pre Open on – works fine

Pre Open off – does not capture image from trigger

Full Speed – used in all above

Safe mode – see below...

Exposure time:

0.5s to 0.9 s – no line. Just noise

1s – line, Intensity = 3828

1.1s – line, Intensity = 49307

1.2s – line, Intensity = 65535

1.3s – line, Intensity = 65535 – therefore saturation

Full speed (sync)/ safe mode (async)

Exactly the same intensity for each exposure time as stated above happens if using sync or async. Used delay times in async from 1s to 10s. (NB: LED turns off after 1.5s!) (even when reduced exposure to 0.9s and increased async delay time to 0.5s – just get noise!)

Suggestions: Could be because shutter is pre open?
Async delay not working?

PTG

(Experimental setup set to internal sync. Default parameters used for all other settings in timing tab)

NB: PTG width and delay parameters are 3 orders of magnitude out!!! When set parameters to 1msec, take shot, then go to file information, says that captured for only 1usec!

All settings below using repetitive timing options.

PTG gate width and exposure time (PTG delay set to 0):

- Set PTG gate width to 0, set exposure time to 1s – signal, intensity = 3882
- Set PTG gate width to 1×10^9 , set exposure time to 0 – no signal, noise only!

Vary PTG width, delay and exposure time:

<ul style="list-style-type: none"> • PTG delay = 1×10^6msec (which is actually equal to 1s as 3 orders of magnitude out!) • PTG width = 0 • Exposure = 1s 	Line, Intensity = 16821 (signal expected!)
<ul style="list-style-type: none"> • PTG delay 2×10^6msec (=2s) • PTG width = 0 • Exposure = 1s 	Line, Intensity = 16855 (no signal expected!)
<ul style="list-style-type: none"> • PTG delay 3×10^6msec (=3s) • PTG width = 0 • Exposure = 1s 	Line, Intensity = 16709 (no signal expected!)
<ul style="list-style-type: none"> • PTG delay = 0 • PTG width = 0 • Exposure = 1s 	Line, Intensity = 3674 (same intensity as observed in earlier measurements – therefore delay increases intensity but that's all it seems to do!)

Gain: 20 - intensity 16424

40 - intensity 29947

(working as expected)

NB: Hardware setup: Cleans/skips – No. of cleans = 1, No. of strips per clean = 256.

Submitted: 08/08/03

PTG/Software Problems – after reload of new software

New software loaded over original software (8/8/03).

Checked re-load in Help – WinSpec 2.5.12.2

NB: since the last evaluation I have removed the lens system that optimised the intensity, (setting of focal length of input light). Therefore all intensities are subsequently lower.

Free run (LED on continuous)

– works fine (parameters: slit 2um, gain 20, exposure 100msec = Intensity ~ 5494)

Set LED Timing: Delay = 1sec, Pulse = 0.5sec

Internal Sync

- Repeated each measurement 5 times, I have included 3 of those intensities. (subscript)
- All measurements below taken with settings: slit = 2um, gain = 20, full chip, accumulations = 1, spectra = 1, internal sync, continuous cleans off, shutter normal, pre open on, full speed (sync).

Exposure time = 100msec Gate width = 0 Gate delay = 0	Noise, I ₁ = 575 I ₂ = 500 I ₃ = 480 NB: If take in quick succession - get signal = LED is still on from last shot.
Exposure time = 1s Gate width = 0 Gate delay = 0	Line, I ₁ = 937 I ₂ = 955 I ₃ = 903
Exposure time = 1.1s Gate width = 0 Gate delay = 0	Line, I ₁ = 7085 I ₂ = 7059 I ₃ = 7084
Exposure time = 1.2s Gate width = 0 Gate delay = 0	Line, I ₁ = 13297 I ₂ = 13619 I ₃ = 13526
Exposure time = 0 Gate width = 1s (1x10 ⁶ msec as 3 orders of magnitude out!) Gate delay = 0	Noise, I ₁ = 560 I ₂ = 500 I ₃ = 495 NB: no benefit from taking in quick succession as in first measurement
Exposure time = 0 Gate width = 1s (1x10 ⁶) Gate delay = 0.5 (0.5x10 ⁶)	Noise, I ₁ = 540 I ₂ = 530 I ₃ = 510
Exposure time = 0 Gate width = 1s (tried setting to 1x10 ³ in case 'file information' is wrong) Gate delay = 0.5s (0.5x10 ³)	Noise, I ₁ = 500 I ₂ = 495 I ₃ = 510
Exposure time = 0 Gate width = 1s (1x10 ⁶) Gate delay = 1s (1x10 ⁶)	Noise, I ₁ = 540 I ₂ = 510 I ₃ = 485

Safe mode (async)

Exposure time = 0 Gate width = 1s (1x10 ⁶) Gate delay = 0 Safe mode delay = 0.5s	Noise, I ₁ = 560 I ₂ = 510 I ₃ = 500 NB: no benefit from taking in quick succession as in first measurement
Exposure time = 1s Gate width = 0 Gate delay = 0 Safe mode delay = 0.5s	Line, I ₁ = 907 I ₂ = 932 I ₃ = 947
Exposure time = 1s Gate width = 0 Gate delay = 0 Safe mode delay = 1s	Line, I ₁ = 992 I ₂ = 969 I ₃ = 982
Exposure time = 1s Gate width = 0 Gate delay = 0 Safe mode delay = 2s	Line, I ₁ = 926 I ₂ = 955 I ₃ = 971

Exposure time = 1s Gate width = 0 Gate delay = 0 Safe mode delay = 3s	Line, I ₁ = 952 I ₂ = 937 I ₃ = 955
Exposure time = 1s Gate width = 0 Gate delay = 0 Safe mode delay = 5s	Line, I ₁ = 992 I ₂ = 963 I ₃ = 965 NB: Does not seem to be adding delay of 5s, I count approx 1s!

Parameter Sweep

Slit = 2um, gain = 20, internal sync, full speed (sync), exposure time = 1s, gate delay and width = 0.

NB: Hardware settings; No. of cleans = 1, strips per clean = 256

- Continuous cleans off
 - all previous settings
- Continuous cleans on – No response
 - trigger not received.

Continuous cleans off for all settings below

- Shutter – normal, pre open – off
 - No response
- Shutter – disabled closed, pre open – on
 - Noise, I = 500 (repeated 5 times)
- Shutter – disabled closed, pre open – off
 - No response
- Shutter – disabled open, pre open – on
 - Signal, I₁= 1466 I₂= 1378 I₃= 1434
- Shutter – disabled open, pre open – off
 - No response
- Shutter – disabled open, pre open – on, continuous cleans –on
 - No response!!!

External Sync

Slit 2um, gain 20, full speed (sync), exposure time = 1s, gate width and delay = 0.

- Continuous cleans – off, Normal, Pre open – on
 - No response
- Continuous cleans – off, disabled open, pre open – on
 - No response

Lastly

Standard settings, Internal sync.

Exposure time = 1s Gate width = 0 Gate delay = 1s (1x10 ⁶)	Line, I ₁ = 2932 I ₂ = 2933 I ₃ = 2966
Exposure time = 1s Gate width = 0 Gate delay = 5 (5x10 ⁶)	Line, I ₁ = 2697 I ₂ = 2763 I ₃ = 2710
Exposure time = 1s Gate width = 0 Gate delay = 0	Line, I ₁ = 985 I ₂ = 962 I ₃ = 971

Submitted: 19/08/03

PTG/Software Problems – with new controller

NB: since the last evaluation I have re-setup the lens system that optimised the intensity, (setting of focal length of input light). Therefore all intensities are subsequently higher than last document.

Free run (LED on continuous)

– works fine (parameters: slit 5 μ m, gain 20, exposure 1msec)

Set LED Timing: Delay = 1sec, Pulse = 0.5sec

Internal Sync

- Repeated each measurement 3 times.
- All measurements below taken with settings: slit = 5 μ m, gain = 20, full chip, accumulations = 1, spectra = 1, internal sync, continuous cleans off, shutter normal, pre open on, full speed (sync).

Exposure time = 100msec Gate width = 0 Gate delay = 0	Noise, I ₁ = 682 I ₂ = 683 I ₃ = 698
Exposure time = 0.9s Gate width = 0 Gate delay = 0	Noise, I ₁ = 668 I ₂ = 680 I ₃ = 667
Exposure time = 1s Gate width = 0 Gate delay = 0	Line, I ₁ = 1605 I ₂ = 1577 I ₃ = 1562
Exposure time = 1.1s Gate width = 0 Gate delay = 0	Line, I ₁ = 14764 I ₂ = 15738 I ₃ = 15781
Exposure time = 1.2s Gate width = 0 Gate delay = 0	Line, I ₁ = 29587 I ₂ = 29330 I ₃ = 28568
Exposure time = 1.3s Gate width = 0 Gate delay = 0	Line, I ₁ = 43374 I ₂ = 43771 I ₃ = 43369
Exposure time = 0 Gate width = 1s (1000msec) Gate delay = 0	Noise, I ₁ = 679 I ₂ = 622 I ₃ = 607
Exposure time = 0 Gate width = 1s (1x10 ⁶) Gate delay = 0	Noise, I ₁ = 633 I ₂ = 612 I ₃ = 630
Exposure time = 0 Gate width = 2s (1x10 ⁶) Gate delay = 0	Noise, I ₁ = 685 I ₂ = 611 I ₃ = 605
Exposure time = 0 Gate width = 1s (1x10 ⁶) Gate delay = 0.5s (0.5x10 ⁶)	Noise, I ₁ = 658 I ₂ = 606 I ₃ = 618
Exposure time = 0 Gate width = 1s (1x10 ⁶) Gate delay = 1s (1x10 ⁶)	Noise, I ₁ = 664 I ₂ = 617 I ₃ = 630

Parameter Sweep

Slit = 5 μ m, gain = 20, internal sync, full speed (sync), exposure time = 1s, gate delay and width = 0.

NB: Hardware settings; No. of cleans = 1, strips per clean = 256

Continuous cleans – off Shutter – normal Pre open – on	Line, I ₁ = 1537 I ₂ = 1567 I ₃ = 1471
Continuous cleans – on Shutter – normal Pre open – on	Line, I ₁ = 1685 I ₂ = 2043 I ₃ = 1633
Continuous cleans – off Shutter – normal Pre open – off	No response to trigger.
Continuous cleans – on Shutter – normal Pre open – off	No response to trigger.
Continuous cleans – off Shutter – disabled opened Pre open – on	Line, I ₁ = 2323 I ₂ = 2258 I ₃ = 2394
Continuous cleans – on Shutter – disabled opened Pre open – on	Line, I ₁ = 2778 I ₂ = 3271 I ₃ = 3385
Continuous cleans – on Shutter – disabled opened Pre open – off	No response to trigger
Continuous cleans – off Shutter – disabled opened Pre open – off	No response to trigger
Continuous cleans – off Shutter – disabled closed Pre open – on	Noise, I ₁ = 656 I ₂ = 621 I ₃ = 610
Continuous cleans – on Shutter – disabled closed Pre open – on	Noise, I ₁ = 581 I ₂ = 578 I ₃ = 577
Continuous cleans – off Shutter – disabled closed Pre open – off	No response to trigger
Continuous cleans – on Shutter – disabled closed Pre open – off	No response to trigger

External Sync

Slit 5 μ m, gain 20, full speed (sync).

Exposure time – 1s Gate width - 0 Gate delay - 0 Continuous cleans – on Shutter – Normal Pre open – on	No response to trigger
Exposure time – 0	No response to trigger

Gate width – 1s (1x10 ⁶) Gate delay - 0 Continuous cleans – on Shutter – Normal Pre open – on	
Exposure time – 0 Gate width - 1s (1x10 ⁶) Gate delay - 1s (1x10 ⁶) Continuous cleans – off Shutter – Normal Pre open – on	No response to trigger

Lastly – glitches!**Gate Delay**

Standard settings, Internal sync.

Exposure time = 1s Gate width = 0 Gate delay = 1s (1x10 ⁶)	Line, I ₁ = 5150 I ₂ = 5167 I ₃ = 5280
Exposure time = 1s Gate width = 0 Gate delay = 5s (5x10 ⁶)	Line, I ₁ = 5126 I ₂ = 4938 I ₃ = 4939
Exposure time = 1s Gate width = 0 Gate delay = 0	Line, I ₁ = 1537 I ₂ = 1440 I ₃ = 1522

ROI

While ‘playing around’ with kit I noticed another glitch that I thought I would bring to your attention. Like the Delay glitch, it is repeatable but not expected!

CCD Readout (main tab) – Full chip Slit Height (ROI tab) – 256 Exposure time – 1s Gate width – 0 Gate delay - 0	Line, I ₁ = 1547 I ₂ = 1547 I ₃ = 1489 Number of strips (y axis on graph) = 256
CCD Readout – ROI Slit Height – 256 Exposure time – 1s Gate width – 0 Gate delay - 0	Line, I ₁ = 46351 I ₂ = 22221 I ₃ = 24937 Number of strips = 1 Completely different shaped graph to previous readings, (called Graph X) same graph for all 3 shots. (Saved)
CCD Readout – ROI Slit Height – 1 Exposure time – 1s Gate width – 0 Gate delay - 0	Line, I ₁ = 1475 I ₂ = 1479 I ₃ = 1419 Number of strips = 1 Same graph as ‘original’, (saved).
CCD Readout – Full chip Slit Height – 1 Exposure time – 1s Gate width – 0 Gate delay - 0	Line, I ₁ = 1499 I ₂ = 1449 I ₃ = 1564 Number of strips = 256! Same graph as ‘original’, (saved).
CCD Readout – full chip Slit Height – 1 Exposure time – 0 Gate width – 1s (1x10 ⁶) Gate delay - 1s (1x10 ⁶)	Noise, I ₁ = 652 I ₂ = 622 I ₃ = 605 Number of strips = 256!

Spectra Number

As the above settings are not what expected, I also characterised the settings gained when working with:- Main tab; No. of spectra, Accumulations.

PTG settings; On CCD accumulations, Software accumulations

No. of spectra - 5 Accumulations - 1 On CCD accumulations – 1 Software accumulations – 1 CCD Readout - ROI Slit height – 256	First shot has ‘graph X’ shape Graph changes with each shot Graph eventually saturates Number of strips – 5! (saved)
No. of spectra - 5 Accumulations - 1 On CCD accumulations – 1 Software accumulations – 1 CCD Readout - Full Slit height – 256	First shot has ‘original’ graph shape Each shot increases intensity of graph but doesn’t change graph shape Graph eventually has flat top 5 th shot = ‘program performed illegal operation – WinSpec shut down!’
No. of spectra - 5 Accumulations - 1 On CCD accumulations – 1 Software accumulations – 1 CCD Readout - Full Slit height – 10	First shot has ‘original’ graph shape 5 Frames, 1 Accumulation (status bar) Number of strips – 256! Other strips, (2-256), have different shape to strip 1, this disappears with each ‘shot’
No. of spectra - 1 Accumulations - 5 On CCD accumulations – 1 Software accumulations – 1 CCD Readout - ROI Slit height – 256	First shot has ‘graph X’ shape 1 frame, 5 accumulations (status bar) Number of strips – 1! (saved)
No. of spectra - 1 Accumulations - 5 On CCD accumulations – 1 Software accumulations – 1 CCD Readout - Full Slit height – 10	First shot has ‘original’ graph shape Number of strips – 256! Other strips, (2-256), have different shape to strip 1, this disappears with each ‘shot’
No. of spectra - 1 Accumulations - 1 On CCD accumulations – 5 Software accumulations – 1 CCD Readout - ROI Slit height – 256	Displays nothing till last ‘shot’ taken. Number of strips – 1 (saved)
No. of spectra - 1 Accumulations - 1 On CCD accumulations – 5 Software accumulations – 1 CCD Readout - Full Slit height – 10	Displays nothing till last ‘shot’ taken. Saturates Graph looks like ‘original’ Number of strips - 256
No. of spectra - 1 Accumulations – 1 (5) On CCD accumulations – 1 Software accumulations – 5 CCD Readout - ROI Slit height – 256	First shot is similar to ‘graph X’ shape. Frames 1, accumulations 5 (status bar) Number of strips – 1 (saved) When changing software accumulations in PTG settings, the number of accumulations on the main tab also changes. If you set this to 1 – it sets the PTG settings (software accumulations) to 1 also.

Appendix H:

Dummys Guide to:

Acton Spectrometer with WinSpec and Grams software.

Author N. Lucas

Legend:

- When referring to drop down menus the menu will be underlined corresponding to the quick key, then subsequent menus will be separated with a '/'.
e.g. File/Open...
- Salient points are in **bold** to allow 'skim' reading more easily.

Introduction

This is a very brief guide to using this piece of kit. I recommend you skim read the whole document before proceeding to 'Dummy Example', (sec: 5).

Good luck!

Contents

Dummys Guide to:	185
Acton Spectrometer with WinSpec and Grams software.	185
Introduction.....	185
Contents	185
1) <i>Turning On</i>	186
2) <i>Turning Off</i>	186
3) <i>WinSpec Buttons</i>	186
4) <i>Experimental Setup</i>	187
5) <i>Dummy Example</i>	189
6) <i>Optimising Spectrometer Parameters</i>	190
7) <i>Calibration</i>	191
8) <i>Display Layout</i>	193
9) <i>Multiple Frames</i>	193
10) <i>Troubleshooting</i>	195

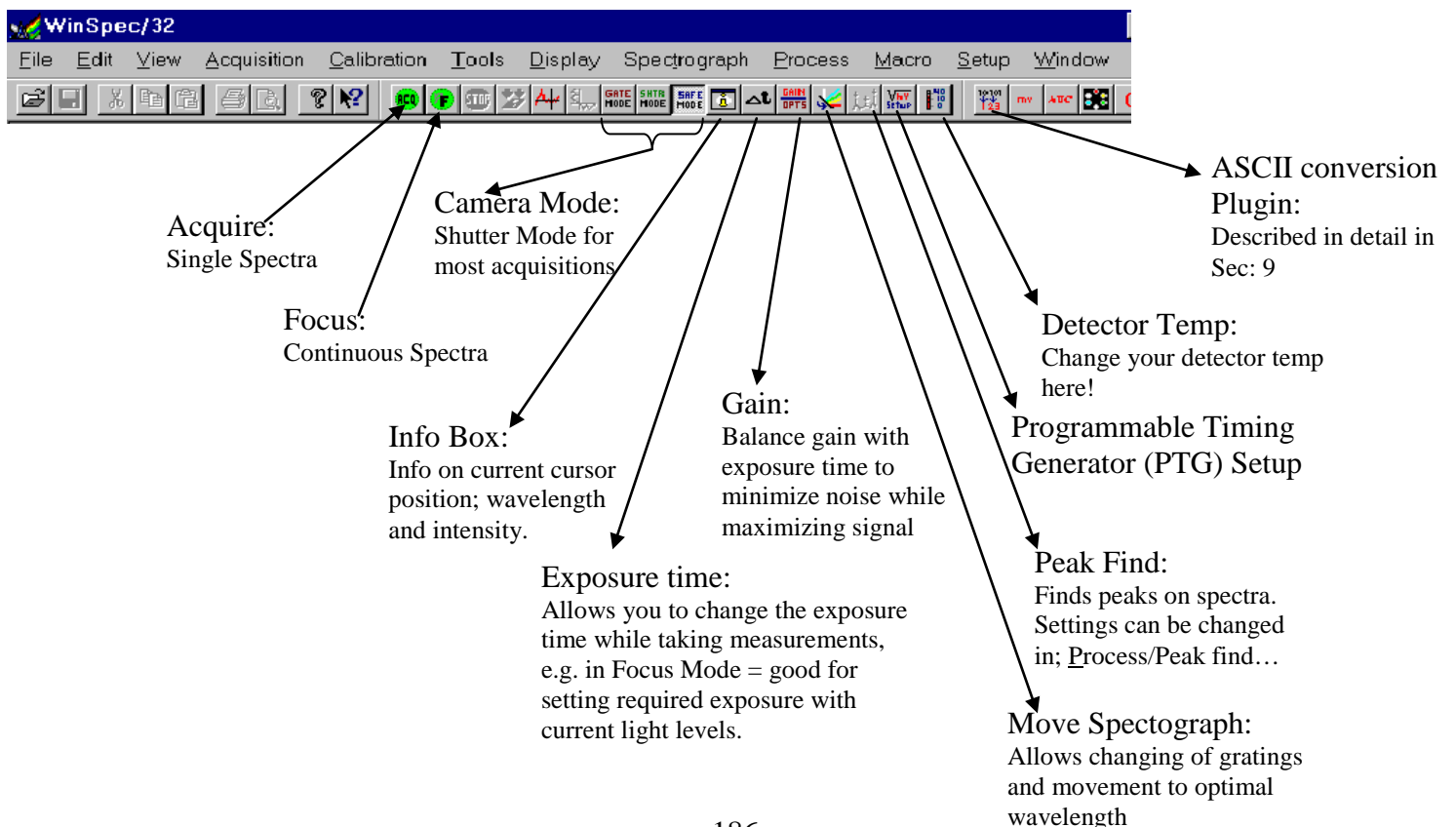
1) Turning On

- Turn on the spectrometer by the **red switch** on **extension lead** located behind spectrometer.
- Check that the **MCP** is on, located on the back of the camera. (**turn off when finished with equipment**)
- Open **WinSpec** on the computer.
- When you open choose 'Keep In Safe Mode'.
- You will also hear an audible bleep, this is the camera safety buzzer, it will sound when you open WinSpec and when you change the gain.
- **If it bleeps at other times you are allowing too much light into the spectrometer onto the camera, you should reduce the intensity immediately.**

2) Turning Off

- Close WinSpec
- Turn off red switch on extension lead
- **Turn off MCP**

3) WinSpec Buttons



4) Experimental Setup

In order to setup an experiment you need to define the experimental setup parameters, this can be done in one menu, (rather than using the toolbar buttons).

- Acquisition/Experiment Setup...

- **Main,**

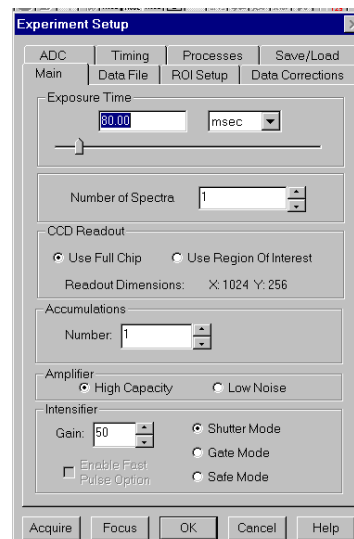
Exposure; How long the **shutter** is **open** to obtain an image on CCD.

No. of spectra; **How many ‘frames’** you would like, good for analysing changes over time.

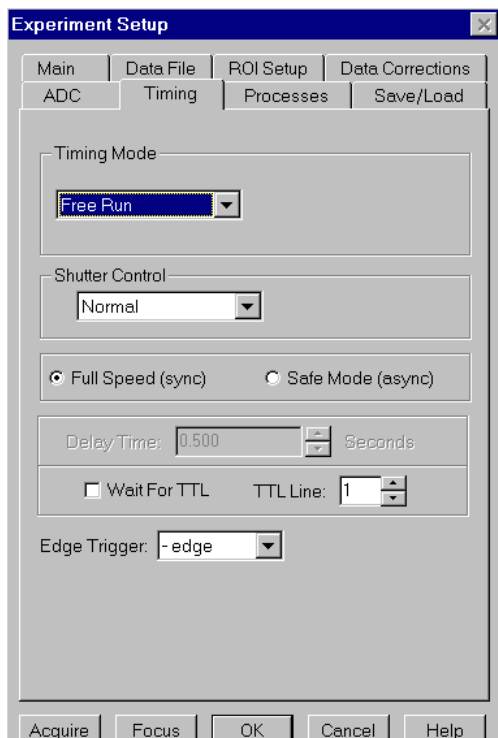
No. of acquisitions; How many **accumulations of each image** you would like, good for increasing the intensity of each ‘frame’.

Gain; Increasing the gain increases the intensity but it also increases the noise.

Shutter mode; Three options available,
 Safe – the shutter will not open,
Shutter – normal **mode for taking a spectra**
 Gate – Used for timed gated experiments.



NB: Carefully balance gain, exposure and slit width to obtain the best intensity and precision in measurements. Increasing slit width decreases resolution but increases intensity. Increasing the exposure time too much can saturate the detector/camera, but it needs to be high enough to obtain an adequate image. Increasing gain increases intensity but also amplifies the noise.



• **Timing.**

Timing Mode;

<i>Free run</i>	Normal acquisition mode
<i>Internal sync</i>	allows you to use the PTG
<i>External sync</i>	Allows you to sync from an external source

Shutter control; leave on Normal

Full speed (sync)/Safe mode (async);
Use **full speed**. Safe mode used mostly when focusing – puts a delay between each acquisition, (set in delay time).

Wait for TTL; Leave un-ticked – not used.

Edge Trigger; Leave as is – not necessary.

• **ROI Setup,**

This allows you to set the **area of the chip** you would like to use.

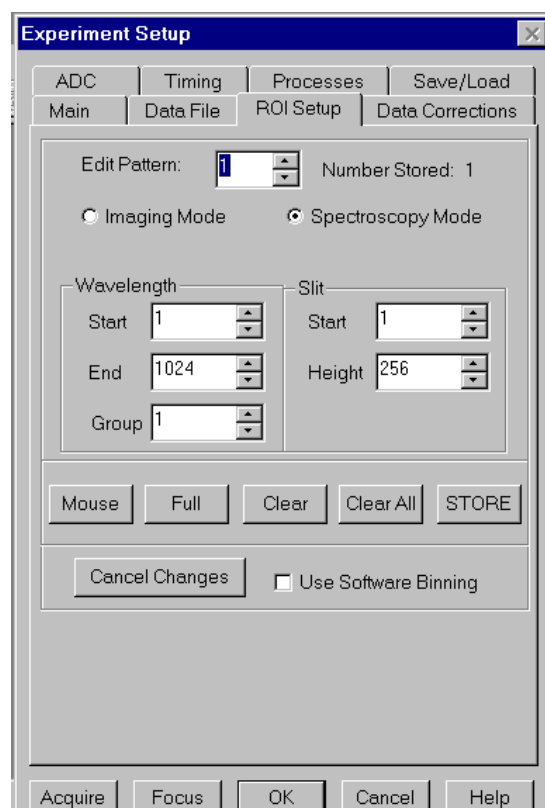
The width of the chip that you would like to use is given by wavelength range.

The height of the active area is give by slit height.

It also allows you to **capture an image** from the CCD.



If changing to imaging mode, you must also change the display layout, (sec. 8)

Once you have changed the ROI you must **hit store to save the changes.**



5) Dummy Example

If this is your first experiment, I have made an example to make your life easy!

- Turn everything on!
- Open WinSpec in safe mode
- Run through the calibration procedure.
- Click, Acquisition/Experiment Setup...
- Choose your settings, typical values for parameters would be:-
 - Slit Width: 5 μ m (slit is located on side of spectrometer, a micrometer gauge is used to change the slit width.)
 - Exposure time: 10msec
 - Spectra: 1
 - CCD Readout: Full chip
 - Accumulations: 1
 - Amplifier: High capacity
 - Gain: 20
 - Shutter mode
- Turn off room lights
- Click ok
 - For now you will not need the other tabs in experimental setup.
- Click Acquire 
 - Clicking acquire initially ensures you are able to check you are not saturating the CCD. If the intensity is very low with these experimental parameters you can then click Focus  and vary the experimental parameters using the toolbar buttons while observing the changes.
- You have acquired your spectra!
 - If you have no spectra, go to 'Optimising Spectrometer Parameters', (sec: 5), or try 'Troubleshooting', (sec: 10)
- Save as required.

6) Optimising Spectrometer Parameters

- In the dummy example you have set up the initial experimental parameters to allow capture of your first spectra.
- To optimise the parameters to give you the best signal output, **Focus** mode can be used. This acquisition procedure allows you to **adjust parameters** while the spectra on the **screen continually refreshes**. (using the toolbar buttons at this stage is recommended)
- To start with always use a **small slit width**, (use your common sense on this one – how much light do you have incident on the spectrograph, etc.. A small width would be approx 2 μ m), as you increase the width of the slit you can observe the increase in intensity at the expense of broadening of the spectral lines.
- Try to start with a **small exposure time**, (Again, this depends on the amount of light you have incident on the spectrograph. Refer to ‘Dummy Example’, (sec: 5) for rough estimates.) this will ensure you do not saturate the chip.
- Find your spectra’s peaks by changing the wavelength range and/or grating. Once you have found your spectral lines you can move to a high resolution grating such as the 2400g/mm grating.
- Once a spectra is observed play around with the gain and exposure to give you the best signal, always work with the smallest slit width you can get away with.
- Once you are happy with the signal output, you are ready to work in acquisition mode with timing procedures and multifiles.

7) Calibration

Initially you should use the Cadmium lamp to check the systems calibration.

Good **parameters** for the Cd lamp are:-

Slit width: **5 μ m** (slit is located on side of spectrometer, a micrometer gauge is used to change the slit width.)

Exposure time: **80msec**


Gain: **50**

ROI: **Full chip**



Timing: **Free run**

Mode: **Shutter**

(WITH THESE PARAMETERS YOU SHOULD GET AN INTENSITY OF APPROX 1000 WITH THE 150G/MM GRATING)

Pick the **150g/mm grating** (by clicking the button Move Spectrograph ) and Move to: **480nm**

If the calibration is good you should observe lines at:

(click the peak find button  or info button  to observe your wavelengths)

Wavelength	Colour	State
643.9	Red	Singlet
508.6	Green	Triplet
480.0	Blue/Green	Triplet (strongest line)
467.8	Blue	Triplet
441.5	Violet	

The accuracy resolution and spectral window are affected by which grating you are using, 2400g/mm being the most accurate, 150g/mm covering the largest spectral window.

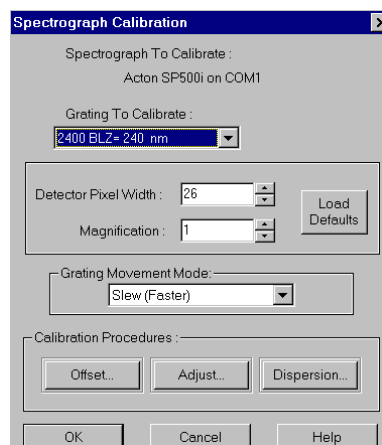
The details are summarised below:

Grating groove density	2400g/mm, ruled grating, blazed at 240nm	600g/mm, ruled grating, blazed at 1 micron	150g/mm, ruled grating, blazed at 300nm
Nominal spectral window for a 25mm wide detector	21.25nm	85nm	340nm
Resolution for an ICCD based on 4pixels (100microns)	0.085nm	0.34nm	1.36nm
Wavelength accuracy	+/- 0.1nm	+/- 0.4nm	+/- 1.6nm

If the wavelengths do not correspond to the expected wavelengths or the wavelengths observed do not lie within the resolution parameters illustrated above, a **re-calibration** will need to be performed.

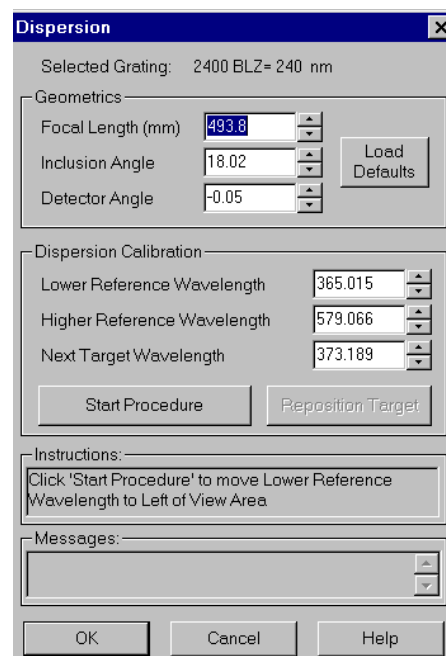
Instead of a full calibration, you are able to input previous calibration settings. To do this you need to go to; **Spectrograph/calibrate...**

- Check that the Detector Pixel Width is: 26
- Pick the grating you are going to calibrate.
- You will need to calibrate each grating in turn.



The settings you need to input are:

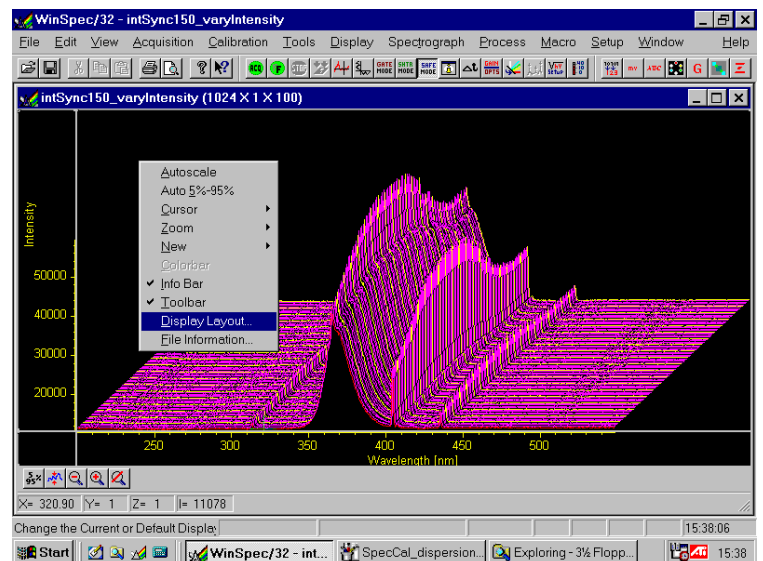
	Grating	2400g/mm	600g/mm	150g/mm
Offset	Offset value	-29	-31.5	-28.5
Adjust	Adjust value	-7.84954e-005	0	-0.000880887
Dispersion	Focal Length	493.8	495	500
	Inclusion Angle	18.02	18.87	17.17
	Detector Angle	-0.05	-0.05	0



- Once you have re-calibrated, acquire a spectra to ensure the calibration has been accepted.

8) Display Layout

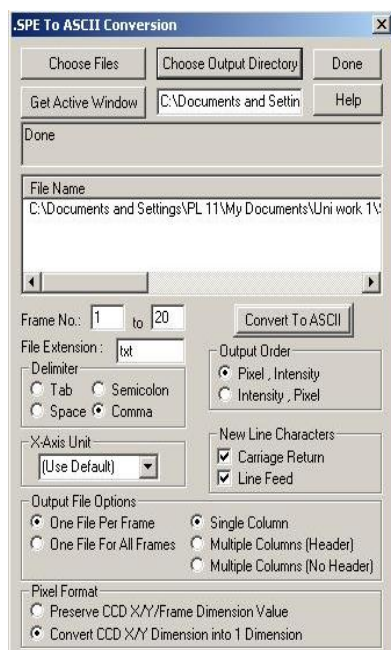
- To change your display layout **right click** on your spectra window.
- The dialogue box allows you to make many changes, such as 3d graph, image mode etc.. To keep changes you must click ‘save as default’.
- The image show here is in 3D mode, with marker curves on every 5 frames.




9) Multiple Frames

- When working with multiple frames (and single frames) it is convenient to view them in Grams, as this allows you to do extra processing not available in WinSpec.

In order to view a spectra in Grams you must first convert it to ASCII.

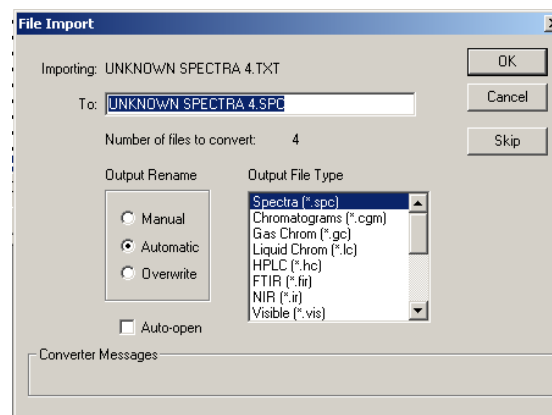


- Firstly, click the **convert to ASCII** button  on the toolbar.
- Now click ‘Get Active Window’.
- Enter the No. of frames **you have**, i.e. 1 to 100, 1 to 50 etc..
- Choose your output directory by clicking button and browsing your computer.
- Lastly, enter the rest of the settings as shown in the adjacent picture.
- When completed click ‘convert to ASCII’
- When the conversion is complete the dialogue box will display ‘Done’ (underneath Get Active window)

Next you need to open Grams, (you will need the dongle to open grams.)

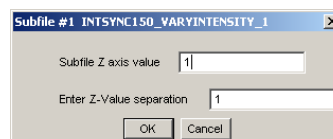
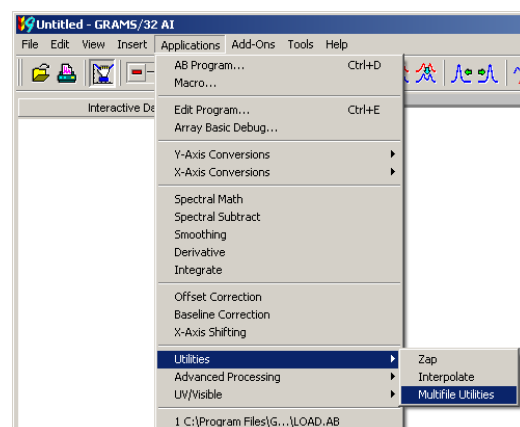
- click File/import..
(leave file types the way they are)
- Pick ASCII X,Y Data Pair Format (Non-Even X Spacing)
- Click Import
- Change the file type to All Files (*.*)
- Find and highlight all the .txt files you have just converted from WinSpec and click open.

- Choose: Output Rename, automatic
(the output name will default to the same as the input name. If you choose manual, you will have to rename each new file individually!)
- Pick: Output File Type, Spectra (*.spc)



Lastly you will need to build your multifile in Grams.

- Click, Applications/Utilities/Multifile utilities.
- Build your file from singles
- Pick **Numbered** files with **Standard Z-axis** label.
- Choose **Arbitrary** for **Z-axis** label.
- Your **Z spacing** (Selected) needs to be **Even**.
- Use a **New Filename**, then enter you preferred file name.
- Select your first sequential file. (number 1 in list of converted files)
- Check that the total number of files is correct.
- Lastly, enter **Subfile Z axis value** as **1**



10) Troubleshooting

Q: I am getting no response at all from spectrometer...

A: In order to check that you are getting light into the spectrometer, move the grating (any grating) to a wavelength of 0. Then acquire a spectra. You should get a strong line at zero order. If you are not check:

- That the MCP on the back of the camera is turned on.
- That the system is in shutter mode.
- If both of these are on, try increasing your exposure time.
- Still no response? Try moving to a different wavelength range, (you may have no spectral lines in range you are looking at). Alternatively, change to 150g/mm grating, this grating has a large spectral window, so you should be able to identify where your spectral lines are.
- If you are getting a zero order line but no spectra, you will need to calibrate the system, (sec: 7).

Appendix I:

Dummys Guide to: Spectrophotometer plotting operation

Author N. Lucas

DOS

- Create a file that you will write to:
 - cd C:\files
 - Edit *file.txt*
 - (Alt f) Save
 - (alt f) Exit

(to get to windows – alt + enter or ‘win’)

Windows

- program manager
- (alt f) File), Run, terminal.exe (found in windows directory)
- (alt f) File), Open, spec.trm
- (alt t) Transfers), receive text file
- Pick file to write to – c:\files\file.txt

Spectrophotometer

- Click PLOT

Windows, terminal.exe

- Transfers, stop
- File, exit

DOS

- cd \files
- Trm2tx2.exe
 - C:\files\file.txt
 - C:\files\fileout.txt
 - When says ‘Done’, press enter
- Copy c:\files\fileout.txt a:\fileout.txt
- Test your file? – edit c:\files\fileout.txt

NB: When opening in excel:

- Column B – y-axis
- Column D – x-axis

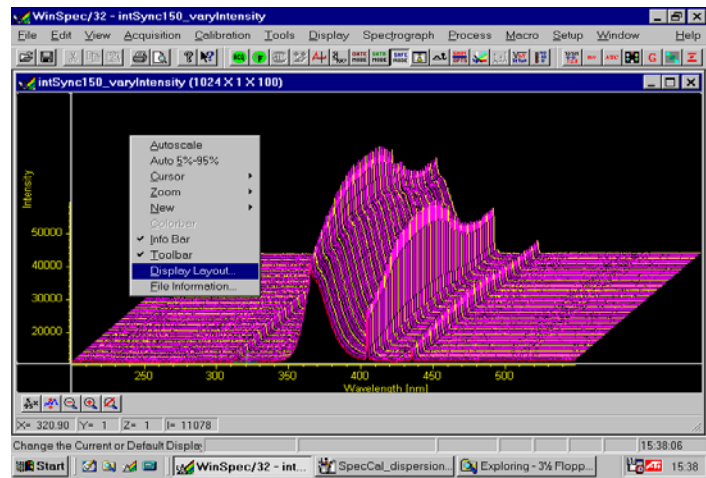
Appendix J:

Dummys Guide to:

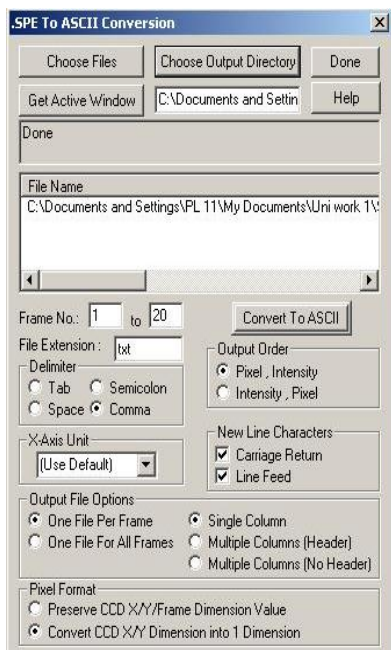
Conversion from WinSpec to Grams & Multifile Building


Author N. Lucas

1. Open the File in WinSpec
2. Change x axis (pixel) to x axis (nm):
 - a. right click on the graph
 - b. Display Layout...
 - c. Axes Tab
 - d. Units: (change to nm)



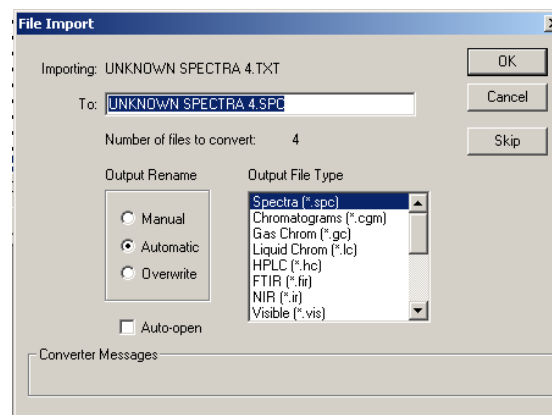
3. Convert it to ASCII then build a multifile in Grams:



- Firstly, click the **convert to ASCII** button  on the toolbar.
- Now click 'Get Active Window'.
- Enter the No. of frames **you have**, i.e. 1 to 100, 1 to 50 etc..
- Choose your output directory by clicking button and browsing your computer.
- Lastly, enter the rest of the settings as shown in the adjacent picture.
- When completed click 'convert to ASCII'
- When the conversion is complete the dialogue box will display 'Done' (underneath Get Active window)

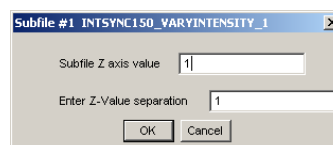
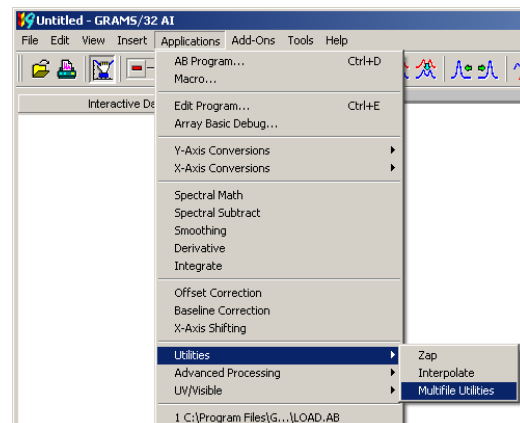
Next you need to open Grams, (you will need the dongle to open grams.)

- click **File/import..**
(leave file types the way they are)
- Pick **ASCIIXYS; ACSII X,Y Data Pair Format (Non-Even X Spacing)**
- Click **Import**
- Change the file type to **All Files (*.*)**
- Find and highlight all the **.txt** files you have just converted from WinSpec and click **open**.
- Choose: **Output Rename, automatic**
(the output name will default to the same as the input name. If you choose manual, you will have to rename each new file individually!)
- Pick: **Output File Type, Spectra (*.spc)**
- Click **OK**
- Open the converted files in Grams



If you need to build your **MULTIFILE** in Grams.

- Click, **A**pplications/Utilities/Multifile utilities.
- Build your file from singles
- Pick **Numbered** files with **Standard Z-axis** label.
- Choose **Arbitrary** for **Z-axis** label.
- Your **Z spacing** (Selected) needs to be **Even**.
- Use a **New Filename**, then enter you preferred file name.
- Select your first sequential file. (number 1 in list of converted files)
- Check that the total number of files is correct.
- Lastly, enter **Subfile Z axis value** as **1**



Appendix K:

Notes pertaining to catalogue data of elemental line spectra

VI/16 Line Spectra of the Elements (Reader, Corliss 1980-1981)

Line Spectra of the Elements

Reader J., Corliss Ch.H.

<CRC Handbook of Chemistry and Physics; NSRDS-NBS 68 (1980-1)>

ADC_Keywords: Spectroscopy ; Atomic physics

Description:

This catalog contains wavelength information for 99 different atomic species. The wavelengths for about 46,610 spectral lines of neutral through quadruply ionized atoms are tabulated. The information is presented in a general table of headers and references for each element and for each element a table of relative intensities, wavelengths ordered numerically, chemical elements, and stages of ionization indicated for each line in the wavelength range 40 to 40,000 Angstroms. Listed in the 99 data files are lines that appear in emission from the vacuum ultraviolet to the far infrared. For most atoms these lines are chosen from much larger lists so as to include the stronger observed lines in each spectral region. Below 2000 Angstroms the wavelengths are in vacuum; above 2000 Angstroms the wavelengths are in air. Wavelengths given to three decimal places are suitable for spectrograph calibration purpose such as Ne, Ar, Kr, Fe in the air region and C, N, O, Si, and Cu in the vacuum region. The intensity estimates are useful only as a rough indication of the appearance of a spectrum. The literature references as they appear the Handbook of Chemistry and Physics are given in a separate file.

File Summary:

FileName	Lrecl	Records	Explanations
ReadMe	80	.	This file
catalog.dat	58	46663	the catalog data
refs.dat	206	488	references to the catalog (refz, ref)
hcp_refs.dat	80	481	Refs. of CRC Handbook of Chemistry and Physics
notes.dat	89	430	notes & references to CRC Handbook Ch. & Ph. from original table headers

See also:

6086 : Bibliography of Atomic Line Identification Lists (Adelman 1996)

Byte-by-byte Description of file: catalog.dat

Bytes	Format	Units	Label	Explanations
1- 2	I2	---	Z	atomic number
4- 5	I2	---	ion	? ion
7- 11	I5	---	Int	*? spectral line intensity on arbitrary scale
13- 16	A4	---	line	notes on spectral line
18- 27	F10.3	0.1nm	wavel	wavelength in Angstroms
29	A1	---	Air_Vac	flag for wavelength in Air or Vacuum
31- 32	A2	---	Element	symbol for element
34- 37	A4	---	Spectrum	spectrum of element
39- 43	A5	---	oxide	spectral line belongs to oxide ???
45- 49	I5	---	bwavel	? truncated wavelength
51- 53	A3	---	note	no explanation for this field was given
55- 56	I2	---	refZ	reference section
57- 58	I2	---	ref	reference number in section

Note on Int: The spectral line intensities for each element are given as a guide to the relative strengths of a line in the spectrum of that element. From element to element and author to author different measures may have been employed to derive these numbers.

Byte-by-byte Description of file: refs.dat

Bytes	Format	Units	Label	Explanations
1- 2	I2	---	refZ	Reference section by atomic number
3- 4	I2	---	ref	? reference number in section
5-200	A196	---	text	*reference text

Note on text: In some cases the reference number is missing and the references are ordered by the element and spectrum which then start the reference text separating the identification and reference by a colon.

Byte-by-byte Description of file: hcp_refs.dat

Bytes	Format	Units	Label	Explanations
1- 80	A80	---	text	references to Handbook of Chem. and Phys.

The original data files contained embedded headers and references. That information for each elemental data file was extracted and used to create the file refs.dat. In the file notes.dat other information from the table header of each element including the references to the table in the Handbook of Chemistry and Physics are given. These references can be found in the hcp_refs.dat file described above.

Byte-by-byte Description of file: notes.dat

```

-----
Bytes Format Units Label Explanations
-----
1- 8 A8 --- element abbreviated element (alphabetical by element)
10- 89 A80 --- text references to the table of references in file
                    hcp_refs.dat extracted from the original
                    file headers
-----

```

Remarks:

The brief description for the data was prepared by J. Lyu based on documentation accompanying the catalog. Additional reformatting was done by Paul Kuin (ADC). The original data and text were separated. The data were reformatted and ion number was included. All elements were combined in one data file. The header information was separated to the file refs.dat and notes.dat. Additional notes were included as required in the ReadMe documentation.

```

=====
=====
(End)    Paul Kuin [NASA/ADC] 07-Oct-1996

```

Appendix L:

Pascal program for spectral line search, Author N. Lucas

```

program wavefini;
uses crt,dos;
const err: array[1..3] of real=(0.1,0.4,1.6);(nanometers)
var F:text;
    R1:text;
    exinf:array[0..5] of char;
    av :array[0..2] of char;
    esymb:array[0..3] of char;
    spec :array[0..5] of char;
    oxide:array[0..6] of char;
    wave:real;
    anumb,ion,int,refsec,refno,lno:longint;
    grating,wn,wavenumb,j,k,l,m,n,o,p,q,s,t,z:integer;
    first:boolean;
    upperlim,lowerlim,wavearray:array [0..20] of real;
    wavenumbx: string[2];w1:string[1];
    P1: string[9];
    P2: string[4];
    curfile: string[15];
(*****
Procedure multpeak;
begin
    writeln('How many wavelengths to be input? (max=10)');
    readln(wavenumb);
    writeln('Which grating was used? ');
    writeln('ENTER: 1 for 2400g/mm,');
    writeln('    2 for 600g/mm,');
    write('    3 for 150g/mm : ');
    readln(grating);
    for wn := 1 to wavenumb do
    begin
        write('What is wavelength ',wn:1,'? '); readln(wavearray[wn]);
    end;
    for j:=1 to wavenumb do
    begin
        upperlim[j]:= wavearray[j]+err[grating];
        lowerlim[j]:= wavearray[j]-err[grating];
        writeln('Upperlimit for wavelength ',j:1,' is: ',upperlim[j]:10:4);
        writeln('Lowerlimit for wavelength ',j:1,' is: ',lowerlim[j]:10:4);
    end;
    writeln('Press Enter to start analysis..');
    readln;
end;
(*****

```

```
begin
  clrscr;
  multpeak;
  assign(F,'c:\ASdata.txt');
  reset(F);
  lno:=0;
  first:=true;
  while (anumb<500) do
  begin
    (lno:=lno+1;)
    read(F,anumb);
    write(anumb:3);
    read(F,ion);
    write(ion:3);
    read(F,int);
    write(int:6);
    read(F,exinf[0]); (read tab)
    write(' ');
    j:=0;
    repeat
      j:=j+1;
      read(F,exinf[j]);
    until exinf[j]=chr(9);
    j:=j-1;
    for k:=1 to j do write(exinf[k]:1); (write(' no of chars is 'j,' ');)
    write(' ');
    read (F,wave);
    write(wave:7:4);
    read(F,av[0]); (read tab)
    write(' ');
    l:=0;
    repeat
      l:=l+1;
      read(F,av[l]);
    until av[l]=chr(9);
    l:=l-1;
    for m:=1 to l do write(av[m]:1);
    write(' ');
    n:=0;
    repeat
      n:=n+1;
      read(F,esymb[n]);
    until esymb[n]=chr(9);
    n:=n-1;
    for o:=1 to n do write(esymb[o]:1);
    write(' ');
    s:=0;
    repeat
      s:=s+1;
      read(F,spec[s]);
```

```

until spec[s]=chr(9);
s:=s-1;
for t:=1 to s do write(spec[t]:1);
write(' ');
p:=0;
repeat
p:=p+1;
read(F,oxide[p]);
until oxide[p]=chr(9);
p:=p-1;
for q:=1 to p do write(oxide[q]:1);
read(F,refsec);
write(refsec:5);
read(F,refno);
write(refno:5);
read;
wave:=(wave/10); (change to nm)
for z:=1 to wavenumb do
begin
if z<10 then
begin
str(z,w1);
wavenumbx:=concat('0',w1);
end
else str(z,wavenumbx);
P1:= 'c:\output';
P2:= '.txt';
curfile:= P1 + wavenumbx + P2;
assign(R1,curfile);
if first then
begin
rewrite(R1);
end
else append(R1);
if (wave>=lowerlim[z]) and (wave<=upperlim[z]) then
begin
write(R1,anumb:1,chr(9),ion:1,chr(9),int:1,chr(9));
for k:=1 to j do write(R1,exinf[k]:1);
write(R1,chr(9),wave:4:4);
write(R1,chr(9));
for m:=1 to l do write(R1,av[m]:1);
write(R1,chr(9));
for o:=1 to n do write(R1,esymb[o]:1);
write(R1,chr(9));
for t:=1 to s do write(R1,spec[t]:1);
write(R1,chr(9));
for q:=1 to p do write(R1,oxide[q]:1);
writeln(R1,chr(9),refsec:2,chr(9),refno:2);
end;
close(R1);

```



```
end;  
    writeln; (writeln(' In ',In);)  
    first:=false;  
end;  
close(F);  
writeln('Press Enter to complete analysis..');  
readln;  
end.
```

Appendix M:

Access queries to interrogate spectral data, Author N. Lucas

```
Option Compare Database
Private Sub two_wavelengths_Click()
On Error GoTo Err_two_wavelengths_Click
    Dim stDocName As String
    stDocName = "Between wavelengths?"
    DoCmd.OpenQuery stDocName, acNormal, acEdit
Exit_two_wavelengths_Click:
    Exit Sub
Err_two_wavelengths_Click:
    MsgBox Err.Description
    Resume Exit_two_wavelengths_Click
End Sub
Private Sub single_wavelength_Click()
On Error GoTo Err_single_wavelength_Click
    Dim stDocName As String
    stDocName = "Single wavelength or all"
    DoCmd.OpenQuery stDocName, acNormal, acEdit
Exit_single_wavelength_Click:
    Exit Sub
Err_single_wavelength_Click:
    MsgBox Err.Description
    Resume Exit_single_wavelength_Click
End Sub
Private Sub single_wavelength1_Click()
On Error GoTo Err_single_wavelength1_Click
    Dim stDocName As String
    stDocName = "Single wavelength or all"
    DoCmd.OpenQuery stDocName, acNormal, acEdit
Exit_single_wavelength1_Click:
    Exit Sub
Err_single_wavelength1_Click:
    MsgBox Err.Description
    Resume Exit_single_wavelength1_Click
End Sub
Private Sub single_or_all_1_Click()
On Error GoTo Err_single_or_all_1_Click
    Dim stDocName As String
    stDocName = "Single wavelength or all 1"
    DoCmd.OpenQuery stDocName, acNormal, acEdit
Exit_single_or_all_1_Click:
    Exit Sub
Err_single_or_all_1_Click:
    MsgBox Err.Description
    Resume Exit_single_or_all_1_Click
```

```
End Sub
Private Sub single_or_all_2_Click()
On Error GoTo Err_single_or_all_2_Click
    Dim stDocName As String
    stDocName = "Single wavelength or all 2"
    DoCmd.OpenQuery stDocName, acNormal, acEdit
Exit_single_or_all_2_Click:
    Exit Sub
Err_single_or_all_2_Click:
    MsgBox Err.Description
    Resume Exit_single_or_all_2_Click
End Sub
Private Sub single_or_all_3_Click()
On Error GoTo Err_single_or_all_3_Click
    Dim stDocName As String
    stDocName = "Single wavelength or all 3"
    DoCmd.OpenQuery stDocName, acNormal, acEdit
Exit_single_or_all_3_Click:
    Exit Sub
Err_single_or_all_3_Click:
    MsgBox Err.Description
    Resume Exit_single_or_all_3_Click
End Sub
Private Sub single_or_all_4_Click()
On Error GoTo Err_single_or_all_4_Click
    Dim stDocName As String
    stDocName = "Single wavelength or all 4"
    DoCmd.OpenQuery stDocName, acNormal, acEdit
Exit_single_or_all_4_Click:
    Exit Sub
Err_single_or_all_4_Click:
    MsgBox Err.Description
    Resume Exit_single_or_all_4_Click
End Sub
Private Sub single_or_all_5_Click()
On Error GoTo Err_single_or_all_5_Click
    Dim stDocName As String
    stDocName = "Single wavelength or all 5"
    DoCmd.OpenQuery stDocName, acNormal, acEdit
Exit_single_or_all_5_Click:
    Exit Sub
Err_single_or_all_5_Click:
    MsgBox Err.Description
    Resume Exit_single_or_all_5_Click
End Sub
```

Appendix N:

VBA program for spectral line search, Author N. Lucas

Option Compare Database

Option Explicit

Private Sub cmdMultWave_Click()

Dim varElement, varIons, varWaveNumb, varGrating As Variant

Dim sngErr As Single

Dim bytGrating As Byte

Dim intLV_WN, intLV_lim, intLV_WL, intWaveNumb As Integer

Dim sngErrArray(1 To 3), sngWaveArray(1 To 100), sngUpperLimArray(1 To 100),
sngLowerLimArray(1 To 100) As Single

Dim strSQL, strSQLIons, strSQLFinal As String

Dim db, db1 As Database

Dim rs, rsIon, rsIonWav As Recordset

Dim appExcel As Excel.Application 'app - application

Dim wkb As Excel.Workbook 'wkb - workbook

Dim wks, wksName As Excel.Worksheet 'wks - worksheet

Dim rng As Excel.Range 'rng - range

Dim wavelength As Single

sngErrArray(1) = 1

sngErrArray(2) = 4

sngErrArray(3) = 16

WavelengthsQuestion:

varWaveNumb = InputBox("How many wavelengths to be input?")

If varWaveNumb < 1 Then

MsgBox "Please enter an Integer, greater than or equal to 1", vbInformation

GoTo WavelengthsQuestion

ElseIf varWaveNumb = "" Then

MsgBox "You pressed 'ok' or 'cancel'. Program exected!", vbExclamation

Exit Sub

ElseIf IsNumeric(varWaveNumb) = False Then

MsgBox "Enter a number please", vbCritical

GoTo WavelengthsQuestion

ElseIf varWaveNumb > 99 Then

MsgBox "Please limit to less than 99 for now", vbInformation

GoTo WavelengthsQuestion

End If

GratingQuestion:

```
varGrating = InputBox("Which grating did you use? Enter: 1 for 2400g/mm, 2 for
600g/mm, 3 for 150g/mm")
If varGrating < 1 Then
  MsgBox "Please enter an Integer, greater than or equal to 1", vbInformation
  GoTo GratingQuestion
ElseIf varGrating = "" Then
  MsgBox "You pressed 'ok' or 'cancel'. Program exected!", vbExclamation
  Exit Sub
ElseIf IsNumeric(varGrating) = False Then
  MsgBox "Enter a number please", vbCritical
  GoTo GratingQuestion
ElseIf varGrating > 3 Then
  MsgBox "Please limit your answer to 1, 2 or 3", vbInformation
  GoTo GratingQuestion
End If
```

'ElementQuestion:

```
'varElement = InputBox("What elements do you want to search?")
'or varElement = InputBox("How many elements do you want to search?") loop for
each time...
```

'StoreOfWaveArray:

```
For intLV_WN = 1 To varWaveNumb
  sngWaveArray(intLV_WN) = (InputBox("What is wavelength " & intLV_WN & "
(in Angstroms)?"))
  'sngWaveArray(intLV_WN) = sngWaveArray(intLV_WN) * 0.1
Next intLV_WN
```

'StoreOfUpp&LowLims:

```
For intLV_lim = 1 To varWaveNumb
  sngUpperLimArray(intLV_lim) = sngWaveArray(intLV_lim) +
sngErrArray(varGrating)
  sngLowerLimArray(intLV_lim) = sngWaveArray(intLV_lim) -
sngErrArray(varGrating)
Next intLV_lim
```

IonQuestion:

```
varIons = InputBox("How many Ions do you want to include in search? 1 to 5")
If varIons < 1 Then
  MsgBox "Please enter an Integer, greater than or equal to 1", vbInformation
  GoTo IonQuestion
ElseIf varIons = "" Then
  MsgBox "You pressed 'ok' or 'cancel'. Program exected!", vbExclamation
  Exit Sub
ElseIf IsNumeric(varIons) = False Then
  MsgBox "Enter a number please", vbCritical
  GoTo IonQuestion
ElseIf varIons > 5 Then
  MsgBox "A maximum of 5 please.", vbInformation
```

```
    GoTo IonQuestion
End If

'StringsToetherWithVariables and PutsInDatabase:
For intLV_WL = 1 To varWaveNumb
    strSQL = "Select * From tblAtomicSpectraData Where ([wavelength]>=" &
sngLowerLimArray(intLV_WL) & "" _
    & " And [wavelength] <=" & sngUpperLimArray(intLV_WL) & " ) And [ion] <="
& varIons
    Set db = CurrentDb
    Set rs = db.OpenRecordset(strSQL)
    If intLV_WL = 1 Then
        Set appExcel = New Excel.Application
        Set wkb = appExcel.Workbooks.Add
    End If
    If intLV_WL >= 4 Then
        Set wks = wkb.Worksheets.Add
    End If
    Set wks = wkb.Worksheets("Sheet" & intLV_WL & "")
    wkb.Worksheets("Sheet" & intLV_WL & "").Name = sngWaveArray(intLV_WL)
    Set rng = wks.Range("A1")
    appExcel.Visible = True
    rng.CopyFromRecordset rs
Next intLV_WL

End Sub
```

Appendix O:

VBA programmes for data analysis, correlation and formatting. Author N. Lucas

```

Option Explicit
Sub mcroCopyYData()
  Dim varShtNm As Variant
' mcroCopyYData Macro
' Macro recorded 15/12/2005 by Natasha Lucas
' Keyboard Shortcut: Ctrl+g
  varShtNm = InputBox("Please enter sheet name")
  Sheets(varShtNm).Select
  Range("B1").Select
  Range(Selection, Selection.End(xlDown)).Select
  Application.CutCopyMode = False
  Selection.Copy
  Sheets("Data").Select
  Range("B3") = varShtNm
  Range("B4").Select
  'ActiveSheet.Paste
  Selection.PasteSpecial Paste:=xlPasteValues, Operation:=xlNone, SkipBlanks _
    :=False, Transpose:=False
  Columns("B:B").Select
  Selection.Insert Shift:=xlToRight
  Sheets(varShtNm).Select
End Sub

```

```

Option Explicit
Sub mcroCompileDataToPeakData()
' Macro recorded 03/03/2007 by Natasha Lucas
'ctrl + j
Dim varRange As Variant
Dim varRow As Variant
varRange = InputBox("what is the range you would like, e.g. 151 'NB c:q")
varRow = InputBox("what row number would you like to paste the data to")
Sheets("data").Select
  Range("C" & varRange & ":q" & varRange).Select
  Selection.Copy
  Sheets("peak data").Select
  Range("D" & varRow).Select
  Selection.PasteSpecial Paste:=xlPasteValues, Operation:=xlNone, SkipBlanks _
    :=False, Transpose:=False
End Sub

```

```
Option Explicit
Function PressFind_p1_Style(PressCodeArg)
  If PressCodeArg = "p1" Then
    PressFind_p1_Style = "1600"
  ElseIf PressCodeArg = "p2" Then
    PressFind_p1_Style = "1500"
  ElseIf PressCodeArg = "p3" Then
    PressFind_p1_Style = "1400"
  ElseIf PressCodeArg = "p4" Then
    PressFind_p1_Style = "1300"
  ElseIf PressCodeArg = "p5" Then
    PressFind_p1_Style = "1200"
  ElseIf PressCodeArg = "p6" Then
    PressFind_p1_Style = "1100"
  ElseIf PressCodeArg = "p7" Then
    PressFind_p1_Style = "1000"
  ElseIf PressCodeArg = "p8" Then
    PressFind_p1_Style = "780"
  ElseIf PressCodeArg = "p9" Then
    PressFind_p1_Style = "530"
  ElseIf PressCodeArg = "p10" Then
    PressFind_p1_Style = "300"
  ElseIf PressCodeArg = "p11" Then
    PressFind_p1_Style = "100"
  ElseIf PressCodeArg = "p12" Then
    PressFind_p1_Style = "0.05"
  End If
End Function
```

```
Option Explicit
Sub mcroSelect()
' Macro recorded 27/02/2007 by Natasha Lucas
Dim wks As Worksheet
Dim varWkb As Variant
Dim varWKbnm As Variant
Dim varRange As Variant
Dim varColumn As Variant
Dim varLVi As Variant
Dim varLVx As Variant
Dim varCurNum As Variant
Dim varDir As Variant
Dim varFileNo As Variant
Dim varPasteWkb As Variant
varWKbnm = InputBox("Please put in the center variable, eg iris size or part number")
'varRange = InputBox("Please enter the cell reference required, eg B311") you can use this if you wish - if you don't, don't forget to change the range lower down!
```



```

varColumn = InputBox("Please enter the column you would like to input the data
to")
varFileNo = InputBox("please enter the number of sequential files")
varDir = InputBox("Please enter the file extension where cut and paste files are
based")
varPasteWkb = InputBox("please enter the workbook you would like to paste to")
For varLVi = 2 To (varFileNo + 1)
varLVx = varLVi - 1
varWkb = "exp173ap7_vac_253_" & varLVx & ".txt"
'varWkb = "exp194a_" & varWkbnm & "_253_" & varLVx & ".txt"
'picking the workbook
Workbooks.OpenText Filename:= _
varDir & "\" & varWkb & "" _
, Origin:=xlMSDOS, StartRow:=1, DataType:=xlDelimited, TextQualifier:= _
xlDoubleQuote, ConsecutiveDelimiter:=False, Tab:=True, Semicolon:=False, _
Comma:=False, Space:=False, Other:=False, FieldInfo:=Array(1, 1), _
TrailingMinusNumbers:=True
'getting the data
Range("b288").Select
Selection.Copy
Workbooks.Open Filename:= _
varDir & "\" & varPasteWkb & ""
'Windows("varPasteWkb").Activate
Sheets("avg data").Select
Range(varColumn & varLVi).Select
ActiveSheet.Paste
ActiveWindow.Close savechanges:=True
'closing the file
Windows(varWkb).Activate
Application.CutCopyMode = False
ActiveWindow.Close
Next varLVi
End Sub

```

Option Explicit

```

Sub mcroSelectSheets()
' mcroSelectSheets Macro
' Macro recorded 28/02/2007 by Natasha Lucas
' Keyboard Shortcut: Ctrl+r
Dim wks As Worksheet
Dim varWks As Variant
Dim varWKbnm As Variant
Dim varRange As Variant
Dim varColumn As Variant
Dim varLVi As Variant
Dim varLVx As Variant
Dim varCurNum As Variant
Dim varWkb As Variant
Dim varShtNm As Variant

```

```

'varWkbnm = InputBox("Please put in the shot number")
varRange = InputBox("Please enter the cell reference required, eg B311") 'you can
use this if you wish - if you don't, don't forget to change the range lower down!
varColumn = InputBox("Please enter the column you would like to input the data
to")
'varWkb = InputBox("please enter the name of the workbook you would like to past
to")
varWkb = "AVG_157_si pressure varn_595_252nm.xls" ' InputBox("please enter
the file name that you are working on")
'getting the data
Windows(varWkb).Activate
For varLVi = 2 To 16
varLVx = varLVi - 1
'varShtNm = InputBox("what is the sheet name")
'varWks = varWkb      ""exp118p7_air_253_" & varLVx & ""
Sheets(varShtNm).Select
Range(varRange).Select
Selection.Copy
Sheets("peak data").Select
Range(varColumn & varLVi).Select
ActiveSheet.Paste
Next varLVi
End Sub

```

```

Option Explicit
Sub mcrCompileData1()
'mcrCompileData1 Macro
'Macro recorded 01/03/2007 by Natasha Lucas
Dim varLVi As Variant
Dim varWkb As Variant
Dim varLVx As Variant
Dim varPasteWkb As Variant
Dim varCutWkb As Variant
Dim varDir As Variant
Dim varWKbnm As Variant
'varCutWkb = InputBox("Please enter the name of the file you would like to cut
from (excluding no. and file extension)")
varDir = InputBox("Please enter the file extension where cut and paste files are
based")
varPasteWkb = InputBox("Please enter name of the file you wish to paste to (inc.
file extension)")
Do Until varWKbnm = "x"
varWKbnm = InputBox("Please put in the center variable, eg iris size or part
number - when completed enter 'x'")
If varWKbnm = "x" Then Exit Do
For varLVi = 2 To 16
varLVx = varLVi - 1
varWkb = "exp185_mut8l_" & varWKbnm & "_276_" & varLVx & ".txt"
Workbooks.OpenText Filename:= _

```

```
varDir & "\" & varWkb & "" _
, Origin:=xlMSDOS, StartRow:=1, DataType:=xlDelimited, TextQualifier:= _
xlDoubleQuote, ConsecutiveDelimiter:=False, Tab:=True, Semicolon:=False, _
Comma:=False, Space:=False, Other:=False, FieldInfo:=Array(1, 1), _
TrailingMinusNumbers:=True
Range("A1:B1").Select
Range(Selection, Selection.End(xlDown)).Select
Selection.Copy
Workbooks.Open Filename:= _
varDir & "\" & varPasteWkb & ""
'Windows(varPasteWkb).Activate
If varLVx = 1 Then
    Sheets.Add
    ActiveSheet.Name = varWKbnm
    Range("B1").Select
    ActiveCell.FormulaR1C1 = varLVx
    Range("A2:B2").Select
    ActiveSheet.Paste
    Columns("B:B").Select
    Selection.Insert Shift:=xlToRight
    ActiveWindow.Close savechanges:=True
ElseIf varLVx > 1 Then
    Sheets(varWKbnm).Select
    Range("B1").Select
    ActiveCell.FormulaR1C1 = varLVx
    Range("A2:B2").Select
    ActiveSheet.Paste
    Columns("B:B").Select
    Selection.Insert Shift:=xlToRight
    ActiveWindow.Close savechanges:=True
End If
Windows(varWkb).Activate
Application.CutCopyMode = False
ActiveWindow.Close
Next varLVi
Loop
End Sub
```

Appendix P:

Pascal program to analyse the intensity of selected emission peaks,

Author N. Lucas

```

program peakshot;
uses crt;
const err: array[1..3] of real=(0.1,0.4,1.6);(nanometers)
var F:text;
    R1:text;
    name1:array[0..3] of char;
    name2:array[0..3] of char;
    w1,int:real;
    shot:integer;
    lno:longint;
    grating,wn,wavenu,shotnumb,b,j,q,z:integer;
    first,loop1:boolean;
    upperlim,lowerlim,wavearray:array [0..50] of real;
    wavenumbx: string[3];w1:string[1];w2:string[2];
    P1: string[9];
    P2: string[4];
    curfile: string[15];
    nowfile: string[15];
(*****)
Procedure multpeak;
begin
    writeln('How many peaks to search? (max 50)');
    readln(wavenu);
    writeln('How many shots to analyse? (max 99)');
    readln(shotnumb);
    writeln('Which grating was used? ');
    writeln('ENTER: 1 for 2400g/mm,');
    writeln('    2 for 600g/mm,');
    write('    3 for 150g/mm : ');
    readln(grating);
    for wn := 1 to wavenu do begin
        write('What is wavelength of peak ',wn:1,'? (nm) '); readln(wavearray[wn]);
    end;
    for j:=1 to wavenu do begin
        upperlim[j]:= wavearray[j]+err[grating];
        lowerlim[j]:= wavearray[j]-err[grating];
        writeln('Upperlimit for wavelength ',j:1,' is: ',upperlim[j]:10:4);
        writeln('Lowerlimit for wavelength ',j:1,' is: ',lowerlim[j]:10:4);
    end;
    writeln('Press Enter to start analysis..');
    readln;
end;

```

```

begin
  clrscr;
  multpeak;
  loop1:=true;
  for b:=1 to shotnumb do begin (loops over number of shots)
    if b<10 then begin (finds/makes name of input file)
      str(b,w1);
      wavenumbx:=concat('0',w1);
    end
    else str(b,wavenumbx);
    P1:= 'c:\PTable';
    P2:= '.txt';
    nowfile:= P1 + wavenumbx + P2;
    assign(F,nowfile);
    reset(F);
    repeat begin (loops over number of rows)
      read(F,w1); (reads input file)
      write(w1:7:4);
      read(F,int);
      write(int:14:4);
      writeln;
      for z:=1 to wavenumb do begin (loops over number of wavelengths)
        if z<10 then begin (finds/makes name of output file)
          str(z,w1);
          wavenumbx:=concat('0',w1);
        end
        else str(z,wavenumbx);
        P1:= 'c:\output';
        P2:= '.txt';
        curfile:= P1 + wavenumbx + P2;
        assign(R1,curfile);
        if loop1 then begin
          rewrite(R1);
        end
        else append(R1);
        if (wl>=lowerlim[z]) and (wl<=upperlim[z]) then begin
          writeln(R1,wl:4:4,chr(9),b:4,chr(9),int:9:4);
          (writes data to output file)
        end;
        close(R1);
      end;
      loop1:=false;
    end
    until wl<100;
    close(F);
    writeln;
  end;
  writeln('Press Enter to complete analysis..');
  readln;
end.

```

Appendix Q:

Pascal program to calculate the relative standard deviation of a dataset, Author N. Lucas

```
program relstddev;
uses crt;
var n,vn,x:longint;
    xbar,newvalue,SD,RSD: real;
    valuearray:array[0..100]of real;

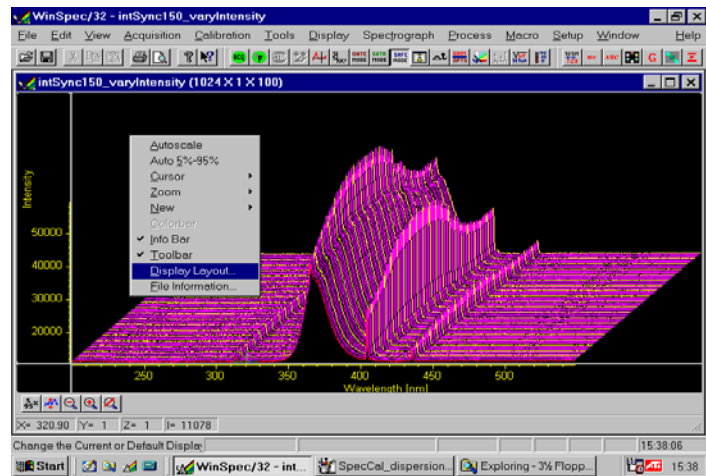
begin
  clrscr;
  write('How many values to be input? (max=100) '); readln(n);
  writeln;
  for vn:=1 to n do begin
    write('What is value ',vn:1,'? '); readln(valuearray[vn]);
  end;
  newvalue:=0;
  for x:=1 to n do begin
    newvalue:= (newvalue + valuearray[x]);
  end;
  xbar:=(newvalue/n);
  newvalue:=0;
  for x:=1 to n do begin
    newvalue:= (newvalue + (sqr(valuearray[x]-xbar)));
  end;
  SD:=sqrt(newvalue/(n-1));
  RSD:=((100*SD)/xbar);
  writeln;writeln;
  writeln('Average is:',xbar:8:1);writeln;
  writeln('Standard Deviation is:',SD:8:1);writeln;
  writeln('Relative Standard Deviation is:',RSD:8:1,'%');
  writeln;writeln;
  writeln('Press enter to continue');
  readln;
end.
```

Appendix R:

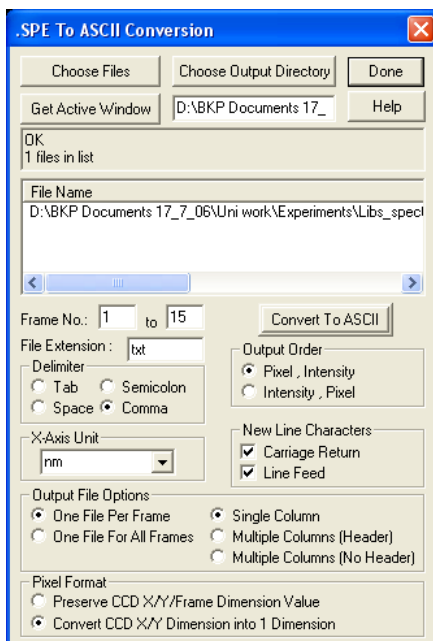
Dummys Guide to: Acquire a Depth Profile


Author N. Lucas

4. Open the File in WinSpec
5. Change x axis (pixel) to x axis (nm):
 - a. right click on the graph
 - b. Display Layout...
 - c. Axes Tab
 - d. Units: (change to nm)



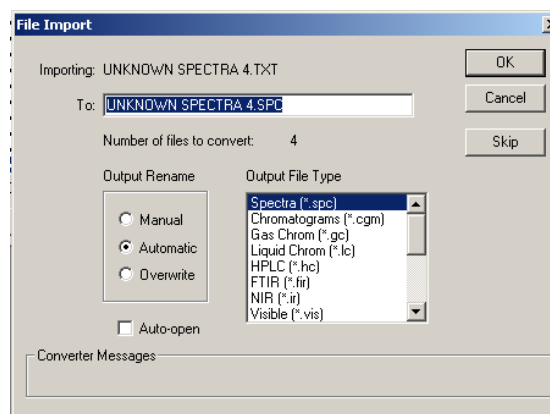
6. Convert it to ASCII then build a multiframe in Grams:



- Firstly, click the **convert to ASCII** button  on the toolbar.
- Now click 'Get Active Window'.
- Enter the No. of frames **you have**, i.e. 1 to 100, 1 to 50 etc..
- Choose your output directory by clicking button and browsing your computer.
- Lastly, enter the rest of the settings as shown in the adjacent picture.
- When completed click 'convert to ASCII'
- When the conversion is complete the dialogue box will display 'Done' (underneath Get Active window)

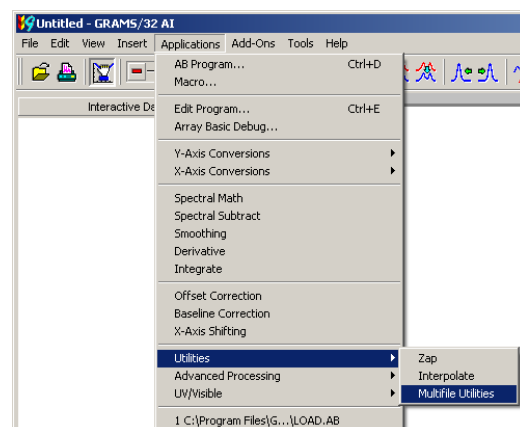
Next you need to open Grams, (you will need the dongle to open grams.)

- click File/import..
(leave file types the way they are)
- Pick ASCII X,Y Data Pair Format (Non-Even X Spacing)
- Click Import
- Change the file type to All Files (*.*)
- Find and highlight all the .txt files you have just converted from WinSpec and click open.
- Choose: Output Rename, automatic
(the output name will default to the same as the input name. If you choose manual, you will have to rename each new file individually!)
- Pick: Output File Type, Spectra (*.spc)

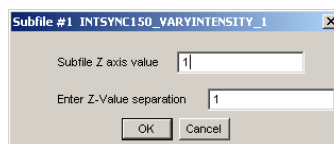


Lastly you will need to build your multifile in Grams.

- Click, Applications/Utilities/Multifile utilities.
- Build your file from singles
- Pick **Numbered** files with **Standard Z-axis** label.
- Choose **Arbitrary** for **Z-axis label**.
- Your **Z spacing** (Selected) needs to be **Even**.
- Use a **New Filename**, then enter you preferred file name.
- Select your first sequential file. (number 1 in list of converted files)
- Check that the total number of files is correct.



- Lastly, enter **Subfile Z axis value** as 1



7. Save the Peak Tables for each subfile in multifile

Before doing this use the 'Plot with Peak tools' tab and adjust the 'Peak Picking Settings' to optimum for your chosen peaks.

- a. Pick the next subfile using:

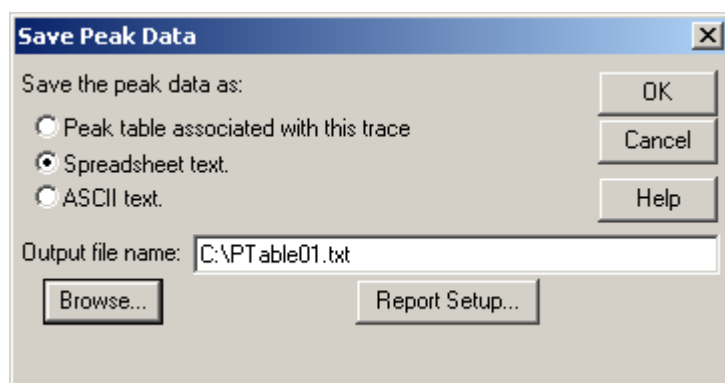


- b. Save the Peak Table using:



- c. Save as Spreadsheet text

- d. Save files as:
C:\Ptable#.txt



8. Open Excel worksheets: (or add them to VBA using attached code below)

- a. VBA Format PTable.xls
- b. VBA Graphs PTable.xls
- c. VBA Graphformat Ptable.xls

9. Run ♠ macro (or go to: Tools, Macro, Macros, FPT - run)

NB: You will need to know the number of shots taken
You should save the file when prompted!

10. Run Peakshot.pas (not in excel – separate program!)

NB: You will need to know the number of shots taken and the number of peaks/wavelengths to be searched. Choose the wavelengths from the Galactic program that you would like to search for. **Write down wavelength and the order you entered them, you will need them again later!**

11. Run ♣ macro (or go to: Tools, Macro, Macros, GPT - run)

NB: When prompted, keep the data on the clipboard.

12. Run 'format graph' macro (Click on graph you want to format, hit ctrl&g, the graph should be formatted and put onto sheet1.)

When completed rename sheet1 if necessary.

When prompted enter the wavelength of the peak referring to the data set currently plotting. (you have this written down from earlier!). Each subsequent time you are prompted, enter the next wavelength you searched, **following strict order**

with how you entered them on the Peakshot Program

13. Your depth profile spreadsheet should now be finished!

VBA Programs:

```
Sub FPT()
' FPT Macro
' Macro recorded 07/04/2004 by Natasha Lucas
' Keyboard Shortcut: Ctrl+f
  myPeak = Application.InputBox("Enter number of Shots? (max 99)")
  For y = 1 To myPeak
    ChDir "C:\"
    If y < 10 Then
      filem = "C:\PTable0" + Format(y) + ".txt"
    Else
      filem = "C:\PTable" + Format(y) + ".txt"
    End If
    Workbooks.OpenText Filename:=filem, Origin:=xlMSDOS, StartRow:=1,
    DataType:=xlDelimited, TextQualifier:=xlDoubleQuote, _
      ConsecutiveDelimiter:=False, Tab:=True, Semicolon:=False, Comma:=False _
      , Space:=False, Other:=False, FieldInfo:=Array(1, 1), _
      TrailingMinusNumbers:=True
    Rows("1:3").Select
    Selection.Delete Shift:=xlUp
    ActiveWorkbook.Save
    ActiveWindow.Close
  Next y
End Sub
```

```
Sub GPT()
' GPT Macro
' Macro recorded 13/04/2004 by Natasha Lucas
Dim mysheet As Worksheet
Dim mychart As Chart
Workbooks.Add
  mySave = Application.InputBox("Enter the new filename you would like...")
  ActiveWorkbook.SaveAs Filename:=mySave, FileFormat:=xlNormal, _
    Password:="", WriteResPassword:="", ReadOnlyRecommended:=False, _
    CreateBackup:=False
  myShot = Application.InputBox("Enter number of shots taken")
  myPeak = Application.InputBox("Enter number of peaks searched? (max 50)")
  For y = 1 To myPeak
    ChDir "C:\"
    If y < 10 Then
      filem = "C:\output0" + Format(y) + ".txt"
    Else
      filem = "C:\output" + Format(y) + ".txt"
    End If
```

```
Workbooks.OpenText Filename:=filenm, Origin:=xlMSDOS, StartRow:=1,
DataType:=xlDelimited, TextQualifier:=xlDoubleQuote, _
    ConsecutiveDelimiter:=False, Tab:=True, Semicolon:=False, Comma:=False _
    , Space:=False, Other:=False, FieldInfo:=Array(1, 1), _
    TrailingMinusNumbers:=True
Cells.Select
Selection.Copy
ActiveWorkbook.Close
Windows(mySave).Activate
'create a new worksheet
Set mysheet = Sheets.Add(Type:=xlWorksheet) '<<
mysheet.Paste
Application.CutCopyMode = False
'rename the new sheet
mysheet.Name = y
Set mychart = Sheets.Add(Type:=xlChart) '<<
mychart.ChartType = xlXYScatter '<<
mychart.Location Where:=xlLocationAsNewSheet
mychart.SetSourceData Source:=mysheet.Range("B:C"), PlotBy:=xlColumn
'myChartnm = Application.InputBox("Enter wavelength of current peak, starting
with first")
ActiveWorkbook.Save
Next y
End Sub
```